IN VITRO BIOACTIVITY OF THE SURFACE-TREATED Ti6Al4V OPEN CELL FOAMS

A Thesis Submitted to
the Graduate School of Engineering and Sciences of
İzmir Institute of Technology
in Partial Fulfillment of the Requirements for the Degree of

DOCTOR OF PHILOSOPHY

in Mechanical Engineering

by
Uğur TÜRKAN

June 2010
İZMİR

We approve the thesis of **Uğur TÜRKAN**

_____

Prof. Dr. Mustafa GÜDEN
Supervisor

_____

Prof. Dr. Muhsin ÇİFTÇİOĞLU
Committee Member

_____

Assoc. Prof. Dr. Oğuz BAYRAKTAR
Committee Member

_____

Assoc. Prof. Dr. Mustafa TOPARLI
Committee Member

_____

Assist. Prof. Dr. Alper TAŞDEMİRCİ
Committee Member

01 June 2010

_____

Prof. Dr. Metin TANOĞLU
Head of the Department of Mechanical Engineering

_____

Assoc. Prof. Dr. Talat YALÇIN
Dean of the Graduate School of Engineering and Sciences

ACKNOWLEDGEMENTS

It has been an opportunity to have been studied by my advisor, Prof. Dr. Mustafa GÜDEN. I would like to extend my utmost appreciation to him, for his valuable advice and guidance, as well as his endless patience without which this thesis would not have been possible.

I am very grateful to my institution, İzmir Institute of Technology, for providing me research facilities during my PhD study.

Special thanks go to specialists Mr. Gökhan Erdoğan, Mrs. Duygu Oğuz Kılıç, Miss. Mine Bahçeci and Evrim Yakut for the analysis of XRD, SEM and AFM.

I would like to appreciate deeply my room-mates Mücahit Sütçü, Emre Yalamaç and Sinan Yüksel for the moments that we shared together.

Last but not least, I wish to express my gratitude to my lady and son, Hacer and Yusuf Selim Türkan, for their encouragement support and patience during the course of my studies here at Iztech.

ABSTRACT

IN VITRO BIOACTIVITY OF THE SURFACE-TREATED Ti6Al4V OPEN CELL FOAMS

The effects of commonly used chemical surface treatment methods including alkali and nitric acid treatment and acid etching on biomimetic CaP deposition and bacterial adhesion (*S. epidermidis)* of an open cell Ti6Al4V foam using two different powders, powder 1 (P1) and powder 2 (P2) were investigated in a simulated body fluid (SBF) solution up to 14-day. The optimum conditions of nitric acid and alkali surface treatment for the biomimetic CaP coating of the studied foams were also determined using the surface response methodology. Alkali treatment induced a relatively thin layer of porous $Na_2Ti_5O_{11}$ on the flat surface and inside the pores, while nitric acid treatment did not affect the surface roughness; it increased surface area difference significantly by introducing nano scale undulations on the surface. A uniform CaP layer formation was found on the flat surface and interior of the pores of untreated foam samples after 14-day of SBF immersion. However, alkali treatment and nitric acid treatment reduced the immersion time of CaP layer formation for P2 foam samples. The GIXRD, SEM and FTIR analysis showed that the CaP layer was in the form of carbonated hydroxyapatite (CHA). The porous $Na_2Ti_5O_{11}$ surface layer formed in alkali treated foam specimens promoted the bacterial retention on the foam particles. A correlation between the nano metric scale surface roughness and the associated bacterial colonization was further shown. Based on response surface methodology, the following experimental design conditions were found to induce a uniform coating in alkali treated P1 and P2 foam specimens: 1M NaOH at 20°C for 12.5h. For nitric acid treated P1 and P2 foams, the optimum condition was found as 20% nitric acid solution at 40°C for 1h.

ÖZET

YÜZEY İŞLEMİ GÖRMÜŞ AÇIK HÜCRELİ Ti6Al4V KÖPÜKLERİN BİYOAKTİVİTESİ

Bu çalışmada, genel olarak kullanılan kimyasal yüzey işlemlerinden, alkali yüzey işlemi, nitrik asit yüzey işlemi ve asit dağlama, açık hücreli iki farklı toz; toz1 ve toz2 kullanılarak üretilen, Ti6Al4V köpük malzemelerin yapay vücut sıvısı (YVS) içinde biyomimetik CaP kaplamasına etkisi incelenmiştir. Ayrıca yüzey işleminin, bakteri (*S. epidermidis)* tutunmasına etkisi de incelenmiştir. Nitrik asit ve alkali yüzey işleminin optimum koşulları biyomimetik CaP kaplama için yüzey etki metodu kullanılarak belirlenmiştir. Yüzey işlemi yapılmamış örneklerin düz yüzeylerinde ve gözenekleri içinde düzgün CaP tabakası YVS içinde 14 gün bekletilmesi sonrasında elde edilmiştir. Alkali yüzey işlemi ve nitrik asit yüzey işlemi bu süreyi toz2 örnekler için kısaltmıştır. Alkali yüzey işlemi, yüzeyde gözenekli $Na_2Ti_5O_{11}$ tabakası oluştururken, nitrik asit yüzey işlemi yüzey pürüzlülüğünü değiştirmemiş ve yüzey alanı farkını oldukça artırarak yüzeyde nano boyutlu dalgalar oluşturmuştur. GIXRD, SEM ve FTIR analizleri, oluşan CaP tabakasının karbonatlı hidroksiapatit yapısında olduğunu göstermiştir. Alkali yüzey işlemi gören örneklerde oluşan gözenekli $Na_2Ti_5O_{11}$ tabakası bakteri tutunmasını artırmıştır. Nanometre boyutlu yüzey pürüzlülüğü ile bakteri tutunması arasında bir ilişki olduğu gözlenmiştir. Yüzey etki metoduna göre, düzgün CaP tabakası alkali yüzey işlemi için 1M NaOH solüsyonu–20°C –12.5 saat ve nitrik asit yüzey işlemi için ise %20 nitrik asit–40°C –1 saat koşullarda elde edilmiştir.

To my Family

TABLE OF CONTENTS

LIST OF FIGURES

LIST OF TABLES

CHAPTER 1

INTRODUCTION

1.1. Background

Titanium (Ti) and its alloys are commonly used in biomedical applications including hard tissue replacements due to its good biocompatibility, high strength to weight ratio, relatively low elastic modulus and superior corrosion resistance as compared with other metallic biomaterials such as cobalt alloys and stainless steel (Biehl and Breme 2001, Katti 2004, Long and Rack 1998). When a human hard tissue (Figure 1.1) is damaged as a result of the accidents and aging, it is surgically substituted by an implant. The requirements for the endoprosthetic materials vary with the regions in which the implants are inserted and the functions to be provided (Liu, et al. 2004).

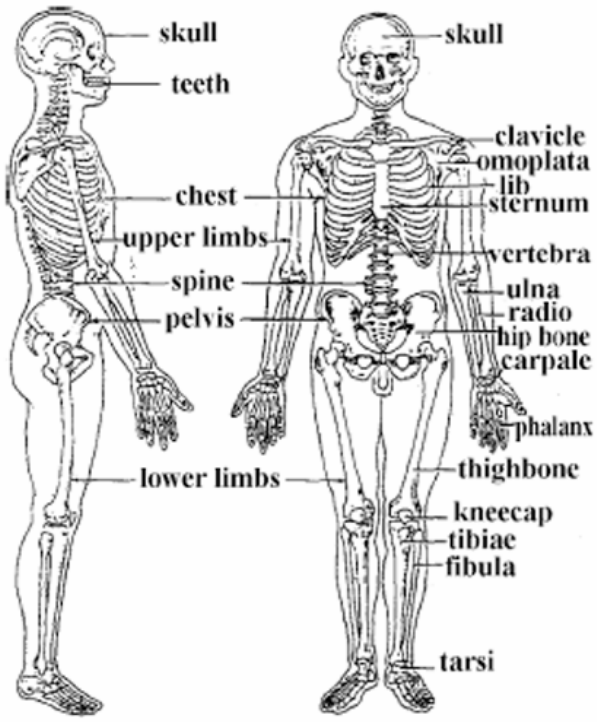

Figure 1.1. Hard tissue replacements used in human body
(Source: Liu, et al. 2004).

Ti and its alloys are known to be bioinert, i.e. when inserted into human body they show no reaction with the body fluid, while the biocompatibility of Ti alloys arises from the presence of an extremely thin passive oxide film on the surface. This oxide film, when exposed to air, forms spontaneously. The chemical composition of the oxide layer in Ti6Al4V alloy was determined to be predominantly composed of TiO_2 with some minor contribution of V and Al oxide (Feng, et al. 2002, Sittig, et al. 1999, Takadama, et al. 2001b). The oxide layer thickness was measured 4 nm (Callen, et al. 1995). In the absence of oxide film, the driving force for the corrosion of metallic orthopedic implant alloys is very high and corrosion rates would also be high. The integrity of these films has been strongly correlated with the chemical and mechanical stability of orthopedic implants.

Four grades of commercially pure Ti are currently used in the processing of surgical implants. Table 1.1 tabulates the chemical composition of commercially pure grades of Ti together with that of biomedical grade of Ti6Al4V alloy. The corresponding mechanical properties of the commercially pure grade Ti and Ti6Al4 alloy are further tabulated in Table 1.2. The impurity levels of the biomedical grade Ti, particularly oxygen level, have great effects on the strength and elongation as tabulated in the same table and therefore, should be controlled very carefully.

Table 1.1. Chemical compositions of Ti and Ti6Al4V alloy
(Source: Peters 2003).

Element	Grade 1	Grade 2	Grade 3	Grade 4	Ti6Al4V
Nitrogen	0.03	0.03	0.05	0.05	0.05
Carbon	0.1	0.1	0.1	0.1	0.08
Hydrogen	0.015	0.015	0.015	0.015	0.0125
Iron	0.2	0.3	0.3	0.5	0.25
Oxygen	0.18	0.25	0.35	0.4	0.13
Titanium			Balance		

Table 1.2. Mechanical properties of Ti and Ti6Al4V alloy (ASTM F136)
(Source: Peters 2003).

Property	Grade 1	Grade 2	Grade 3	Grade 4	Ti6Al4V
Tensile strength (MPa)	240	345	450	550	860
Yield strength (MPa)	170	275	380	485	795
Elongation (%)	24	20	18	15	10
Reduction of area (%)	30	30	30	25	25

Ti and its alloys are classified as α, near-α, α+β and metastable α or stable β (Figure 1.2). In the same manner, the alloying elements added to Ti can also be categorized as neutrals such as Sn and Z, α-stabilizers such as Al, O, N and C, β-stabilizers such as Mo, V and Nb, (Peters 2003).

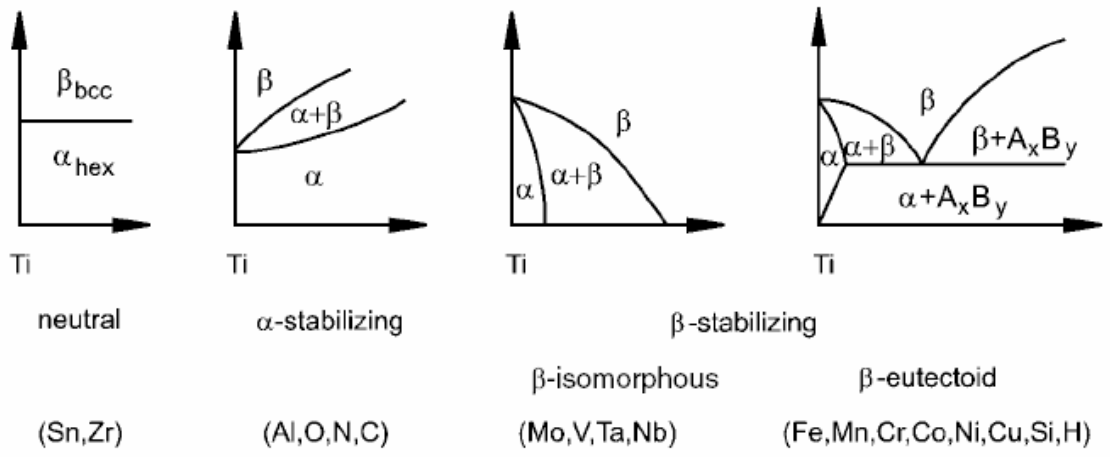

Figure 1.2. The effect of the alloying elements on phase diagrams of Ti alloys (Source: Peters 2003).

Today, the bulk form of Ti is still widely used in implant processing. However, the bulk form of Ti has problems of (i) interfacial instability, (ii) elastic modulus mismatch and (iii) anchorage with the host tissue (Kienapfel, et al. 1999), (Hallab, et al. 2003), (Hacking, et al. 2000, Li, et al. 2005, Song, et al. 1999). One of the prerequisites for the hard tissue replacement is the reliable anchoring of the implant to the surface of host tissue (Pilliar 1983). There have been numerous attempts to overcome these problems. One way of improving elastic modulus mismatch and anchorage is to use porous implants. Three distinct types of porous implants are commonly investigated: (1) porous layer coated solid material; (2) fully porous materials and (3) porous metal segment joined to a solid metallic part. Porous Ti alloys posses a set of unusual properties compared to bulk structure. They are crushable and exhibit varying elastic modulus and Poisson's ratio. The pores are necessary for bone generation as they allow the migration and proliferation of osteoblasts and mesenchymal cells responsible for bone formation. In addition, a porous structure improves the mechanical gripping between the implant and surrounding tissue, providing mechanical stability at the interface (Karageorgiou and Kaplan 2005). The pore size and porosity level affect the bone generation properties. Hulbert et al. (Hulbert, et al. 1970) reported that the

minimum pore size required for bone regeneration was ~100 μm. Relatively large size of pores showed substantial bone ingrowth, while smaller pores (75-100 μm) resulted in unmineralized osteoid tissue formation. The fibrous tissue penetration occurred when the pore size ranged between 10 and 75 μm. The optimal pore sizes of metallic foams for attachment, differentiation and growth of osteoblast cells may range between 200 and 500 μm.

The porous surface coating technology for the orthopedic implants was developed in the early 1970s (Hahn and Palich 1970, Welsh, et al. 1971). The coating layer is usually formed by sintering uniform size beads or fibers either through isostatic pressing sintering or loosely packing sintering (Zhang, et al. 2005). Calcium Phosphate (CaP) coating of porous surfaces has been found to have beneficial effects on the bone-generating properties, improving the implant fixation to bone. The surface treatments of Ti further increase the bioactivity of Ti through modifying the surface structure. According to Kokubo et al. (Kokubo 1998), an essential requirement for in vivo bone growth on synthetic materials is the formation of a CaP layer on the materials surface. This bone like apatite seems to activate signaling proteins and cells to start the cascade of events that results in bone formation.

1.2. Objectives

Previous studies on the surface treatment of porous Ti and its alloys and its effect on bioactivity were dominantly focused on CaP coating of sintered powder beads. There have been no systematic studies on CaP coating of Ti6Al4V foams in the literature. The aim of this study is, therefore, to investigate the effects of most widely used surface treatment methods including alkali and nitric acid surface treatment and acid etching on the CaP deposition of an open cell Ti6Al4V foam (60% porous and 300-500 μm in pore size) developed for biomedical applications in a simulated body fluid (SBF) solution up to 14-day. The characterization of surface treated and untreated Ti6Al4V open cell foams was performed using small angle X-ray diffraction (GIXRD), scanning electron microscopy (SEM), atomic force microscopy (AFM) and frouier transform infrared spectroscopy (FTIR). The optimum conditions of nitric acid and alkali surface treatment for the biomimetic CaP coating of the studied open cell Ti6Al4V foams were further investigated using the surface response methodology. The

effects of alkali and nitric acid surface treatment on *Staphylococcus Epidermidis* adhesion on the surface of Ti6Al4V foams were also investigated. A correlation between the nano metric scale surface roughness and the associated bacterial colonization was shown.

CHAPTER 2

SURFACE MODIFICATION OF Ti ALLOYS

2.1. Background

The material surface of the implants plays an important role in the response of the biological environment when it is used in human body. In Ti implants, the normal manufacturing steps usually lead to an oxidized, contaminated surface layer that is often stressed and plastically deformed, non-uniform and rather poorly defined. Such surfaces are clearly not appropriate for biomedical applications; therefore, surface treatments are generally performed in order to improve the surface characteristics. Another important reason of surface modification is that specific surface properties that are different from those of the bulk are often required. For example, in order to accomplish biological integration, it is necessary to have good bone formability. In blood-contacting devices such as artificial heart valves blood compatibility is crucial. In other applications, good wear and corrosion resistance are also required. The proper surface modification techniques not only retain the excellent bulk attributes of Ti and its alloys, such as relatively low modulus, good fatigue strength, formability and machinability, but also improve the specific surface properties required by different clinical applications (Liu, et al. 2004).

The improvement of bioactivity of Ti and its alloys using various surface modification methods are reviewed in this section. These methods are classified in three general groups as mechanical, physical and chemical treatments. However, the emphasis in this section is on the chemical surface treatment methods as these methods were used in the surface modifications of the studied foam samples in this thesis study.

2.2. Mechanical and Physical Methods

Widely used mechanical surface modification methods include machining, grinding, polishing and grit blasting, which involve physical treating, shaping and/or

removing the materials surfaces. The main objective of the mechanical surface modification is to form specific surface topographies and roughness, remove the surface contamination and/or improve the adhesion in subsequent bonding steps.

Physical surface treatments include thermal spraying, plasma spraying, physical vapor deposition and ion implantation. These treatments improve the near surface crystal structure, modifying the surface properties such as wear, corrosion resistance and friction coefficient. During physical surface modification, the chemical reactions do not occur: in this case, the formation of surface modified layer, film or coating, is mainly driven by the thermal, kinetic, and electrical energy. In the thermal spraying process, the melted coating material in the form of liquid droplets is used to coat a substrate at a high speed (kinetic energy). Physical vapor deposition leads to growth of a film by the reaction between a substrate surface and adjacent vapor which supplies the coating material in the form of atoms, molecules or ions, generated from a target and transported to the substrate surface on which condensation and reactions with atoms of the surface lattice take place.

In the thermal spray process, the coating is formed by a continuous build-up of successive layers of liquid droplets, softened material domains and hard particles. Thermal spraying requires a device that creates a high temperature flame or a plasma jet. Therefore, thermal spraying is often divided into flame spraying and plasma spraying. The principal difference between flame and plasma spraying is the maximum temperature achievable. The coating material is heated by the gases in the flame spray torches and electrical current provides energy to the plasmatrons. In flame spraying, the temperature is limited by the internal heat of combustion of the fuel gas. Conventional oxyacetylene torches reach temperatures around 3000 K. Plasma spraying, which use electrical energy as the source to create the plasma can provide relatively high temperatures that are determined by the energy input. Plasma spraying includes atmospheric plasma spraying and vacuum plasma spraying. The process uses an electrical arc to melt and spray materials onto a surface. The high energy and density available in a plasma jet have made plasma spraying one of the popular thermal spraying techniques. The density, temperature, and velocity of the plasma beam are important in the coatings. The temperature of a plasma beam depends mainly on the degree of ionization, which is determined by the type of plasma gas and the parameters of the plasma torch. The temperature in the core region is relatively constant at about 12000 K and dramatically decreases towards the nozzle. Almost all materials can be

melted in the plasma jet. In addition to these two techniques, other thermal spraying techniques, such as arc spraying, detonation gun spraying, laser spraying and high velocity oxy-fuel spraying, are also widely used by the industry.

In the physical vapor deposition (PVD) process, the target materials are evaporated or sputtered to form atoms, molecules or ions that are subsequently transported to the substrate surface, on which condensation and sometimes reactions take place, leading to film growth. The important processes parameters in PVD include (1) the generation of particles from the target materials, (2) transport and film growth and (3) particle energy, density, substrate temperature and reactive gas properties. PVD processes are characterized by high coating density and strong adhesion, multi-component layers, low substrate temperature, and a myriad of coating and substrate materials. The evaporation is carried out in a vacuum, typically 0.1–1 Pa, so that the evaporated atoms undergo a collision-less transport prior to condensation on the substrate. The substrate is usually held at ground potential. The deposition rate is typically 10–25000 nm/min. In the sputtering process, positive argon ions produced in a glow discharge bombard the target materials (cathode) dislodging atoms that enter into the vapor phase and are deposited onto the substrate. The typical gas pressure in the chamber is 2–15 Pa and the deposition rate is 25–1000 nm/min.

Ion beam processing is a process in which energetic ions are introduced into the surface layer of a solid substrate via bombardment. The use of energetic ions affords the possibility of introducing a wide range of atomic species independent of thermodynamic factors thus making it possible to obtain impurity concentrations and distributions of particular interest. Ion implantation includes conventional beam-line ion implantation and plasma immersion ion implantation. Conventional beam-line ion implantation is a line-of sight process in which ions are extracted from an ion source, accelerated as a collimated and mass-selected beam to high energy, and then bombard into the work piece.

2.3. Chemical Methods

Chemical methods include chemical treatment, electrochemical treatment (anodic oxidation), sol–gel, chemical vapor deposition (CVD) and biochemical modification. In these methods, chemical reactions occur at the interface between an

implant and a solution. In CVD, the chemical reactions between chemicals in the gas phase and the sample surface result in the deposition of a non-volatile compound on the substrate. On the other hand, in sol–gel process, no chemical reaction occurs at the interface between the sample surface and solution or gel, but rather in the solution.

Chemical surface treatment methods such as, alkali and nitric acid treatment and acid etching remove/deform or form a new surface layer phase near the surface crystal structure. The biocompatibility of Ti is attributed to the formation of an extremely thin layer of TiO_2 on its surface. The characteristics/atomic structure of the oxide film grown at room temperature on pure Ti is schematically shown in Figure 2.1. The amorphous or nanocrystalline oxide film is typically few nm thick and is mainly composed of stable TiO_2. The TiO_2/Ti interface has an O to Ti concentration ratio that varies gradually from 2 to 1 from TiO_2 film to a much lower ratio in the bulk. In addition the organic species like hydrocarbons adsorb and metal-organic species, such as alkoxides or carboxylates of Ti also exist on the outer most surface layer whose concentrations depend on not only surface conditions, but also the exposure time to air. This oxide layer reacts with hydroxyl ions when it is exposed to a solution containing hydroxyl groups, OH, as shown in Figure 2.1.

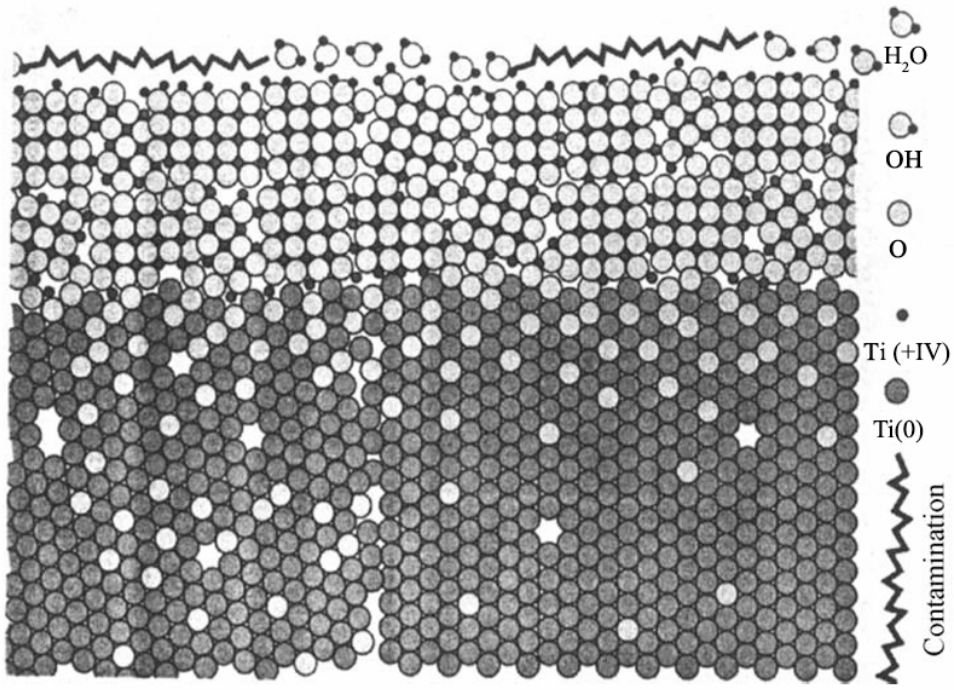

Figure 2.1. Schematic view of oxide film on pure Ti
(Source: Peters 2003).

Hydroxide ions attached to metal cations possess acid/base properties depending on the type of the metal cations and the coordinate bonds with the cations. Hydroxides or hydro-complexes of multivalent (e.g. Ti^{IV}) cations are generally ‘‘amphoteric’’, that is, exhibiting both acid and base (or alkaline) character. The underlying hydrolysis reactions of Ti in aqueous solution are as following,

$$Ti\text{-}OH+H_2O \leftrightarrow [Ti\text{-}OH]^- + H_3O^+ \quad (2.1)$$

$$Ti\text{-}OH+H_2O \leftrightarrow [Ti\text{-}OH_2]^- + OH^- \quad (2.2)$$

Reaction (1) leads to the formation of positive charges on the surface and reaction (2) negative charges. The two types of hydroxides have been linked with different bonds to Ti surface cations and basic hydroxide coordinated to one Ti cation (bridge coordination) leading to increased polarization and electron transfer from the oxygen atom to Ti cation. As a quantitative measure, the isoelectric point is often used to investigate the surface charges. The isoelectric point values of TiO_2 vary between 5 and 6.7. In water with a neutral pH, a small negative charge forms on the surface of Ti due to a fraction of the acidic hydroxides being deprotonated, while almost all of the basic and a large part of the acidic groups are still present in neutral form. In a basic aqueous solution, the negative charges on Ti surface increases at increasing pH values.

2.3.1. Acid Etching

Acid treatment is often used to remove the oxide layer, clean the surface contamination and form a uniform surface finish (Liu, et al. 2004). A combination of the acids is frequently used to pre-treat Ti (Nanci, et al. 1998). A solution composed of 10–30 vol% of HNO_3 and 1–3 vol% of HF in distilled water has been used as a standard solution for acid treatment. Hydrofluoric acid that readily attacks TiO_2 reacts with Ti to form soluble titanium fluorides and hydrogen. Incorporation of hydrogen in Ti can cause embrittlement of the surface layer, but a ratio of nitric acid to hydrofluoric acid of 10 to 1 can minimize the formation of free hydrogen. Takeuchi et al. (Takeuchi, et al. 2003) investigated the decontamination efficiency of three acids, $Na_2S_2O_8$, H_2SO_4, and HCl to Ti surface and found that HCl was an excellent decontamination agent because it

could easily dissolve Ti salts and not weaken Ti surface. Acid etching generally leads to a thin surface oxide layer (<10 nm). The oxide layers has been shown to grow slowly in air, from 3 to 6 nm during a 400-day of period (Sittig, et al. 1999). The oxide layer on Ti is predominantly TiO_2, but residues from the etching solution are frequently observed, particularly chemicals containing fluorine. It is also known that some treatments can lead to hydrogen incorporation in the surface region below oxide layer (Taborelli, et al. 1997). These residues can remain even after post-thermal treatment of the etched surfaces. In addition, the acid treatment was often used to combine other treatment methods to improve the properties of Ti and its alloys. Wen et al.(Wen, et al. 1998b, Wen, et al. 1997) reported that the bioactivity of Ti alloy was improved by two-step chemical treatment: acid etching ($HCl + H_2SO_4$) and alkaline solution treatment.

2.3.2. Alkali Treatment

Kim et al. (Kim, et al. 1996) showed for the first time that alkali surface treatment and subsequent heat treatment improved the bioactivity of Ti. The developed method enables the formation of a biologically active bone-like apatite layer on the surface of bioactive ceramics, such as bioglass, hydroxyapatite and glass–ceramic A/W(Kokubo, et al. 1996). In alkali surface treatment, the materials are first immersed in a 5–10 M NaOH or KOH solution for 24 h, followed by rinsing with distilled water and ultrasonic cleaning for 5 min. The specimens are then dried in an oven at 40°C for 24 h and finally heat treated at a temperature between 600 and 800°C for 1 h. Because of the strong tendency of Ti to oxidize, the heat treatment is performed at a pressure of 10^{-4}- 10^{-5} Torr. After the treatment, a porous layer forms on the surface of Ti (Figures 2.2(a)–(c)). The thin film XRD spectra performed on the surface alkali and heat treated Ti samples showed the formation of a sodium titanate hydrogel layer on Ti substrate (Figure 2.3). A large amount of crystalline sodium titanate as well as rutile and anatase precipitates were seen after thermal treatment at 800°C for 1 h (Figure 2.3). After soaking in SBF for 4-week, the alkali heat treated Ti showed bone-like apatite formation on the surface, indicating that alkali and heat treatment increased the bioactivity of Ti.

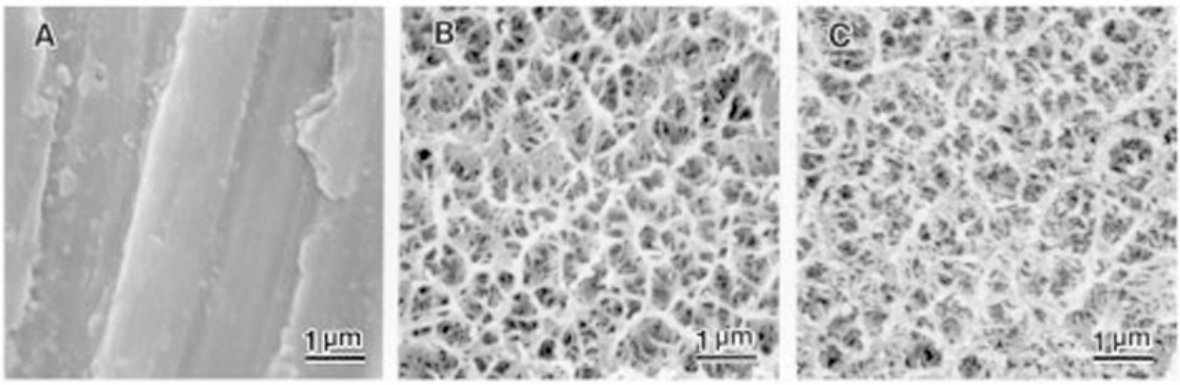

Figure 2.2. SEM surface micrographs of (a) untreated, (b) alkali treated and (c) alkali and heat treated Ti6Al4V alloy (Source: Kim, et al. 2000).

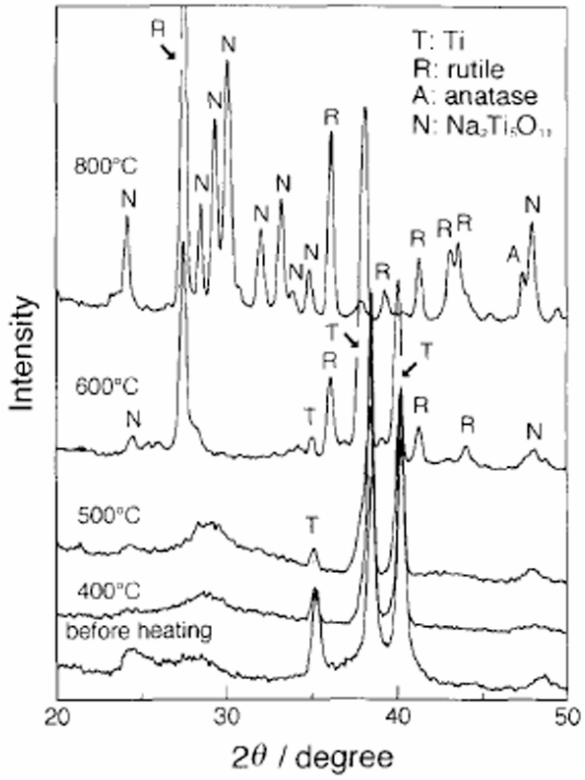

Figure 2.3. TF-XRD spectra of the surfaces of Ti soaked in 10 M NaOH at 60°C for 24 h then heat treated at various temperatures for 1h (Source: Kim, et al. 1996).

During alkali treatment, the native TiO_2 layer formed on the surface partially dissolves in alkaline solution because of the corrosive attack of OH groups as,

$$TiO_2+NaOH \rightarrow HTiO_3^-+Na^+ \quad (2.3)$$

This process is assumed to proceed simultaneously with the hydration of Ti as,

$$Ti+3OH^- \rightarrow Ti(OH)^+ + 4e^- \quad (2.4)$$

$$Ti(OH)^+ + e^- \rightarrow TiO_2.H_2O + 1/2H_2 \quad (2.5)$$

$$Ti(OH)_3^+ + OH^- \leftrightarrow Ti(OH)_4 \quad (2.6)$$

A further hydroxyl attack to hydrated TiO_2 produces negatively charged hydrates on the surface of the substrate as,

$$TiO_2.nH_2O + OH^- \leftrightarrow HTiO_3^-.nH_2O \quad (2.7)$$

It was shown that when Ti metal was soaked in NaOH solution, sodium and oxygen penetrated up to 1 μm into the surface of Ti metal, with the content gradually decreasing with increasing depth, giving a gradient structure (Kokubo 2008). Following NaOH treatment, the heat treatment at 600°C was shown to accelerate only oxygen penetration into deeper part of Ti metal while disturbing the gradient structure. The induced layer after NaOH treatment was shown to consist of sodium hydrogen titanates ($Na_xH_{2x}Ti_yO_{2y+1}$: $0<x<2$ and y=2, 3, or 4) which were later transformed into sodium titanates ($Na_2Ti_yO_{2y+1}$: y=5, 6, etc). Wei et al. (Wei, et al. 2002) conducted an optimization study on a NaOH treated Ti6Al4V alloy. The optimization parameters were the molarity of solution, the process temperature and the heat treatment temperature. The high temperature treatment was shown to form an oxide layer on Ti. An optimum heat treatment temperature of 600°C was reported based on the bonding strength and the rate of apatite formation.

2.3.3. Nitric Acid Treatment

Commercially pure Ti and Ti6Al4V alloy are customarily subjected to a passivation treatment in order to produce an inert surface layer by increasing the surface oxide film thickness. ASTM-F86 used as surface passivation protocol contains nitric acid. In this protocol, the concentration of nitric acid is 20-40%. It has been recently shown that nitric acid treatment in fact increases the surface energy of Ti implants, not significantly affecting the surface roughness (Lu, et al. 2007). Nitric acid treatment of grade 4 Ti at 60°C for 600 min using 65% acid concentration increased the surface energy nearly 24% as compared with polished Ti. On the other hand, the nitric acid

treatment of grade 2 Ti at room temperature for 10 min using 30% concentration changed the surface energy only about 2% (Kilpadi, et al. 1998). Correlations between Ti surface composition and the surface energy were also made.

Although a variety of studies were conducted on the nitric acid passivation of Ti surfaces; few of these have been on the biomimetic CaP deposition ability of the nitric acid surface treated Ti. Chen et al. (Chen, et al. 2003) used nitric acid passivation as a pretreatment for alkali treatment to form a bioactive layer on an Ni-Ti alloy. Ca and P adsorption on nitric acid passivated Ti surfaces immersed in Hank's solution showed Ca and P containing layer equivalent to 4.0 ionic monolayers even after 16-day of immersion (Chang and Lee 2002). Lu et al. (Lu, et al. 2008) correlated the bioactivity of Ti with the functional groups formed on the surface after nitric acid treatment. When Ti metal is subjected to nitric acid treatment, the following reaction occurs,

$$3Ti+4HNO_3=3TiO_2.H_2O+4NO \quad (2.8)$$

A passive Ti oxide layer forms on the surface. However, Callen et al. (Callen, et al. 1995) reported that nitric acid treatment in fact reduced the thickness of the oxide layer on Ti6Al4V alloy, while it had no effect on the thickness of the oxide layer of on commercially pure Ti.

2.4. Effects of Surface Modification on the Bioactivity of Ti Metals

The Williams dictionary of biomaterials defines the bioactivity as a phenomenon by which a biomaterial elicits or modulates biological activity. Bioactivity also refers to the material interaction with the surrounding bone to form a chemical bond to this tissue (bone-bonding). Bioactive materials are actually bone-bonding materials and characterized by the formation of a very tight chemical bond with bone. Bone tissue forming reactions start from the implant surface and induce the formation of a continuous transition from tissue to implant surface. It is noted that Ti without any surface treatment is bioinert. Various techniques including the methods explained in pervious section have been developed to deposit bioactive CaP coating on Ti to increase its bioactivity. Recently, the biomimetic method, in which a CaP coating is formed in the SBF solution on Ti metal, has attracted considerable attention as being simple and

inexpensive method. It can also deposit CaP layer on rough surfaces such as porous coating on the implants and bulk foamy implants.

. Pure Ti, Ti6Al4V, Ti6Al2NbTa and Ti15Mo5Zr3Al substrates immersed in 10M NaOH solution at 60°C for 1-24 h and subsequently heat treated at 600°C formed dense and uniform bonelike apatite layer on the surfaces after 4-week of SBF immersion (Kim, et al. 1996). A rectangular pure Ti metal treated with 10M NaOH (with following heat treatment) was soaked in SBF to from bonelike apatite layer, then implanted into a rabbit's tibia (Yan, et al. 1997a). Ti metal was tightly bonded to living bone through the apatite layer on its surface (Figure 2.4). The tensile test conducted showed significant increase in the failure load as compared with uncoated controls as shown in Figure 2.5. The surface modified TiInNbTa and Ti6Al4V ELI alloys treated 5.0M NaOH for 24 h then subsequently heat treated at 600°C showed earlier hydroxyapatite formation on the surface (Lee, et al. 2002). Gil et al.(Gil, et al. 2002) reported a uniform apatite coating layer formation on the surface of pure Ti plates treated with 0.5M NaOH solution at 60°C for 24 h and following heat treatment at 600°C after 3-day of SBF immersion. The effect of heat treatment on the apatite forming ability of an alkali treated Ti metal (5.0M NaOH solution at 60°C for 24 h) in SBF was investigated (Kim, et al. 1997). The amount of the apatite formed decreased with increasing the heat treatment temperature above 700°C, resulting from the formation of a TiO_2 layer on the surface.

Jalota et al. (Jalota, et al. 2006) investigated the effect of carbonate content and buffer type on calcium phosphate formation in SBF solution. Ti6Al4V strips treated with 5.0M NaOH (without any heat treatment) were soaked in *c*-SBF, *Tas*-SBF and *r*-SBF for a period of 7, 14 and 21 days. Calvarial rat osteoblast cells, designated 7 F2 were used for cell attachment studies on the SBF-coated strips. They indicated that the differences in the coating morphology and surface coverage were assessed for each SBF solution. *In vitro* rat osteoblast culture tests performed on the apatitic CaP coatings were found to favor the TRIS-buffered, 27mM SBF solutions (i.e., *Tas*-SBF) by yielding increased cell viability and protein concentrations. In addition, Jalota et al. (Jalota, et al. 2007b) developed a crack-free biomimetic coating protocol for Ti6Al4V strips using 5M NaOH treatment and 1.5x *t*-SBF.

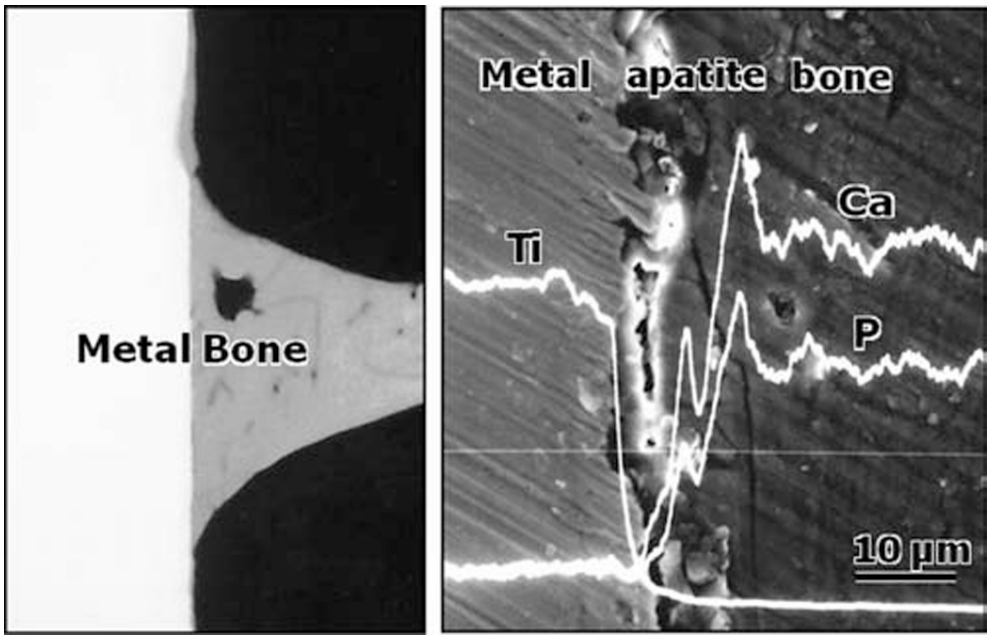

Figure 2.4. Contact microradiograph and SEM-EDX picture of a cross-section between rabbit tibia and alkali and heat treated Ti metal (Source: Yan, et al. 1997a).

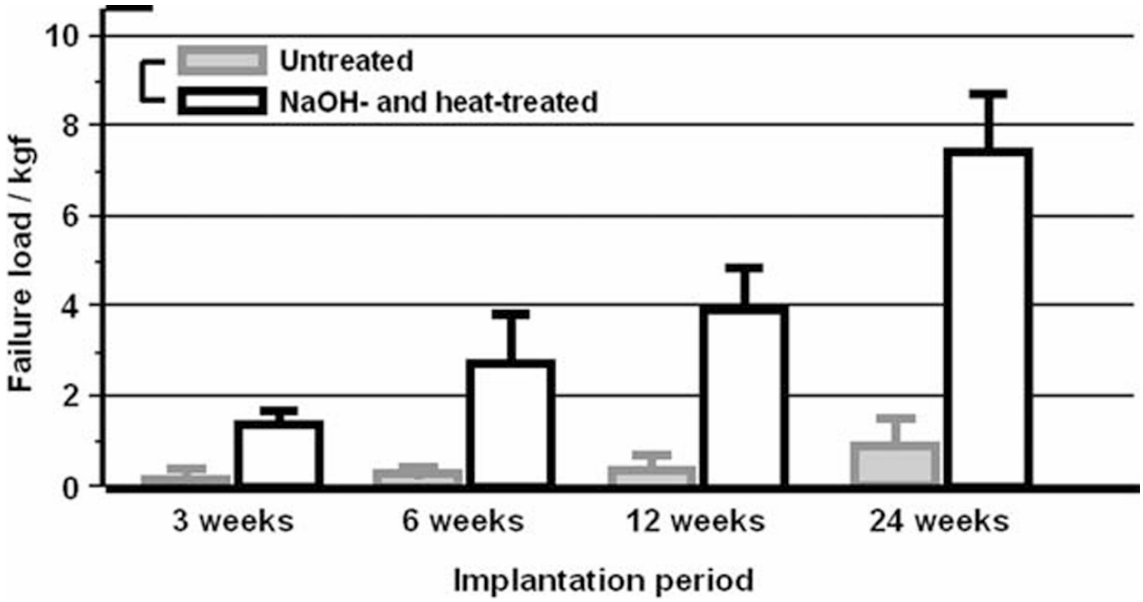

Figure 2.5. The failure load of untreated and alkali and heat treated Ti metal as a function of implantation period into rabbit tibia (Source: Yan, et al. 1997a).

The surface of a Ti6Al4V alloy was electrochemically activated in a 5M NaOH solution at room temperature using 200 mV polarization voltages (Xie and Luan 2008). Electrochemical activation induced a porous structure with nanometer topographic features and in alkaline environment promoted the bone like hydroxyapatite coating. A bone like apatite growth mechanism/model on alkali-heat treated Ti metal in SBF was

developed based on TEM observation (Takadama, et al. 2001a), X-ray photoelectron spectroscopy analysis (Kim, et al. 2003, Takadama, et al. 2001b) and zeta potential measurements. The variation of the zeta potential of alkali and heat treated Ti metal in SBF is shown in Figure 2.6. One of the main characteristics of metal oxides in aqueous solution is the point of zero charge (PZC), which represents the pH value of aqueous solution at which an immersed oxide surface has zero net charge. If the solution pH is greater than the pH at point of zero charge, the metal oxide is negatively charged; on the other side, if the solution pH is lower than the pH at point of zero charge of metal oxide, the metal oxide is positively charged. The charged surface and surrounding solution form a thin double layer, to which oppositely charged ions are attracted and initial reaction starts between the charged metal oxide and the attracted ions (Xie and Luan 2008). The zeta potential of the treated Ti metal initially gives a negative value in the SBF, but increases with increasing soaking time, passing through a maximum positive value. PZC of the TiO_2 was reported to be in the range of 5.5–6.0 resulting in a negatively charged surface due to the combination of Ti with that of OH ions in the coating solution after the immersion at a pH of 6.50.

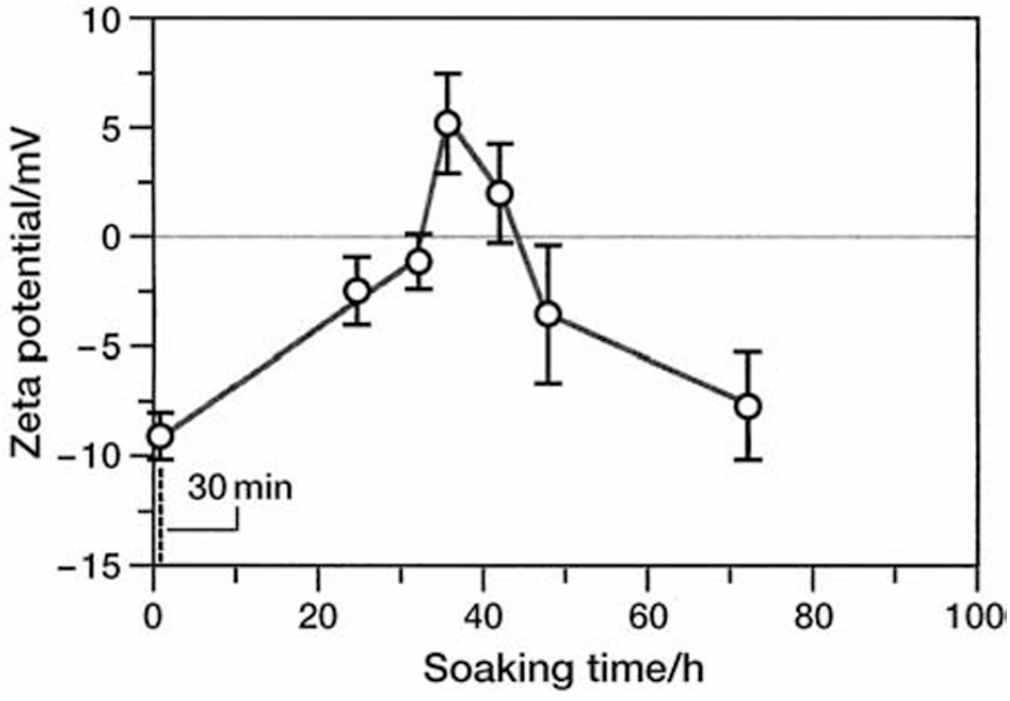

Figure 2.6. The variation of zeta potential of alkali and heat treated Ti metal with soaking time in SBF (Source: Kokubo, et al. 2004).

Schematic drawing of the mechanism of apatite formation on Ti metal after alkali and heat treatment in SBF is shown in Figure 2.7. Immediately after immersion, the metal forms Ti-OH groups on its surface via exchanging Na^+ ions of the surface sodium titanate layer with H_3O^- ion in the fluid. The Ti-OH groups formed on the metal are negatively charged and combine with the positively charged Ca^{2+} ions in the fluid, resulting in the formation of an amorphous calcium titanate layer. As the calcium ions accumulate, the metal surface gradually gains an overall positive charge. The positively charged metal surface attracts the negatively charged phosphate ions in SBF, forming an amorphous CaP layer. This CaP spontaneously transforms into the crystalline apatite. This transformation occurs due to the much lower solubility (i.e., thermodynamic phase stability) of hydroxyapatite than the amorphous CaP in SBF. With the formation of CaP apatite on the surface, the super-saturation of simulated physiological solution promotes the preferential nucleation of apatite on the already-formed apatite. The formation of the apatite coating proceeds by the spontaneous growth, consuming calcium and phosphate ions from the surrounding SBF. A theoretical analysis indicated that the formation of hydroxyapatite exhibited a higher thermodynamic preference than that of octacalcium phosphate and dicalcium phosphate (Lu and Leng 2005).

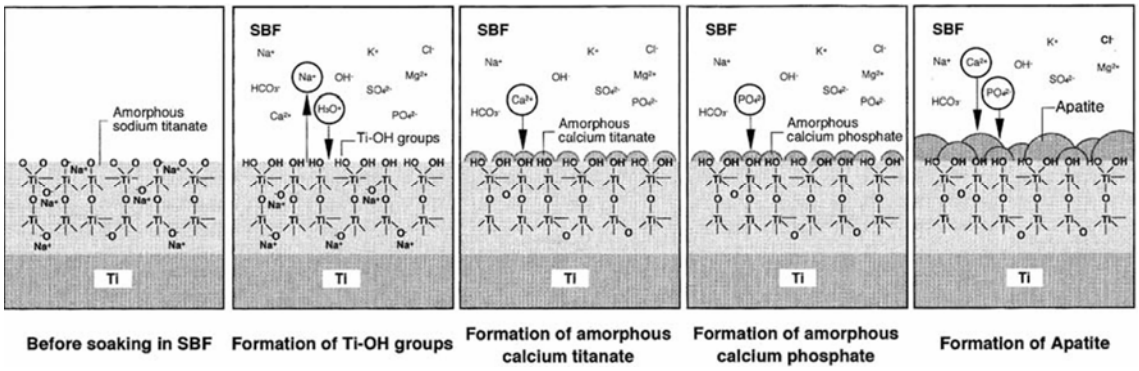

Figure 2.7. Schematic representation of the mechanism of apatite formation in alkali and heat treated Ti metal in SBF (Source: Takadama, et al. 2001b).

Zhang et al.(Zhang, et al. 2005) studied the electrochemical deposition and biomimetic deposition of CaP on porous Ti. The porous Ti prepared by the sintering of Ti beads at 1300°C was acid etched (48% H_2SO_4 and 18% HCl for 1 h at 60°C) and then alkali treated (5M NaOH solution at 60°C for 5 h). Both deposition methods produced CaP coatings on the inner pore surfaces, while biomimetic deposition formed a thicker and more uniform coating layer than electrochemical deposition. The crystal

structure of the coating was found octacalcium phosphate regardless of the deposition method. In a similar study, the sintered spherical pure Ti powders (500 μm) were subjected to 0.5, 1.0, 5.0 and 10.0 M NaOH treatment at 60°C for 24 h and subsequently heat treated at 600°C (Liang, et al. 2003). Porous Ti subjected to 0.5 and 1.0 M NaOH aqueous solutions did not show any apatite formation after 28-day of SBF immersion due to the relatively small porous network structure on the surfaces.

Jalota et al. (Jalota, et al. 2007) studied the osteoblast ploriferation on neat and apatite-like calcium phosphate coated titanium foam scaffolds. The 5M NaOH treated titanium foam and flat Ti6Al4V strips/springs were soaked in 1.5x *Tas*-SBF for 7-day. 7F2 rat osteoblast cells were used for the cell attachment test of untreated, NaOH treated and SBF coated samples. Titanium foams with interconnected pores and Ti6Al4V strips/springs were coated biomimetically with apatite-like calcium phosphates in 7days by using TRIS-buffered, 27mM HCO_3^- containing 1.5×*Tas*- SBF solution. In terms of osteoblast attachment, NaOH-treated surface has the least amount of cells attached, whereas the SBF-coated surfaces had the most.

The effects of chemical treatments and/or surface-induced bonelike apatite on the bone-bonding ability of Ti implants were investigated in rabbit tibiae (Yan, et al. 1997b). Smooth-surfaced, alkali and heat treated and bonelike apatite formed Ti plates were implanted into the tibial metaphyses of mature rabbits. The implants were harvested at 4, 8, and 16 weeks after implantation and subjected to tensile tests and histological evaluations. Results showed that treated implants exhibited significantly higher failure loads than untreated Ti implants. Histological examination showed that treated Ti implants directly bonded to bone tissue during the early post implantation period, whereas untreated Ti implants formed direct contact with the bone only after 16 weeks. The results suggested that chemical treatments accelerated the bone-bonding behavior of Ti implants and enhanced the strength of bone-implant bonding by inducing a bioactive surface layer on Ti implants. It was also reported that the new bone formation was observed only in the inner pores of the porous Ti block, not in the outer pores (Fujibayashi, et al. 2001). The effects of alkali treatment on the bone bonding ability of porous Ti interbody fusions were also investigated (Takemoto, et al. 2007). Porous Ti implants produced by space holding particles (porosity 50%, average pore size 303 μm, compressive strength 116.3 MPa) were treated with a 5M NaOH solution at 60°C for 24 h, 0.5mM HCI at 40°C for 24 h and subsequently heat treated at 600°C. Ten adult female beagle dogs underwent anterior lumbar interbody fusion at L6–7 using

either BT implants or untreated implants, followed by posterior spinous process wiring and facet screw fixation. Radiographic evaluations were performed at 1, 2, and 3 months postoperatively using X-ray fluoroscopy. Histological examination demonstrated a large amount of new bone formation with marrow-like tissue in the treated implants and primarily fibrous tissue formation in the untreated implants. Lu et al.(Lu, et al. 2007) investigated the biomimetic CaP coatings on nitric acid-treated Ti surface. Ti was initially acid etched (a volume ratio of 98% H_2SO_4:3%HCI:H_2O=1:1:1) at 60°C for 1h, then was immersed in nitric acid solution (65% HNO_3:H_2O=1:1) at 60°C for 10 h. Acid etching did not induce any CaP coating, while nitric acid treatment induced a continues CaP coating layer after 10-day of SBF immersion. It was shown that at least 1 h nitric acid treatment was required for imparting CaP induction ability to Ti surface. In addition, acid etching prior to the nitric acid treatment was shown to be not necessary for CaP induction.

Lu et al.(Lu, et al. 2008) investigated the relationship between the surface energy and CaP formation in SBF. Acid etched samples showed a relatively lower surface energy (22.56 mJ/m^2) and no CaP formation, whereas nitric acid treated samples showed relatively high surface energy (82.17 mJ/m^2) and hence large amount of CaP formation on the surface. This result is also consistent with the classical heterogeneous nucleation theory. In classical nucleation theory, the critical free energy ΔG_{heter} for heterogeneous nucleation depends on the supersaturation of the solution (S), the temperature (T), the surface energy of the substrate (σ_s) and the nucleolus (σ) and the interfacial energy of the substrate/nucleolus (σ_i) (Markov 1995, Mullin 2001) as,

$$\Delta G^*_{heter} = \Delta G^*_{\text{hom}} \frac{\Delta\sigma}{2\sigma} = \frac{16\pi v^2\sigma^2}{3k^2T^2(\ln S)^2} \cdot \frac{\sigma + \sigma_i - \sigma_s}{2\sigma} \tag{2.9}$$

where, k is the Boltzman's constant; $\Delta\sigma$ is the net interfacial energy and ΔG^*_{hom} is the critical free energy for the nucleation. The reduction in the critical energy resulting in a low energy barrier heterogeneous nucleation can be achieved by increasing the supersaturation and reducing the net interfacial energy. It is further noted that the bioactivity largely depends on Ti-OH concentrations, not on OH concentration formed on the surface as a result of the surface treatment. Lu et al. (Lu, et al. 2008) reported that alkali and heat treated surface with a low OH concentration showed better

bioactivity than acid etched surface although the latter has higher OH concentration. Not all of the OH groups on acid etched surface would contribute to the formation of CaP and only OH groups in the outmost layers in contact with SBF would be effective during CaP mineralization. The concentration of reactive OH groups on the surfaces of both hydrophilic and hydrophobic TiO_2 particles was investigated by XPS and FTIR analysis to be quite lower than that of total OH groups (Erdem, et al. 2001), only parts of OH groups participated specific reactions. Secondly, it is likely that only those OH groups bond to Ti could be effective during CaP mineralization. As a matter of fact, Ti-OH has been already assumed to be an important surface group which plays an important role in the bioactive Ti surface (Kokubo and Takadama 2006).

CHAPTER 3

NUCLEATION THEORY AND CALCIUM PHOSPHATE PHASES

3.1. Classical Nucleation Theory

Gibbs showed that the formation of a new phase preceded by the formation of the small clusters of atoms called nuclei and marked that the condition of supersaturation alone was not sufficient for a system to begin to crystallize. Gibbs considered the nuclei having the same properties as the bulk phase. This oversimplified picture is certainly a significant step towards the understanding of the transitions between different states. The surface to volume ratio of the small size phases are large as compared with that of macroscopic entities. The fraction of Gibbs free energy of a system containing small particles is due to high surface energy (Markov 1995).

Nucleation can be classified as primary and secondary nucleation (Figure 3.1). The term primary will be reserved for all cases of nucleation in systems that do not contain crystalline matter. On the other hand, nuclei are often generated in the vicinity of crystals present in a supersaturated system; this behavior will be referred to as secondary nucleation. The nucleation may also occur spontaneously (homogeneous) or it may be induced artificially (heterogeneous).

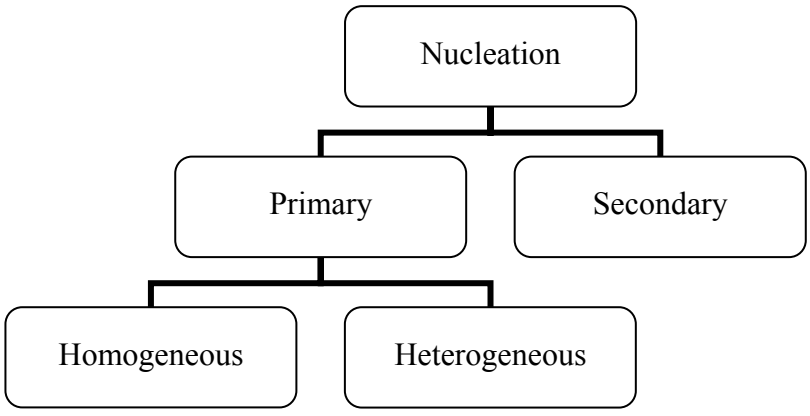

Figure 3.1. Classification chart of nucleation

3.1.1. Homogeneous Nucleation

Homogeneous nucleation is the initial appearance of a new phase during a first-order phase transition. The small nuclei formed spontaneously in a supersaturated solution overcome the nucleation barrier. However, a nucleus will redissolve rather than grow if the size cannot exceed a critical value called critical nucleus. The classical nucleation theory (CNT) offers a simple thermodynamic explanation as to why small crystal nuclei are less stable than the supersaturated parent phase (Mullin 2001). The decrease in free energy due to the transfer of N particles from the metastable liquid to the solid state is approximated as $N\Delta\mu$, where $\Delta\mu=\mu_{\text{solid}} - \mu_{\text{liquid}}$ is the difference in chemical potential between the solid and the liquid state. The CNT estimates for the free-energy cost involved in the creation of the surface area A of the nucleus is γA, where γ is the surface free energy of the solid-liquid interface. The free-energy costs are greater for small nuclei because they have a higher ratio of surface area to bulk volume, so small crystallites have to reach the critical nucleus to survive. According to CNT, the total Gibbs free-energy cost to form a spherical crystallite with radius r (Auer and Frenkel 2001) is

$$\Delta G = \frac{4}{3}\pi r^3 \rho_s \Delta\mu + 4\pi r^2 \gamma \tag{3.1}$$

where, ρ_s is the number-density of the solid. The first term on the right hand side of Equation 3.1 is a “bulk” term that expresses that the solid is more stable than the supersaturated fluid. This term is negative and proportional to the volume of the crystallite. The second term is a “surface” term that takes into account the free-energy cost of creating a solid-liquid interface. This term is positive and proportional to the surface area of the crystallite. The function ΔG goes through a maximum where $d\Delta G/dr = 0$ at r_c and the height of the nucleation barrier is (Auer and Frenkel 2001)

$$\Delta G_{crit} = \frac{16\pi\gamma^3}{3(\rho_s |\Delta\mu|)^2} \tag{3.2}$$

The crystal-nucleation rate J per unit volume at which nuclei are formed depends exponentially on ΔG_{crit} as,

$$J = \kappa \exp(-\Delta G_{crit} / kT) = \kappa \exp\left[-\frac{16\pi}{3} \gamma^3 / (\rho_s |\Delta\mu|)^2 \right] \quad (3.3)$$

where, T is the absolute temperature, k is the Boltzmann's constant, and κ is a kinetic pre-exponential. Equations. 3.2 and 3.3 imply that the height of the nucleation free-energy barrier, ΔG_{crit}, is proportional to $\gamma^3/|\Delta\mu|^2$, emphasizing how strongly the nucleation rate depends on both supersaturation and interfacial energy.

The direct observation of crystal nucleation is difficult; therefore, simulations provide insights into the structure, shape, and packing of critical nuclei. Auer and Frenkel's (Auer and Frenkel 2001) simulations showed that the face-centered cubic and hexagonal close packed stacking form equally likely. In the early stages of nucleation, the random-hexagonal close-packed structure is simply more stable than fcc packing. Later, this metastable rhcp structure transforms into the stable fcc structure. Auer and Frenkel (Auer and Frenkel 2001) also suggested that if the range of sizes of the suspended colloidal particles was sufficiently large, the colloidal mixture would be truly amorphous and cannot crystallize due to increase of the solid-liquid interfacial free energy at high supersaturations. These simulation results provide possible clues that the pathway to the final crystalline state of CaP will pass through all the less stable states in order of increasing stability, or the resulting amorphous materials cannot transform into the crystallite phase. The first observed example of such a process in a living organism is seen in the chiton, a mollusk that has mineralized teeth that are used for scraping rocks to extract lgae buried beneath the surface. The outer layer of the tooth contains magnetite, a hard magnetic mineral. It forms from a disordered ferrihydrite precursor phase. The inner layer of the tooth contains carbonated apatite, similar to the mineral present in bone which forms by way of an amorphous calcium phosphate precursor phase. The hallmark of the biological strategy for making certain mineralized skeletal parts is that the first-formed solid deposits as disordered and often hydrated phases that, with time, transform into the stable crystalline deposit.

The CNT assumes that the critical nuclei are spherical due to surface tension and have the same structure as the stable bulk phase that is nucleating. However, Gasser et. al. (Gasser, et al. 2001) have observed elliptical nuclei by using confocal microscopy in which the crystallite surfaces are quite rough. The surface roughness is associated with high surface free energy, which may facilitate the attachment of particles to the nucleus,

thereby contributing to a more rapid nucleation. The assumption of a spherical nucleus may be disputed because the critical nucleus could be anisotropic with different free energy costs associated with different faces. This would have repercussions on the growth rate, as different faces are likely to grow at different rates. Yau and Vekilov (Yau and Vekilov 2000) reported direct observations of small (100 nm scale) crystallites" taking part in the very first stages of crystallization of the protein apoferritin, which has a relatively slow time scale for crystallization because of its large size. Surprisingly, the critical nucleus of apoferrition resembles a raft, consisting of a nearly planar layer of crystal with a partial second layer on top (Mullin 2001). The shape of the critical nucleus could have a large effect on its energy and therefore on the subsequent rate of crystal formation. One possibility is that the critical nucleus is not crystalline but rather a disordered, liquid-like aggregate of molecules, with crystallinity appearing only at later stages in the growth process.

3.1.2. Heterogeneous Nucleation

The addition of small "seed" particles to a supersaturated solution can greatly increase the rate at which crystals nucleate. This process is qualitatively better understood, when the seed has the same structure as the crystal that it spawns. Ostwald explained that supercooled liquids can be made to crystallize by the introduction of a small seed crystal. However, the microscopic mechanism of seeding by a "foreign" substance is still not well understood. The CNT provides a natural explanation as to why a seed crystal or a foreign object facilitates crystal nucleation; in the absence of a seed, a rare, spontaneous fluctuation is needed to form a crystal nucleus that exceeds the critical size. However, crystallization can proceed spontaneously if we add to the metastable liquid phase a seed crystal or a foreign particle that is larger than the critical nucleus. In homogeneous nucleation, the increase in the size of an embryo must overcome a free energy nucleation barrier before it can reach a critical radius and become a stable growing crystal. In the presence of foreign objects, the nucleation barrier may be reduced to(Mullin 2001)

$$\Delta G = \Delta G_{\text{hom}} f(m,x)(0 \le f(m,x) \le 1) \tag{3.4}$$

where *f(m,x)* is the interfacial correlation factor, varying from 0 to 1, describing the lowering of the nucleation barrier due to the presence of additive molecules or a suitable substrate. This factor will depend upon supersaturation, the interfacial interaction parameter *m*, and the relative size of foreign particles (*x*. *m*) (γ_{af} - γ_{ac})/γ_{cf}, where γ_{af}, γ_{ac}, and γ_{cf} are the interfacial free energies between the foreign particle (a) and fluid (f) and crystal nucleus (c) interface; γ_{cf} depends on the correlation and structural match between the nucleating phase and the substrate. R_s/r_c (where r_c is the critical size of nuclei) $2\Omega\gamma_{cf}/kT$ ln(1 + σ), Ω is the molecular volume per growth unit, and R_s is the average radius of spherical shaped foreign particles). When the interaction between the nucleating phase and the substrate is optimal, *f*(*m*,*x*) f =0. Conversely, if the interfacial correlation is very poor, *f*(*m*,*x*) f =1, and the additive molecule or the substrate exerts almost no influence on the nucleation barrier. It can be seen that *f*(*m*,*x*) describing the interfacial correlation between biominerals and substrates will increase with supersaturation. This implies that an increase of supersaturation will drive the substrates/biominerals from an interfacial structural matched state (a lower *f*(*m*,*x*)) to a state of higher mismatch (a higher *f*(*m*,*x*)). Taking into account the effect of the additive molecule or the substrate on both the nucleation barrier and the transport process, the nucleation rate (Mullin 2001) is given by

$$J = (R^s)^2 N^0 f''(m,x)\left[f(m,x)\right]^{0.5} B \exp\left[-\frac{\Delta G_{homo}}{kT} f(m,x)\right] \qquad (3.5)$$

where N^0 is the density of the foreign particles or substrates and *B* is a kinetic constant. The technical difficulties involved in directly evaluating crystal nucleation have led to other approaches to study initial crystallization events. One of the most common ways to characterize the kinetics of nucleation is to measure the induction period (t_s) prior to nucleation at different supersaturations. By definition, the nucleation rate *J* can be expressed as Eq 3.6,

$$J = 1/(t_s V) \qquad (3.6)$$

where *V* is the volume of the system. Combining Eqs 3.5 and 3.6 yields Eq 3.7,

$$\ln t_s = \frac{\kappa f(m,x)}{\left[\ln(1+\sigma)\right]^2} - \ln\left\{V(R^s)^2 N^0 f''(m,x)\left[f(m,x)\right]^{1/2} B\right\} \qquad (3.7)$$

where κ $[16\pi\gamma_{cr}{}^3\Omega^2/3(kT)^3]$ remains constant under a given set of conditions. According to Eq 3.7, the plot of ln(ts) against $1/[\ln(1 + \sigma)]^2$ will give rise to a straight line whose slope is determined by κ and $f(m)$ (Mullin 2001). Obviously, for a given system (constant κ and B), the slope of the straight line will change according to $f(m,x)$. In this sense, the slope of the ln(ts) against $1/[\ln(1 + \sigma)]^2$ plot gives the relative $f(m,x)$ for the system. Through the analysis of $f(m,x)$ changes and correspondingly the interfacial correlations between the substrate and HAP crystalline phases in terms of the variation of the slope, collagen fibers have been found to serve as much better templates than other common foreign particles by more effectively lowering the nucleation barrier of HAP. Interestingly, some biomolecules such as chondroitin sulfate may suppress the supersaturation-driven interfacial structure mismatch and promote the formation of ordered HAP crystallites.

Lu and Leng (Lu and Leng 2005) studied the theoretical analysis of calcium phosphate precipitation in simulated body fluid. In this study, CaP formation was analyzed based on classical crystallization theories of thermodynamics and kinetics. The analysis indicated that HA precipitation exhibited a higher thermodynamic driving force than OCP and DCPD in SBF. OCP precipitation was found kinetically favorable in SBF. The HA nucleation rate was significantly affected by the pH value. High pH environment is favorable for HA nucleation and the HA nucleation rate approaches the nucleations rate of OCP when the pH value approaches. DCPD does not have a thermodynamic driving force of precipitation in SBF, even though it has kinetic advantages in nucleation. DCPD precipitation becomes possible when the concentrations of calcium and phosphate ions increase to a higher than normal level in SBF. Possible variation of parameter values in the analysis model, such as discrepancies in the interfacial energy data or uncertainty of the contact angle of nuclei on surfaces, does not change these conclusions. However, HA precipitation can be considerably affected by containing carbonate or being deficient in calcium. Generally, precipitation of carbonate-containing HA is more kinetically favorable than that of stoichiometric HA and has a same level of thermodynamic driving force; precipitation of calcium-deficient HA is also more kinetically favorable, but its thermodynamic driving force is lower than that of stoichiometric HA.

3.2. Calcium Phosphate

Calcium phosphates are the chemical compounds of a special interest in many interdisciplinary fields of science, including geology, chemistry, biology and medicine. All calcium phosphates consist of three major chemical elements; calcium, phosphorus and oxygen, which their oxidation states are +2, +5 and –2, respectively These three chemical elements are present in abundance on the surface of our planet: oxygen is the most widespread chemical element of the earth's surface (47 wt%), calcium occupies the fifth place (3.3–3.4 wt%) and phosphorus (0.08–0.12 wt%) is among the first twenty of the chemical elements most widespread on our planet. In addition, the chemical composition of many calcium orthophosphates includes hydrogen, either as an acidic phosphate anion (for example, HPO_4^{2-} or $H_2PO_4^-$), and/or as incorporated water (for example, $CaHPO_4.2H_2O$). Diverse combinations of oxides of calcium and phosphorus (both in the presence of water and without it) provide a large variety of calcium phosphates, which are distinguished by the type of the phosphate anion: ortho- (PO_4^{3-}), meta- (PO_3^-), pyro- ($P_2O_7^{4-}$), and poly-($(PO_3)_n^{n-}$) (Dorozhkin 2007). In the case of multi-charged anions (orthophosphates and pyrophosphates), calcium phosphates are also differentiated by the number of hydrogen ions attached to the anion. Examples include mono-($Ca(H_2PO_4)_2$), di-($CaHPO_4$), tri-($Ca_3(PO_4)_2$), and tetra-($Ca_2P_2O_7$) calcium phosphates.

Most calcium phosphates have different solubility in water, while all dissolve in acids. The calcium to phosphate molar ratios (Ca/P) and the solubilities are important parameters to differentiate the phases each other. Table 3.1 shows the CaP phases and their solubility at different temperatures.

Table 3.1. CaP molar ratio, formula and solubility at different temperatures (Source: Dorozhkin 2007).

Ca/P molar ratio	Compound	formula	solubility 25°C, -log(Ksp)	solubility 37°C, -log(Ksp)	solubility product 25°C,
1.00	Brushite (DCPD)	$CaHPO_4.2H_2O$	6.59	6.73	$1.87x10^{-7}$ M^2
1.00	Monetite (DCPA)	$CaHPO_4$	6.90	6.04	$9.2x10^{-7}$ M^2
1.33	Octacalsium phosphate (OCP)	$Ca_8(HPO_4)_2(PO_4).5H_2O$	96.6	98.6	$2.5x10^{-99}M^{16}$
1.20-2.20	Amorphous calcium phosphate (ACP)	$Ca_xH_y(PO_4)_z.nH_2O$, n)3-4.5; 15-20% H_2O	-	-	
1.50	α-tricalcium phosphate (α-TCP)	α-$Ca_3(PO_4)_2$	25.5	28.5	$2.8x10^{-29}$ M^5
1.50	β-tricalcium phosphate (β -TCP)	β- $Ca_3(PO_4)_2$	28.9	29.6	$2.5x10^{-30}$ M^5
1.67	hydroxyapatite (HAP)	$Ca_{10}(PO_4)_6(OH)_2$	116.8	117.8	$5.5x10^{-118}$ M^{18}
1.67	fluorapatite (FAP)	$Ca_{10}(PO_4)_6F_2$	120.0	122.3	$5.0x10^{-123}$ M^{18}

In general, lowering Ca/P ratio will result in more acidic and soluble the calcium phosphate phase during the synthesis or induction. It is generally recognized that the crystallization of many calcium phosphates involves the formation of metastable precursor phases that subsequently dissolve as the precipitation reactions proceed. Thus, complex intermediate phases can participate in the crystallization process. Moreover, the *in vivo* presence of small peptides, proteins, and inorganic additives other than calcium and phosphate has a considerable influence on crystallization, making it difficult to predict the possible phases that may form. Studies of apatite mineral formation are complicated by the possibility of forming several calcium phosphate phases. The crystallographic data of calcium phosphate phases are listed in Table 2. The least soluble phase is hydroxyapatite (HAP) and preferentially formed under neutral or basic conditions. Brushite (DCPD) and octacalcium phosphate (OCP) are frequently formed under the more acidic solutions. Even under ideal HAP precipitation conditions, the precipitates are generally nonstoichiometric, suggesting the formation of calcium-

deficient apatites. Both DCPD and OCP have been involved as possible precursors to the formation of apatite phase. This may occur by the initial precipitation of DCPD and/or OCP followed by transformation to a more apatitic phase (Dorozhkin and Epple 2002). Although DCPD and OCP are often detected during *in vitro* crystallization, *in vivo* studies of bone formation rarely show the presence of these acidic calcium phosphate phases (Johnsson and Nancollas 1992). Latter, the situation is more complicated, since a large number of ions and molecules are present that can be incorporated into the crystal lattice or adsorbed at the crystallite surfaces. In biological apatite, DCPD and OCP are usually detected only during pathological calcification, where the pH is often relatively low (Johnsson and Nancollas 1992). In normal *in vivo* calcifications, these phases have not been found, suggesting the involvement of other precursors or the formation of an initial amorphous calcium phosphate phase (ACP) followed by transformation to apatite.

3.2.1. Amorphous Calcium Phosphate

Amorphous calcium phosphate is mainly formed as a transient phase during the formation of calcium posphates in aqueous systems. Usually ACP is the first phase precipitated from a supersaturated solution prepared by rapid mixing of solutions containing ions of calcium and orthophosphate. ACP is thought to be formed at the beginning of the precipitation due to a lower surface energy than that of OCP and HA. The amorphization level of ACP increases with the increasing concentration of calcium- and phosphate-containing solutions, as well as at a high solution pH and a low crystallization temperature. A continuous gentle agitation of as precipitated ACP in the mother solution, especially at elevated temperatures, results in a slow recrystallization and formation of better crystalline compounds, such as CDHA.

Table 3.2. Crystallographic data of calcium phosphate
(Source: Dorozhkin and Epple 2002).

Compound	Space group	unit cell parameters
(DCPD)	monoclinic *Ia*	a=5.812(2), b=15.180(3), c= 6.239(2) Å, β=116.42(3)°
(DCPA)	triclinic *P1*	a=6.910(1), b=6.627(2), c=6.998(2) Å, α= 96.34(2)°,β= 103.82(2)°, γ= 88.33(2)°
(OCP)	triclinic *P1*	a=19.692(4), b=9.523(2), c=6.835(2) Å, α =90.15(2)° β=92.54(2)°, γ=108.65(1)°
(α-TCP)	monoclinic $P2_1/a$	a=12.887(2), b=27.280(4), c=15.219(2) Å, β =126.20(1)°
(β -TCP)	rhombohedral *R3Ch*	a=b=10.4183(5), c=37.3464(23) Å, γ=120°
(HAP)	monoclinic $P2_1/b$ or hexagonal $P6_3/m$	a=9.84214(8), b=2a, c= 6.8814(7) Å, γ=120°, a=b=9.4302(5), c=6.8911(2) Å, γ=120°
(FAP)	hexagonal $P6_3/m$	a=b=9.367, c=6.884 Å, γ=120°

The chemical composition of ACP strongly depends on the solution pH and the concentrations of mixing solutions. For example, ACP with Ca/P ratios in the range of 1.18 (precipitated at solution pH = 6.6) to 1.53 (precipitated at solution pH = 11.7) and even to 2.5 have been described. The presence of ions of pyrophosphate, carbonate and/or magnesium in solution during the crystallization increases the formation of ACP and slows down its further transformation into more crystalline calcium orthophosphates, while the presence of fluoride has the opposite effect. FTIR spectra of ACP show broad featureless phosphate absorption bands. Electron microscopy of ACP usually shows spherical particles with diameters in the range of 20–200 nm without distinct morphology. However, there is the possibility that ACP has an apatitic structure but with a crystal size so small, that it's X-ray is amorphous. This is supported by X-ray absorption spectroscopic data (EXAFS) on biogenic and synthetic samples. On the other hand, it was proposed that the basic structural unit of ACP is a 9.5 Å diameter, roughly spherical cluster of ions with the composition $Ca_9(PO_4)_6$. These clusters were found experimentally as first nuclei during the crystallization of HA, and a model was developed to describe the crystallization of HA as a step-wise assembly of these units.

3.2.2. Brushite (DCPD)

The DCPD crystals are formed during the transformation of ACP into crystal phase and consist of chains of $CaPO_4$ arranged parallel to each other. Lattice water molecules are interlayered between the calcium phosphate chains as shown in Figure 3.2.

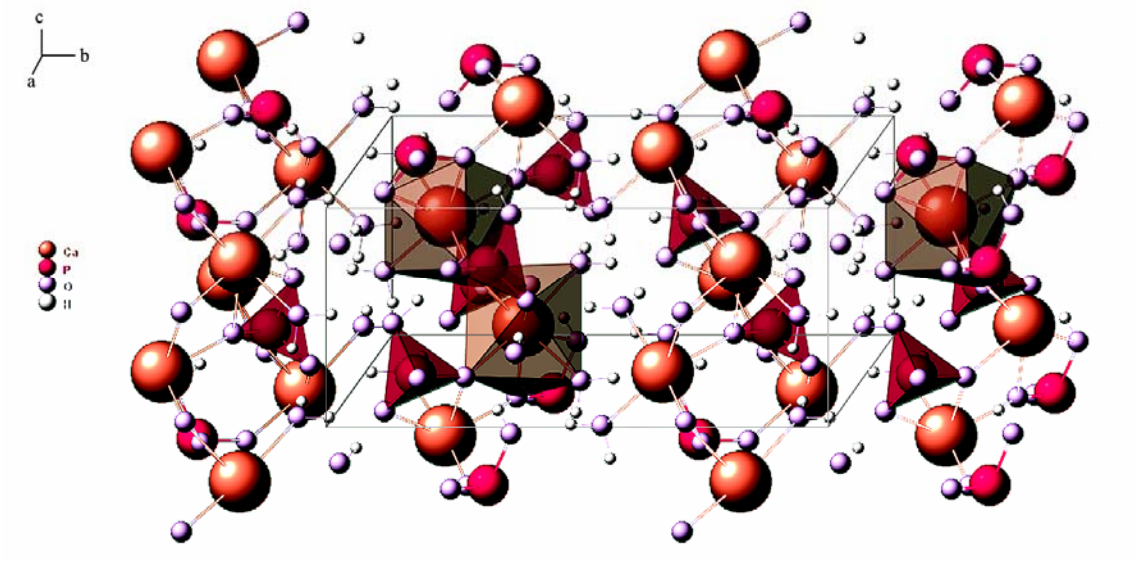

Figure 3.2 Crystal structure of DCPD
(Source: Webmineral-Brushite 2010)

Anhydrous calcium hydrate phosphate or monetite (DCPA) is less soluble than DCPD due to the absence of water inclusions. This phase is rarely seen *in vivo*, although Young and Brown suggested that the apparent absence of this phase might be due to difficulties of detection as a consequence of its weak X-ray diffraction pattern. DCPD has been proposed as an intermediate in both bone mineralization and enamel dissolution.

X-ray diffraction was used to determine the atomic structure of the {010} interface of DCPD with water using surface. Since this biomineral contains water layers as part of its crystal structure, special ordering properties at the interface are expected. This interface consists of two water bilayers with different ordering properties. The first is highly ordered and can be considered as part of the brushite crystal structure. The second water bilayer exhibits no in-plane order but shows only layering in the perpendicular direction. It has been proposed that the low level of water ordering at the interface is correlated with the low solubility of DCPD in water. Below pH 6.5, DCPD

is the dominant phase, while above this pH the formation of ACP and octacalcium phosphate (OCP) is more considerable. On the other hand, although DCPD and OCP form readily from solution, they are thermodynamically metastable with respect to HAP and serve as precursor phases (Wang, et al. 2008). The order of the precipitation from a supersaturated solution is governed not only by the thermodynamic solubility product but also by kinetic factors. Thus, the solid-phase first precipitated undergoes changes in solution toward phases of higher stability.

3.2.3. Monetite (DCPA)

Dicalcium phosphate anhydrous (DCPA, $CaHPO_4$; the chemically correct name is calcium hydrogen orthophosphate anhydrous; the mineral monetite) is the anhydrous form of DCPD. Like DCPD, DCPA can be crystallized from aqueous solutions but at 100°C. The crystal structure of the monetite is shown in Figure 3.3.

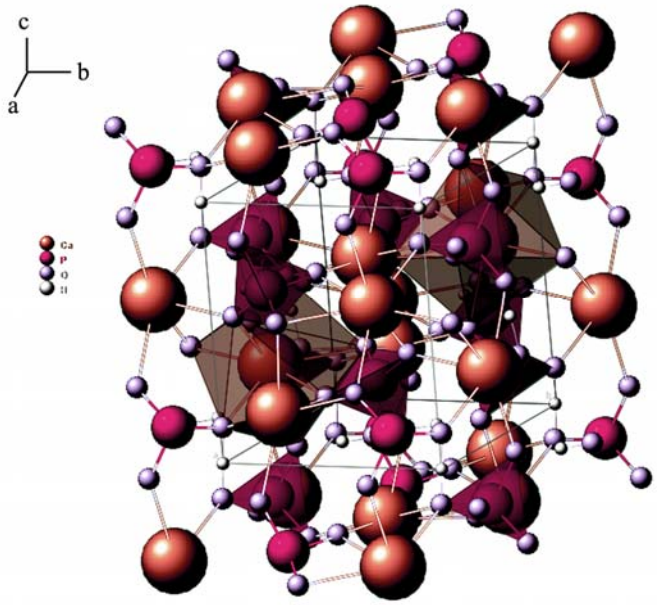

Figure 3.3 Schematic illustration of crystal structure of DCPA
(Source: Webmineral-Monetite 2010)

Unlike DCPD, DCPA occurs in neither normal nor pathological calcifications. It is used in calcium phosphate cements. Other applications include using as a polishing agent, a source of calcium and phosphate in nutritional supplements (e.g., in prepared breakfast

cereals, enriched flour, and noodle products), a tabletting aid and a toothpaste component. In addition, it is used as a dough conditioner in food industry.

3.2.4. Octacalcium Phosphate (OCP)

Octacalcium phosphate (OCP) has a significant biological relevance due to its role as a possible precursor during the formation of carbonated apatite in the hard tissues of vertebrates. OCP has a remarkable structural similarity to HAP due to its layered structure involving apatitic and hydrated layers (Mathew, et al. 1988). The triclinic structure of OCP displays remarkable similarities to the hexagonal structure of HAP because the unit cell of OCP consists of apatitic layers, and apatitic layers alternate with hydrated layers parallel to the (100) face, while the hydrated layer contains lattice water and less densely packed calcium and phosphate ions. Morphologically, OCP crystallizes as {100} blades of triclinic pinacoidal symmetry, elongated along the *a*-axis and bordered by the forms {010}, {001}, and {011}. It is generally assumed that, in solutions, the hydrated layer of the (100) face is the layer most likely exposed to solution. The water content of OCP crystals is about 1/5 that of DCPD, and this is partly responsible for its lower solubility. The similarity in crystal structure between OCP and HAP is one reason that the epitaxial growth of these phases is often observed. The hydrated layer of the OCP unit cell may form an inter phase between HAP and the surrounding solution. If this occurs, the epitaxial intergrowth of OCP and HAP is favored. A “central OCP inclusion” (also known as a “central dark line”) is seen by TEM in many biological apatites and was explained recently by the inherent lattice mismatch between OCP and HAP. A solid state 31P homonuclear double-quantum (DQ) NMR study showed that the bladelike OCP crystals will transform into hexagonal rod-shaped HAP crystals as the pH of the reaction mixture increases slowly from 4.35 to 6.69. A trace amount of monetite is involved in this transformation process as an intermediate phase at pH values of about 5 OCP is unstable relative to HAP and tends to hydrolyze according to the reaction:

$$Ca_8H_2(PO_4)_6{\cdot}5H_2O+2Ca^{2+}\rightarrow Ca_{10}(PO_4)_6(OH)_2+4H^+ \qquad (3.8)$$

This structural relationship between OCP and HAP and its transformation from OCP to HAP provide a rational basis for understanding physiologically important phenomena such as (i) a possible mechanism for incorporation of impurities and defects into dental enamel and (ii) a rationale as to why teeth may vary in their caries susceptibility. In dental apatites, part of the lattice ions of HAP are substituted by ions such as CO_3^{2-}, F-, Na^+, and K^+. In particular, the incorporation of carbonate has a considerable influence on the physical and physicochemical properties of the solid. K^+- and CO_3^{2-}-containing HAP formed by the hydrolysis of OCP is to be considered as interlayered mixtures of OCP and carbonated apatite. The stoichiometry of the apatite layers in the K^+- and CO_3^{2-}-containing HAP conforms to that of HAP in which the lattice ions are substituted by K^+ and CO_3^{2-}.

3.2.5. Tricalcium Phosphate (TCP)

β-Tricalcium phosphate (β-TCP, β-$Ca_3(PO_4)_2$) cannot be precipitated from aqueous solutions. It is a high temperature phase of calcium orthophosphates, which only can be prepared by thermal decomposition, e.g. of CDHA, at temperatures above 800°C (Slosarczyk and Piekarczyk 1999). Apart from the chemical preparation routes, ion-substituted β-TCP can be prepared by calcining of bones: such type of β-TCP is occasionally called ‘‘bone ash’’.

At temperatures above 1125°C, it transforms into the high-temperature phase α-TCP. Being the stable phase at room temperature, β-TCP is less soluble in water than α -TCP (Table 3.1). Pure β-TCP never occurs in biological calcifications. In biomedicine, β-TCP is used in calcium phosphate bone cements. In combination with HA, β-TCP forms the biphasic calcium phosphate (BCP). Both β-TCP and BCP are widely used as a bone substitution bioceramics. Pure β-TCP is added to some brands of toothpaste as gentle polishing agent.

α-Tricalcium phosphate (α-TCP, α-$Ca_3(PO_4)_2$; the chemically correct name is calcium orthophosphate tribasic alpha) is usually prepared from β-TCP at heating above 1125°C and it might be considered as a high temperature phase of β-TCP. However, at the turn of the millennium, it was discovered that if calcium orthophosphates were doped with a certain amount of silica (approx. 1 mol of SiO_2 per 1 mol of HA), α-TCP

would become stable at lower temperatures of 800–1000°C. Such type of α-TCP is called ‘‘silicon stabilized a-TCP’’(Sayer, et al. 2003).

Although α-TCP and β-TCP have exactly the same chemical composition, they differ by the crystal structure (Table 3.2) and solubility (Table 3.1). In addition, β-TCP is more stable than the α-phase (Sayer, et al. 2003). Therefore, α-TCP is more reactive in aqueous systems, has a higher specific energy and it can be hydrolyzed to a mixture of other calcium phosphates. It never occurs in biological calcifications but in medicine chemically pure α-TCP is occasionally used in calcium phosphate cements. However, the silicon stabilized α-TCP (more precisely as a biphasic composite with HA) has been commercialized as a starting material to produce bioresorbable porous ceramic scaffolds to be used as artificial bone grafts.

3.2.6. Hydroxyapatite (HA)

This is the most common and well-known phase studied for a number of biomedical applications owing to its similarity to natural bone. Chemically it is represented as $Ca_{10}(PO_4)_6(OH)_2$ and is characterized by a Ca/P ratio of 1.67. Stoichiometric HA has monoclinic structure with space group P21/b with lattice parameters a = 9.4215 Å, b = 2a, c = 6.8815 Å, and = 120°. Figure 3.4 shows the crystal structure of the HA.

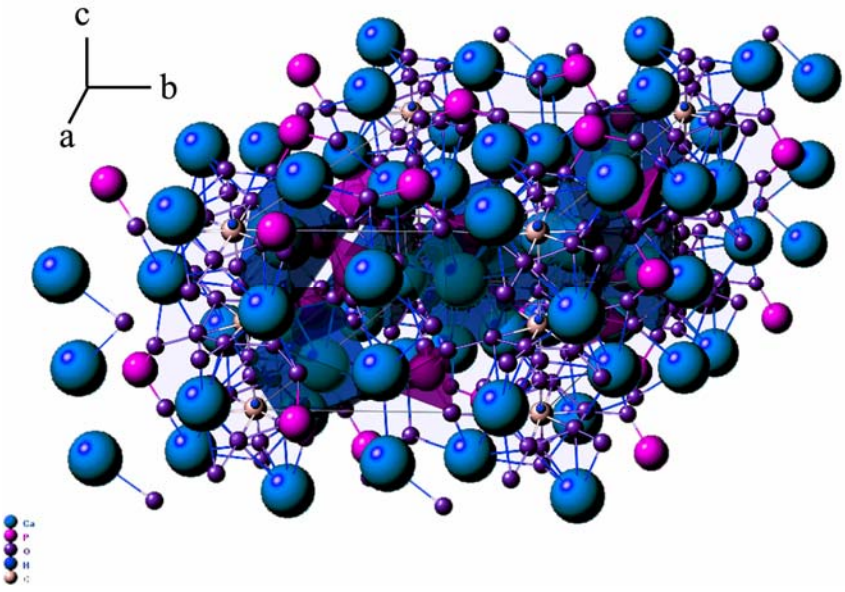

Figure 3.4. Hydroxyapatite crystal structure
(Source: Webmineral-hydroxyapatite 2010).

It has also structure with space group P63/m. However, it is difficult to obtain the exact stoichiometry (Ca/P ratio) in HA because of the different Ca/P ratios that can be stabilized depending on the synthesis method and conditions employed. Various HA phases can be formed, which can be categorized into calcium-deficient hydroxyapatite, oxy-hydroxyapatite, and carbonated hydroxyapatite (CHA) depending on the type of environment employed in the synthesis steps. Biological apatites differ chemically from ideal HA, in that, they often include cations such as Mg^{2+}, Na^{+}, and K^{+} and anions such as Cl^{-} and F^{-}, which can be introduced into the HA lattice by substitution of one or more Ca^{2+}. However, the major substituent in biological apatite is carbonate, which in bone mineral occurs at levels of 5-8 wt% (Kumta, et al. 2005).

Bioactive materials such as CPC provide direct bone contact at the implant-bone interface and guide bone formation along their surface, effects which are collectively termed osseoconduction (Ducheyne, et al. 1990). Amorphous calcium phosphate coatings are more soluble than the crystalline phosphates and present more rapid bone formation and produce higher cell differentiation in vitro studies. For good bone apposition thickness of calcium phosphate coatings on implant surface has to be at least 10 μm (Zhu, et al. 2003).

HA has shown the ability to bind chemically to bone. For this reason it is proposed as a suitable coating material to provide stronger early fixation of uncemented prostheses. And similarity between synthetic HA and mineral phase of the bone is suggested as a reason for HA being an early material to be used for biocompatible metallic implants. HA-coated specimens achieve bone mineralization directly on the coating surface. The advantages appear to be greater bone growth and penetration depth, with a more direct contact between the tissue and the implant surface. It is also observed that samples without HA coating show lack of direct bone deposition on the titanium surface.

HA coatings on implants show long-term survival and have very low reliability under tensile loads. Hence they should be used as small unloaded implants such as in middle ear or coatings on metal implants. HA has lower fracture toughness compared to the human bone but its mechanical stability can be enhanced by reinforcing with bio-inert metal oxides such as zirconia and alumina.

Calcium-deficient hydroxyapatites [$Ca_{10-x}(PO4)_{6-x}(HPO4)_x(OH)_{2-x}$ where $0 < x < 1$] are of greater biological interest than the stoichiometric HA since Ca/P ratio in bone is nearer to 1.5. Calcium-deficient apatite plays an important role in several processes

such as bone remodeling and bone formation. Both stoichiometric- and calcium-deficient HA are chemically and structurally similar to the mineral constituent of human hard tissue. However, bone mineral essentially has the structure of the calcium-deficient apatite, but it is similar to stoichiometric HA chemically and compositionally.

Tough HA and other calcium phosphates produce bioactivity their use introduce several potential complications including fatigue of the coatings, possibility of separation or delamination of the ceramic layer and premature coating dissolution. Despite these concerns, several studies have demonstrated beneficial effects of HA/TCP coating.

CHAPTER 4

PROCESSING AND CHACTERIZATION OF OPEN CELL Ti6Al4V FOAMS FOR BIOMEDICAL APPLICATONS

4.1. Introduction

The bulk material forms of Ti and its alloys including Ti6Al4V have been widely used in orthopedic implants due to their good biocompatibility, high strength to weight ratios, relative low elastic modulus, high fatigue strength and excellent corrosion resistance as compared with widely used implant metals including cobalt alloys and stainless steels (Long and Rack 1998). Nevertheless, the porous implant components based on biocompatible metallic materials (e.g. Ti and Ti6Al4V) are known to promote interactions between bone and the surrounding tissue (Pilliar 1987). Pores facilitate the bone tissue formation, allowing the migration and proliferation of osteoblasts and mesenchymel cells. In addition, a porous surface provides mechanical interlocking between the implant and the surrounding bone, enhancing mechanical stability at the interface. The minimum pore size suitable for the bone replacement was reported larger than 100 μm (Hulbert, et al. 1970), while the tendency of fibrous tissue formation increased above the pore size of 1 mm (Bobyn and Miller 1994). Furthermore, the relatively low elastic moduli of porous metals as compared with those of bulk metals are expected to reduce the extent of stress shielding, which causes well-known *implant loosening,* and hence to prolong implant life-time (Long and Rack 1998). By reducing the "elastic-mismatch" as well as "strength-mismatch" between metallic implant and bone, it is expected to have better performance of implant-bone compound which can be called as "iso-elastic multi-material system". For this purpose numbers of innovative investigations have been undertaken world-wide.

Open cell Ti foams and powder compacts, potentially to be used in biomedical applications, were prepared using the space holder (Bram, et al. 2000, Wen, et al. 2001, Wen, et al. 2002a) and the sintering of powder compacts (Oh, et al. 2003) processes, respectively. The similar processing routes namely the sintering of powder compacts and the space holder methods are used to produce biocompatible interconnected Ti and

Ti6Al4V powder compacts and open cell foams, respectively. Although the modulus values of sintered Ti compacts and Ti foams of varying porosities were found to be comparable with that of natural bone, the compressive strength values were lower than those of cortical bone due to the relatively low yield strength of Ti powder used (Oh, et al. 2002, Wen, et al. 2002a). This experimental study is therefore conducted in order to produce relatively high strength open cell foams that can potentially be used in biomedical applications including human cortical bone replacement. For this, Ti6Al4V foams with a porosity level nearly 60% were prepared using two different commercially available biomedical grade Ti6Al4V powders. The foam samples were further characterized through compression testing at a quasi-static strain rate in order to determine the effect of powder type and sintering temperature on the foam mechanical properties. The final aim of the work was the optimization of the foam preparation process based on the microstructural and mechanical properties to satisfy the bio-mechanical design requirements for certain implants.

4.2. Experimental

4.2.1. Materials for Foam Processing

Ti6Al4V foams were prepared using commercially available gas atomized spherical particle powders, received from Crucible Research Company. The chemical composition of the powder complied with ASTM 1580-1 standard (ASTM F 1580-95, Standard specification for titanium and Ti6Al4V alloy powders for coating surgical implants) as tabulated in the Table 4.1. Powder 1 (P1) was 45-150 μm in particle size, with an average particle size of 94 μm and Powder 2 (P2) 30-90 μm in particle size, with an average particle size of 66 μm. Ammonium bicarbonate (Aldrich) sieved in a particle size range of 315-500 μm was used as space holder by an amount of 60 vol%.

Table 4.1. Chemical composition of Ti6Al4V powders (wt %).

Element	Al	V	O	Fe	C	H	N	Cu	Sn	Ti
ASTM F1580-1	5.5-6.75	3.5-4.5	0.2	0.3	0.08	0.015	0.05	0.1	0.1	Bal.
P1	6.27	4.0	0.149	0.05	0.085	-	0.011	-	-	Bal.
P2	6.39	4.04	0.152	0.048	0.09	-	0.011	-	-	Bal.

Table 4.2. Powder sieve analysis of Ti6Al4V powders (%).

Opening in microns	150	105	90	74	63	53	45
P1	99.9	68.5	-	33.1	19.4	16.5	2.8
P2	100	100	99.3	69.4	46.2	39.7	22.6

4.2.2. Powder Compaction

The foams were prepared using space holder method. The processing steps of space holder method are schematically presented in Figure 4.1. The process starts with mixing of metal powders with a suitable space holder material, followed by a compaction step (e.g. uniaxial and isostatic pressing) that produces metal powder-space holder mixture compact. The green compact is then heat treated at a relatively low temperature to release the space holder, resulting in an unfired open cell foam metal structure. Finally, the compact is sintered at relatively high temperatures to provide structural integrity. This method allows a direct near net-shape fabrication of foamed implant components with a relatively homogeneous pore structure and a high level of porosity (60-80%). Green powder compacts of 40x40x10 mm in size were compacted at room temperature inside a tool steel die at a pressure of 400 MPa using a polyvinyl alcohol (PVA) solution (10% by volume) as the binding material in an amount of 2% by weight.

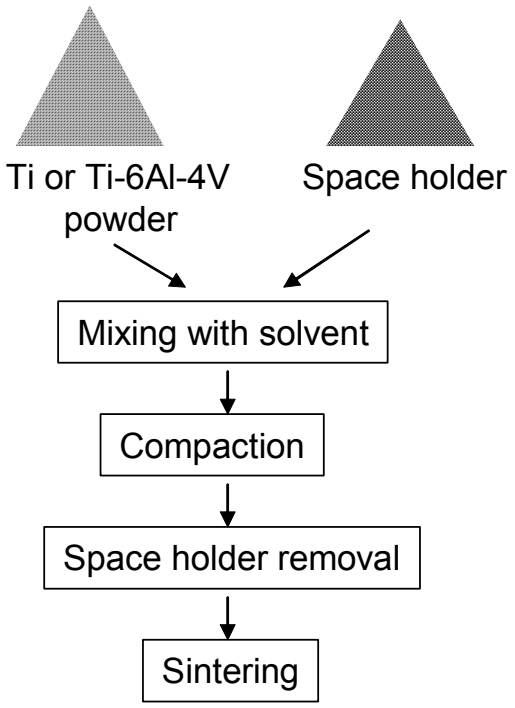

Figure 4.1. Processing steps of space holder method.

4.2.3. Sintering

The sintering of green compacts was performed in a tightly enclosed horizontal tube furnace (Figure 4.2(a)) under the high purity (99.998%) Ar atmosphere at 1200, 1250, 1300 and 1350 ^{o}C for 2 h. The compacts were inserted into the furnace at room temperature inside an enclosed Ti box on a graphite plate (Figure 4.2(b)) which prevented the bonding between Ti box and compacts. The compacts were heated and cooled with a rate of 5 ^{o}C per min. In the heating cycle, the compacts were kept at 450 ^{o}C for ½ hour in order to allow the complete burning of the binder.

(a)

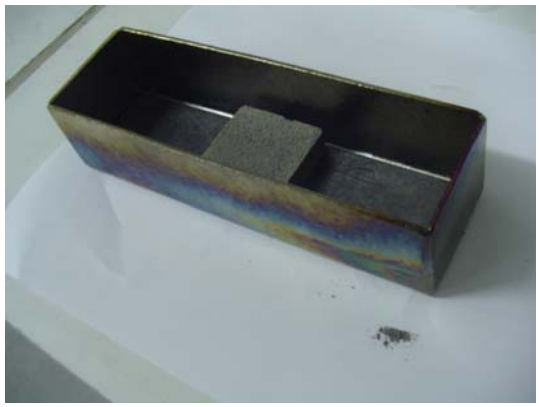

(b)

Figure 4.2. (a) Tube furnace and (b) enclosed Ti box used to process of Ti6Al4V foams.

4.3. Characterization Techniques

4.3.1. Microscopic Studies

Microscopic analyses were performed on vacuum epoxy-mounted as-received powders and sintered foams using optical microscopy and a Philips XL30-SFEG SEM with an Energy Dispersive X-ray (EDX) analyzer. Vacuum mounting was performed using a vacuum mounting device shown in Figure 4.3. In the mounting process, 200 ml epoxy was mixed with 1 ml initiator and 2 ml accelerator and then poured onto the compacts under vacuum atmosphere. The polished cross-sections of samples were etched with Kroll's reagent (3 cm^3 of HF and 6 cm^3 of HNO_3 in 100 ml of H_2O).

Figure 4.3. Vacuum-mounting equipment.

4.3.2. X-ray Diffraction and Thermogravimetric Analysis

X-ray measurements were made with a θ/2θ diffractometer with Cu Kα x-rays (λ = 1.5404 for the 8.05 keV x-rays) from a high intensity x-ray tube (Philips Xpert). The voltage and current used were 45.0 kV and 40 mA, respectively. The 2θ range for the specimens was 30 to 100 degrees, which gives a scan time of about 2 h for the step widths and times used in this experiment (0.05° and 4 s, respectively). The experimental data were evaluated using Expert Manager software.

A Perkin Elmer Diamond Thermo-Gravimetric Analyzer (TGA) was used to analyze the thermo gravimetric behaviour of space holder and binder.

4.3.3. Density and Porosity Measurements

Porosity measurements were performed using the Archimedes' method after coating the surface of the compacts with paraffin to prevent penetration of water into the pores. After measuring the density of the compacts, porosities (P) were calculated via density values using the following equations;

$$\rho = \frac{w_d}{w_d - w_f} \tag{4.1}$$

and

$$P = 1 - \frac{\rho}{\rho_{th}} \tag{4.2}$$

where, w_d is the weight of the sample in air, w_f is the weight of the sample in water, respectively and ρ_{th} is the density of Ti6Al4V, 4.42 $g.cm^{-3}$.

4.4. Results and Discussion

4.4.1. Powders

SEM micrographs of powders are shown in Figures 4.4(a) and (b) for P1 and P2, respectively. Particles are noted to contain satellites attached to them resulting from the powder atomization process as seen in Figures 4.4(a) and (b). The size distributions of the P1 and P2 are further shown in Figure 4.5. In P1, nearly 80%, while in P2 only about 50% of particles are larger than 63 μm, which is basically showing the quite different particle distributions in the powders. Since few percentages of relatively small particles are found in P1, the particle size distribution is considered nearly mono modal. On the other hand, the particle size distribution in P2 is near bimodal composing of relatively large (90 μm) and small (30-40 μm) particles as seen in Figure 4.4(b). The average powder size was found to be nearly 94 μm for P1 and 66 μm for P2. The specific surface area (SSA) of the powders was determined 0.0694 $m^2.g^{-1}$ and 0.112 $m^2.g^{-1}$ for P1 and P2, respectively.

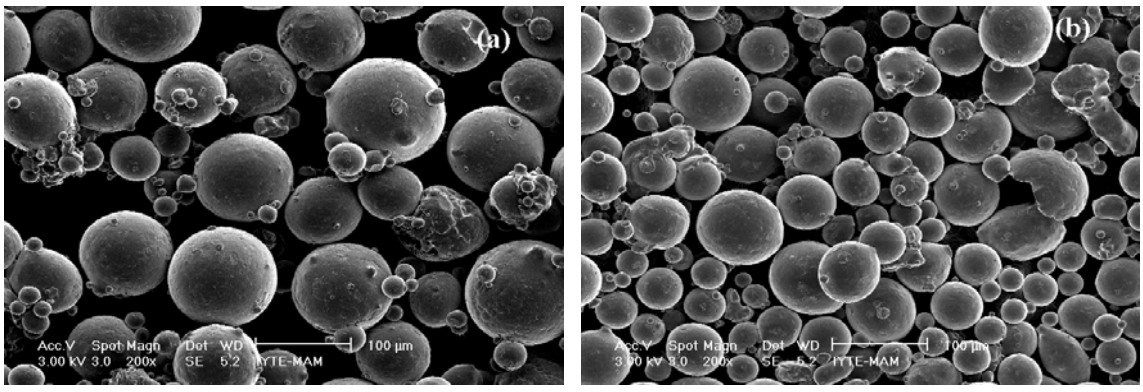

Figure 4.4. SEM micrographs showing the particles in (a) P1 and (b) P2.

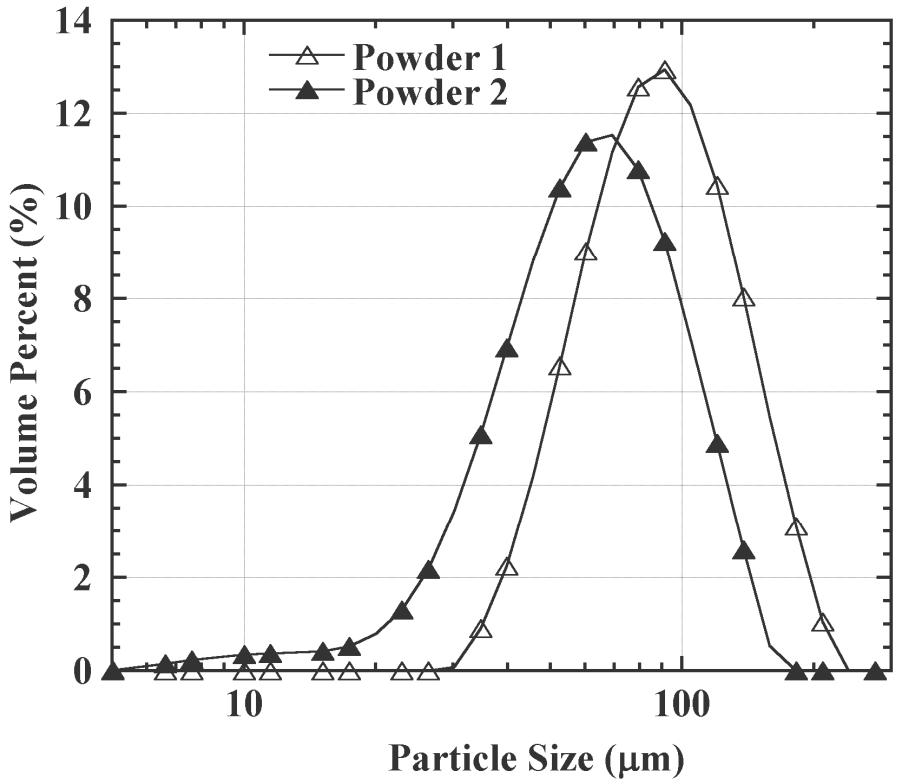

Figure 4.5. Size distribution of Ti6Al4V powder particles.

4.4.2. TGA Results

TGA and dTGA of PVA, ammonium bicarbonate and urea are sequentially shown in Figures 4.6(a), (b) and (c). PVA decomposition starts at 90°C and continues up to 490°C (Figure 4.6 (a)). PVA has two endothermic reaction temperatures, 318 and 440°C. The ammonium bicarbonate decomposition starts at 50 ^{o}C and ends up at 175°C (Figure 4.6(b)). Ammonium bicarbonate decomposition is shown by the following reaction,

$$NH_4HCO_{3\,(s)} \rightarrow NH_{3\,(g)} + H_2O_{(g)} + CO_{2(g)} \qquad (4.3)$$

The endothermic reaction of ammonium bicarbonate occurs at the decomposition stage by the formation of ammonia, carbon dioxide and water vapor. The decomposition of urea starts at about 100 ^{o}C and ends up at 600 ^{o}C (Figure 4.6(c)). Ti and its alloys are known to be very reactive and can easily form interstitial solid solutions with other elements including carbon, oxygen and nitrogen. Since the presence of these elements is

detrimental for the ductility, the reaction between Ti powder and the cracking products of the space holder in a temperature range of 300-600°C must be avoided (Bram, et al. 2000, Wen, et al. 2001, Wen, et al. 2002a). It is therefore proposed that space holder should be removed at temperatures below about 200°C (Bram, et al. 2000). TGA clearly showed that the decomposition of urea continues until about 600°C, while ammonium bicarbonate decomposition finished at about 175°C. Therefore ammonium bicarbonate was selected as space holder for the studied foams.

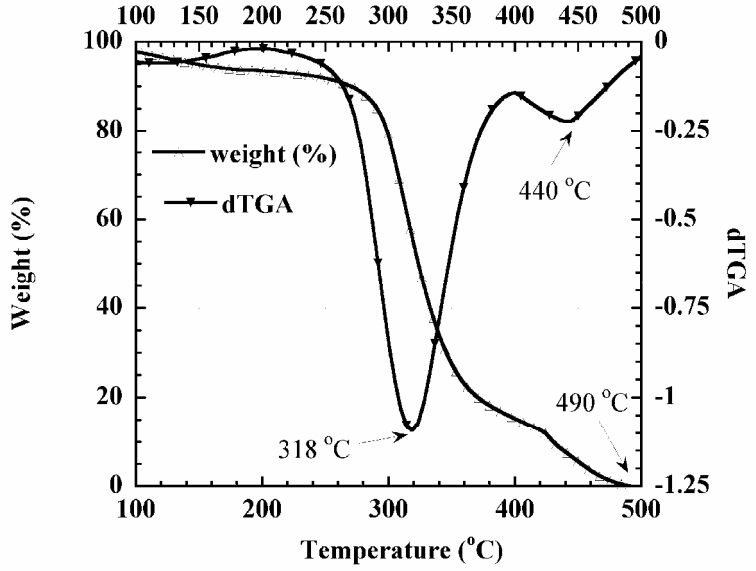

(a)

Figure 4.6. TGA and dTGA of (a) PVA, (b) ammonium bicarbonate and (c) urea.

(cont. on next page)

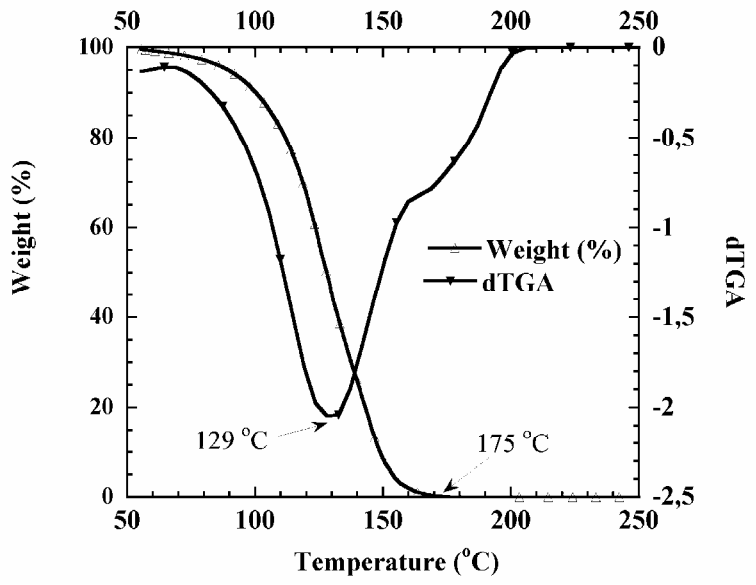

(b)

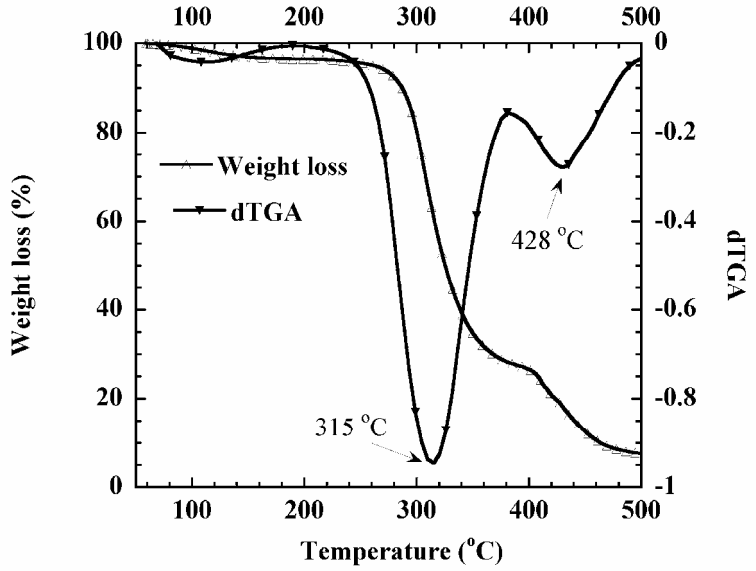

(c)

Figure 4.6. (cont.)

4.4.3. XRD & SEM Results

The microstructures of the as-received powders are shown in Figures 4.7(a) and (b). The microstructure of P1 and P2 is composed of needle-like α phase which is also known as acicular alpha (α). Figures 4.8 and 4.9 further show the XRD spectra of the P1 and P2 foams sintered at 1200, 1250, 1300 and 1350°C, respectively. In the same figures, the XRD spectra of the as-received P1 and P2 are also shown for comparison.

As is expected, the microstructure of the powders, after sintering above 1000 ^{o}C, transforms from fully needle-like α-phase into Widmanstätten microstructure of colonies of β lathes (bcc and rich in V) and α platelets (hcp and rich in Al). The β phase x-ray peak intensity increases with increasing sintering temperature for both P1 and P2 foam specimens. This may be attributed to the interstitial substitution of the V into α phase. The increased β phase x-ray intensity is also higher in P2 foam than in P1 foam due to higher surface area of P2.

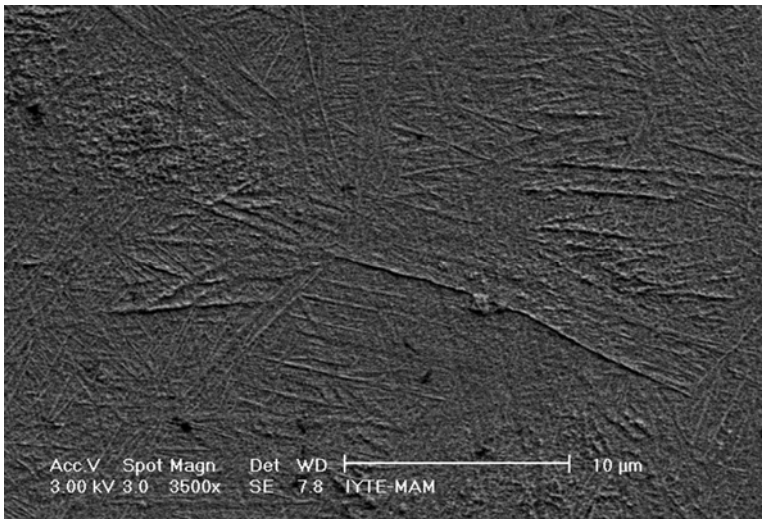

(a)

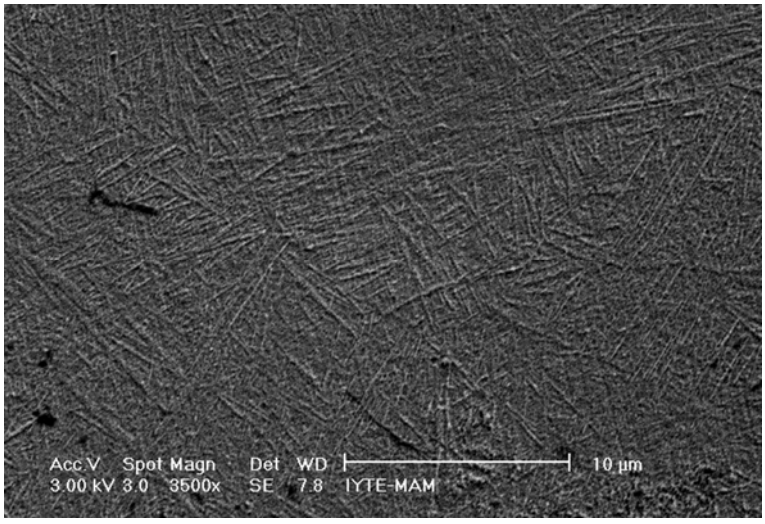

(b)

Figure 4.7. The microstructure of the as-received powders, (a) P1 and (b) P2.

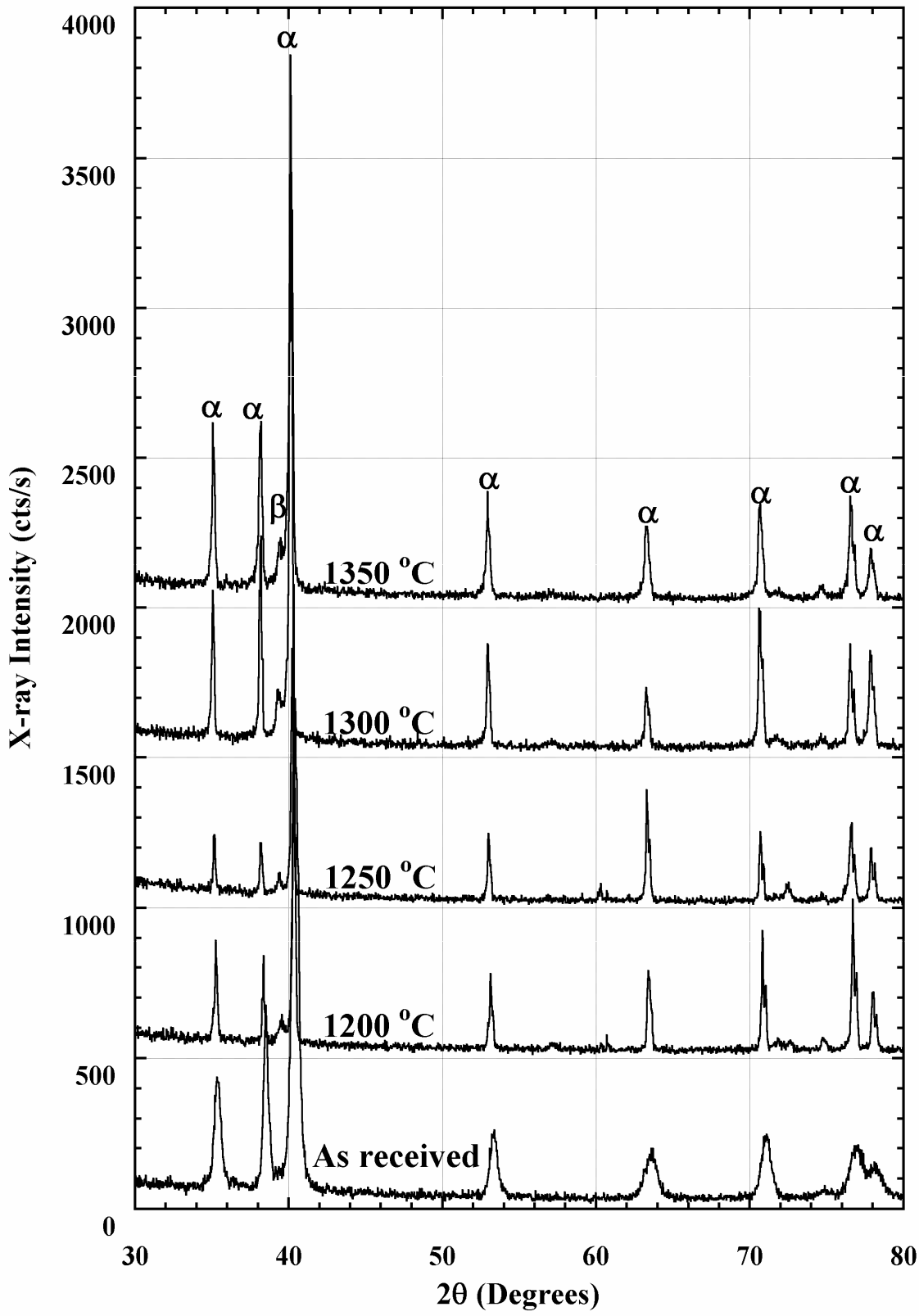

Figure 4.8. XRD spectra of the as-received P1 and sintered P1 Ti6Al4V foam specimens at increasing sintering temperature.

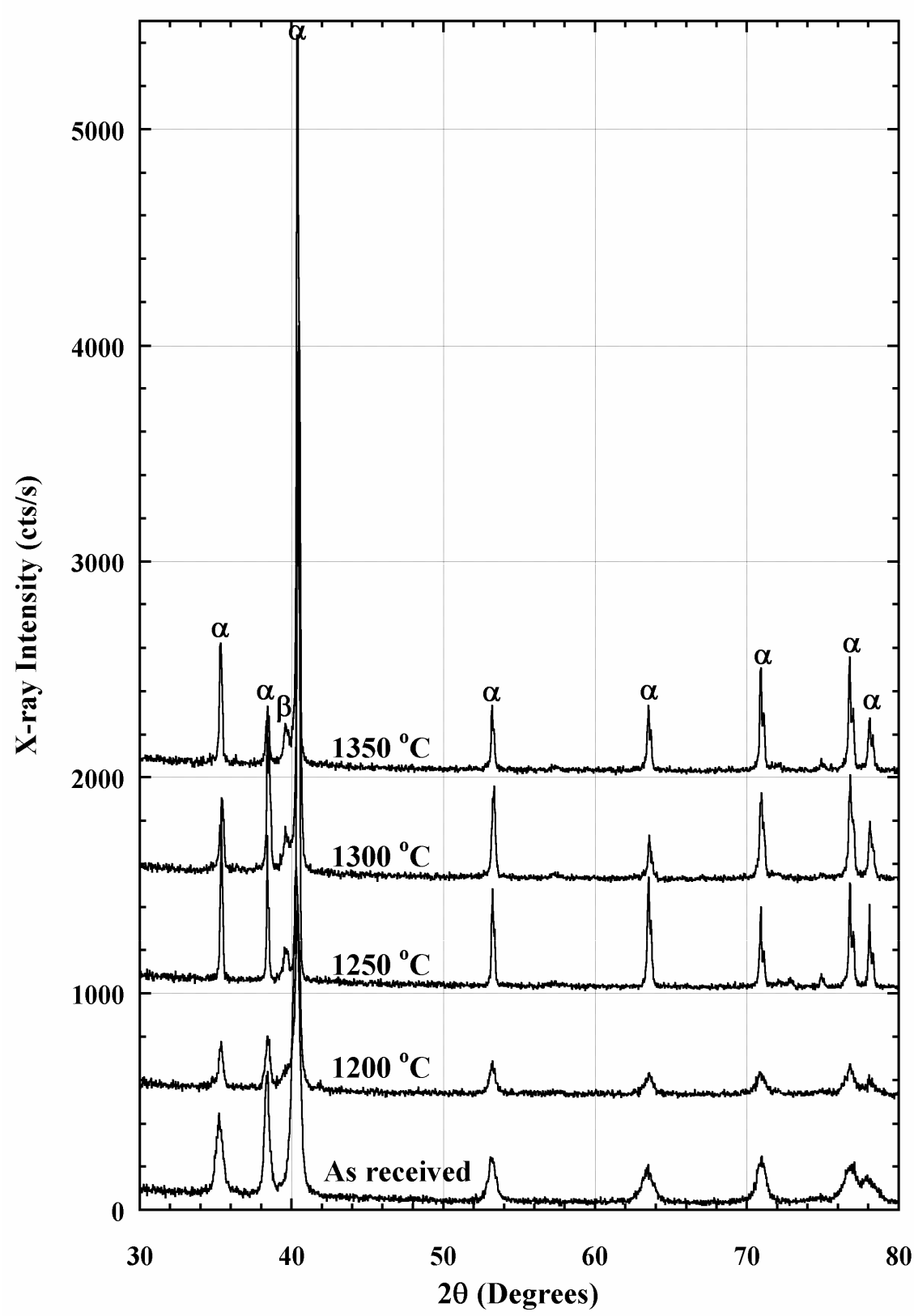

Figure 4.9. XRD spectra of the as-received P2 and sintered P2 Ti6Al4V foam specimens at increasing sintering temperature.

The SEM micrographs of the sintered P1 and P2 foam particle microstructure are shown in Figure 4.10. The lathlike structures seen in the micrographs are the Windmanstaten structure. The Widmanstatten is resulted from the sintering Ti6Al4V powder at relatively high temperatures above the β-transition temperature (940°C) and subsequent slow cooling in the furnace under Ar atmosphere. Table 4.3 tabulates the oxygen content of P2 foam sintered between 1200 and 1350°C. As is tabulated in Table 4.3, the tendency for the oxidation of the powders increases with increasing sintering temperature. Although, the sintering was performed under high purity (99.998%) argon atmosphere, the oxidation of the particle surface took place due to the extreme reactivity of Ti to oxygen.

Table 4.3. Oxygen content of P2 and P2 foam particles sintered between 1200 and 1350°C.

Sintering Temperature (°C)	Oxygen Content (wt.%)
As received	0.149
1200	0.6±0.1
1250	0.66±0.01
1300	0.67±0.01
1350	0.9±0.1

The elemental EDX analysis of α and β phases of the foam specimens sintered at different temperatures are tabulated in Table 4.4. The colonies of β lathes (bcc) are seen in this table rich in V and α plates (hcp) and rich in Al. As is tabulated in Table 4.4, V-content in α-phase varies between 1.6 and 3.8 at.%, while it varies between 10 to 18.6 at.% in β-phase. However, Al content of β-phase is lower than that of α-phase. The β-phase thickness of the foam specimens further increases with increasing sintering temperature up to 1350°C.

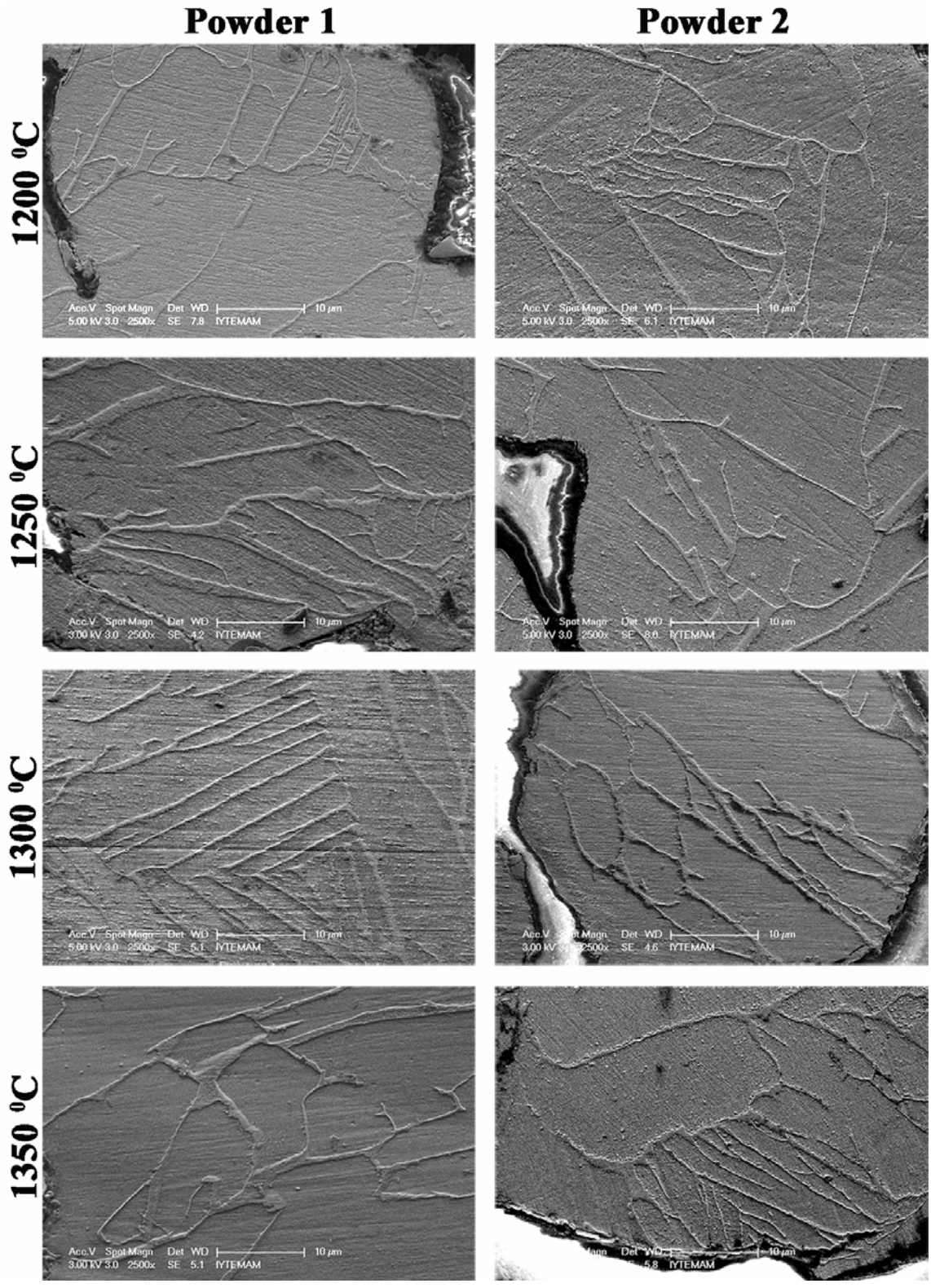

Figure 4.10. SEM micrographs of Widmanstatten structure of P1 and P2 foam particles sintered at different temperatures.

Table 4.4. EDX analysis of α and β phases of P1 and P2 foam.

Temperature (°C)	Phases					
	α-Phase			β-Phase		
	Ti (at.%)	Al (at.%)	V (at.%)	Ti (at.%)	Al (at.%)	V(at.%)
1200-1	83.05	13.47	3.48	75.39	5.96	18.65
1200-2	84.67	13.27	2.05	72.86	6.06	21.09
1250-1	84.78	11.35	3.87	82.84	6.85	10.31
1250-2	83.99	13.27	2.73	80.16	7.39	12.45
1300-1	85.62	12.12	2.26	76.38	5.63	17.99
1300-2	85.76	11.90	2.34	79.09	5.99	14.92
1350-1	86.08	12.26	1.66	77.093	5.39	16.68
1350-2	86.12	11.82	1.45	78.92	5.42	15.61

Figures 4.11 (a) and (b) show SEM micrographs of typical particle surface of P1 and P2 foam, respectively. In the micrographs, the thermal etch lines are clearly visible on the particle surfaces. These lines results from the high temperature sintering due to the dislocation movement. Thermal etch lines are the characteristics of Ti samples sintered at high temperatures in a vacuum.

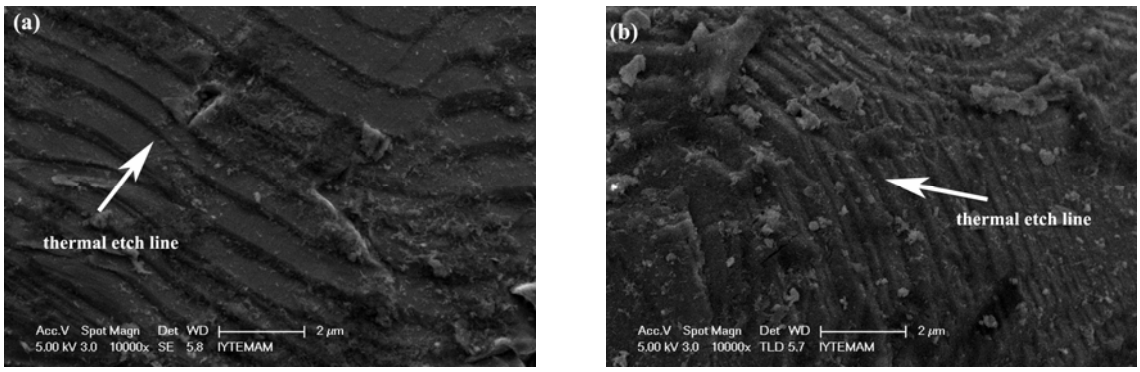

Figure 4.11. SEM micrograph of foam particle surfaces, (a) P1 and (b) P2 foam.

The representative optical micrograph of the resulting cell structure of the prepared foams is shown in Figure 4.12. The cellular structure of foams comprises two different pore size ranges. Relatively larger and irregular shaped cells (macro pores) with the sizes of 300-500 μm result from the spaces left by the irregular shaped space holder. While, smaller pores of 1-30 μm (micro pores) found in between the sintered Ti6Al4V particles in the cell walls/cell edges result from the incomplete sintering process.

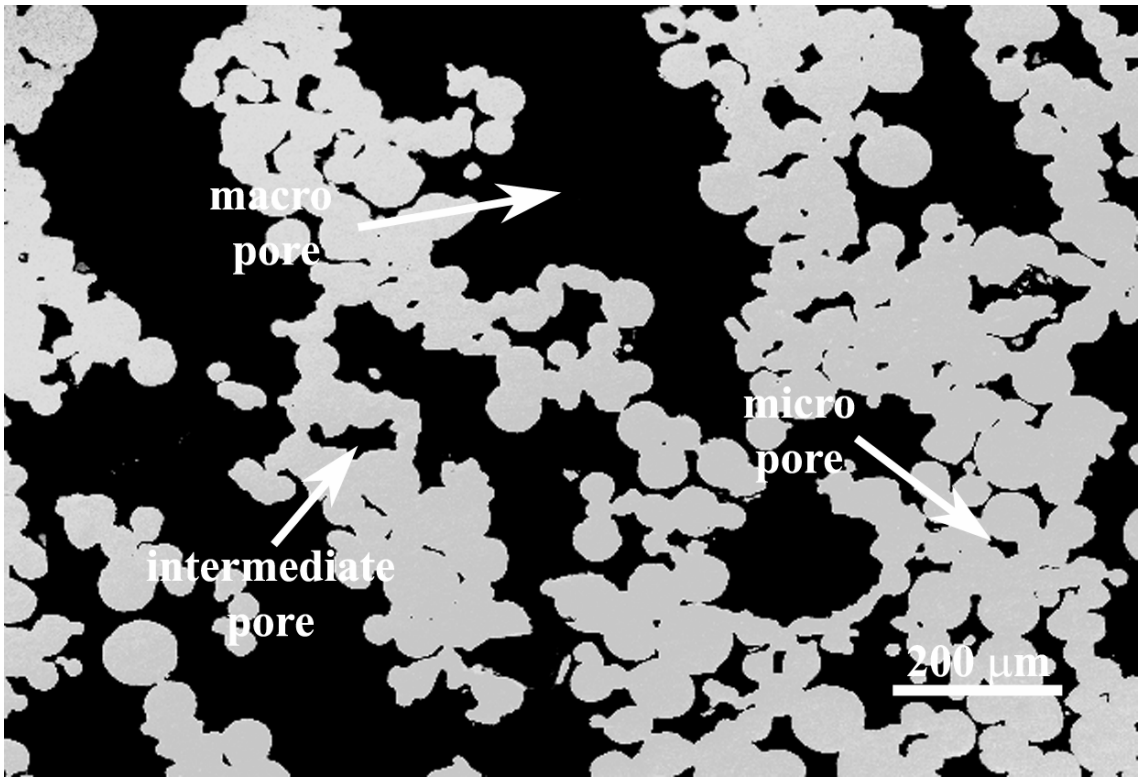

Figure 4.12. Typical cell structure of Ti6Al4V foam.

The percent mean porosities and densities of P1 and P2 foams sintered at 1200, 1250, 1300 and 1350°C are tabulated in Table 4.5. The porosity of the sintered foam specimens varies between 58.1 and 62.2%. The variations in the percent porosities between the foams sintered at different temperatures were likely due to the variations in the amount of space holder used in relatively small samples used for the porosity measurements. The final mean porosities of the foams were quite similar and corresponded nearly to the starting volume percentages of the space holder.

Table 4.5. Mean porosity and density of the foams sintered at different temperatures.

Powders	Temperature (°C)	Density (g/cm^3)	Mean porosity (%)	Std. Dev.
1	1200	1.761	60.1	0.732
	1250	1.799	59.3	0.716
	1300	1.749	60.4	0.603
	1350	1.697	61.6	0.652
2	1200	1.714	61.2	0.856
	1250	1.707	61.4	0.658
	1300	1.670	62.2	0.435
	1350	1.850	58.1	0.596

Typical compression stress-strain curves of P1 and P2 foams sintered at 1200, 1250, 1300 and 1350 ^{o}C are shown in Figures 4.13(a) and (b) as a function of sintering temperature, respectively. Essentially, P1 and P2 foams show generally similar trends in compression stress-strain behaviors: the initial elastic deformation is followed by an inelastic deformation until maximum stress. The elastic moduli and proportional limits of the foams are calculated in the initial region of the stress-strain curves as depicted in Figure 4.13(a). Following the initial part or proportional limit the stress values rises to a maximum stress (compressive strength) and the corresponding strain is taken as the failure strain as shown in Figure 4.13(a). The effect of increasing sintering temperature is to increase the elastic modulus, proportional limit, compressive strength and failure strain of the foams. The elastic moduli of P2 foams are found 1.5 and 2.5 GPa at sintering temperatures of 1200 and 1350 ^{o}C, respectively. While, the elastic moduli of P1 foams increase from 1 to 1.5 GPa when the sintering temperature increases from 1200 to 1350 ^{o}C. The modulus of natural bone was reported to vary between 1 to 20 GPa (Rho, et al. 1998); therefore, the elastic modulus range of 60% porous Ti6Al4V foams (1-2.5 GPa) are comparable with the elastic modulus of natural bone. The proportional limit of P1 foams increases from 20 MPa at 1200 ^{o}C to 40 MPa at 1350 ^{o}C, while the proportional limit of P2 foams increases from 40 MPa to 70 MPa in the same temperature range. Although sintering temperature increases the compressive strength of the foams prepared, the effect is more pronounced in P2 foams. This is partly due to higher packing ratio of P2, which increases number of contacts and bonding area between the particles.

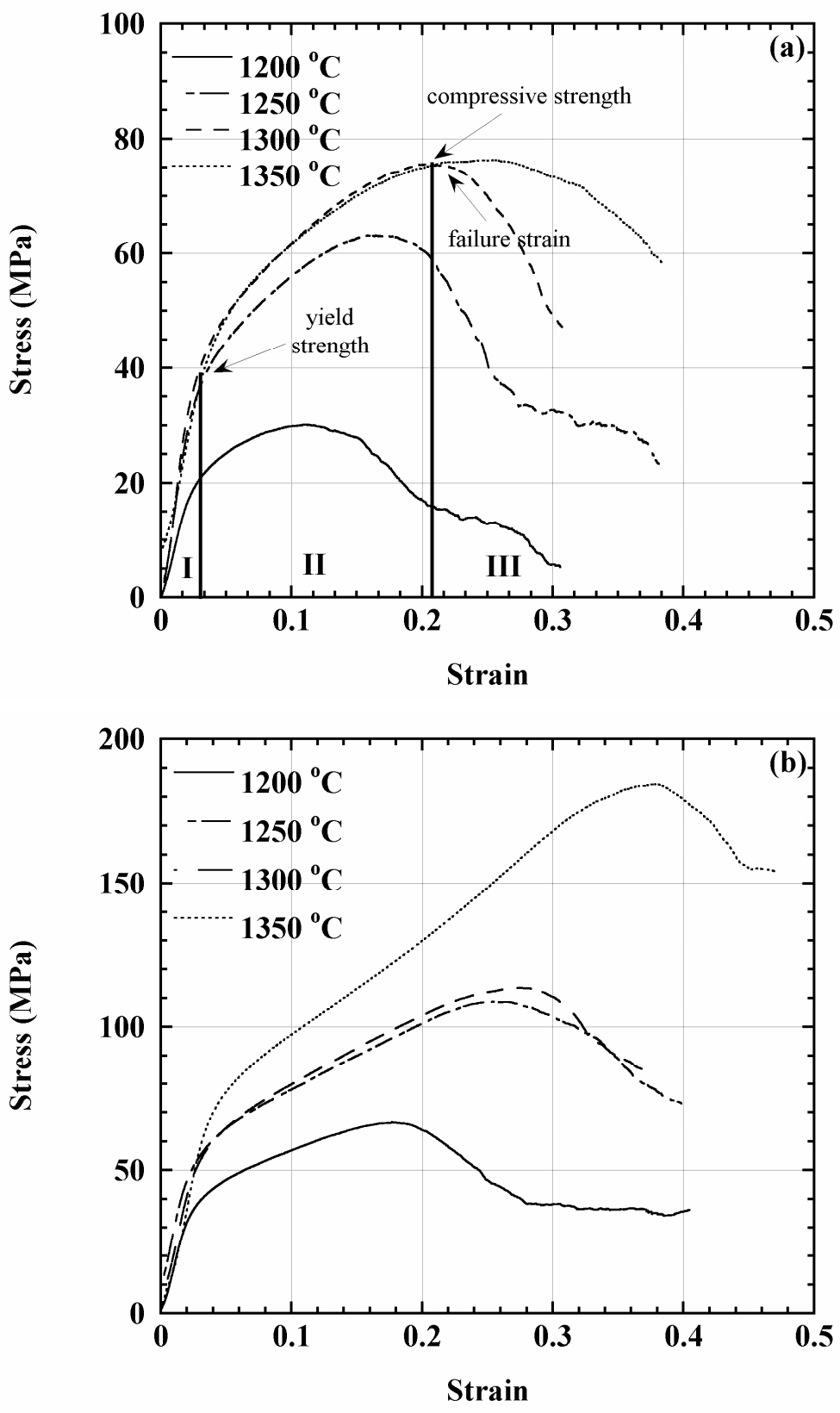

Figure 4.13. Compression stress-strain curves of 60% porous (a) P1 and (b) P2 foams sintered at different temperatures.

The mechanical response of studied foams may be compared with those of ductile open-cell metal foams and interconnected porous powder compacts. Open-cell foam metals are known to show characteristic compressive stress-strain curves consisted of three distinct deformation regions: linear elastic, collapse and densification. In the collapse region the deformation is highly localized and proceeds dominantly by cell edge buckling. This region is characterized by a long plateau stress. In densification region, the material stress increases sharply and approaches to the strength of the bulk metal. The compression deformation behavior of sintered porous Ti6Al4V powder (100-200 μm) compacts of 38% porosity with an average pore size of 63 μm was previously studied (Tasdemirci, et al. 2008). The compacts failed by the deformation zones diagonal to the sample axis at relatively low strains, 4-5%. Particle decohesion was found to lead to the compact failure along the diagonal axis. Therefore, the foams prepared at low sintering temperatures show compression behavior biased toward that of the sintered powder compacts. The failure strains of P1 and P2 foams sintered at the lowest temperature, 1200°C, range between 0.1 and 0.18. At increasing sintering temperatures the foams however show partly sintered compact behavior and partly foamed metal behavior. Figure 4.14 compares the compression stress-strain behavior of previously studied porous Ti6Al4V compacts (Tasdemirci, et al. 2008) and Ti foams (Guden, et al. 2004) with those of P1 and P2 foams sintered at 1350°C. Ti foams prepared with smaller particle sizes had relatively dense cell walls/edges with small micro pores (1-10 μm) in the cell walls; hence, showed compression behaviors similar to those of open cell foams. It is noted in Figure 4.14 that P2 foam sintered at 1350°C shows a proportional limit similar to that of 55% porous Ti foam, although the former contains relatively larger micro pores in the cell walls, showing the potentials of Ti6Al4V powder use in processing stronger foams.

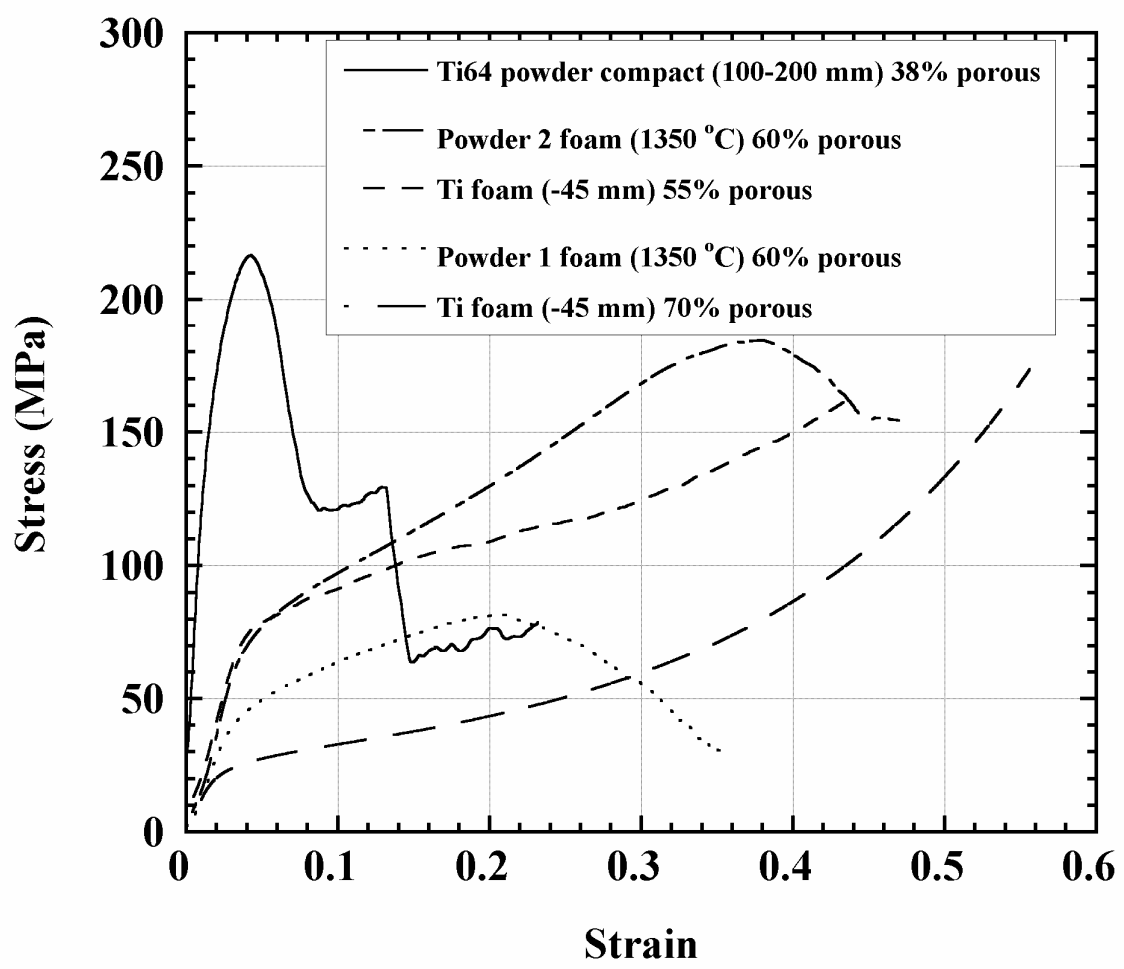

Figure 4.14. Comparison of compression stress-strain behaviors of Ti6Al4V foams with those of Ti6Al4V powder compacts and Ti foams

Present results have also identified several important microstructural effects on the mechanical properties of Ti6Al4V foams prepared by the space holder method. The powder size distribution affects the final mechanical properties of the foams by enhancing the sintering behavior of the particles in the cell walls. Furthermore, bimodal pore size distribution, macro (300-500 μm) and micro (1-30 μm) observed in this study is further well accord with previous studies on Ti foams prepared by the same method (Wen, et al. 2002b). Nevertheless, the micro pores and rough cell wall surfaces were shown to be preferable in osteoinductivity (Chang, et al. 1996). Finally, the interrelationships between porosity and pore size and the effects of compaction pressure should be further investigated in detail for the manufacturing of implant structures with optimum pore size and porosity.

CHAPTER 5

IN VITRO BIOACTIVITY OF UNTREATED AND SURFACE TREATED OPEN CELL Ti6Al4V FOAMS

5.1. Introduction

Porous Ti and Ti6Al4V alloy implants are known to provide better interaction with bone due to the higher degree of bone in-growth and body fluid transport through three-dimensional interconnected arrays of pores, leading to improved implant fixation (Pilliar 1987). The implants based on the porous materials also reduce the extent of well-known stress shielding, which causes the implant loosening (Long and Rack 1998). The current methods of porous Ti and Ti6Al4V alloy processing are virtually based on powder sintering methods, namely the sintering green powder compacts and the space holder method (Ryan, et al. 2006). In the sintering powder compacts method, relatively large powder sizes are generally used; however, the method inherently produces relatively small pore size and low porosity. The pore size and porosity typically range between 53 and 85 μm and 5 and 54%, respectively (Oh, et al. 2003), (Guden, et al. 2005, Guden, et al. 2008). In contrast, the space holder method comes up with relatively larger pore sizes, 200-500 μm, and higher porosities, up to 80% (Wen, et al. 2001). Both methods; however, allow the direct near net-shape fabrications of porous implant components having elastic modulus and strength values comparable with those of natural bone (Guden, et al. 2005, Oh, et al. 2003). Certain implant applications of Ti alloy foams have also been recently exploited including spinal cages used in spinal surgery for bone fixation (Dizlek, et al. 2009). Since these applications require relatively shorter bone fixation periods onto the porous surface, CaP coating of porous surfaces including Ti mesh (Tsukeoka, et al. 2005, Vehof, et al. 2000) and the sintered beads surface coatings (Nguyen, et al. 2004, Tache, et al. 2004) were previously investigated. Various surface treatments were further applied in conjunction with biomimetic CaP coating to fulfill the requirement for in vivo bone growth namely the formation of CaP (bone like apatite). Bone like apatite coating on Ti improves the surface osteoblast cell adhesion and differentiation (Gil, et al. 2002) and increases the

bone bonding strength by allowing an early bone opposition to the implant (Yan, et al. 1997a).

Zhang et. al. (Zhang, et al. 2005) investigated the biomimetic and electrochemical CaP deposition on a 40% porous and 100-300 μm pore size sintered Ti powder compact. The compact specimens were acid etched (AE) and then alkali treated (AT) without subsequent heat treatment before immersing into simulated body fluid (SBF). The results showed that after 6-day of SBF immersion, a continuous, homogeneous CaP coating layer formed in AT compact specimens, whereas no CaP coating layer formation was observed in AE specimens. It was emphasized that alkali treatment was a prerequisite for a uniform CaP coating layer deposition on the inner pores of the compacts; while, the electrochemical deposition resulted in less uniform coating layer, which was mainly attributed to the non uniform current distribution in the porous structure. Liang et. al. (Liang, et al. 2003) studied the effect of alkali treatment and subsequent heat treatment process on CaP deposition in a 40% porous and 250 μm pore size sintered Ti powder compact. The size of porous network structure (sodium titanate hydrogel) was shown to increase with increasing molar concentration of NaOH. In compact specimens with smaller pores of network structure, no apatite coating layer was detected after 28-day of SBF immersion. The lack of apatite formation on the compact particle surfaces with smaller pore sizes of network structure was attributed to low solute concentrations reaching inside the pores. Furthermore, the cell attachment and proliferation increased in a Ti6Al4V alloy, when the surface roughness increased from 0.25 to 0.87 μm (Deligianni, et al. 2001). A critical molar concentration of NaOH (10 M), after which a smooth surface layer formed and resulted in no apatite nucleation after 3-day of SBF immersion was also reported (Wei, et al. 2002). The effect of subsequent heat treatment was found to increase the adherence of sodium titanate layer to Ti substrate (Wei, et al. 2002) and induce a finer porous reticulate structure (Lee, et al. 2002).

A simple method for the predicting the bone bonding potential of the implant materials is based on immersing these materials into simulated body fluid (SBF). According to Kokubo et. al.(Kokubo 2008), an essential requirement for in vivo bone ingrowth on a synthetic material is the formation of a CaP layer on the material's surface, usually called bone like apatite. This bone like apatite seems to activate the signaling proteins and cells to start the cascade of events that result in bone formation.

The previous investigations outlined above were mainly concentrated on CaP deposition in sintered powder compacts in which the pore size and porosity levels were comparably low. The present study was therefore conducted in order to investigate the effect of widely applied surface treatments of Ti and its alloys including alkali and nitric acid surface treatment and acid etching on biomimetic CaP deposition in an open cell Ti6Al4V foam, potentially being used in hard tissue applications. Furthermore, the surface roughness of the foam flat surfaces, before and after deposition, was measured in nano meter scale to assess the effect of surface roughness on CaP deposition. The major requirements of CaP deposition of foamy biomedical structures may include (a) forming a uniform coating layer on the cell edges and interior surfaces of the cells or pores and (b) maintaining the open cell structure of the foam after coating.

5.2. Experimental

5.2.1. Sample Preparation

Small square cross-section plate-like specimens (10x10x3 mm^3) were used for in-vitro investigations. These samples were cut from the sintered Ti6Al4V foam plates (sintered at 1300 ^oC, 60% porous) (Figure 5.1(a)), using a low speed diamond saw. The specimens' square cross-sections (Figure 5.1(b)) were then ground sequentially using 120, 240, 320, 600, 800, 1200 and 2400 grit SiC papers. The surfaces of foam specimens are therefore composed of ground flat regions and the cells (pores). The foam specimens were then cleaned ultrasonically in acetone, then in ethyl alcohol and finally in deionized water for a duration of 15 min for each solution.

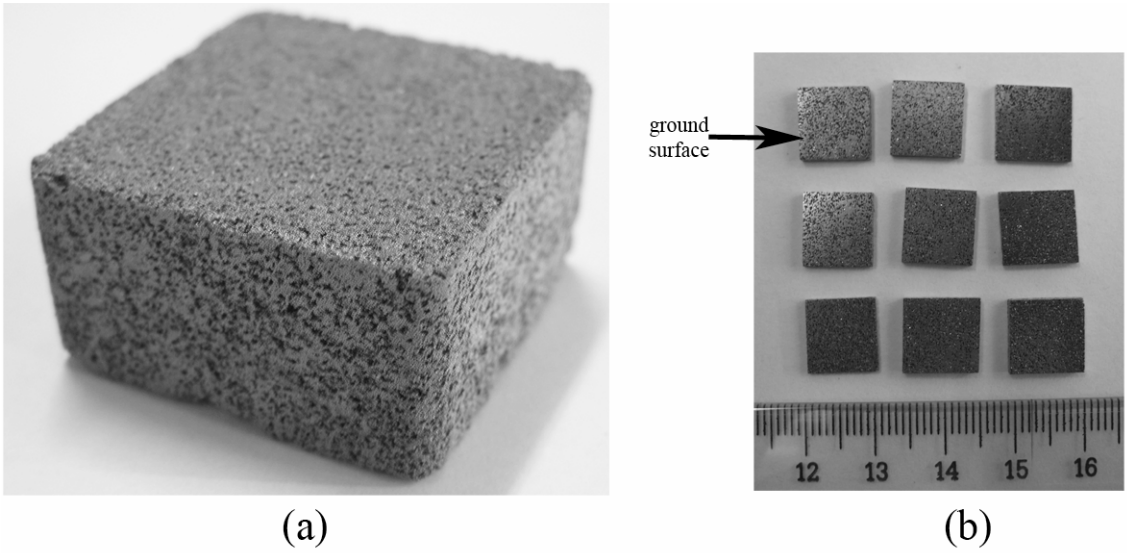

Figure 5.1. (a) The sintered foam plate and (b) test samples for in vitro investigations.

5.2.2. Surface Treatments

Before in-vitro tests, Ti6Al4V foam specimens were exposed to three different surface treatments. In acid etching, the foam specimens were immersed into an 1:1:1 volume ratio solution of H_2SO_4 (98%), HCl (36%) and H_2O at 60°C for 1 h. Nitric acid treatment was performed in a 1:1 volume ratio solution of HNO_3 (65%) and H_2O at 60°C for 5 h. In alkali treatment, the specimens were kept in 100 ml 10M NaOH aqueous solution at 60°C for 24 h. Following the treatments, the specimens were cleaned ultrasonically in deionized water for 15 min and then AE and nitric acid treated (NAT) specimens were dried in air, while AT specimens were dried in an oven at 40°C for 24 h.

5.2.3. Simulated Body Fluid

The SBF solution for in vitro tests was prepared according to the protocol (Bayraktar and Tas 1999, Jalota, et al. 2007a) by dissolving the following analytical reagents in 1 L of deionized water: NaCl, $NaHCO_3$, KCl, Na_2HPO_4, $MgCl_2.6H_2O$, $CaCl_2.2H_2O$, Na_2SO_4 and trishydoxmethylaminomethane. The pH of the solution was adjusted to 7.4 using 1M HCl acid solution. The SBF solution was kept in +4°C in a refrigerator.

5.2.4. In Vitro Bioactivity Test

The surface treated and untreated foam specimens were placed into a polypropylene tube containing 6 ml SBF solution. The tubes were kept at 37°C for 14 days in an incubator. SBF solution of the tubes was refreshed every 24 h. The test specimens were removed from the SBF solution after 1, 3, 5, 7, and 14 days. The tested specimens were washed with deionized water to remove the precipitates and dried in an oven at 40°C for 24 h.

5.3. Characterization Techniques

X-ray measurements were performed using a θ/2θ diffractometer with Cu Kα x-ray (λ = 1.5404 for the 8.05 keV x-ray) from a high intensity x-ray tube (Philips Xpert). The voltage and current used were 45.0 kV and 40 mA, respectively. The x-ray intensity (counts/s) versus 2θ (degrees) data were collected in a computer. The 2θ values ranged between 30 and 100^{o}, with a scan time 1 h and 56 min. The step widths and times were 0.05° and 4 s, respectively. The data were analyzed using Expert Manager Software. The effective depth probed by Cu Kα x-ray (sinθ/2μ where μ is the effective linear absorption coefficient, and approximately equals to 501.25 cm^{-1} for Ti6Al4V alloy used in this study) allowed the characterization of the surface treated and bioactivity tested specimens.

Two different geometries: (1) Bragg Brentano (θ/2θ) and (2) grazing incidence x-ray diffraction geometry were used in the XRD measurements. Bragg Brentano (θ/2θ) method is generally used for powder diffraction, and defined as a symmetric method since the system always detects the scattered x-rays at a diffraction angle, which is equal to the angle of x-rays incident to the surface. Both the sample and the detector move step by step during the measurement. While the samples rotate at an angle of θ, the detector moves two times of this angle (2θ). This method, therefore, detects the diffracted x-rays from the grains oriented parallel to the surfaces. One disadvantage of this geometry is that the effective depth probed by the incident beam always changes during the scan due to the change in the angle of the incident beam. The typical scan range used for most metals ranges from 30 to 100^{o}. Due to the change in the incident

beam angle, the effective depth probed by the beam at 100^o is approximately 3 times deeper than the effective depth probed by the beam at 30^o (the effective depths probed by the beam at 30^o and 100^o are 0.49 μm and 1.4 μm, respectively). This may cause misinterpretation of the results in testing the layered material structures. In grazing incidence x-ray diffraction, the incident x-ray beam is fixed at a predetermined value on the sample and detector scans 2θ degrees. This method provides diffraction only from the planes not parallel to the surface. Normally the method uses very small angles incident to the surface, providing information from very thin layers and is ideally suitable for the examination of typical near surface crystal structures and phases. The main power of the method is to provide the information layer by layer just changing the angle of x-ray beam incident to the sample surface. The effective depth probed by the fixed x-ray beam incident on the sample is mainly dependent on $\sin\omega/\mu$, where ω is the fixed angle and μ is the mass absorption coefficient. The incident angle (ω) used to investigate the surface treated and bioactivity tested foam specimens was 0.5°, while the corresponding effective depth probed by this incident x-ray beam was 174 nm.

A Philips XL30-SFEG SEM with an EDX analyzer was used for microscopic investigations. SEM was used with three detectors, scanning electron and back scattered electron detectors.

The surface morphology and roughness (*Ra*) of foam specimens before and after in-vitro tests were determined using a Nanoscope-IV Atomic Force Microscope (AFM) and tapping tips (Otespa, Veecco) with the spring constant of 12–200 N m^{-1}. At least three AFM surface scans were performed on the arbitrarily chosen areas of foam specimen's flat ground surfaces. The surface roughness values were calculated by averaging the measured surface roughness values of three scans.

A Perkin Elmer Attenuated Total Reflectance Fourier Transform Infrared (ATR-FTIR) Spectrometer was used to analyze the bond structure of the coating layer. The band structure was scanned between 525 and 4000 cm^{-1} (ZnSe crystal).

5.4. Results and Discussion

The GIXRD spectra (incident angle of $\omega=0.5^o$) of untreated, AT, NAT and AE Ti6Al4V P1 foam specimens are shown together in Figure 5.2. The β phase peak seen in the GIXRD spectrum of sintered foam specimen confirms the microscopically observed

transformation of the powder microstructure (Chapter 4), after sintering at 1300 ^{o}C, from fully needle-like α-phase into Widmanstätten microstructure which comprises the colonies of β lathes (bcc and rich in V) and α platelets (hcp and rich in Al). The peaks marked as ‘’*’’ in the spectrum of AT foam specimen in Figures 5.2 and 3 indicate the formation of a thin $Na_2Ti_5O_{11}$ layer on the foam specimen flat surfaces and also on the surfaces particles interior of the cells. The thickness of this layer was measured 500 nm from the SEM pictures of the cross-section of AT foam sample particles (shown later in this section). Acid etching is expected to dissolve/remove the natural oxide layer on Ti6Al4V particle surface, presumably being thickened during the compact sintering at high temperature. Furthermore, the β phase peaks are not seen and the intensity of the diffraction peaks of α phase increases in the GIXRD spectra of AE foam specimen as shown in Figures 5.2 and 3.

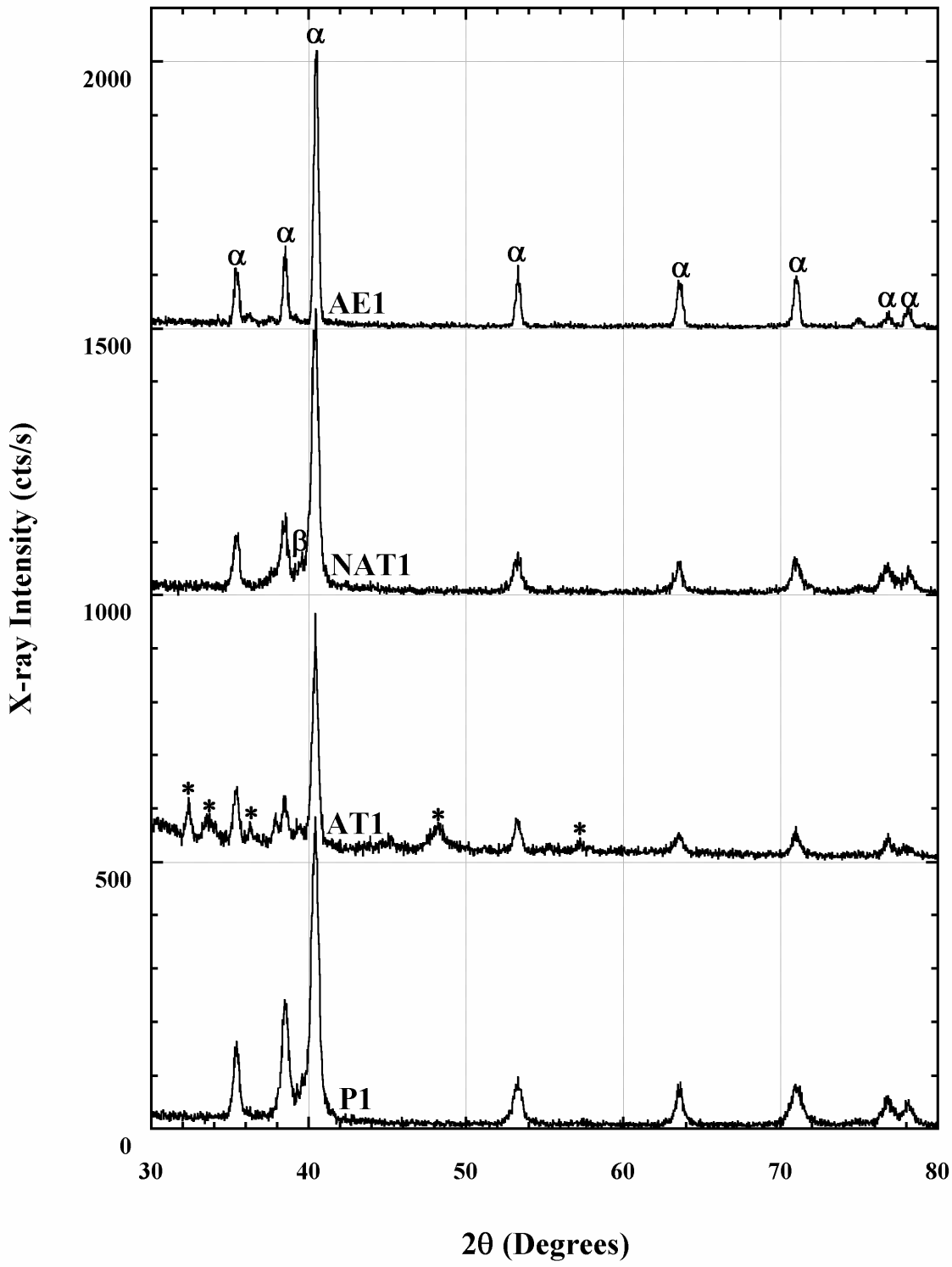

Figure 5.2. GIXRD spectrum of untreated, AT, NAT and AE P1 foam before in vitro bioactivity test.

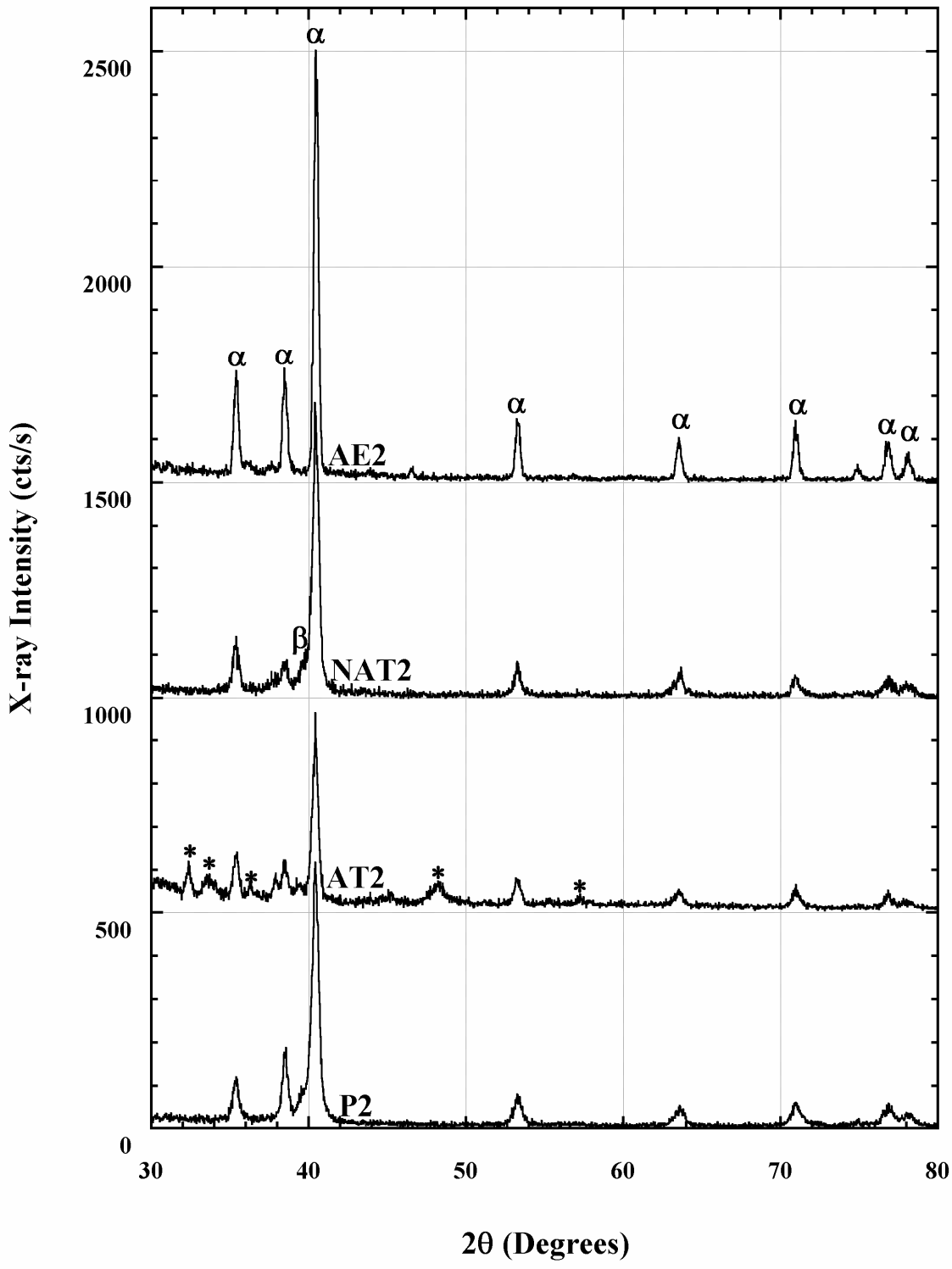

Figure 5.3. GIXRD spectrum of untreated, AT, NAT and AE P2 foam before in vitro bioactivity test.

Figures 5.4(a-f) show the SEM micrographs of untreated foam flat and particle surfaces at different magnifications. Untreated P1 and P2 foam specimens' flat surfaces before SBF immersion, as is expected, are relatively smooth and shows only few grinding lines (Figures 5.4(a), (b) (e) and (f)). Figures 5.5(a-f) further show the SEM micrographs of AT foam flat and particle surfaces at different magnifications before SBF immersion. Alkali treatment results in a relatively rough surface (Figures 5.5(e) and (f)). The surface is mainly composed of a porous $Na_2Ti_5O_{11}$ layer and on this porous layer the cracks are clearly seen in Figures 5.5 (e) and (f). The crack formation may be attributed partly to the difference in the thermal expansion coefficient between Ti6Al4V alloy and the surface layer phase ($Na_2Ti_5O_{11}$) or water loss during drying step. Figures 5.6(e-f) show the SEM micrographs of NAT foam specimen flat and particle surfaces at different magnifications before the SBF immersion. It is noted in Figures 5.6(e) and (f), on the contrary to untreated and AT foam samples, nitric acid treatment induces a relatively smooth surface layer, although few large shallow pits and grinding lines are detected on the surface (Figures 5.6(e) and (f)). Figures 5.7 (e-f) shows the SEM micrographs of AE foam specimen flat and particle surfaces at different magnifications before SBF immersion. The deeper sections seen as lines in Figures 5.7(c-f) are the β phase. Acid etching is found to result in preferential etching of β lathes of Widmanstätten microstructure, proving a higher rate of β phase dissolution in acid etching. The acid etching marks seen in Figures 5.7(c-f) are furthermore noted to be deeper than x-ray penetration depth (~174 nm).

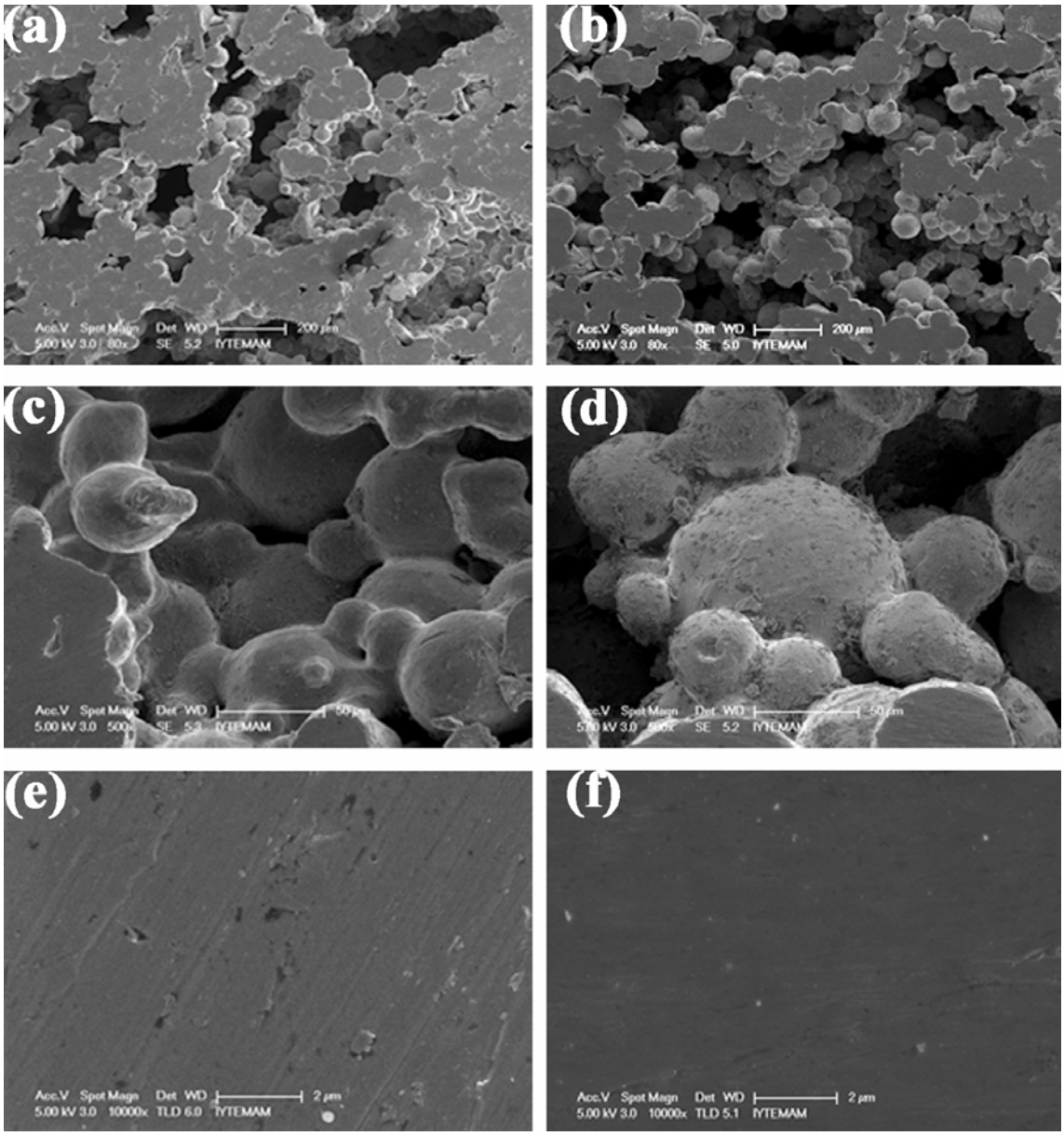

Figure 5.4. SEM micrographs of untreated foam specimen flat surface, (a) P1 foam, (b) P2 foam, (c) interior of the P1 foam cells, (d) interior of P2 foam cells, (e) high magnification of flat surface of P1 foam and (f) high magnification of flat surface of P2 foam before the SBF immersion.

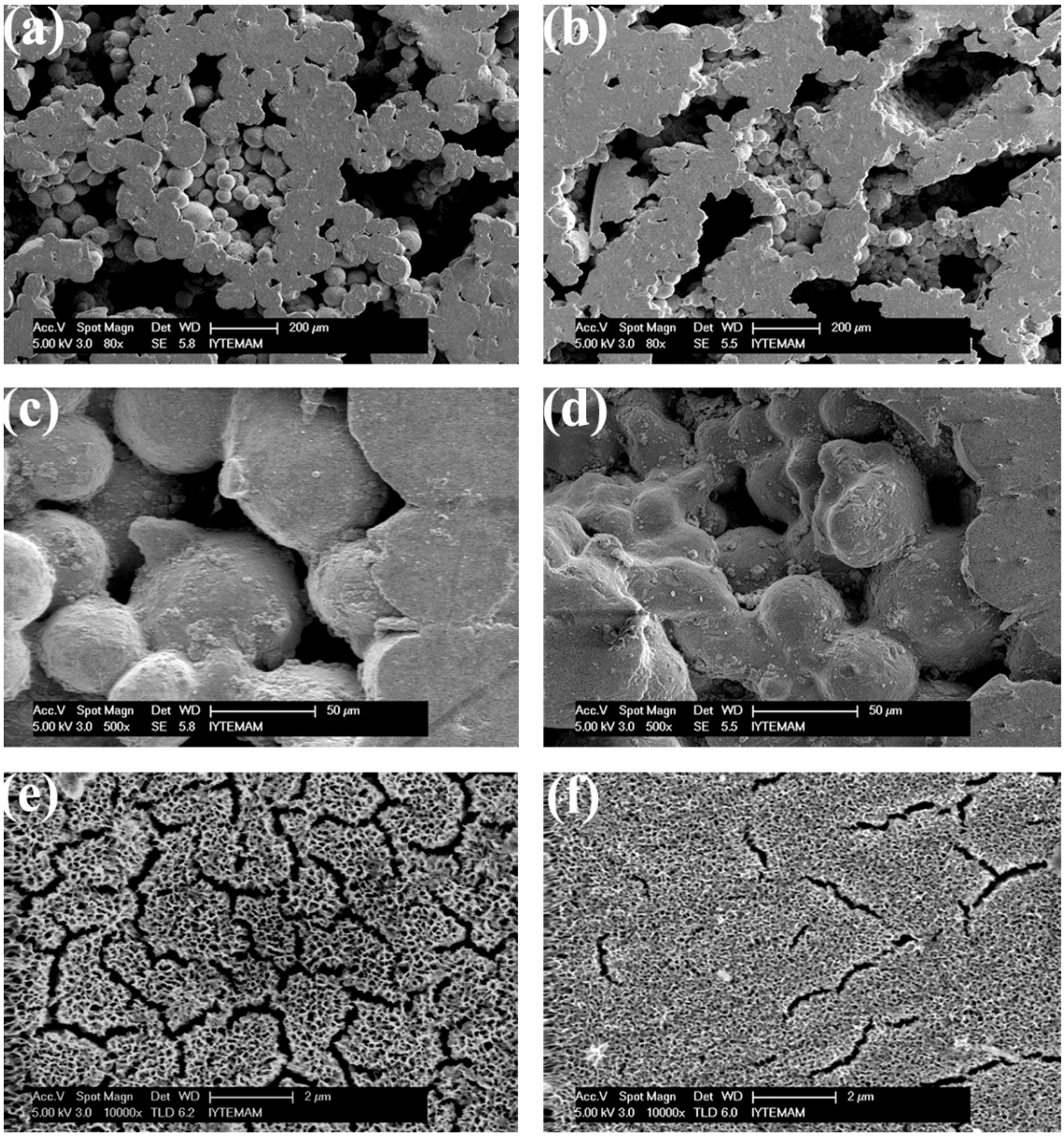

Figure 5.5. SEM micrographs of AT foam specimen flat surface, (a) P1 foam, (b) P2 foam, (c) interior of the P1 foam cells, (d) interior of P2 foam cells, (e) high magnification of flat surface of P1 foam and (f) high magnification of flat surface of P2 foam before the SBF immersion.

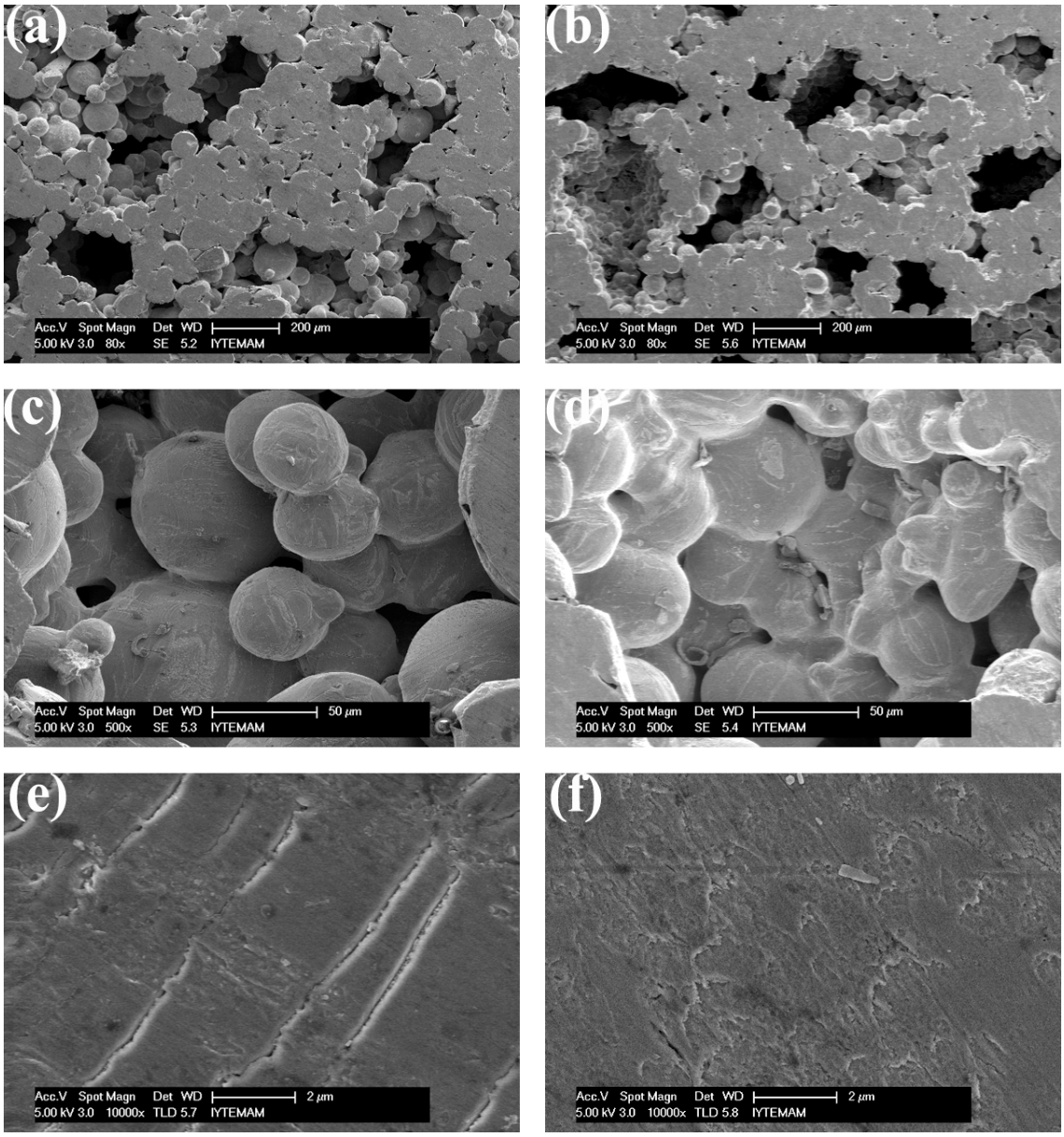

Figure 5.6. SEM micrographs of NAT foam specimen flat surface, (a) P1 foam, (b) P2 foam, (c) interior of the P1 foam cells, (d) interior of P2 foam cells, (e) high magnification of flat surface of P1 foam and (f) high magnification of flat surface of P2 foam before the SBF immersion.

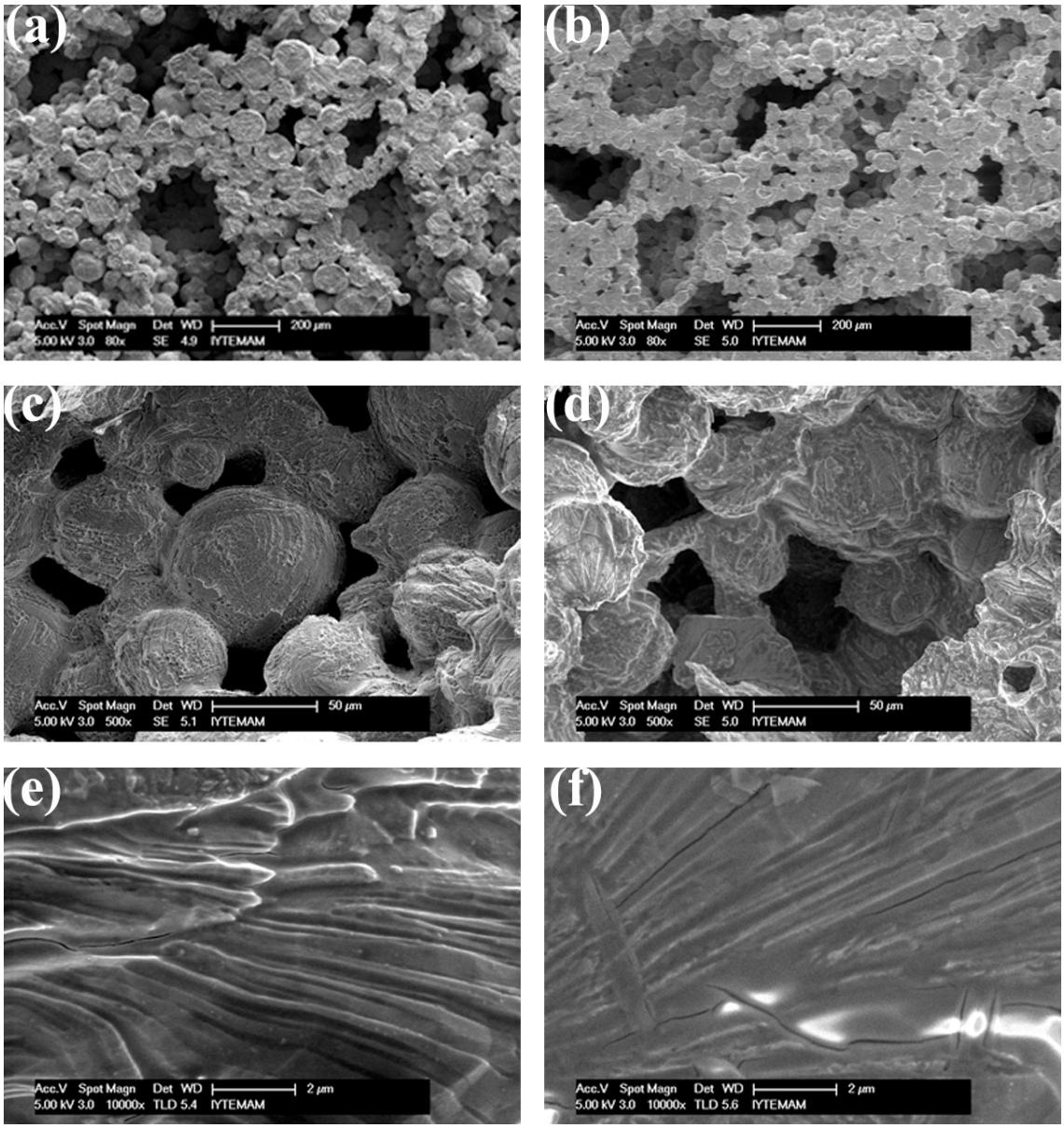

Figure 5.7. SEM micrographs of AE foam specimen flat surface, (a) P1 foam, (b)P2 foam, (c) interior of the P1 foam cells, (d) interior of P2 foam cells, (e) high magnification of flat surface of P1 foam and (f) high magnification of flat surface of P2 foam before the SBF immersion.

The AFM measured Ra and Rq (root mean square) values before SBF immersion are further tabulated in Table 5.1 together with the surface area difference (SAD) values, respectively. The Ra and Rq parameters are measured with an average deviation from a reference line or plane. Since the surface roughness measurements were conducted in a relatively small area, the grinding scratches naturally inducing a macro scale roughness on the surface are avoided in the surface roughness measurements. However, the surface roughness of AE specimens could not be measured in AFM, since the macro scale roughness in these specimens in certain locations was higher than 5 μm, which was a limiting roughness for AFM measurement.

The particle flat section surface AFM micrographs (1.5x1.5 μm^2) of untreated P1 and P2, AT P1 and P2 and NAT P1 and P2 foam specimens are shown sequentially in Figures 5.8(a) and (b), Figures 5.9(a) and (b) and Figures 5.10(a) and (b), respectively. As tabulated in Table 5.1, AT foam specimen shows the highest average surface roughness value (12.642 nm for P1 and 18.065 nm for P2 foam) before SBF immersion. Although, the average surface roughness values of NAT specimens (8.778 nm for P1 and 7.507 for P2 foam) are very much similar to those of untreated foam specimens (8.823 nm for P1 and 7.244 for P2 foam), NAT tended to remove the grinding lines and increased surface area difference greatly by introducing nano scale undulations on the surface (Figures 5.10(a) and (b)). The surface roughness difference between P1 and P2 foam is most probably related to small differences in the particle size and microstructure of the starting powders. AT foam specimens show higher surface roughness as compared with untreated and NAT specimens, as seen in Figures 5.8, 5.9 and 5.10. It is further noted that the P2 foam specimen surface is finer than that of the P1 foam specimen surface.

Table 5.1. Surface roughness values of foam flat surfaces before SBF immersion.

	Ra (nm)	Rq (nm)	SAD (%)
As received P1	8.823	10.715	1.279
NAT P1	8.778	12.012	3.832
AT P1	12.642	15.769	5.477
As Received P2	7.244	10.517	1.284
NAT P2	7.507	9.153	7.815
AT P2	18.065	23.272	9.378

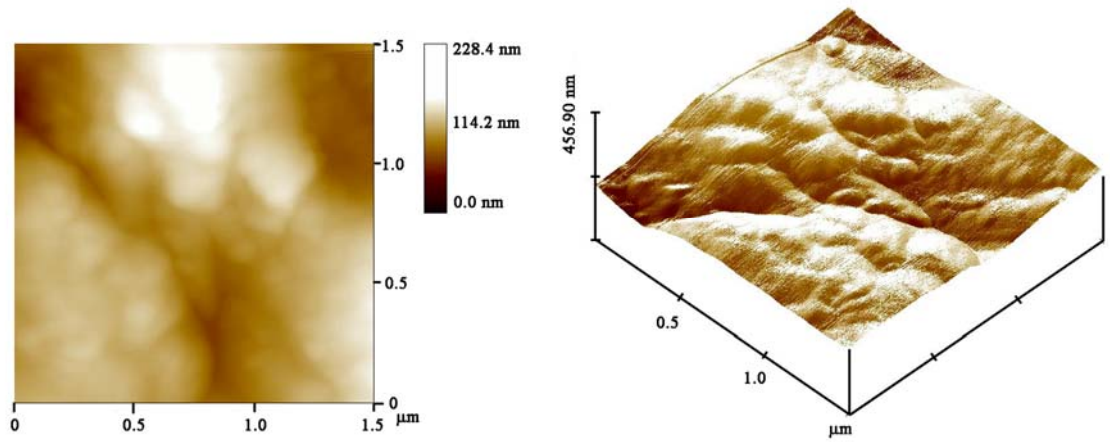

(a)

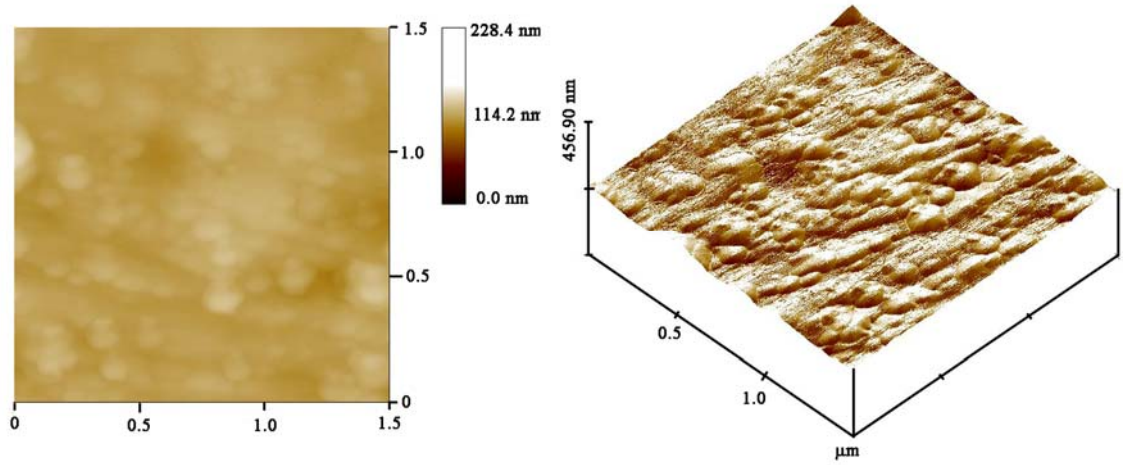

(b)

Figure 5.8. 2D and 3D AFM micrographs of surface topologies of untreated foam specimen, (a) P1 and (b) P2 foam.

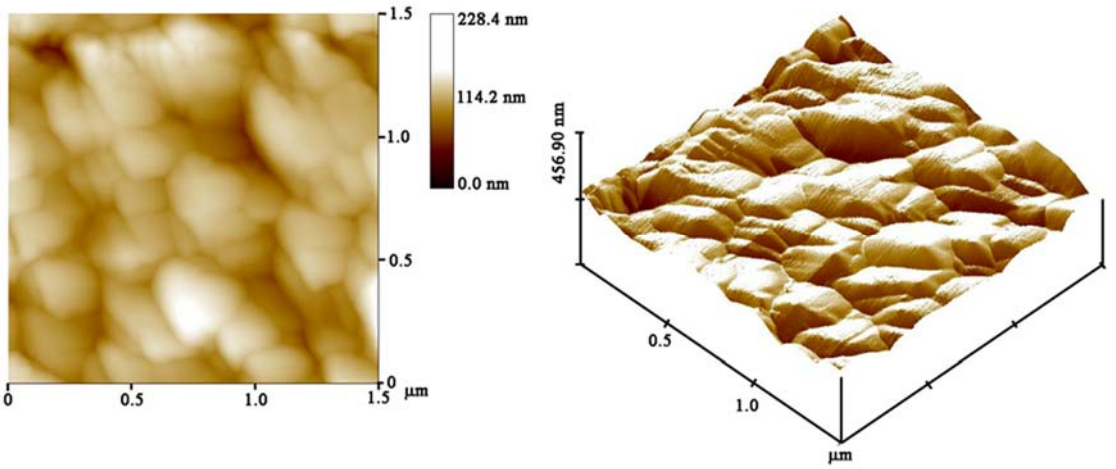

(a)

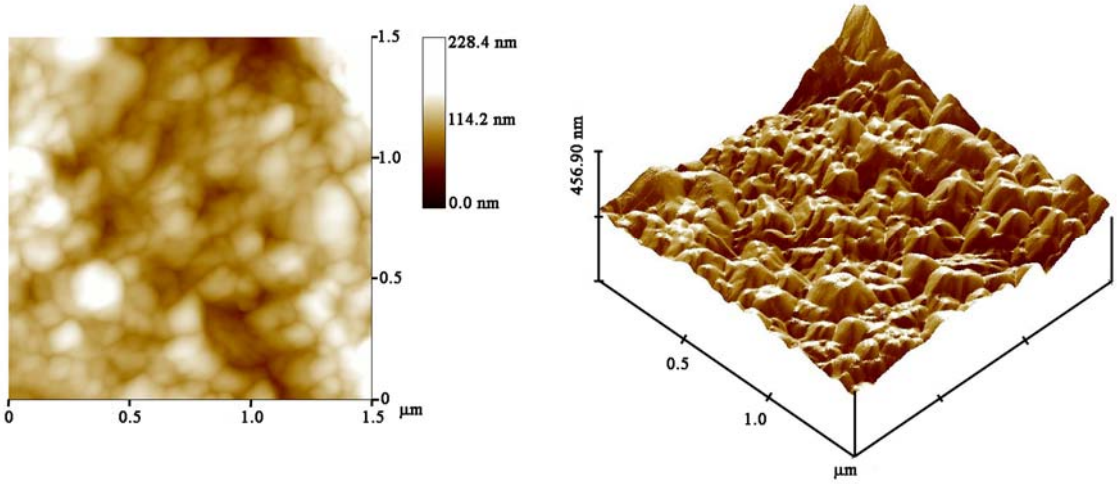

(b)

Figure 5.9. 2D and 3D AFM micrographs of surface topologies of AT foam specimen, (a) P1 and (b) P2 foam.

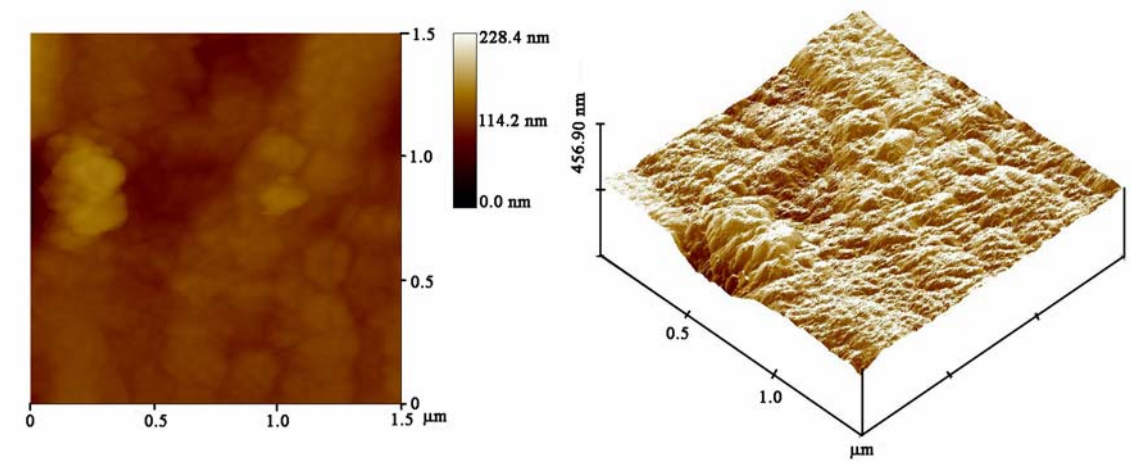

(a)

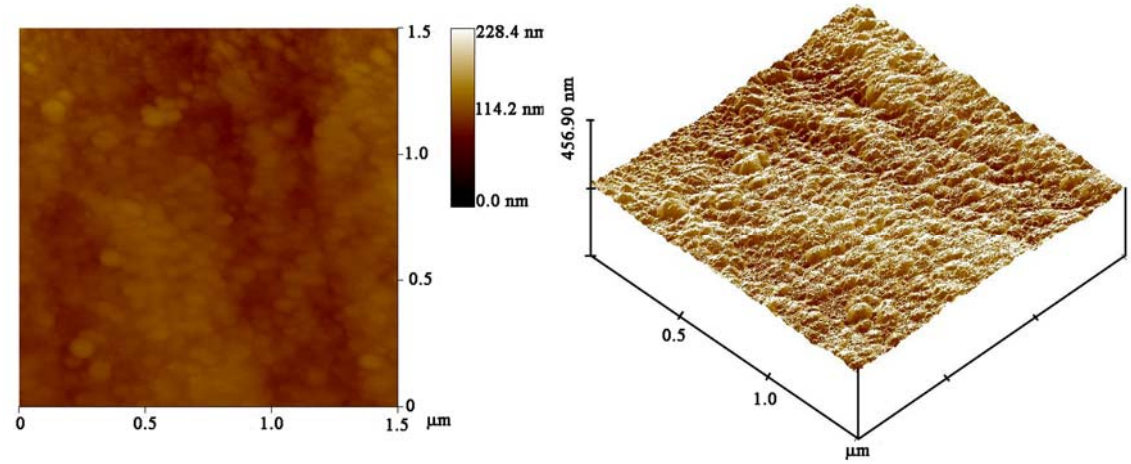

(b)

Figure 5.10. 2D and 3D AFM micrographs of surface topologies of NAT foam specimen, (a) P1 and (b) P2 foam.

Figures 5.11 (a-i) show the SEM micrographs of untreated P1 foam specimens' flat surfaces and interior of the cells after 5, 7 and 14-day of SBF immersion. Only small CaP precipitates are seen after 5-day of SBF immersion (Figures 5.11(a-c)). While, after 14-day of SBF immersion, CaP precipitates are seen to form a continuous coating layer on the flat surfaces and particle surfaces of P1 foam sample as seen in Figures 5.11(g-i). The apatite coating layer on untreated P1 foam specimen is considered to be nonuniform as relatively large size CaP globules are seen on the cut particle edges (Figure 5.11(g)). In some regions on the surface, the coating layer was further observed to be detached (Figure 5.11(h)), showing a weak mechanical griping between the foam surfaces and coating layer. Figures 5.12 (a-i) show the SEM

micrographs of untreated P2 foam specimens flat surfaces and interior of the cells after 5, 7 and 14-day of SBF immersion. As with untreated P1 foam specimen, a continuous CaP coating layer is seen only after 14-day of SBF immersion (Figures 5.12(g-i)).

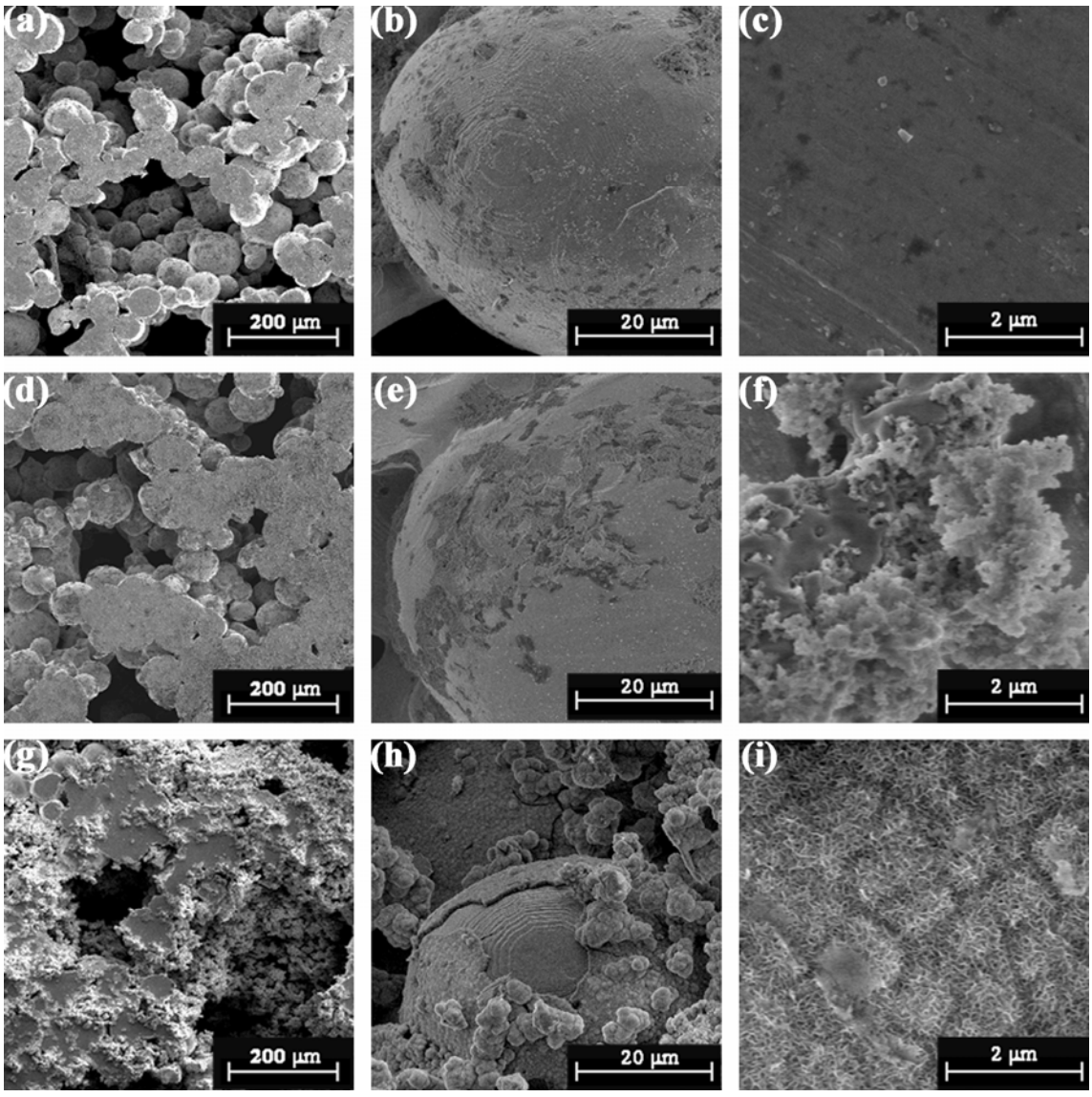

Figure 5.11. SEM micrographs of untreated P1 foam specimens (a) flat surface after 5-day of SBF immersion, (b) interior of the cell after 5-day of SBF immersion, (c) high magnification after 5-day of SBF immersion, (d) flat surface after 7-day of SBF immersion, (e) interior of the cell after 7-day of SBF immersion, (f) high magnification after 7-day of SBF immersion, (g) flat surface after 14-day of SBF immersion, (h) interior of the cell after 14-day of SBF immersion and (i) high magnification after 14-day of SBF immersion.

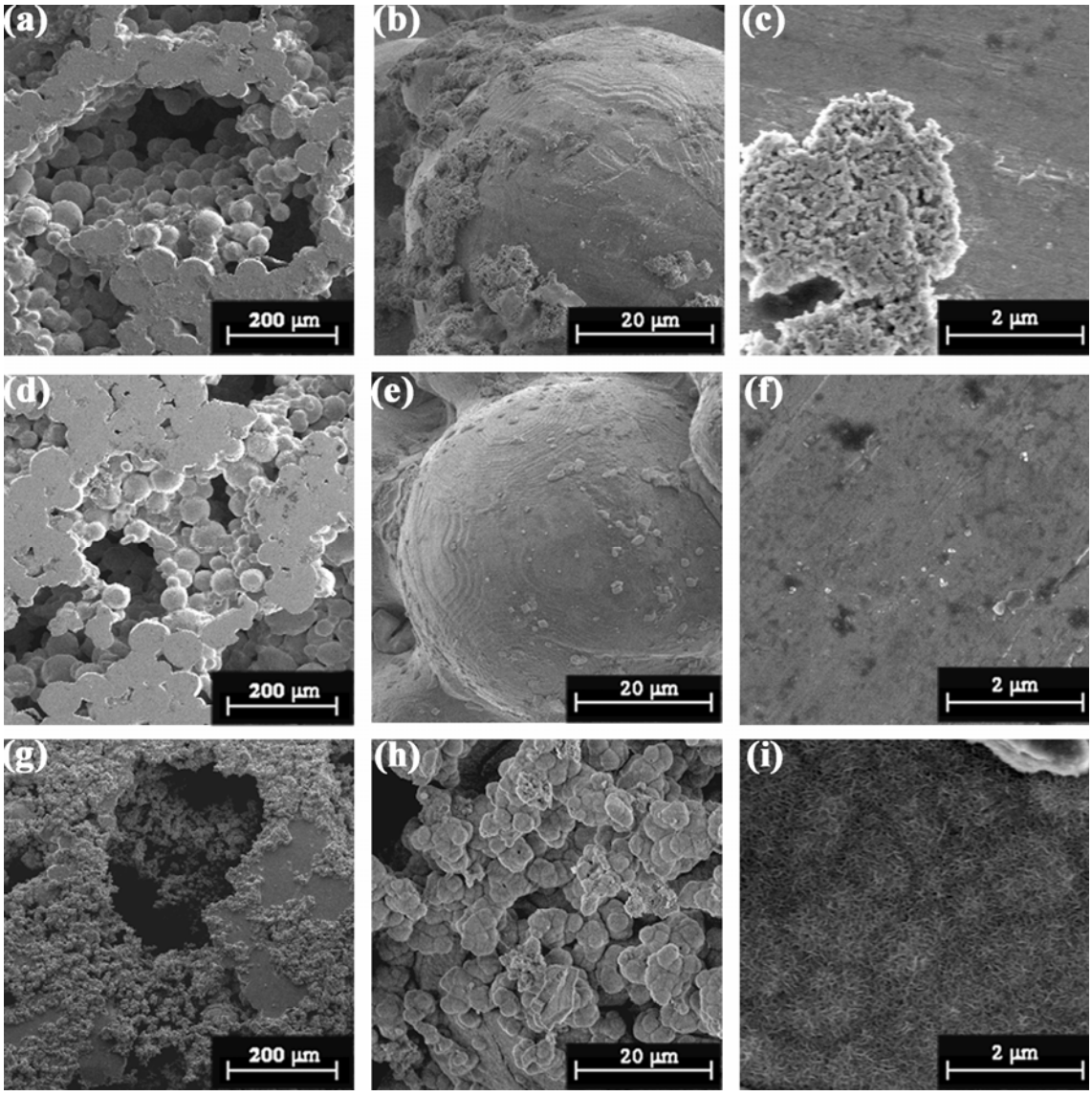

Figure 5.12. SEM micrographs of untreated P2 foam specimens (a) flat surface after 5-day of SBF immersion, (b) interior of the cell after 5-day of SBF immersion, (c) high magnification after 5-day of SBF immersion, (d) flat surface after 7-day of SBF immersion, (e) interior of the cell after 7-day of SBF immersion, (f) high magnification after 7-day of SBF immersion, (g) flat surface after 14-day of SBF immersion, (h) interior of the cell after 14-day of SBF immersion and (i) high magnification after 14-day of SBF immersion.

Figure 5.13 shows the XRD spectra of as received P1 and untreated and 14-day of SBF immersed P1 foam and Figure 14 shows the XRD spectra of as received P2 and untreated and 14-day of SBF immersed P2 foam. CaP layer peaks are marked as "*" in the XRD spectra in Figures 5.13 and 5.14. The XRD spectra shown in these figures indicate the formation of a relatively thin CaP layer on the surface of the substrate. Although the substrate peak intensity of P2 foam specimen is higher than that of P1 foam specimen, the XRD peak intensities of CaP layers of P1 and P2 foam specimens are nearly the same showing the similar layer thicknesses.

Figures 5.15 (a-i) show the SEM micrographs of AT P1 foam flat surfaces and interior of cells after 5, 7 and 14-day of SBF immersion. After 5-day of SBF immersion, the globular CaP forms on the flat surfaces of the foam specimen, while higher degree of CaP formation are seen interior of the cells (Figures 5.15(a) and (b)). After 7-day of SBF immersion, the interior of the cells is fully coated with CaP precipitates (Figures 5.15 (d) and (e)), while the flat surfaces of the foam specimen are not coated with a continues CaP layer. The increasing the SBF immersion time to 14-day, however, results in the formation of a dense CaP layer both on the foam flat surfaces and interior of the cells (Figures 5.15(g) and (h)). The cracks are also seen in CaP layer on the particles interior of the cells (Figure 5.15(h)). Figures 5.16 (a-i) show the SEM micrographs of AT P2 foam flat surfaces and interior of cells after 5, 7 and 14-day of SBF immersion. The sizes of globular CaP are noted in these figures bigger than those of P1 foam specimen. As opposite to P1 foam specimen, after 7-day of SBF immersion, P2 foam flat surfaces are fully coated with a CaP layer (Figure 5.16(d)). This proves a higher rate of CaP deposition in P2 foam specimens as compared with P1 foam specimens.

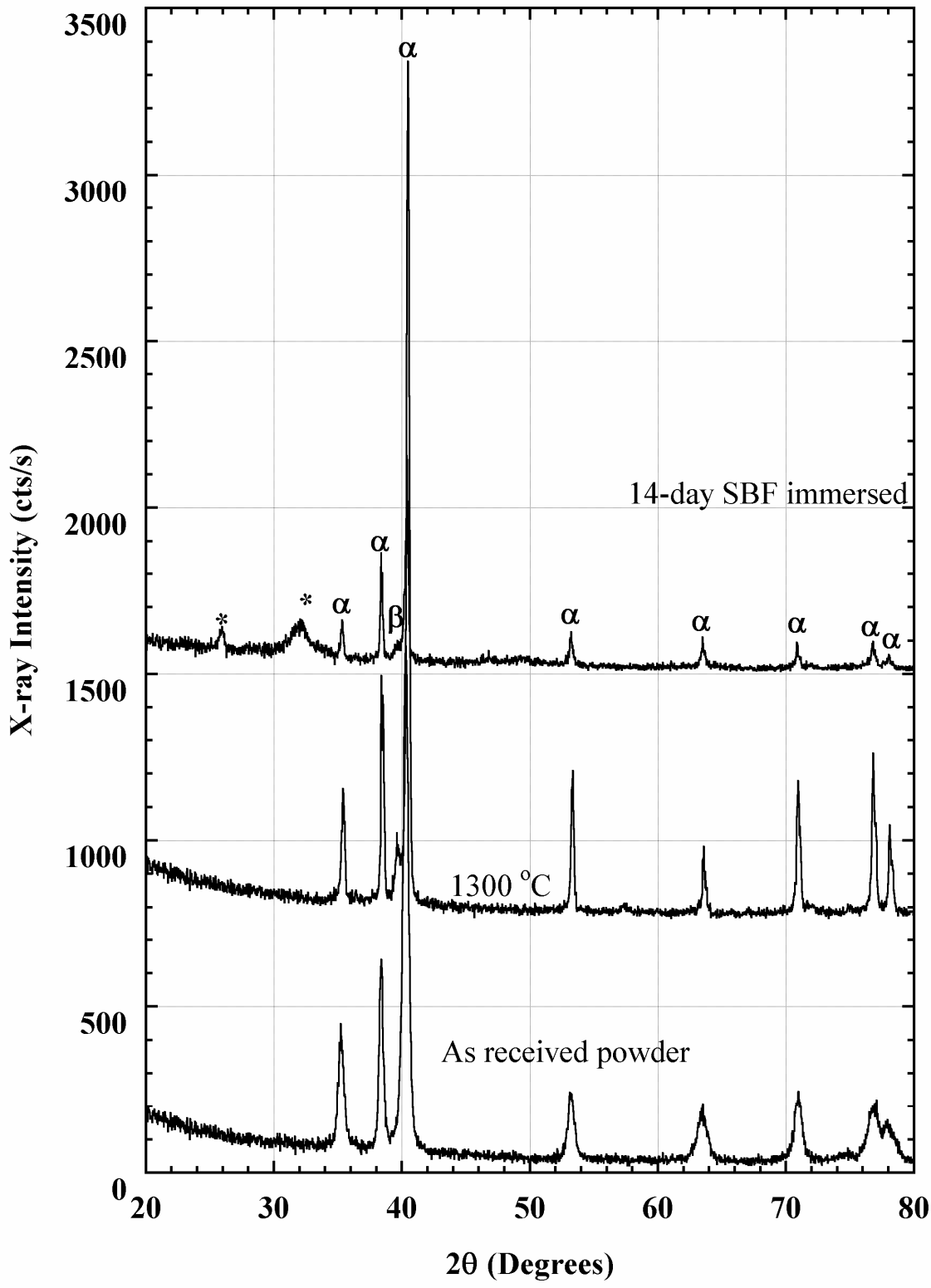

Figure 5.13. GIXRD spectra of as received P1 and untreated and 14-day SBF immersed P1 foam specimen.

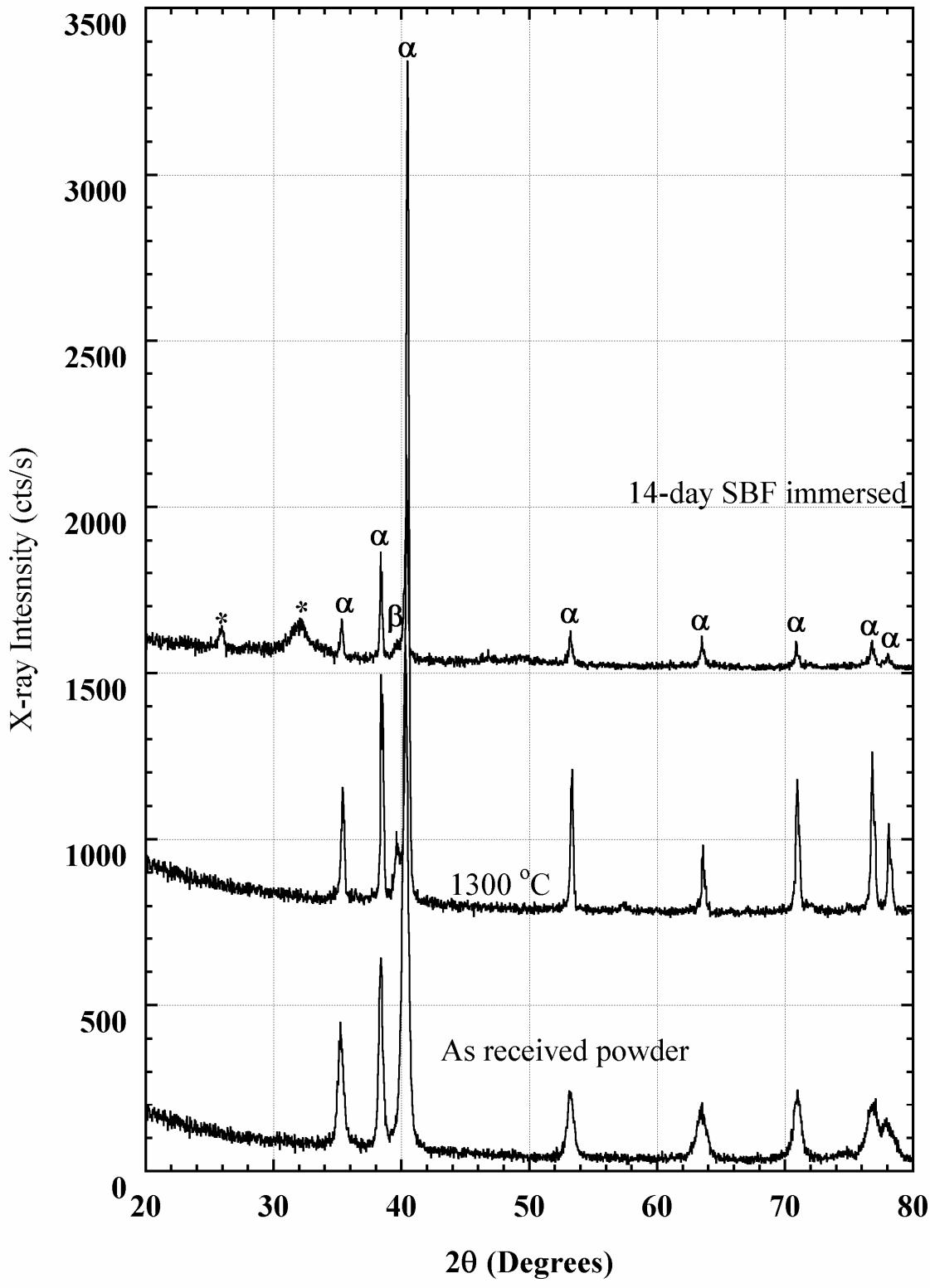

Figure 5.14. GIXRD spectra of as received P2 and untreated and 14-day SBF immersed P2 foam specimen.

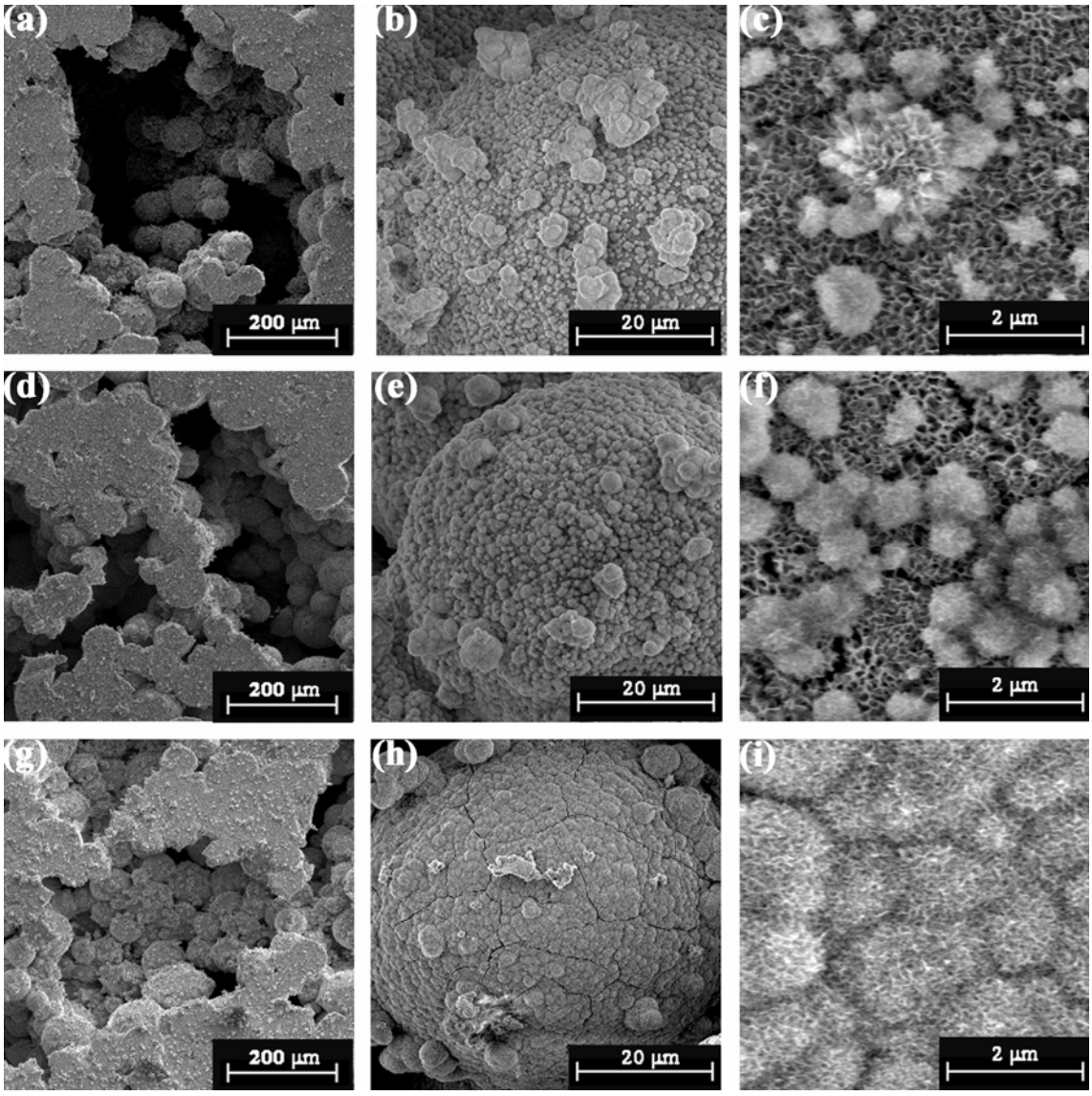

Figure 5.15. SEM micrographs of AT P1 foam specimens (a) flat surface after 5-day of SBF immersion, (b) interior of the cell after 5-day of SBF immersion, (c) high magnification after 5-day of SBF immersion, (d) flat surface after 7-day of SBF immersion, (e) interior of the cell after 7-day of SBF immersion, (f) high magnification after 7-day of SBF immersion, (g) flat surface after 14-day of SBF immersion, (h) interior of the cell after 14-day of SBF immersion and (i) high magnification after 14-day of SBF immersion.

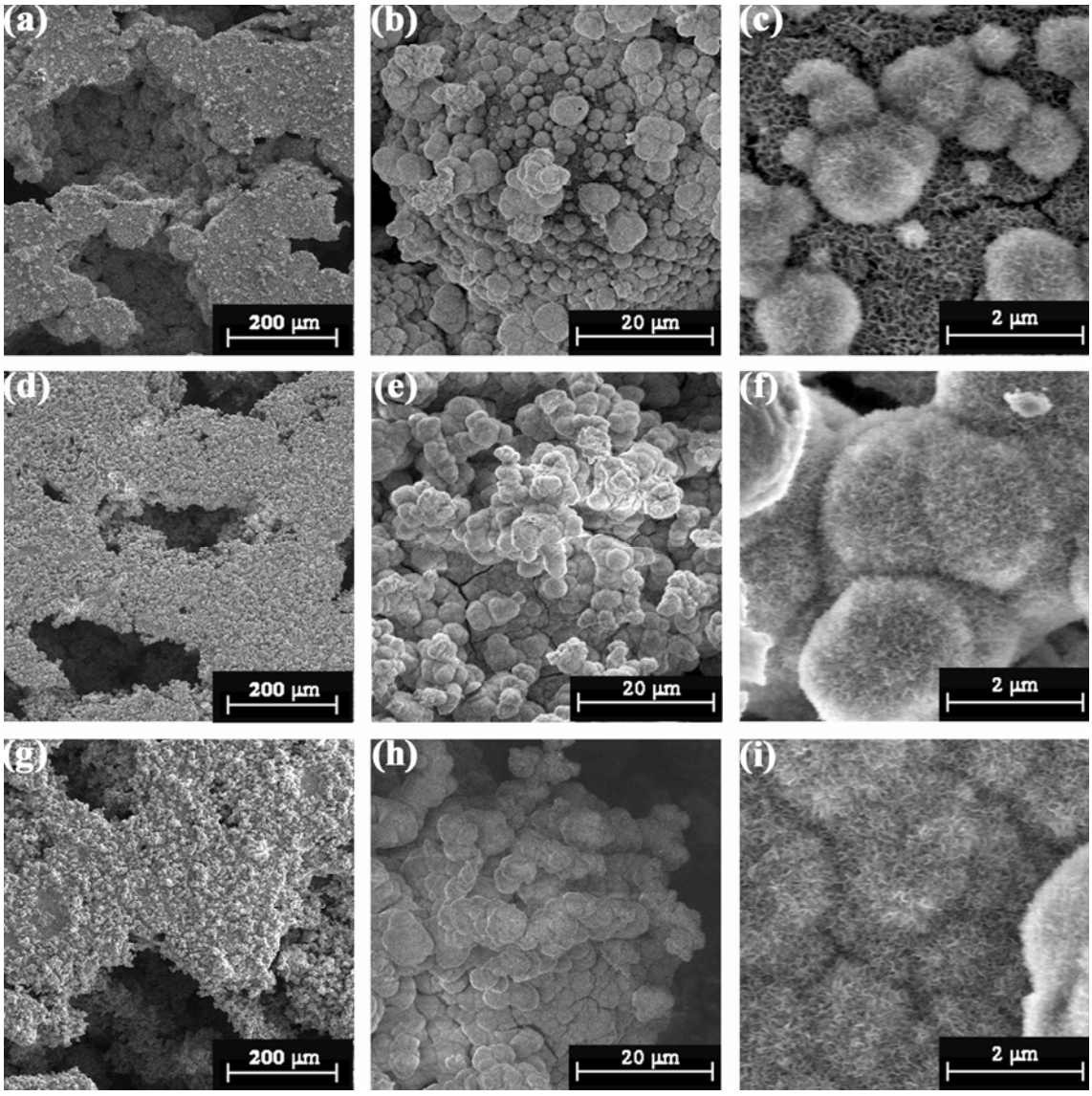

Figure 5.16. SEM micrographs of AT P2 foam specimens (a) flat surface after 5-day of SBF immersion, (b) interior of the cell after 5-day of SBF immersion, (c) high magnification after 5-day of SBF immersion, (d) flat surface after 7-day of SBF immersion, (e) interior of the cell after 7-day of SBF immersion, (f) high magnification after 7-day of SBF immersion, (g) flat surface after 14-day of SBF immersion, (h) interior of the cell after 14-day of SBF immersion and (i) high magnification after 14-day of SBF immersion.

Figure 5.17 shows the GIXRD spectra of AT P1 and P2 foam after 1, 3, 5, 7 and 14-day of SBF immersion. In Figure 5.17, the red color GIXRD spectra belong to P1 foam, while black color GIXRD spectra to P2 foam. In the same figure, the GIXRD spectrum of untreated 14-day SBF immersed P1 and P2 foam are also shown for comparison. The GIXRD spectrum of untreated SBF immersed specimen shown in this figure is fitted with Gaussian Lorentzion distribution (R^2 = 0.9). The fitted spectrum reveals a broad peak at 32°, which is the reflections from (211), (212) and (300) planes of carbonated-hydroxyl apatite (CHA) at 31.037^o, 32.057^o and 32.998^o, respectively. The lattice parameters of hexagonal structure of CHA (JCPDS 9-432) closely match to the calculated lattice parameters of the coating layer (a = 0.944 nm and c = 0.688 nm). CHA peaks are seen in Figure 5.17 after 5-day of SBF immersion in P2 foam specimen and after 7-day of SBF immersion in P1 foam specimen. The GIXRD spectra of the foam specimen also show good agreements with the SEM pictures shown in Figures 5.15 and 16. The continuous CaP is detected microscopically after 7 and 14-day of SBF immersion in P2 and P1 foam specimens, respectively. Above results clearly show that alkali treatment significantly decreases the time for the formation of a continuous CaP coating layer in the foam flat and particle surfaces as compared with untreated foam specimens (14-day).

Figures 5.18 (a-i) show the SEM micrographs of NAT P1 foam flat surfaces and interior of cells after 5, 7 and 14-day of SBF immersion. After 5-day of SBF immersion, tiny CaP particles on the surface of the particles and flat surface of the foam specimens are seen in Figures 5.18 (a-c). After 7-day of SBF immersion, relatively large size of CaP globules are seen not only on the particle surfaces, but also on the surfaces of the flat sections of foam specimen as seen in Figures 18(d-f). After 14-day of SBF immersion, a uniform CaP coating layer is seen on the surfaces of the foam flat sections and the particles (Figures 5.18(g-i)). Figures 5.19 (a-i) show the SEM micrographs of NAT P2 foam flat surfaces and interior of cells after 5, 7 and 14-day of SBF immersion. The globular CaP on the flat surface and interior of the cells starts to form in NAT P2 foam specimen only after 3-day (not shown here) of SBF immersion. However, after 5-day of SBF immersion the foam flat and particle surfaces are fully coated with a uniform CaP layer as shown in Figures 5.19(a-c). It is noted that CaP layer formed in NAT foam specimens are relatively thin as compared with AT foam specimens.

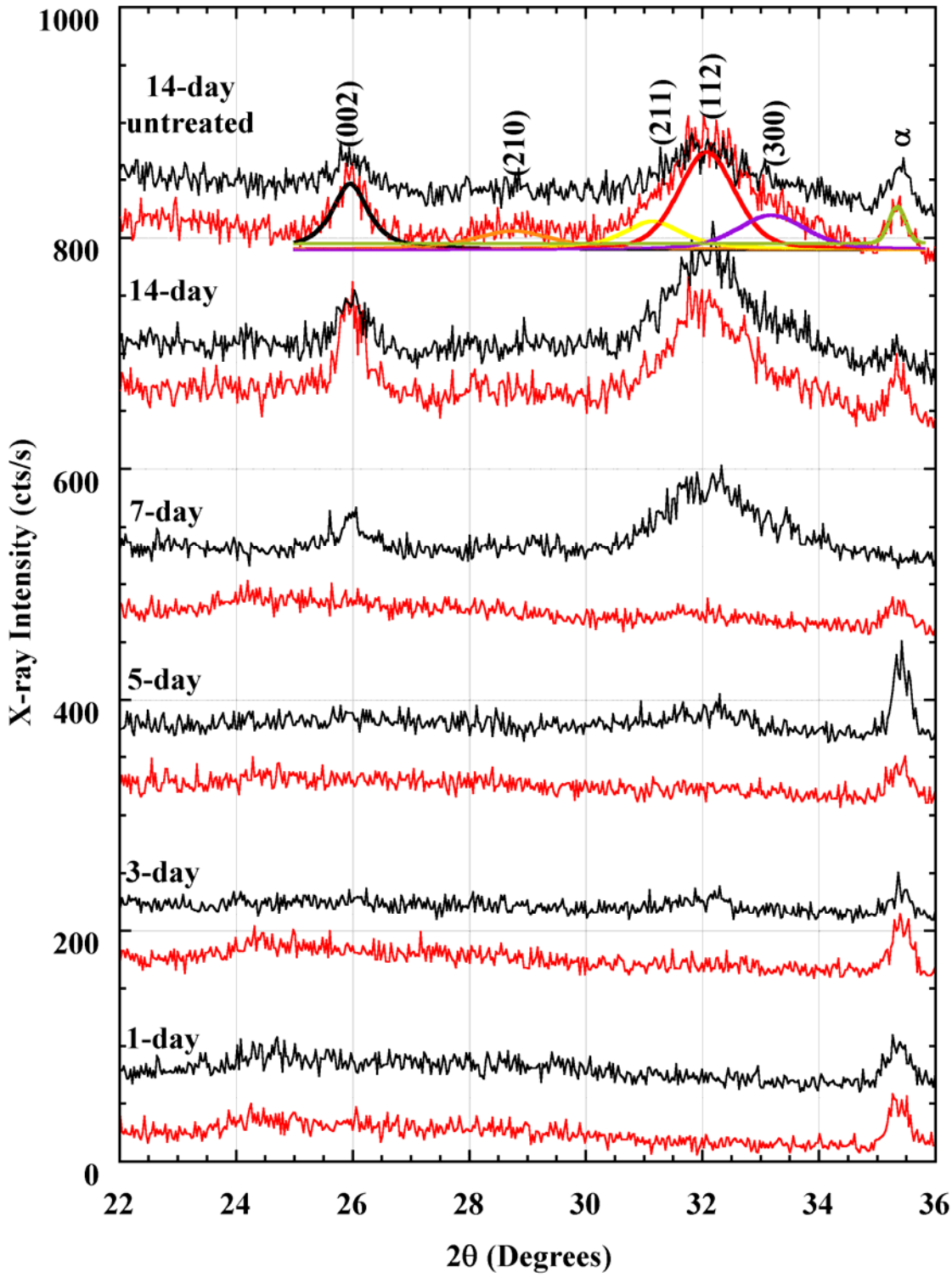

Figure 5.17. GIXRD spectra of AT P1 (red) and P2 (black) foam specimens after 1, 3, 5, 7, 14-day of SBF immersion (GIXRD spectra of untreated 14-day SBF immersed specimen is also shown).

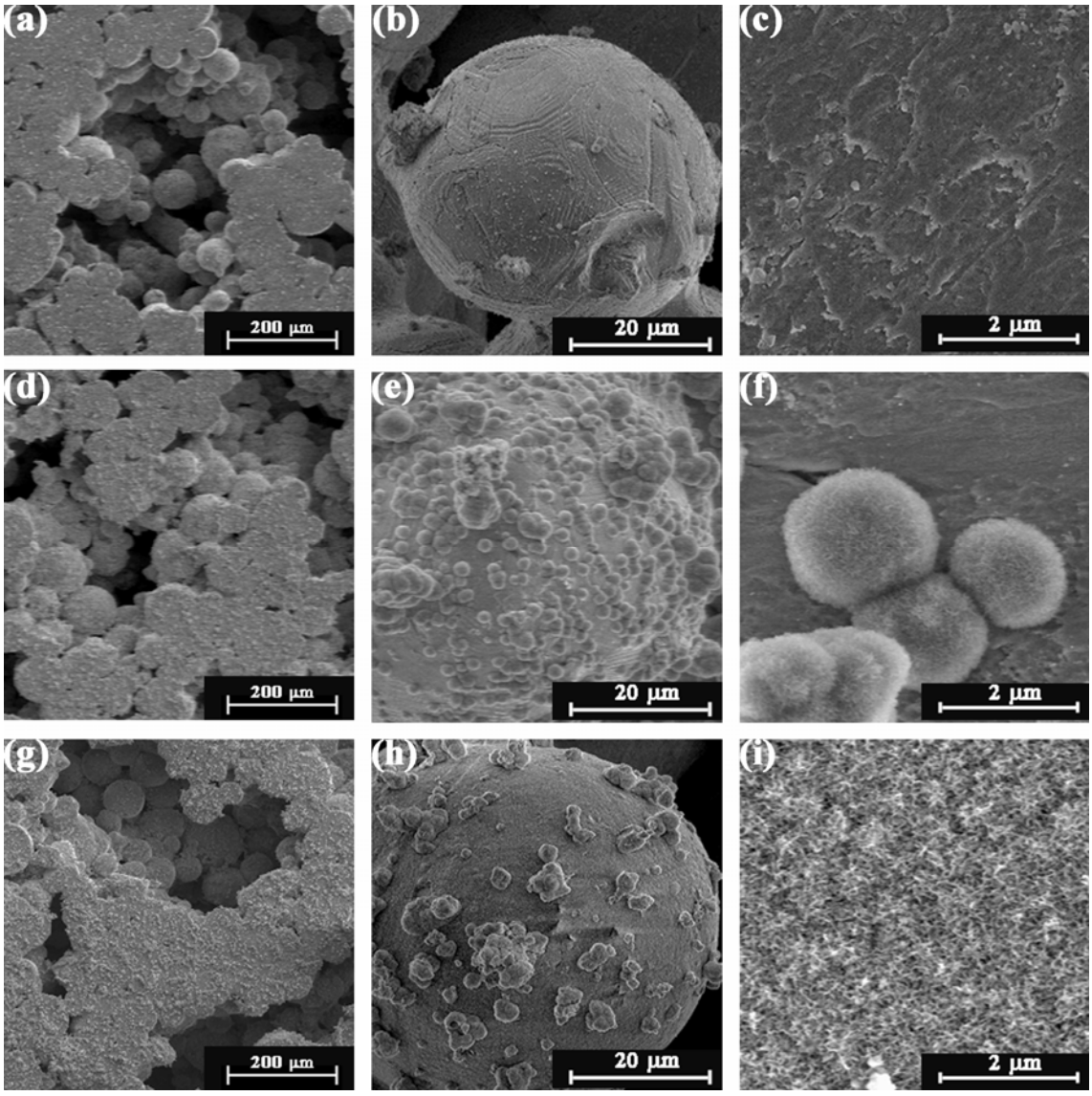

Figure 5.18. SEM micrographs of NAT P1 foam specimens (a) flat surface after 5-day of SBF immersion, (b) interior of the cell after 5-day of SBF immersion, (c) high magnification after 5-day of SBF immersion, (d) flat surface after 7-day of SBF immersion, (e) interior of the cell after 7-day of SBF immersion, (f) high magnification after 7-day of SBF immersion, (g) flat surface after 14-day of SBF immersion, (h) interior of the cell after 14-day of SBF immersion and (i) high magnification after 14-day of SBF immersion.

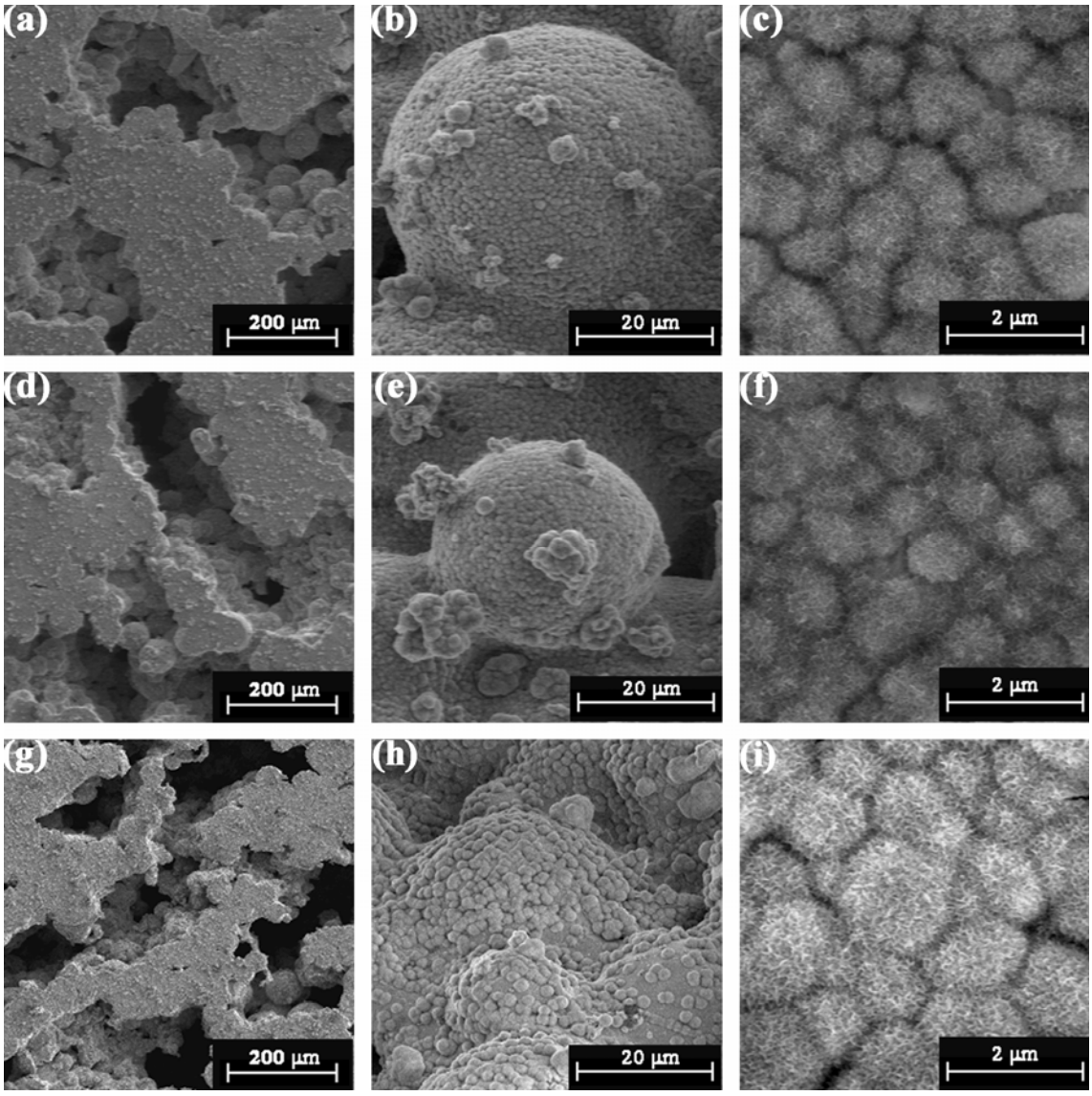

Figure 5.19. SEM micrographs of NAT P1 foam specimens (a) flat surface after 5-day of SBF immersion, (b) interior of the cell after 5-day of SBF immersion, (c) high magnification after 5-day of SBF immersion, (d) flat surface after 7-day of SBF immersion, (e) interior of the cell after 7-day of SBF immersion, (f) high magnification after 7-day of SBF immersion, (g) flat surface after 14-day of SBF immersion, (h) interior of the cell after 14-day of SBF immersion and (i) high magnification after 14-day of SBF immersion.

Figure 5.20 shows the GIXRD spectra of NAT P1 and P2 foam after 1, 3, 5, 7 and 14-day of SBF immersion. The red color GIXRD spectra belong to P1 foam, while black color GIXRD spectra to P2 foam. In the same figure, the GIXRD spectra of untreated 14-day SBF immersed P1 and P2 foam specimens are also shown for comparison. CHA peaks are seen in Figure 5.20 after 5-day of SBF immersion in P2 foam specimen and after 7-day of SBF immersion in P1 foam specimen. The GIXRD spectra of the foam specimens also show good agreements with the SEM pictures of CaP deposition in NAT foam specimens in Figures 5.18 and 5.19. However, the peak intensity of P2 foam at 25° (002) is higher than that of P1 foam after 14-day of SBF immersion. The increased peak intensity of P2 foam specimen indicates the increased crystallinity of CaP layer (Scherer Equation).

Figures 5.21 (a-i) show the SEM micrographs of AE P1 foam flat surfaces and interior of cells after 5, 7 and 14-day of SBF immersion. As noted in Figures 5.21(a-i), acid etching induces relatively rougher surfaces as compared with alkali and nitric acid treatment. The dissolved β-lathes on the surface of the flat surface and interior of the pores are also detectable after 5 and 7-day of SBF immersion (Figures 5.21(a-f)). As seen in Figures 5.21(a-i), CaP layer forms only after 14-day of SBF immersion in AE foam specimens. The CaP layer formed is however relatively thin. Figures 5.22 (a-i) show the SEM micrographs of AE P2 foam flat surfaces and interior of cells after 5, 7 and 14-day of SBF immersion. Tiny CaP globules are seen on the flat and particles surfaces after 5-day of SBF immersion (Figures 5.22 (a-f)). After 14-day of SBF immersion, a number of CaP precipitates is clearly seen on the foam flat sections surface than the particle surfaces interior of the cells (Figures 5.22 (g-i)). Some regions of the particle surfaces are also noted to not completely coated with CaP after 14-day of SBF immersion (Figures 5.22(h-i)).

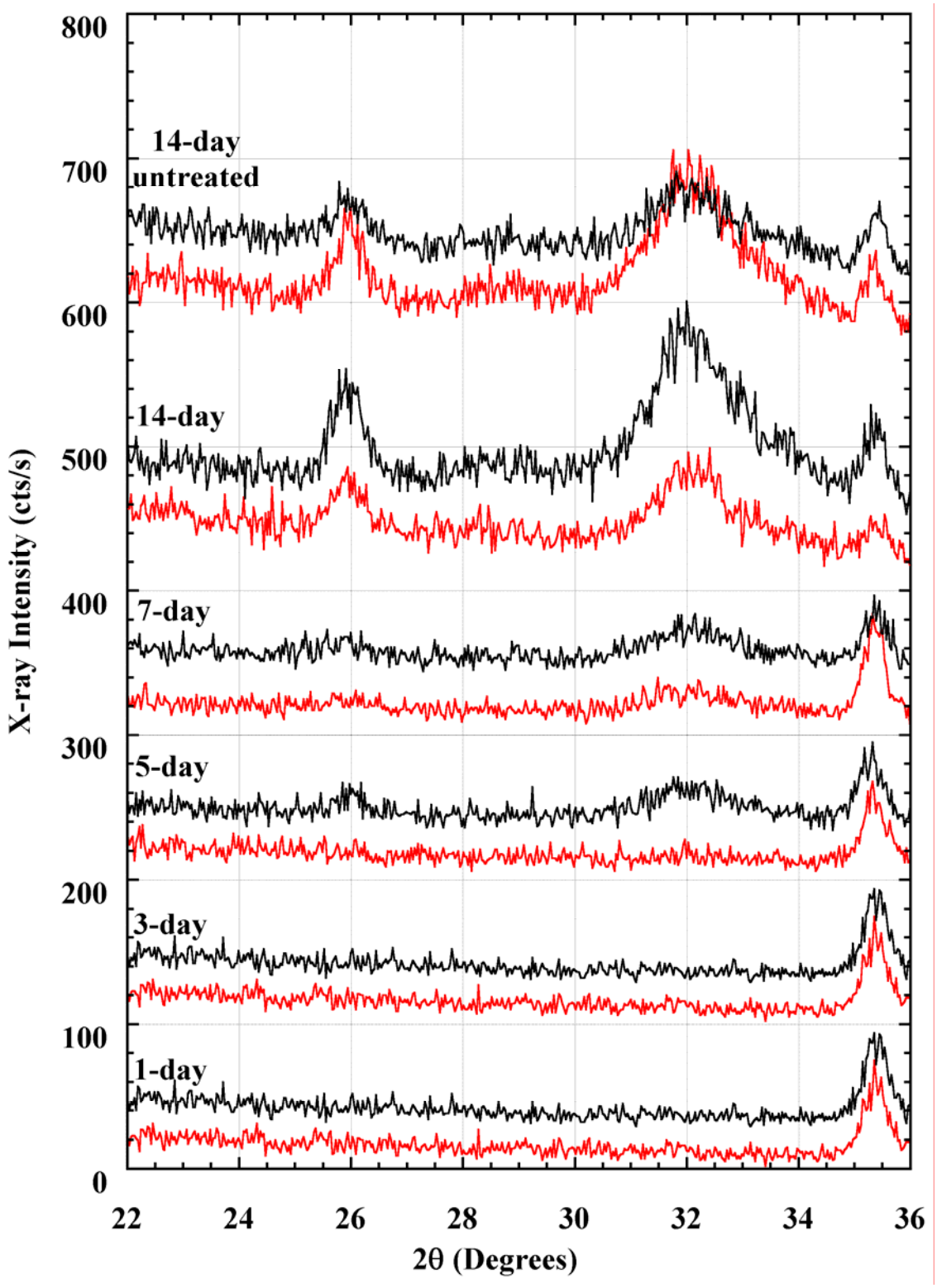

Figure 5.20. GIXRD spectra of NAT P1 (red color) and P2 (black color) foam specimens after 1, 3, 5, 7 and 14-day of SBF immersion.

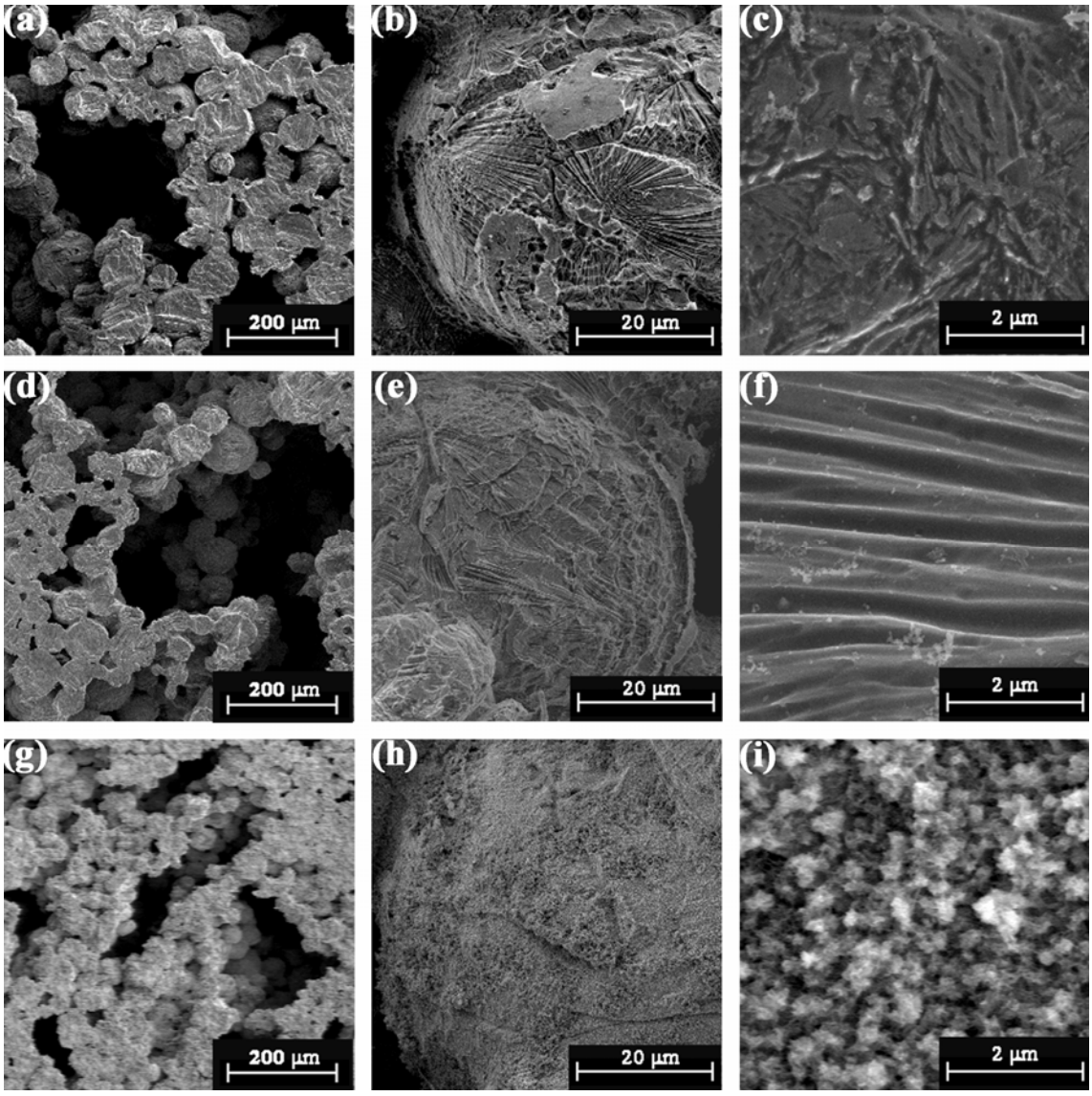

Figure 5.21. SEM micrographs of AE P1 foam specimens (a) flat surface after 5-day of SBF immersion, (b) interior of the cell after 5-day of SBF immersion, (c) high magnification after 5-day of SBF immersion, (d) flat surface after 7-day of SBF immersion, (e) interior of the cell after 7-day of SBF immersion, (f) high magnification after 7-day of SBF immersion, (g) flat surface after 14-day of SBF immersion, (h) interior of the cell after 14-day of SBF immersion and (i) high magnification after 14-day of SBF immersion.

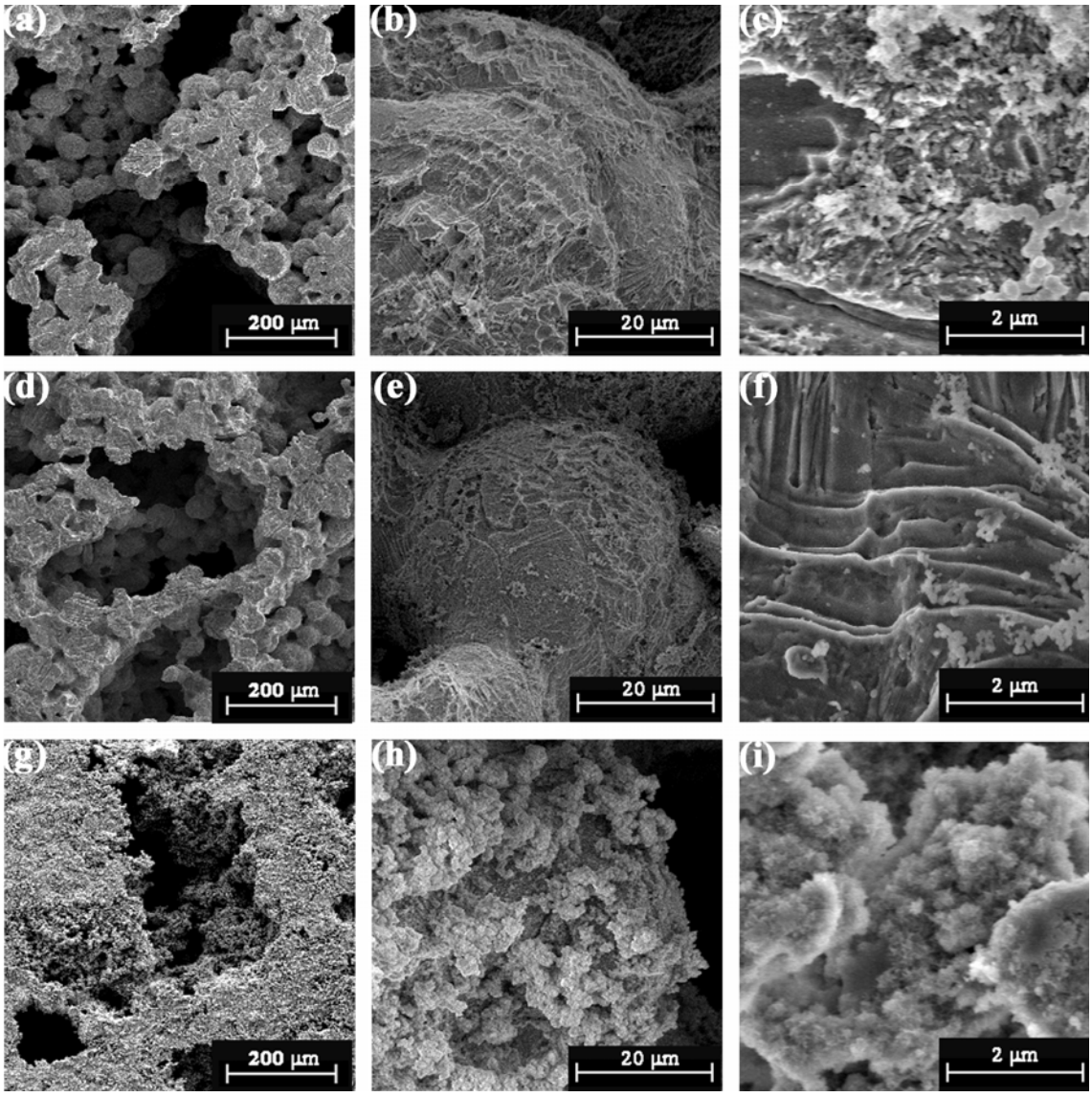

Figure 5.22. SEM micrographs of AE P2 foam specimens (a) flat surface after 5-day of SBF immersion, (b) interior of the cell after 5-day of SBF immersion, (c) high magnification after 5-day of SBF immersion, (d) flat surface after 7-day of SBF immersion, (e) interior of the cell after 7-day of SBF immersion, (f) high magnification after 7-day of SBF immersion, (g) flat surface after 14-day of SBF immersion, (h) interior of the cell after 14-day of SBF immersion and (i) high magnification after 14-day of SBF immersion.

Average crystal size and the lattice constant of CaP layer formed on the surface of the foam specimens after 14-day of SBF immersion are calculated using the Debye Schreer Equation and the results are tabulated in Tables 5.2 and 5.3 for P1 and P2 foam specimens, respectively. The lattice constants of the foam specimens tabulated in Tables 5.2 and 5.3 are very similar to that of CHA card (9-432). The average crystal size of untreated and AT P1 foam specimens are bigger than those of untreated and AT P2 foam specimens, while AE and NAT P2 foam specimens show bigger average crystal sizes than AE and NAT P1 foam specimens.

Table 5.2. Lattice constants and average crystal sizes of untreated and surface treated P1 foam specimens.

P1 foam	$2\theta_1$ (002)	$2\theta_2$ (300)	a (nm)	c (nm)	FWHM	t (nm)
Untreated	25.96	32.95	0.94075	0.68596	0.65	12.45
AT	25.97	32.72	0.94722	0.68560	0.49	16.53
NAT	25.89	33.05	0.93798	0.68760	0.97	8.365
AE	25.87	32.71	0.94743	0.68818	1.36	5.961

Table 5.3. Lattice constants and average crystal sizes of untreated and surface treated P2 foam specimens.

P2 foam	$2\theta_1$ (002)	$2\theta_2$ (300)	a (nm)	c (nm)	FWHM	t (nm)
Untreated	25.90	32.74	0.94672	0.68733	1.14	7.13
AT	25.89	32.84	0.94385	0.68767	0.61	13.30
NAT	25.94	32.79	0.94531	0.68640	0.56	14.41
AE	25.94	32.54	0.95224	0.68633	0.86	9.44

Figures 5.23(a) and (b) show the ATR-FTIR analysis of untreated and 14-day SBF immersed P1 and P2 foam specimens, respectively. The absorption band at 3450 cm^{-1} and bending mode at 1650 cm^{-1} in Figures 5.23(a) and (b) are associated with water. The peaks observed at 1040, 604 and 567 cm^{-1} are due to the stretching of PO_4^{3-} vibrations. The phosphate has tetrahedral structure with four normal modes of vibrations (ν_1, ν_2, ν_3 and ν_4). Only ν_3 and ν_4 are active on the basis of molecular symmetry. The peaks seen at 959 and 875 cm^{-1} indicate the presence of HPO_4^{2-} group.

The bands detected at 1460, 1420 and 875 cm^{-1} show the presence of CO_3^{2-} group. The band at 1550 cm^{-1} labels a CHA type of CO_3^{2-} ion. The carbonate band around 880 cm^{-1} is due to the bending out of plane vibration, while the band at 1550 cm^{-1} is bending mode of carbonate band. ATR-FTIR analysis of AT P1 and P2 foam specimens after 1, 3, 5, 7 and 14-day of SBF immersion are shown in Figures 5.24(a) and (b), respectively. The carbonate and phosphate peaks are visible after 1-day of SBF immersion (Figures 5.24(a) and (b)). This is due to plate like CaP induction in SBF. A small shift of H_2O molecule at 3450 cm^{-1} in the spectrum is also seen after 14-day of SBF immersion. Figures 5.25(a) and (b) show the ATR-FTIR analysis of NAT P1 and P2 foam specimens after 1, 3, 5, 7 and 14-day of SBF immersion, respectively. CaP phase forms after 7-day of SBF immersion in P1 foam specimen and 5-day of SBF immersion in P2 foam specimen. No phase shift is further observed in the spectra of NAT foam specimens. The ATR-FTIR analysis of AE P1 and P2 foam specimens after 1, 3, 5, 7 and 14-day of SBF immersion are shown sequentially in Figures 5.26(a) and (b). As is noted in Figures 5.26(a) and (b), there is no evidence of CaP formation until about 7-day of SBF immersion. CaP formation forms after 14-day of SBF immersion as seen in the same figures. Above results agree with the SEM micrographs and GIXRD spectra of AT and NAT foam specimens. One of the major problems in ATR -FTIR analysis of porous samples is the very strong IR absorbance of water (humidity in air). Water vapor has very sharp IR absorption bands around 1700 and 3700 cm^{-1} that are hard to correct. Therefore, the small IR bands in spectra which are not marked, are due to the water in the pores. This may be prevented by purging the foam specimen with dry nitrogen or by operating the FTIR spectrometer in vacuum.

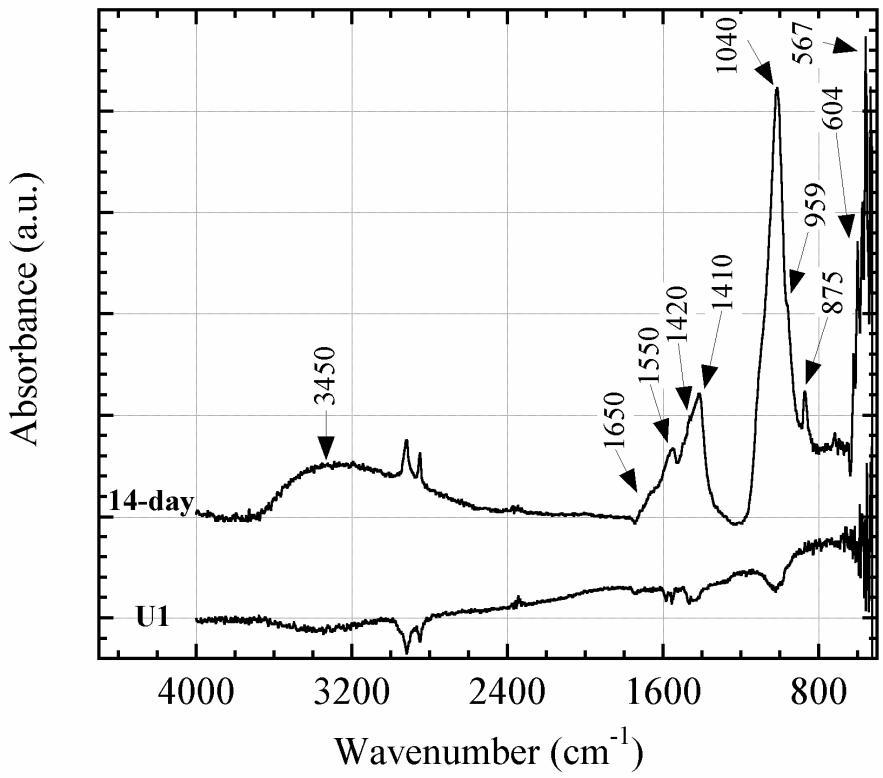

(a)

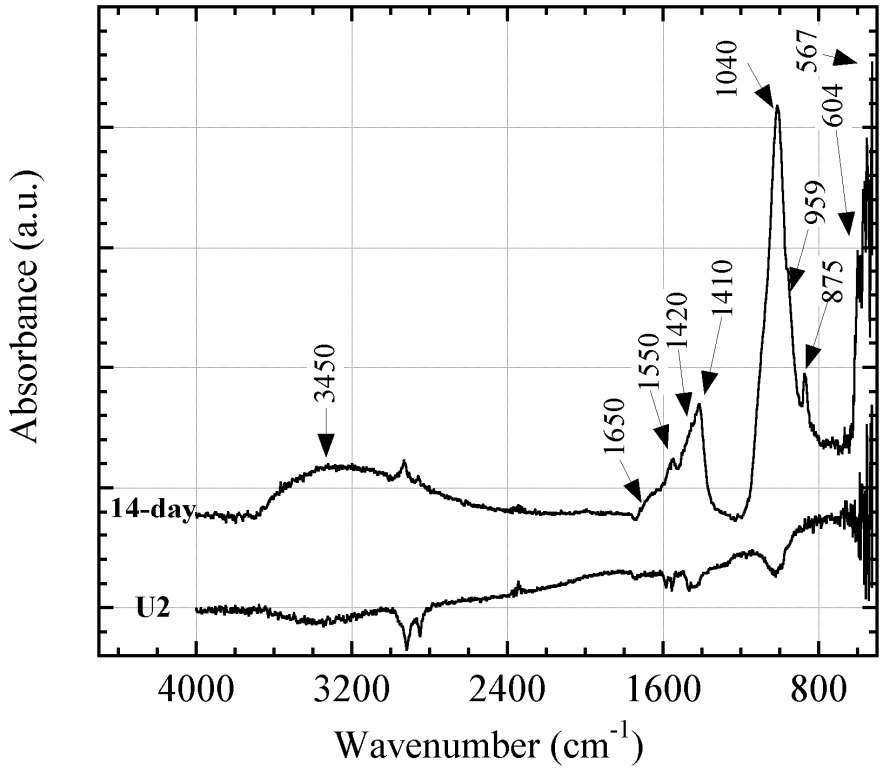

(b)

Figure 5.23. ATR-FTIR analyses of untreated (a) P1 and (b) P2 foam specimens after 14-day of SBF immersion.

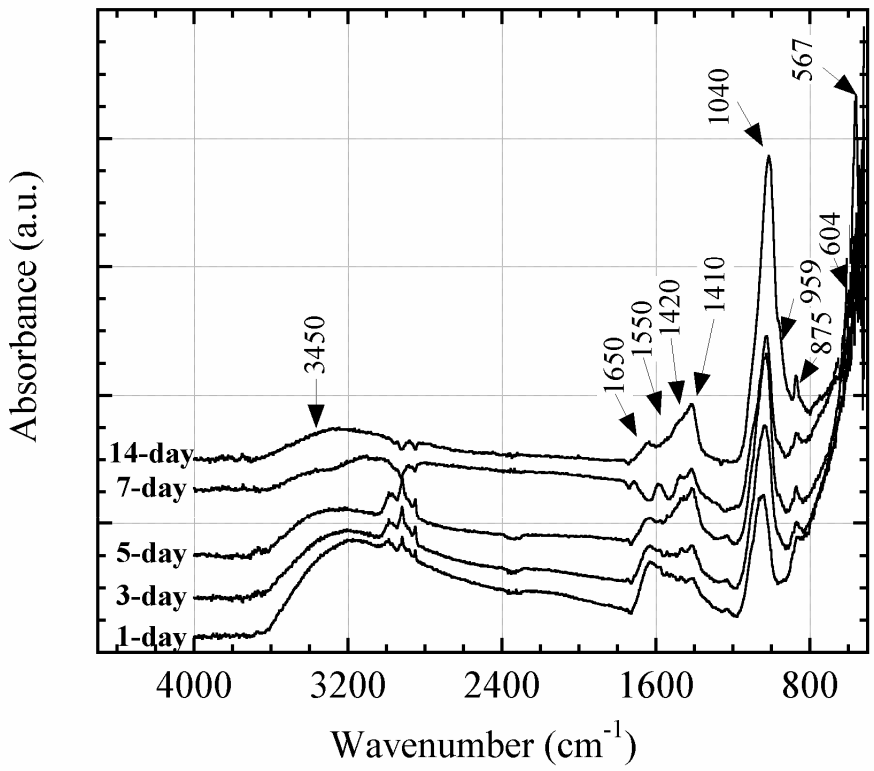

(a)

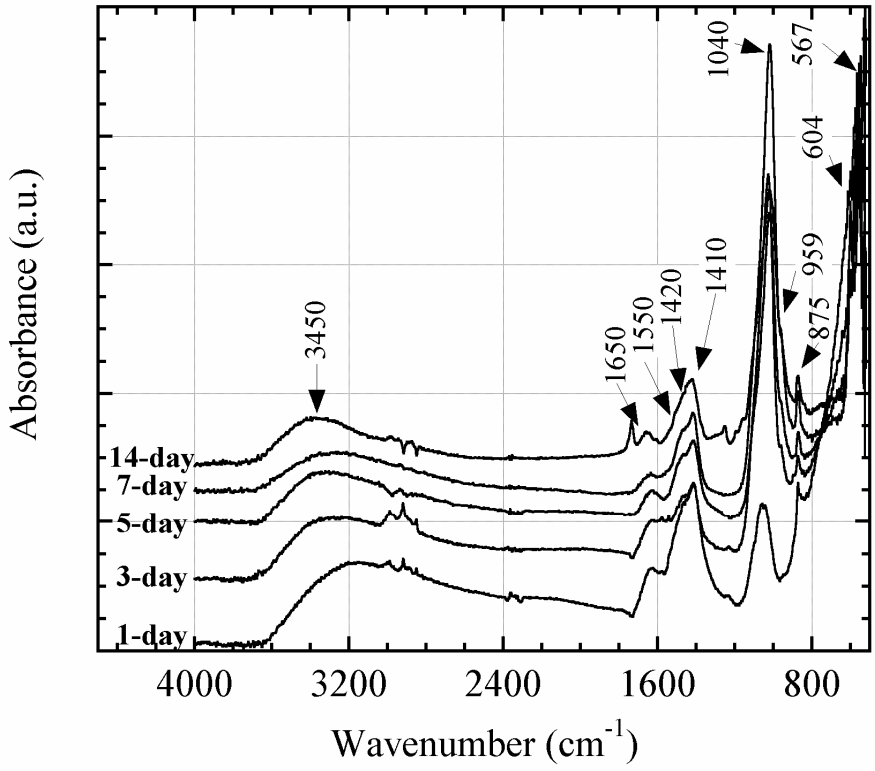

(b)

Figure 5.24. ATR-FTIR analyses of AT (a) P1 and (b) P2 foam specimen after 1, 3, 5 , 7 and 14-day of SBF immersion.

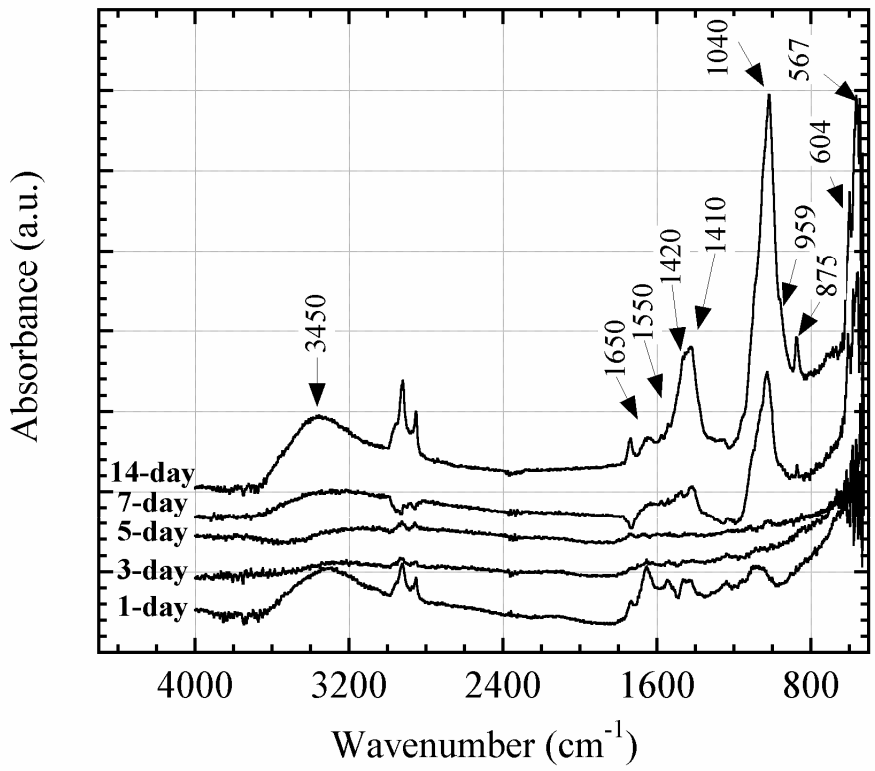

(a)

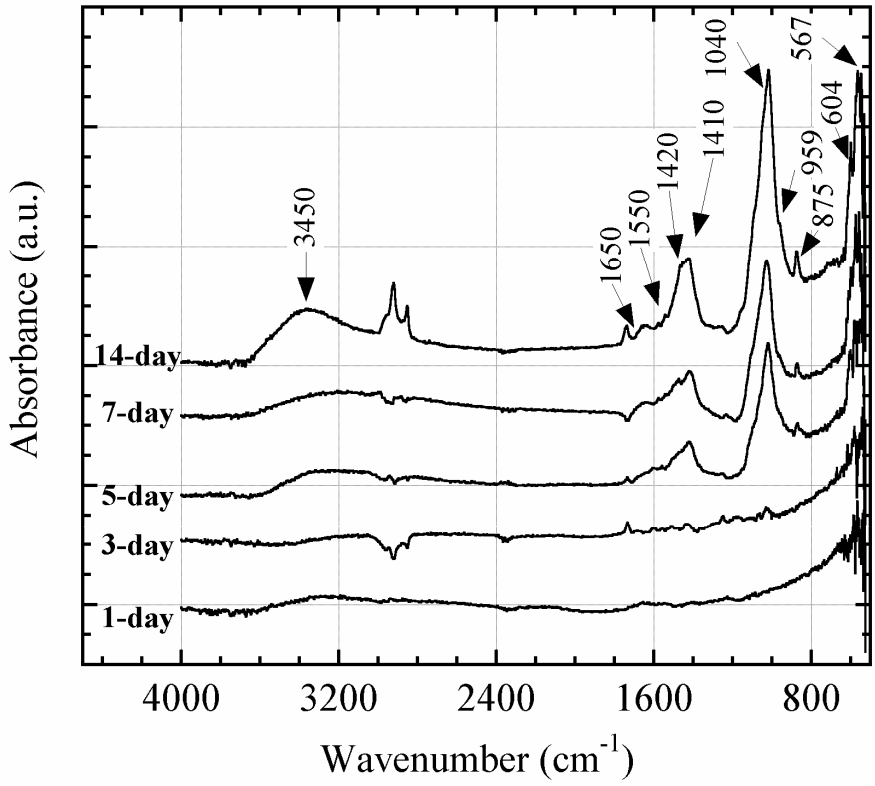

(b)

Figure 5.25. ATR-FTIR analyses of NAT (a) P1 and (b) P2 foam specimen after 1, 3, 5, 7 and 14-dayof SBF immersion.

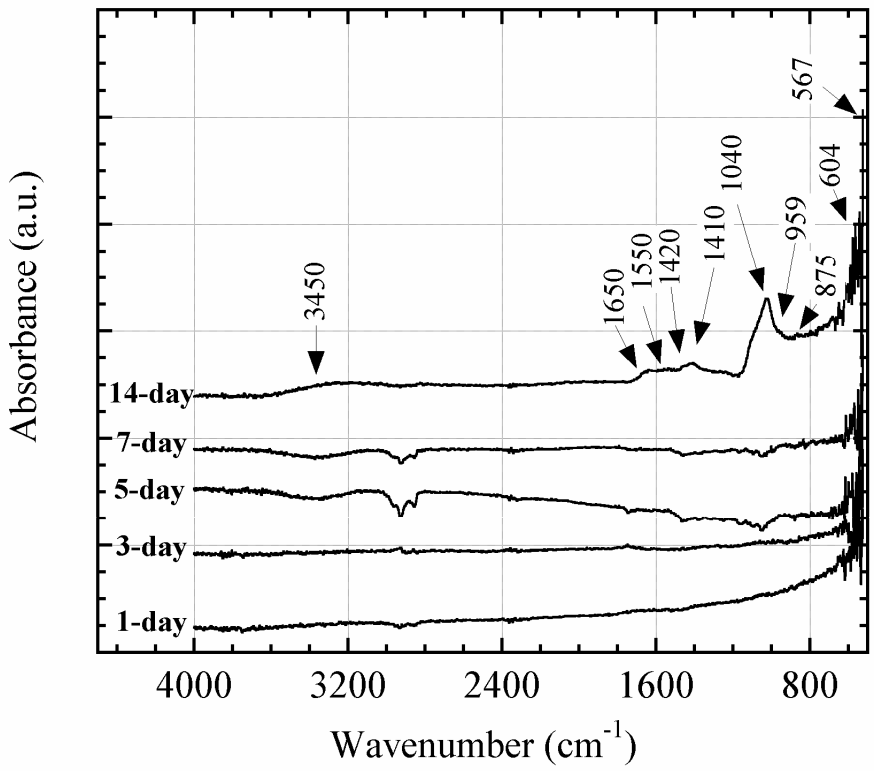

(a)

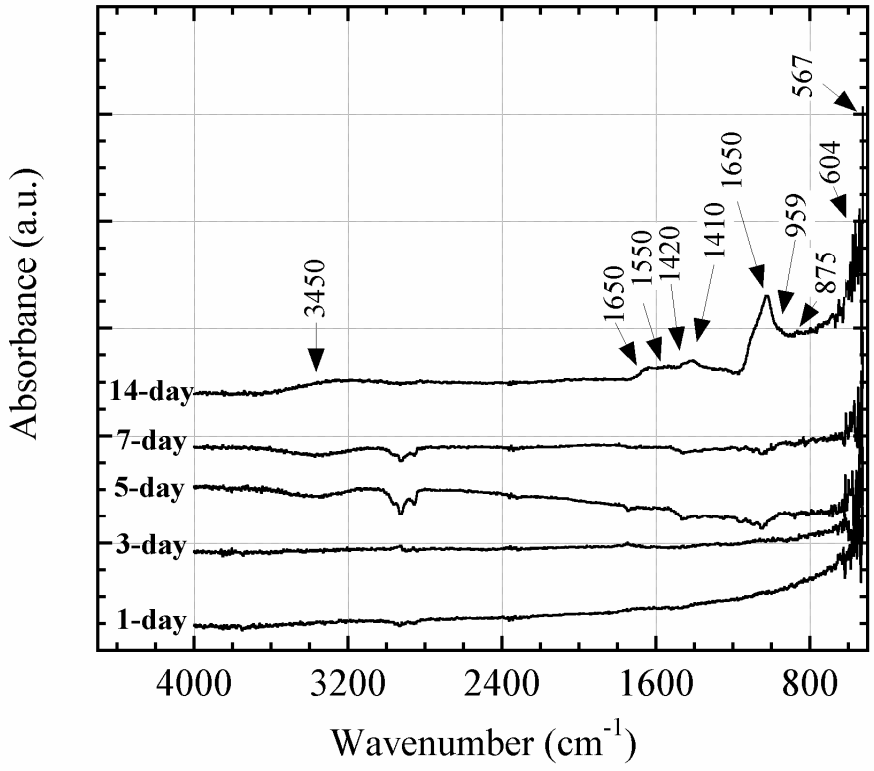

(b)

Figure 5.26. ATR-FTIR analyses of AE (a) P1 and (b) P2 foam specimen after 1, 3, 5, 7 and 14-day ofSBF immersion.

AFM surface roughness values of foam specimens (untreated and surface treated) after SBF immersion are tabulated in Table 5.4. As is tabulated in Table 5.4, the AFM surface roughness values of SBF immersed foam specimens are higher than those of untreated and treated foam specimens before SBF immersion tabulated in Table 5.1. SBF immersion increases the surface roughness values at least 3.2 times. It is also noted in Tables 5.1 and 5.4 that AT foam specimens has the highest surface roughness values before and after SBF immersion.

Table 5.4. The AFM surface roughness of untreated and surface treated P1 and P2 foam specimens after 14-day of SBF immersion.

	Ra (nm)	Rq (nm)	SAD (%)
As Received P1	32.035	41.236	16.659
NAT P1	28.394	35.442	41.581
AT P1	60.15	72.748	59.286
As Received P2	30.04	38.542	15.435
NAT P2	64.678	78.066	37.538
AT P2	50.241	62.9	44.131

Figures 5.27(a) and (b) show sequentially 2D and 3D AFM micrographs (scanned area of 1.5x1.5 μm) of surface topologies of untreated 14-day SBF immersed P1 and P2 foam specimen. In Figure 5.27(b), the crack-like valleys are seen on the untreated P2 foam specimen. These cracks mainly result from the peeling off CaP layer on the flat section of the foam specimens, agreeing with the SEM pictures of CaP layer on untreated foam samples. This also confirms a weak bonding (adhesion) between CaP film and foam particle surfaces. Figures 5.28(a) and (b) show sequentially 2D and 3D AFM micrographs of surface topologies of 14-day SBF immersed AT P1 and P2 foam specimens. AFM micrographs in Figures 5.28(a) and (b) show that CaP particle size on P2 foam specimen is larger than that on P1 foam specimen. Figures 29(a) and (b) show 2D and 3D AFM micrographs of surface topologies of 14-day SBF immersed NAT P1 and P2 foam specimen surfaces, respectively. No surface cracks are detected on the AFM micrographs of AT and NAT foam specimen surfaces.

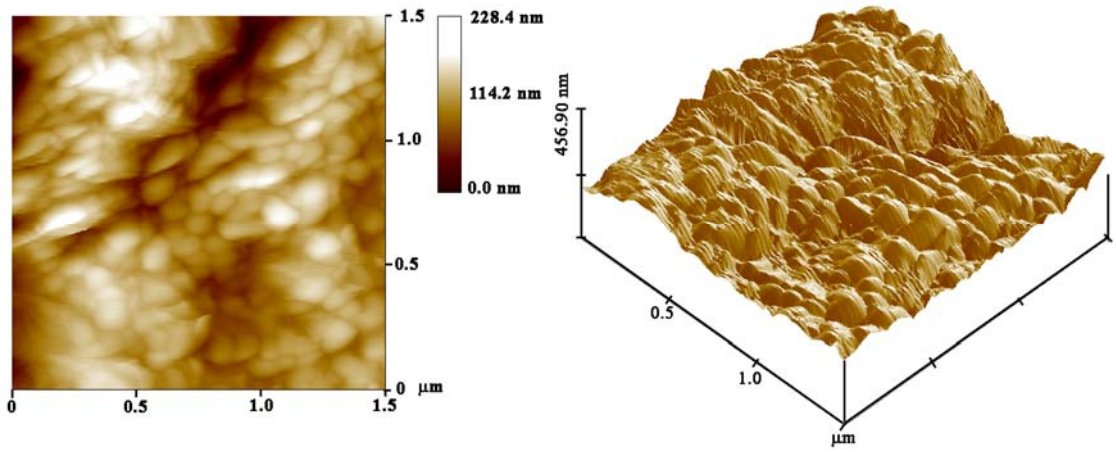

(a)

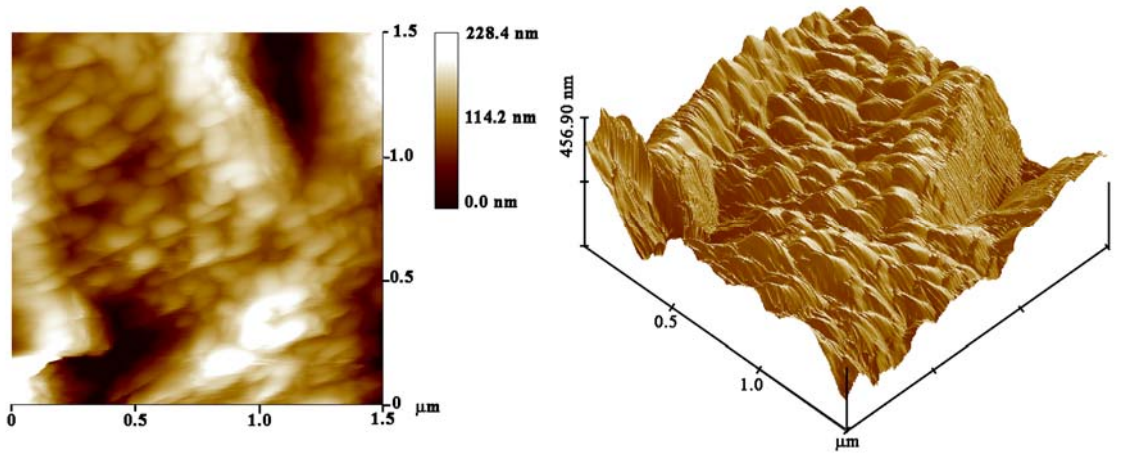

(b)

Figure 5.27. 2D and 3D AFM micrographs of surface topologies of untreated foam specimen after 14-day of SBF immersion, (a) P1 and (b) P2 foam.

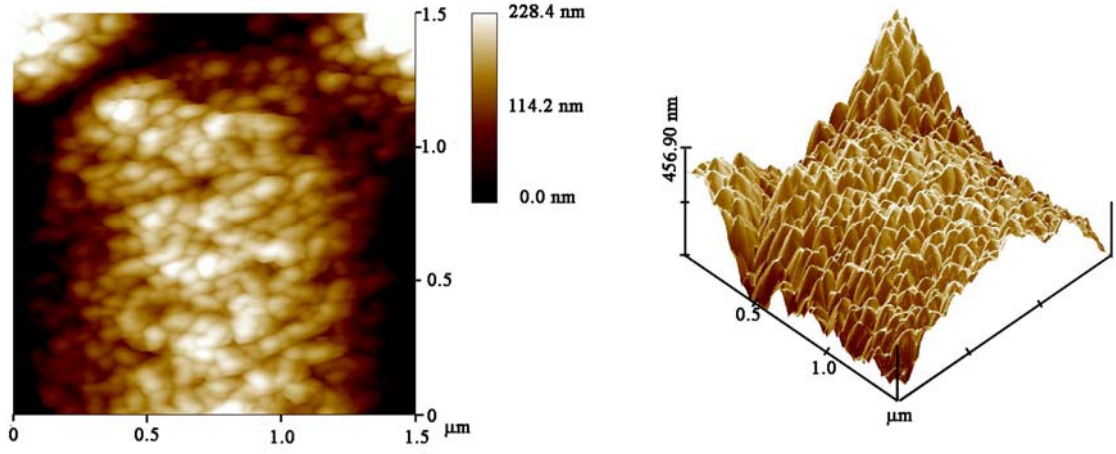

(a)

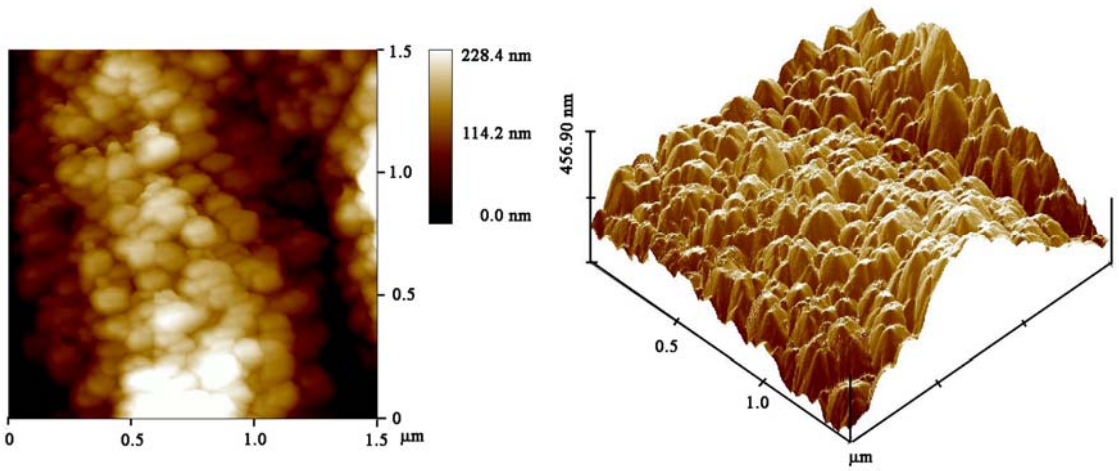

(b)

Figure 5.28. 2D and 3D AFM micrographs of surface topologies of AT foam specimen after 14-day of SBF immersion, (a) P1 and (b) P2 foam.

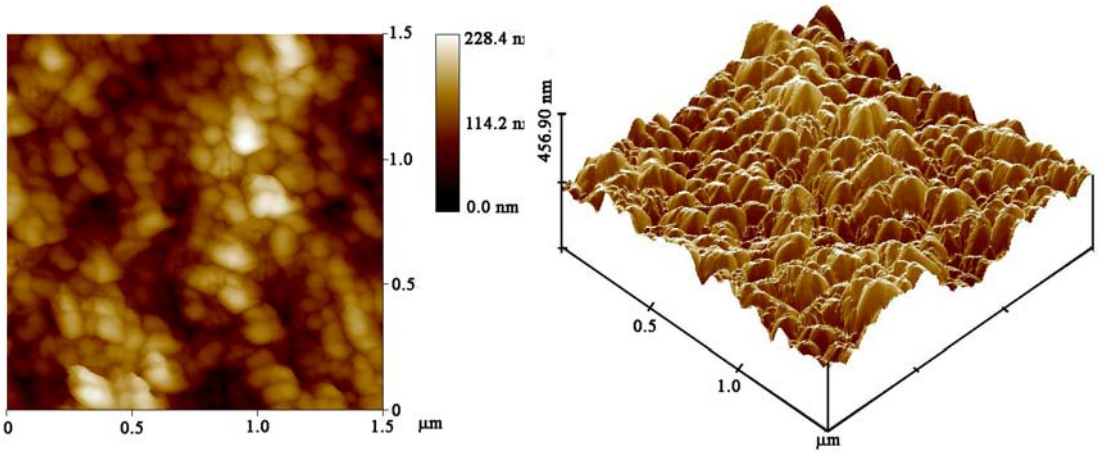

(a)

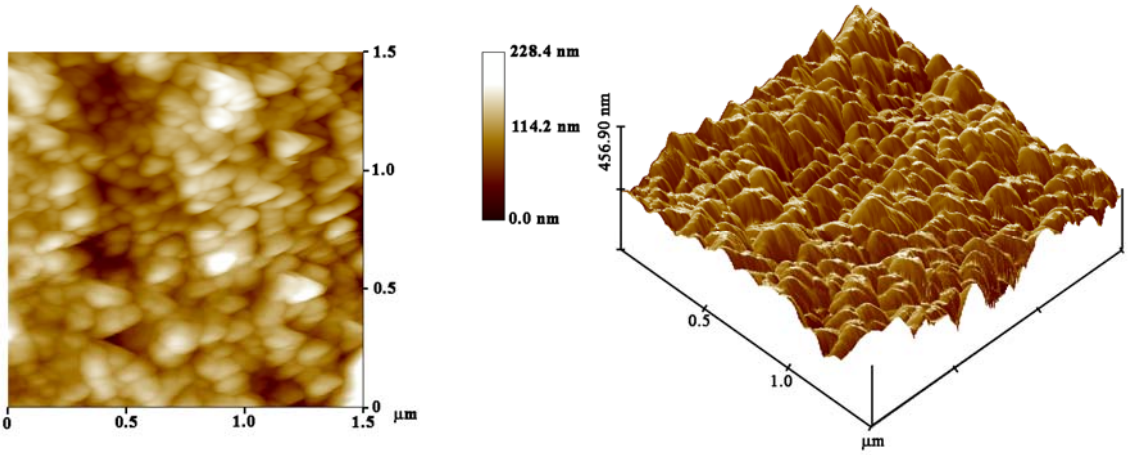

(b)

Figure 5.29. 2D and 3D AFM micrographs of surface topologies of NAT foam specimen after 14-day of SBF immersion, (a) P1 and (b) P2 foam.

Figures 5.30(a-d) show the cross sectional SEM micrographs of the cell wall surfaces (inside the pores) of AT P1 and P2 foam specimens before and after 14-day of SBF immersion. The thickness of sodium titanate layer is measured nearly 500 nm (Figures 5.30(a) and (c)). A continuous CaP coating layer is also seen on the particle surfaces of both P1 and P2 foams as seen in Figures 30(b) and (d). The CaP layer thickness is also measured from these SEM micrographs and found nearly 3 and 3.2 µm in P1 and P2 foam specimen, respectively. The CaP layer thickness of nitric acid treated P1 and P2 foam specimens after 14-day of SBF immersion was measured from the

surface cracks (not shown here) and found to be 0.65 and 0.9 μm, respectively. In addition, the CaP layer thickness of untreated P1 and P2 foam specimens after 14-day of SBF immersion was measured 1.2 and 1.5 μm, respectively.

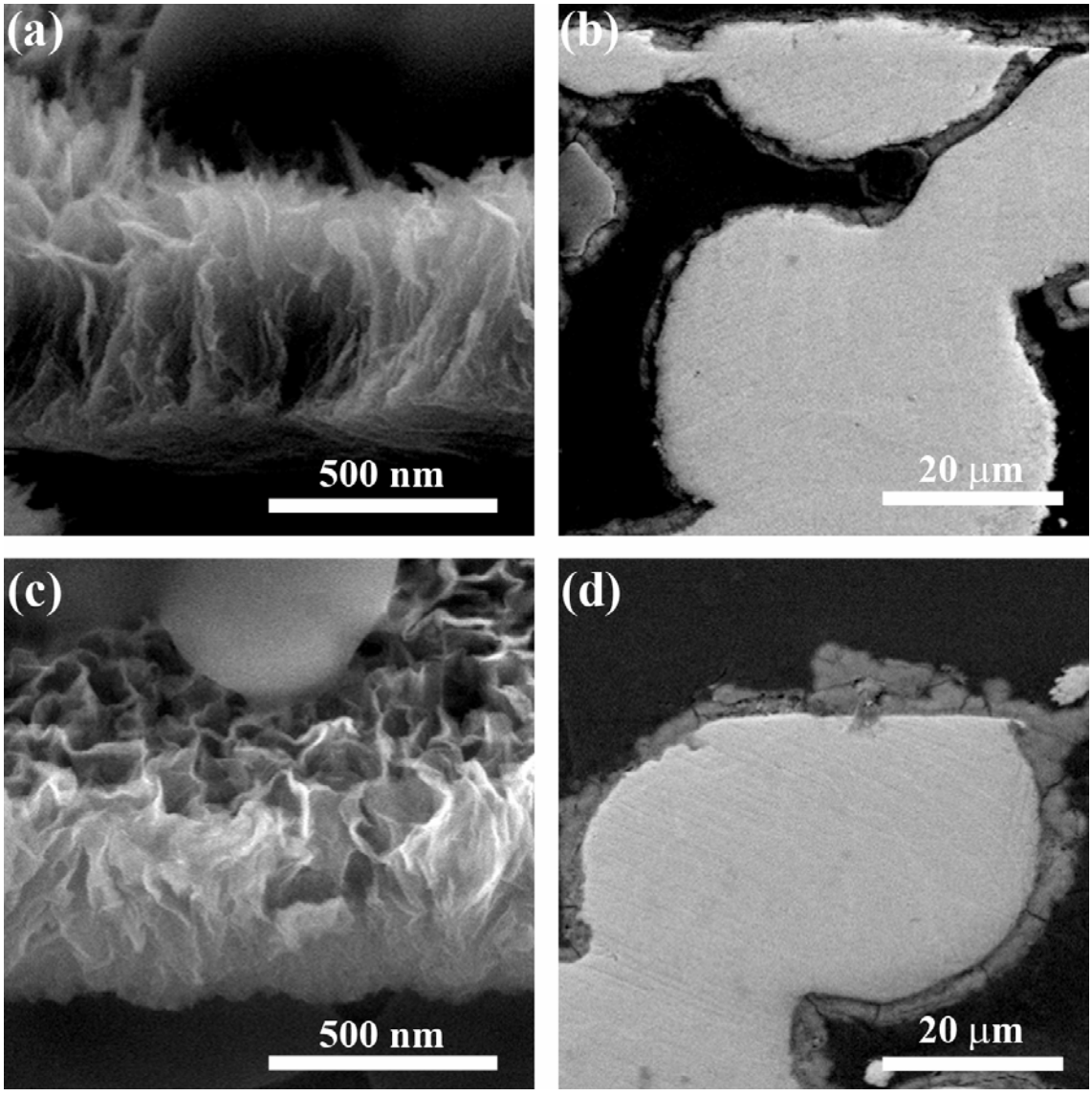

Figure 5.30. Cross sectional SEM micrographs of AT P1 foam specimen (a) before and (b) after 14-day of SBF immersion and AT P2 foam specimen (c) before and (d) after 14-day of SBF immersion.

The bioactivity of Ti metal depends on the surface characteristics including surface topography, surface roughness, surface energy and the amounts of amphoteric Ti-OH groups on the surface. The mechanism of apatite formation on alkali and heat treated Ti in SBF has been recently demonstrated by Kukoba et. al. (Kokubo 2008) and is schematically shown in Figure 5.31. Initially, the surface passive TiO_2 layer on Ti

partially dissolves by the corrosive attack of hydroxyl group, producing negatively charged hydrates based on the following reaction (Kim, et al. 1996, Kim, et al. 1997).

$$TiO_2.nH_2O+OH^- \rightarrow HTiO_3^-.nH_2O \quad (.5.1)$$

The negatively charged $HTiO_3^-.nH_2O$ reacts with positively charged alkali ions in aqueous solution, forming a porous thin sodium titanate gel layer on the surface of Ti (Kim, et al. 1996, Kokubo 2008, Lee, et al. 2002, Wei, et al. 2002). This porous structure is presumed to result from the local corrosion action of OH^- radicals. The morphology of this layer changes with the surface treatment conditions and the applied heat treatment process (Wei, et al. 2002). Titanium oxide surfaces have amphoteric OH sites both in acidic and basic environments and symbolized by Ti-OH and OH. Lu et al. (Lu, et al. 2008) reported that certain treatments such as alkaline treatment increased Ti-OH groups. It should be noted that Ti-OH concentration should not be necessarily equal to that of OH on the same surface. Initially sodium titanate layer releases Na^+ ions by exchanging with H_3O^+ ions in the SBF, forming Ti–OH functional groups on the surface. Then, the reaction between the positively charged Ca^{2+} ions in the SBF and negatively charged Ti-OH functional group on the surface results in the formation of calcium titanate layer. Later, this layer is replaced by an amorphous CaP layer through the reaction between the positively charged Ti surface and the negatively charged phosphate ions in SBF. CaP layer finally transforms into a stable crystalline bonelike apatite. The function of the heat-treatment process applied following the alkali treatment was shown to increase the crystallization of the gel layer and to enhance the adhesion of sodium titanate layer to Ti surface, while it had no beneficial effect on the reduction of the induction period of the apatite formation in SBF (Kim, et al. 1997). The applied subsequent heat treatment process was previously shown to result in oxide formation on the surface (Kim, et al. 1997), which may increase the total oxygen content of Ti6Al4V particles.

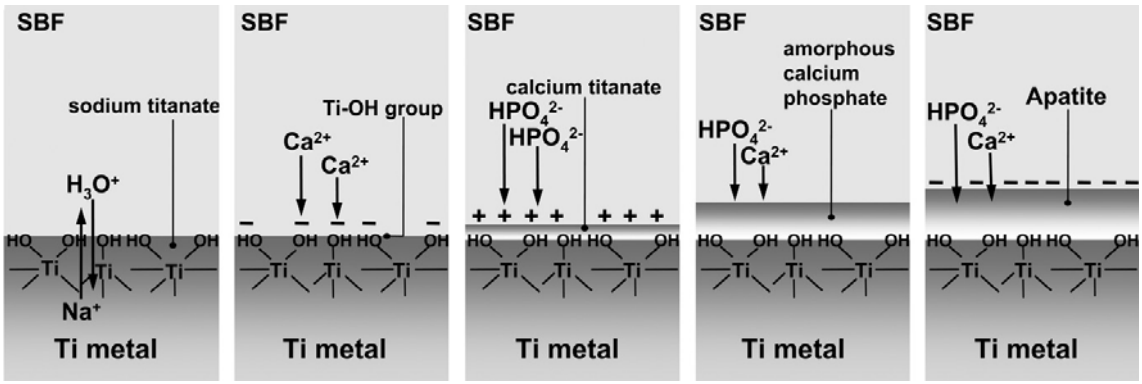

Figure 5.31. Schematic of the mechanism of apatite formation on Ti metal in SBF (Source: Kokubo 2008).

The coating layer homogeneity in porous structures can only be provided by inducing a homogenous coating layer both on the flat surfaces and on the cell wall particle surfaces. The alkali treatment forms a relatively thin and porous sodium titanate layer on the flat surfaces and on the particle surfaces interior of the pores of the foam specimen. This porous layer acts as a nucleating site when the foam specimen is immersed in SBF. Wen et. al.(Wen, et al. 1998a) reported that for apatite nucleation, a submicron pore size porous negatively charged titanium oxide was required. Early researcher (Boehm 1971, Healy and Ducheyne 1992) showed that in an aqueous environment certain amounts of OH^- groups were always present on the surface of titanium oxide. The amount of OH- groups on the surface of micro porous structure could be much larger than that of bulk structure because of the tremendous increased of surface area of the porous structure. The existence of abundant amount of OH^- groups on the surfaces was claimed to be the main reason for the increased bioactivity of sol-gel derived titanium oxide. Concave surfaces were further considered to be more advantageous to the nucleation of inorganic mineral phases than planar or convex surfaces in natural biomineralized system due to the capillary effect.

Acid etching ($HCl+H_2SO_4$) was previously shown to dissolve the natural oxide layer and form a relatively rough surface on Ti (Lu, et al. 2008). Nitric acid treatment, on the contrary, reduced the naturally formed oxide layer on the surface of Ti metal (Callen, et al. 1995, Lee, et al. 1998). The EDX analysis results of the foam specimens, taken both inside the pores and the flat section of the foam specimens are tabulated in Table 5.5. As is seen in Table 5.5, the qualitative oxygen content inside pores of the untreated foam specimens is higher than that of the flat section of the untreated foam

specimens. However, the nitric acid treatment increases the oxygen concentration on the flat section of the P1 and P2 foam specimens. On the other hand, oxygen content of the flat sections is nearly equal after the nitric acid treatment. In contrast, the oxygen content in interior part of the NAT P1 foam is relatively higher than that of NAT P2 foam specimen. In addition, nitric acid treatment reduced the oxygen content inside the pores of P2 foams, while increased the oxygen inside the pores of P1 foams.

Table 5.5. EDX analysis of the untreated and NAT P1 and P2 foam specimens.

Samples	Flat surface (at. %)				Interior of pore (at. %)			
	Ti	Al	V	O	Ti	Al	V	O
Ti-1	65.72	9.41	2.22	22.65	69.57	8.96	4.06	17.41
Ti-2	65.83	9.35	2.30	22.52	50.14	9.47	1.59	38.81
NA-1	74.62	9.78	3.21	12.38	59.13	10.96	1.98	27.94
NA-2	76.39	9.45	3.79	10.37	78.41	8.5	2.30	10.79

Nitric acid treatment was previously shown not to affect the surface roughness, but increased the surface energy (Lu, et al. 2007). In the present study, the AFM surface roughness values of NAT foam specimens are nearly the same with those of untreated foam specimen, agreeing with the results of Lu et.al (Lu, et al. 2007) and Sittig et. al. (Sittig, et al. 1999). This further proves the non preferential etching and low dissolution rates of α and β phase in nitric acid. Barrere et. al. (Barrere, et al. 2004) showed that the surface topography of Ti6Al4V had no affect on the heterogeneous nucleation of CaP, while the growth and mechanical attachment of CaP coating strongly depended on the surface roughness; a rougher surface (R_{max}>0.1 μm) was much more effective for the CaP mechanical attachment to the surface.

The surface roughness parameters (Ra, Rq and SAD) of NAT P1 and P2 foams as function of immersion time are shown in Figures 5.32(a) and (b), respectively. The specimen surface roughness decrease in the first three days of SBF immersion. The initial reaction of Ti metal with the SBF solution is the formation of the Ti-OH groups on the surface, which is proposed to reduce the surface roughness. Then, the surface roughness increases rapidly to 70 nm in P1 and 40 nm in P2 foam specimen after 7-day of SBF immersion. The surface roughness values, Ra and Rq, became constant after 7-day of SBF immersion with a surface value of 35 nm in P2 foam specimen and increase

to 80 nm in P1 foam specimen after 14-day of SBF immersion. In the first 3-day of SBF immersion, the decrease in the surface roughness values may be attributed to the formation of an amorphous CaP layer or a slow etching action of the SBF solution. Furthermore, GIXRD and SEM analysis are found to be insufficient to analyze this very thin amorphous structure formed on the surface.

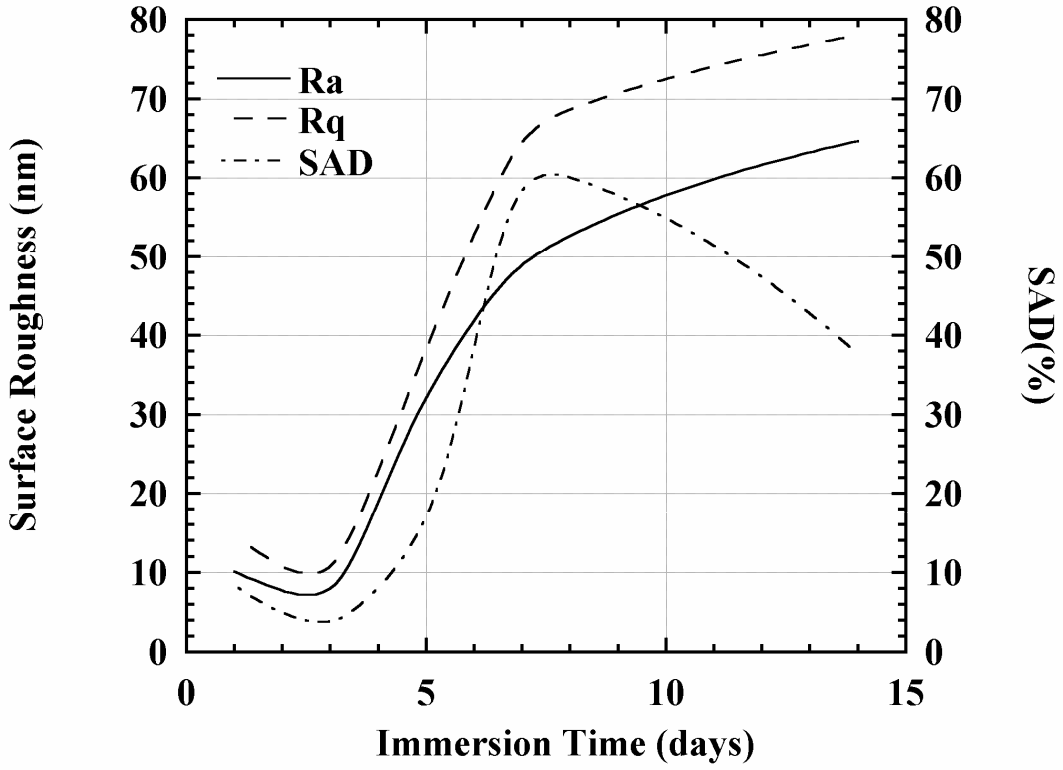

(a)

Figure 5.32. Surface roughness analysis of NAT foam specimens, (a) P1 and (b) P2 foam specimen.

(cont. on next page)

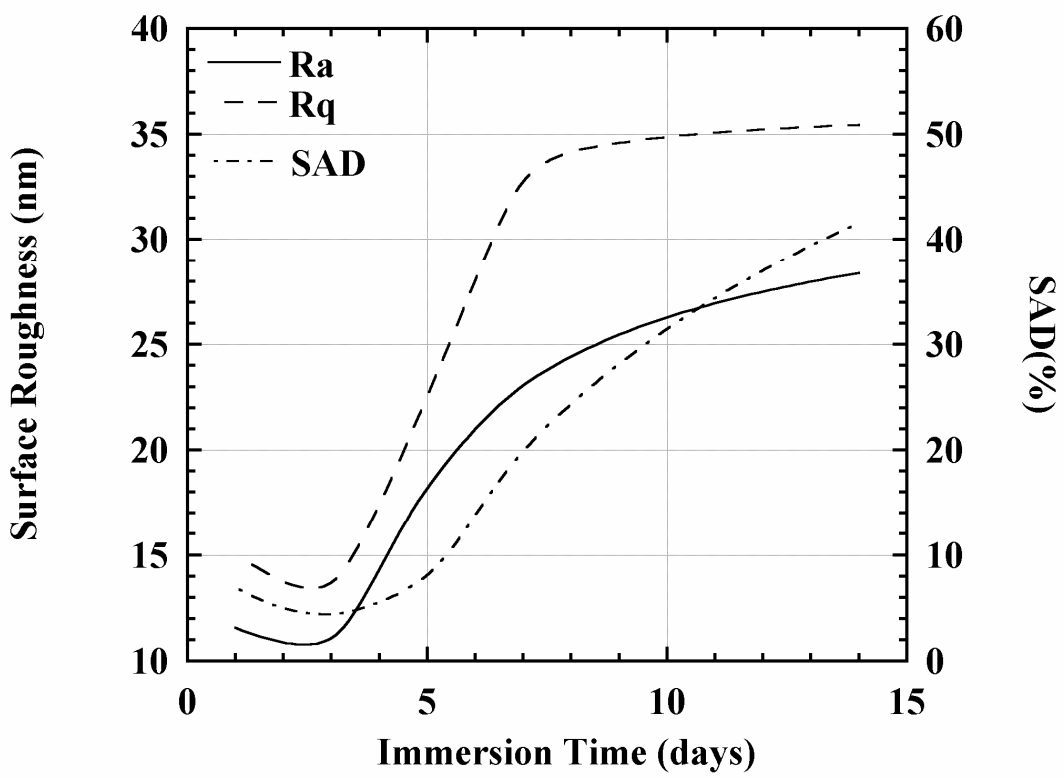

(b)

Figure 5.32. (cont.)

Alkali treatment induces smaller crystal size of CaP layer on the surface than nitric acid treatment and acid etching, which is reflected by the increased intensity of (002) diffraction line in AT specimen shown in Figure 5.8(a). The reduced crystal size of CaP layer of AT foam specimen is also seen in the AFM micrographs shown in Figures 5.10(a) and (b). This is partly attributed to the increased number of heterogeneous nucleation sites in AT foam specimen surfaces. Chen et. al. (Chen, et al. 2009a) indicated that the alkali surface treatment led to increase the surface energy, while decreasing the particle size of the foam. The significant effect of NAT on Ti6Al4V foam specimens is the increase of the surface energy, particularly the polar component of the surface energy.

CaP formation on the Ti surface in supersaturated aqueous solutions is a heterogeneous nucleation process. In classical nucleation theory, the critical free energy $\Delta G^{ce:\sup>ce:\sup het}$ for heterogeneous nucleation depends on the supersaturation of the solution (S), the temperature (T), the surface energies of the substrate (σ_s) and the nucleolus (σ) and the interfacial energy of the substrate/nucleolus (σ_i) (Markov 1995, Mullin 2001) as,

$$\Delta G^{*}_{heter} = \Delta G^{*}_{\text{hom}} \frac{\Delta\sigma}{2\sigma} = \frac{16\pi v^2\sigma^2}{3k^2T^2(\ln S)^2} \cdot \frac{\sigma + \sigma_i - \sigma_s}{2\sigma} \tag{5.2}$$

where, k is the Boltzman's constant; $\Delta\sigma$ is the net interfacial energy and $\Delta G^{*}_{\text{hom}}$ is the critical free energy for the nucleation. Reduction in the critical energy resulting in a low energy barrier heterogeneous nucleation can be achieved by increasing the supersaturation and reducing the net interfacial energy. In porous structures, the nucleation theory is modified as,

$$\Delta G = -RT \ln S + \sigma A \tag{5.3}$$

where σ is the net interfacial energy of nucleation and A is the apatite particle surface area. Equation 5.3 may be used to explain the duration of complete CaP formation of foam specimens in SBF. Complete CaP coating is found 14-day for AT P1 foam specimen and 7-day for AT P2 foam specimen. Nitric acid treatment decreased the time for the formation of CaP layer on the flat surface and interior part of the pores to 5-day for NAT P2 foam specimen. However, the time for complete CaP formation in NAT P1 foam specimen did not change. Two parameters are different between the foam specimens; the energy of the substrate (σ_s) and the particle surface area. The specific surface area of P1 and P2 foam particles was 0.0694 m^2/g and 0.112 m^2/g, respectively. This shows that the SSA of the P2 foam is higher than that of P1 foam specimen, resulting in higher surface area for the CaP formation. The higher surface area will lead to higher adsorption rate to the surface, leading to earlier CaP formation. The typical bond structure of the CHA consists of bands at 875, 1410 and 1420 cm^{-1}. The presence of bond at 1550 cm^{-1} in FTIR results shows that CHA is B-type. In all experiments, since the carbonate content of SBF was fixed constant, B-type CHA formed.

CHAPTER 6

THE OPTMIZATION OF SURFACE TREATMENT

6.1. Introduction

Titanium and its alloys are widely used in biomedical applications because of their good biocompatibility combined with good mechanical properties (Katti 2004). The native oxide layer, which provides biocompatibility, forms on the surface of Ti spontaneously (Callen, et al. 1995). The clinical success of the implants is not only associated with the biocompatibility but also osseointegration, which is described as the direct structural and functional connection between living bone tissue and the surface of an artificial implant. This biological fixation is considered as a prerequisite for a successful implantation. Bonelike apatite coating is usually applied to the surface of Ti in order to overcome the fixation problems (Narayanan, et al. 2008). The applied chemical surface treatment methods such as alkali treatment, nitric acid treatment and acid etching further improve bonelike apatite coating on the implant surface; hence let the formation of a bioactive surface (Faure, et al. 2009, Jonasova, et al. 2004, Kim, et al. 1996, Liang, et al. 2003, Lu, et al. 2007, Vanzillotta, et al. 2006). It is noted that the most widely used chemical surface treatment technique in order to improve the bioactivity of Ti metal is the alkali treatment. The alkali surface treatment is usually performed in a 10M NaOH solution at 60°C for 24 h. Some researchers applied a subsequent heat treatment after alkali treatment to provide further improvement in bonelike apatite coating (Kim, et al. 1997, Lee, et al. 2002). In addition, Ti and Ti6Al4V implants are generally subjected to a passivation treatment to minimize the corrosion in biological environment. The ASTM-F86 standard of the surface passivation refers to a 20-40% nitric acid containing solution treatment. Although, a variety of studies were conducted on the nitric acid passivation of Ti surfaces; few of these have been carried out on the biomimetic CaP deposition ability of the nitric acid surface treatment. It is also noted that there have been few studies on the optimization of surface treatment with respect to the formation of CaP coating on the surface of Ti metal. Wei et al. (Wei, et al. 2002) conducted an optimization study on AT Ti6Al4V

alloy. The optimization parameter selected included the molarity of solution, surface treatment temperature and the heat treatment temperature. An optimum heat treatment temperature of 600°C was proposed based on the bonding strength of the apatite to the surface. In this part of the thesis, the optimum conditions of nitric acid and alkali surface treatment for the biomimetic CaP coating of open cell Ti6Al4V foams were investigated using the response surface methodology (RSM).

6.2. Experimental

6.2.1. Materials

The samples used for the optimization study were Ti6Al4V foam specimens prepared from P1 and P2. Small square cross-section plate-like specimens (10x10x3 mm^3) were used for in-vitro investigations. These samples were cut from the sintered Ti6Al4V foam plates. The specimens' square cross-sections were then ground sequentially using 120, 240, 320, 600, 800, 1200 and 2400 grit SiC papers. The foam specimens were cleaned ultrasonically in acetone, then in ethyl alcohol and finally in deionized water for a duration of 15 min for each solution before in-vitro tests.

6.2.2. Methodology

RSM is a useful technique for modeling the effect of variables on the response. The objective of this methodology is to optimize and identify the most significant variables. The most widely used Box Bhenken design cube technique in RMS is shown in Figure 6.1. In this technique, there are three variables (A, B and C) and the responses are to be determined experimentally shown on the cube as the points. The points are selected at the mid points of the maximum and minimum values of variables and also at the center of the cube. The numbers at each data point represent the number of experiments to be performed.

The selected three design variables and their centers and variations are tabulated in Tables 6.1 and 6.2 for nitric acid and alkali treatment, respectively. The selected variables are as follows X_1: molarity or acid concentration (M), X_2: temperature of the

solution (T), and X_3: time (t), duration of the surface treatment. The Box Bhenken design was implemented using Design Export Software®. The minimum values of nitric acid concentration and treatment temperature and time were selected as 20%, 20 °C and 1h, dictated by the ASTM-F86 standard of the surface passivation. The maximum values were, 65% (the available maximum nitric acid concentration), 60°C and 5 h. The range of molarity, temperature and time of alkali treatment were selected between 1-10M, 20-60 °C, and 1-24 h, respectively.

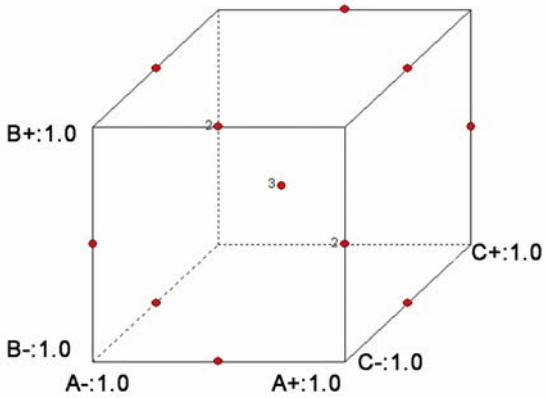

Figure 6.1. Box Bhenken design cube.

Table 6.1. Factors and levels of the experimental design for nitric acid treatment.

	Factor		Centre	Variation
(X_1)	HNO_3 molarity	Vol.%	42.5	22.5
(X_2)	Temperature	°C	40	20
(X_3)	Time	Min	180	120

Table 6.2. Factors and levels of the experimental design for alkali treatment.

	Factor		Centre	Variation
(X_1)	Molarity	M	5.5	4.5
(X_2)	Temperature	°C	40	20
(X_3)	Time	h.	12.5	11.5

For each response, 15 experiments were performed, 12 of them were at the corners and 3 of them at the center of the cube. These data points were used to estimate the coefficients of a reduced second order model, which provided a link between the response (CaP deposition mass) and the variables. The proposed response function can be represented as,

$$Y = b_0 + b_1X_1 + b_2X_2 + b_3X_3 + b_{12}X_{12} + b_{13}X_{13} + b_{23}X_{23} + b_{11}X_1^2 + b_{22}X_2^2 + b_{33}X_3^2 \quad (6.1)$$

where:

$\hat{Y}$: response function,

X_j: coded variable of the system;

b_0: model constant,

b_j: first degree coefficient,

b_{jk}: cross-products coefficients and

b_{jj}: quadratic coefficient

The model coefficients b_0, b_j, b_{jk} and b_{jj} were predicted by the least square fitting of the experimental results obtained at the design points. As in the fitting of any linear model, the analysis of the residuals in a regression model determines the adequacy. This can be done by a normal probability plot, a plot of residuals versus fitted values. This plot must exhibit the absence of any serious violation of the normality assumption.

6.2.3. In Vitro Bioactivity Test

The SBF solution for in-vitro tests was prepared according to the protocol (Bayraktar and Tas 1999, Jalota, et al. 2007a) by dissolving the following analytical reagents in 1 L of deionized water: NaCl, $NaHCO_3$, KCl, Na_2HPO_4, $MgCl_2.6H_2O$, $CaCl_2.2H_2O$, Na_2SO_4 and trishydoxmethylaminomethane. Each foam specimen was placed into a polypropylene tube contained 6 ml SBF solution. The tubes were then kept at 37°C for 14-day in an incubator. The SBF solution of the tubes was refreshed every 24 h. The weight of the specimens before the test or after the surface treatment and after

the test was measured. The difference between these two measurements is the CaP precipitation mass, Δm.

6.3. Results and Discussion

The gravimetric analysis results of the bioactivity tests for the designed response surface experiments are tabulated in Tables 6.3 and 6.4 for nitric acid and alkali treatment, respectively. The Δm values of NAT P1 foam vary between 0.3 and 3.05 mg and NAT P2 foam between 0.45 to 3.05 mg. The Δm values of AT P1 foam as tabulated in Table 6.4 vary between 0.0 and 4.1 mg and AT P2 foam between 0.0 to 2.8 mg. The response model of NAT P1 foam is

$$Y=5.250463-0.04519X_1-0.15014X_2-0.0133X_3+0.000944X_1X_2 +5.56x10^{-05}X_1X_3+0.000115X_2X_3-0.00015X_1^2+0.001438X_2^2+2.26x10^{-05}X_3^2$$

and NAT P2 foam is,

$$Y=5.367959-0.0891X_1-0.15372X_2-0.0095X_3+0.001639X_1X_2 +9.72x10^{-05}X_1X_3+0.000151X_2X_{3+}0.000151X_1^2+0.001047X_2^2+6.51x10^{-06}X_3^2$$

Normal probability vs. residual graphs of NAT P1 and P2 foam are shown in Figures 6.2(a) and (b), respectively. Few data points of P1 foam seen in Figure 6.2(a) are not on the fitting line of the model residuals, showing a higher noise in P1 foam data than P2 foam data. The data points of NAT P2 foam show a good correlation with the fitting line of the model residuals as depicted in Figure 6.2(b)). Figures 6.3(a) and (b) show the design cube of NAT P1 and P2 foam, respectively. On the design cube, the responses of points which are not experimentally determined but predicted from the model are also shown at the corners of the cube.

Table 6.3. Factors and response of NAT P1 and P2 foam.

Run Order	Molarity (%)	Temperature (°C)	Time (min.)	Δm (mg), P1	Δm (mg), P2
1	20	40	60	1.6	0.9
2	20	40	300	1	0.7
3	65	60	180	1.8	3.05
4	42.5	20	60	0.4	0.45
5	65	20	180	0.4	0.45
6	20	60	180	0.85	0.45
7	42.5	40	180	0.5	0.65
8	65	40	300	0.3	1.35
9	42.5	60	300	3.05	2.6
10	42.5	40	180	0.6	0.65
11	42.5	20	300	1	0.85
12	42.5	60	60	1.35	0.75
13	42.5	40	180	0.55	0.65
14	20	20	180	1.15	0.8
15	65	40	60	0.3	0.5

Table 6.4. Factors and response of AT P1 and P2 foam.

Run Order	Molarity (%)	Temperature (°C)	Time (h)	Δm (mg), P1	Δm (mg), P2
1	10	20	12.5	0	0
2	5.5	20	1	0	0
3	5.5	40	12.5	3.5	0
4	5.5	40	12.5	4.1	0.2
5	5.5	40	12.5	2.8	1
6	1	40	24	0.7	0.9
7	1	20	12.5	0.2	0
8	5.5	20	24	0	0
9	10	60	12.5	1.5	0.7
10	1	60	12.5	0.9	1.9
11	5.5	60	1	4.5	0
12	10	40	24	2.8	1.2
13	5.5	60	24	0	2.8
14	10	40	1	1.2	0
15	1	40	1	0	0

The variances (ANOVA) of NAT P1 and P2 foam are further tabulated in Table 6.5. The R^2 values of the quadratic models (R^2 = Sum of squares attributed to the regression/total sum of squares) are 0.72 for P1 and 0.92 for P2 foam. About 80% of the variability in the data for each response on the average is presented by the models. Combined with the satisfactory residual analysis, each model has relatively good fitting

with the data. In statistical testing, the p-value is the probability of obtaining a test statistic at least as extreme as the one that is actually observed. The lower the p-value, the more significant the result is. The temperature ($p<0.0762$) is seem to be the most significant factor for NAT P1 foam, while the temperature ($p<0.0134$) and time ($p<0.0529$) are the most significant factors for NAT P2 foam.

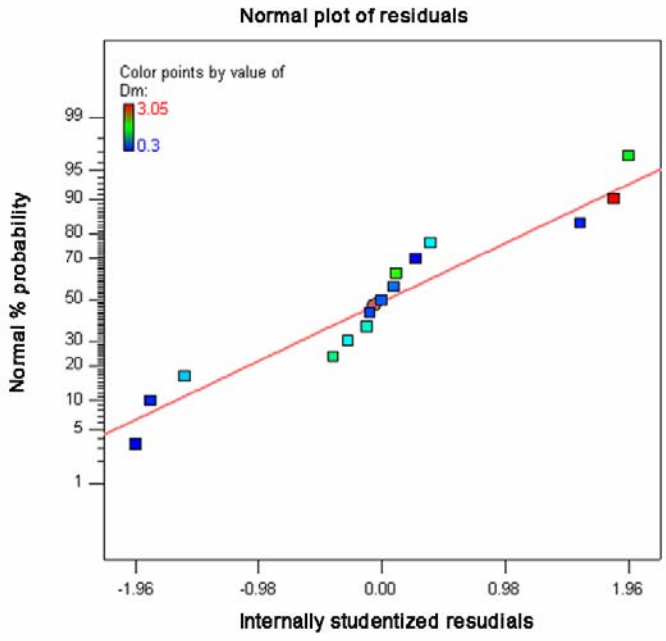

(a)

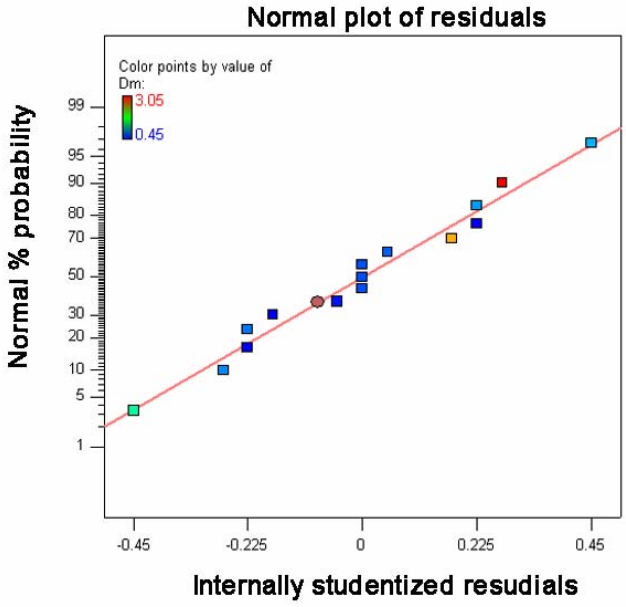

(b)

Figure 6.2. Normal plot of probability vs. residual graph of NAT (a) P1 and (b) P2 foam.

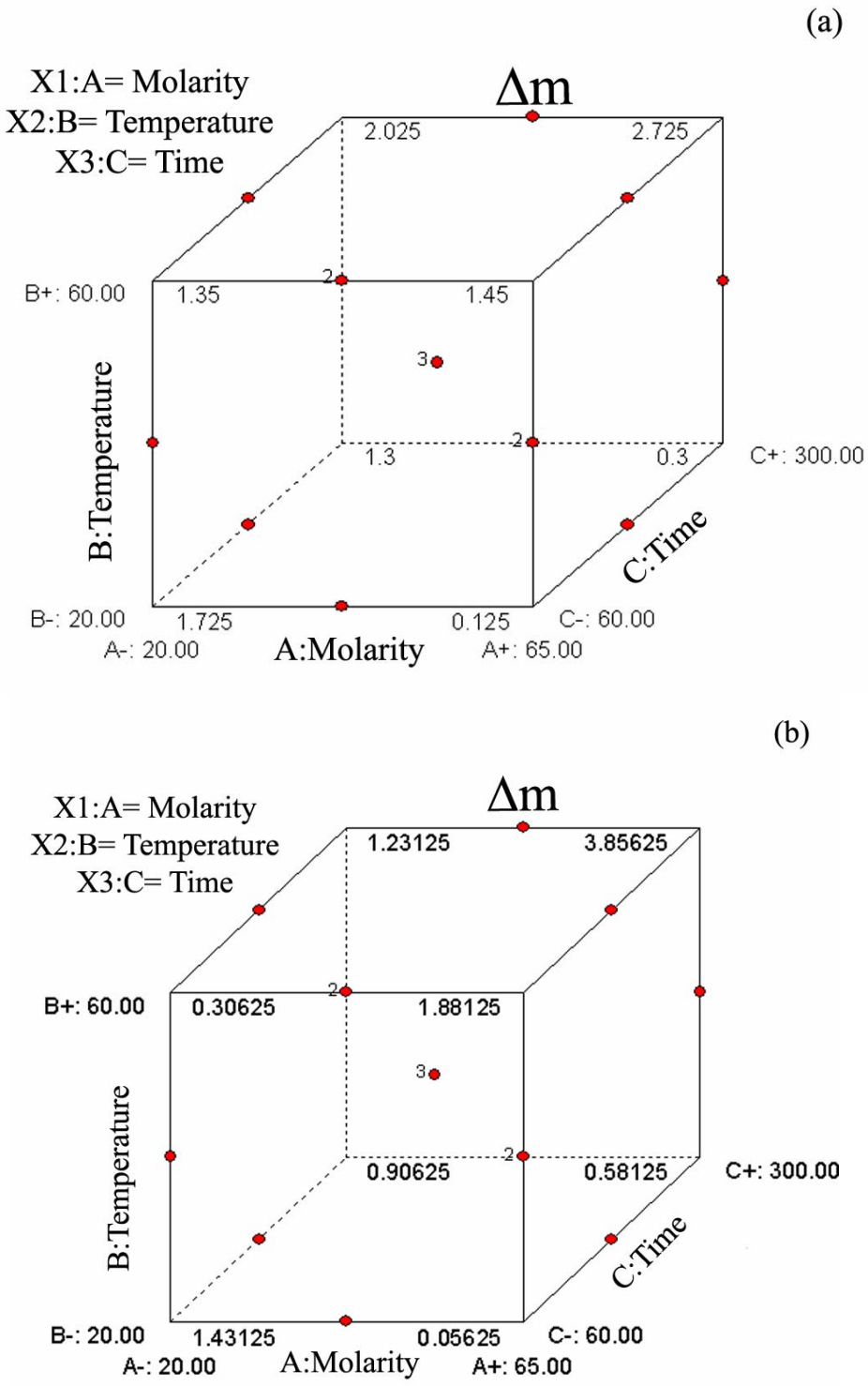

Figure 6.3. Design cube of NAT (a) P1 and (b) P2 foam.

Table 6.5. ANOVA table for the response of NAT P1 and P2 foam.

		Effect	Sum of Squares	df	Mean Square	F Value	p> F
P1 Foam	R-squared=0.72 (0.61)*	X_1-Molarity	0.405	1	0.405	0.95858	0.3725
		X_2-Temperature	2.10125	1	2.10125	4.973373	0.0762
		X_3-Time	0.36125	1	0.36125	0.85503	0.3976
		X_1X_2	0.7225	1	0.7225	1.710059	0.2479
		X_1X_3	0.09	1	0.09	0.213018	0.6638
		X_2X_3	0.3025	1	0.3025	0.715976	0.4361
		X_1^2	0.020769	1	0.020769	0.049158	0.8333
		X_2^2	1.220769	1	1.220769	2.889395	0.1499
		X_3^2	0.39	1	0.39	0.923077	0.3808
		Residual	2.1125	5	0.4225		
		Lack of Fit	2.1075	3	0.7025	281	0.0035
		Pure Error	0.005	2	0.0025		
		Cor Total	7.681	14			
P2 Foam	R-squared=0.92 (0.86)*	Effect	Sum of Squares	df	Mean Square	F Value	p> F
		X_1-Molarity	0.78125	1	0.78125	4.734848	0.0815
		X_2-Temperature	2.31125	1	2.31125	14.00758	0.0134
		X_3-Time	1.05125	1	1.051125	6.371212	0.0529
		X_1X_2	2.175625	1	2.175625	13.18561	0.0150
		X_1X_3	0.275625	1	0.275625	1.670455	0.2527
		X_2X_3	0.525625	1	0.525625	3.185606	0.1344
		X_1^2	0.052067	1	0.052067	0.315559	0.5985
		X_2^2	0.647452	1	0.647452	3.923951	0.1045
		X_3^2	0.032452	1	0.032452	0.196678	0.6759
		Residual	0.825	5	0.165		
		Lack of Fit	0.825	3	0.275		
		Pure Error	0	2	0		
		Cor Total	8.632333	14			

The response surface 3D plot of molarity-temperature, molarity-time and temperature-time of NAT P1 and P2 foams are shown sequentially in Figures 6.4(a) and (b), 6.5(a) and (b) and 6.6(a) and (b). As is seen in Figures 6.4(a) and 6.6(a) high temperatures lead to higher degrees of CaP precipitation, implying that the temperature is the main factor which significantly influences the response function of NAT P1 foam. The molarity and time have insignificant effects on the response of NAT P1 foam within the studied ranges of the variables. As is seen in Figures 6.4(b) and 6.6(b) high temperatures lead to higher degrees of CaP precipitation in NAT P2 foam, similar to NAT P1 foam. The most significant factor is also temperature in NAT P2 foam. While, the molarity and time are more effective on the response of NAT P2 foam as compared with NAT P1 foam.

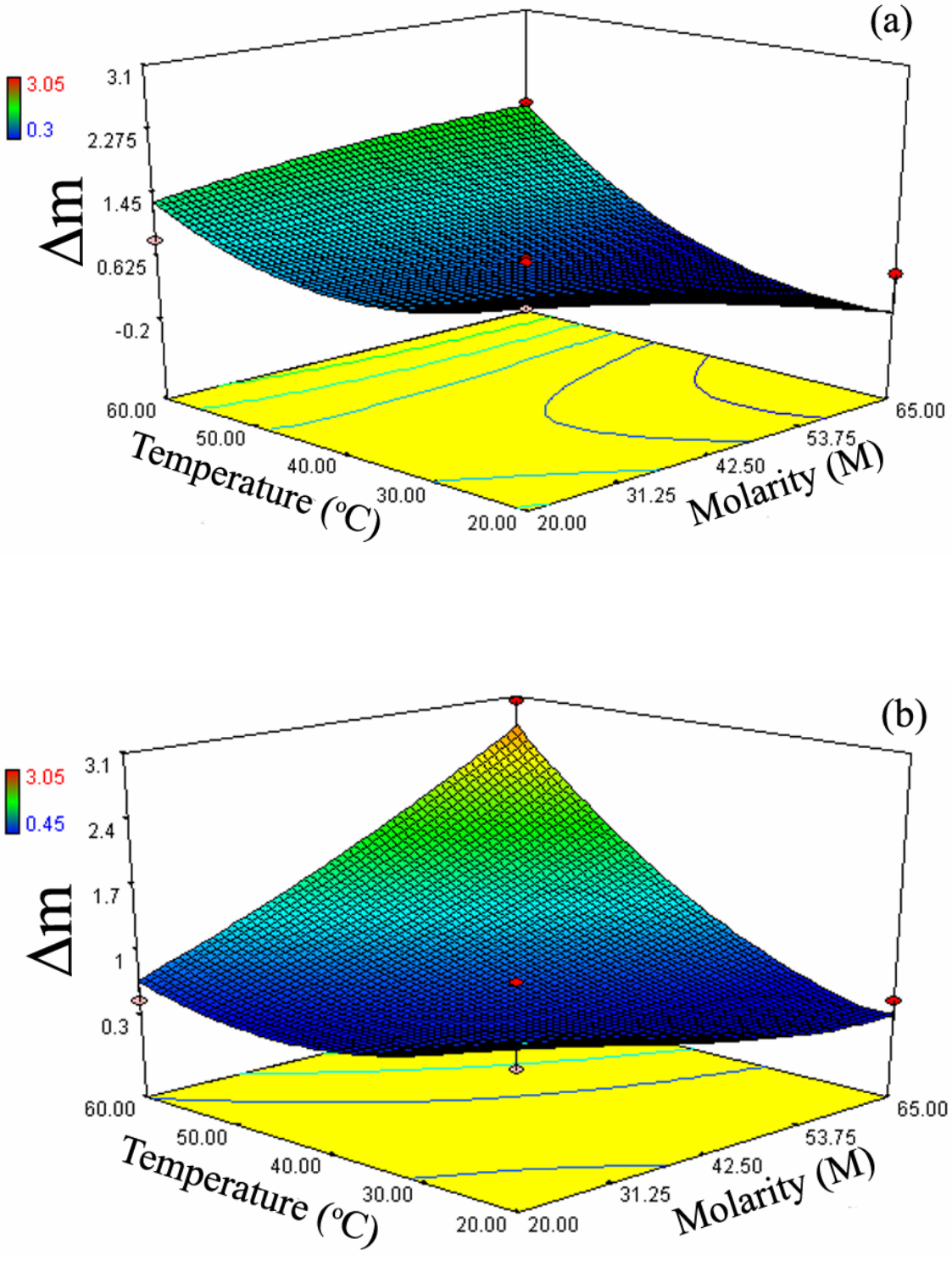

Figure 6.4. The response surface 3D plot of molarity-temperature of NAT (a) P1 and (b) P2 foam.

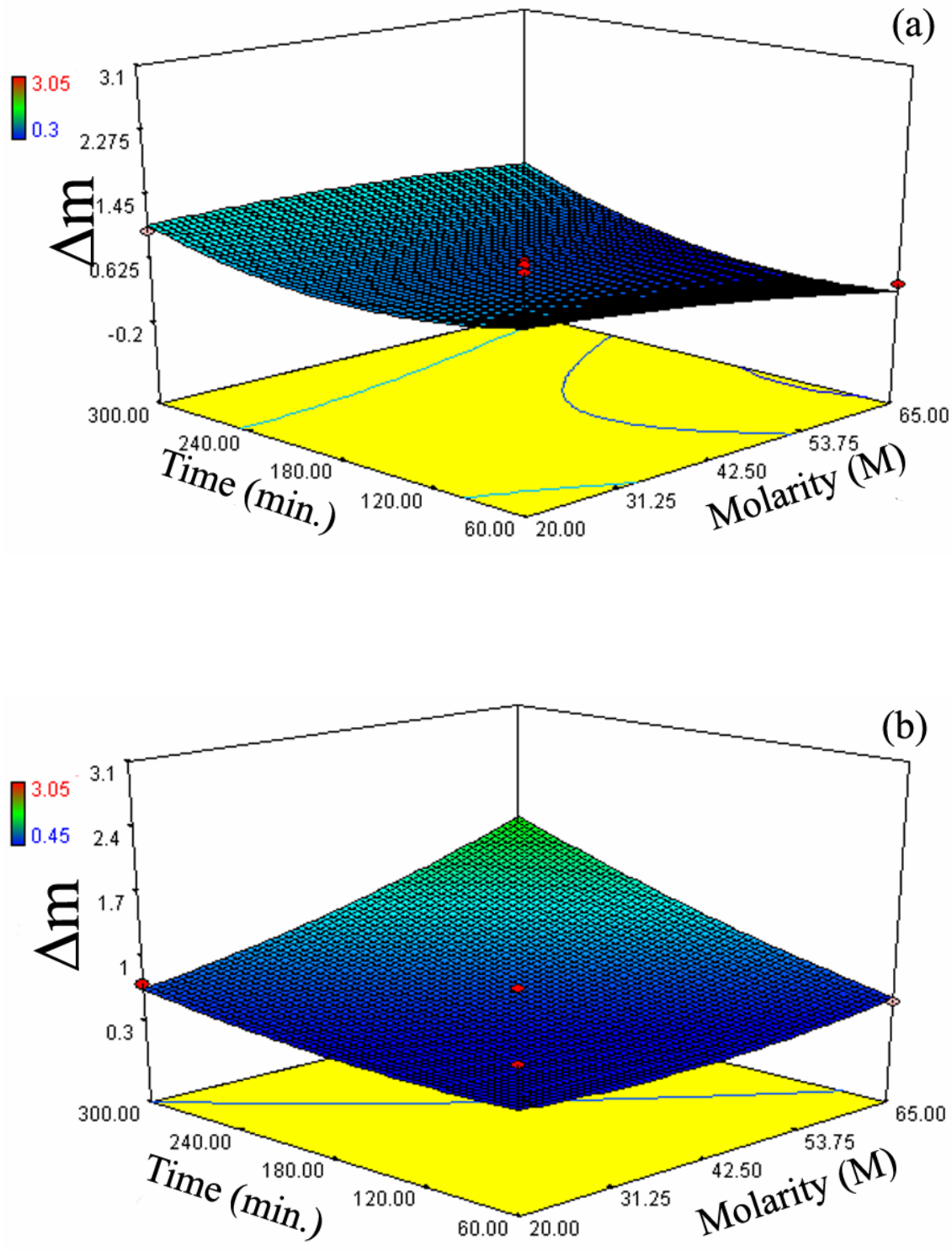

Figure 6.5. The response surface 3D plots of molarity-time of NAT (a) P1 and (b) P2 foam.

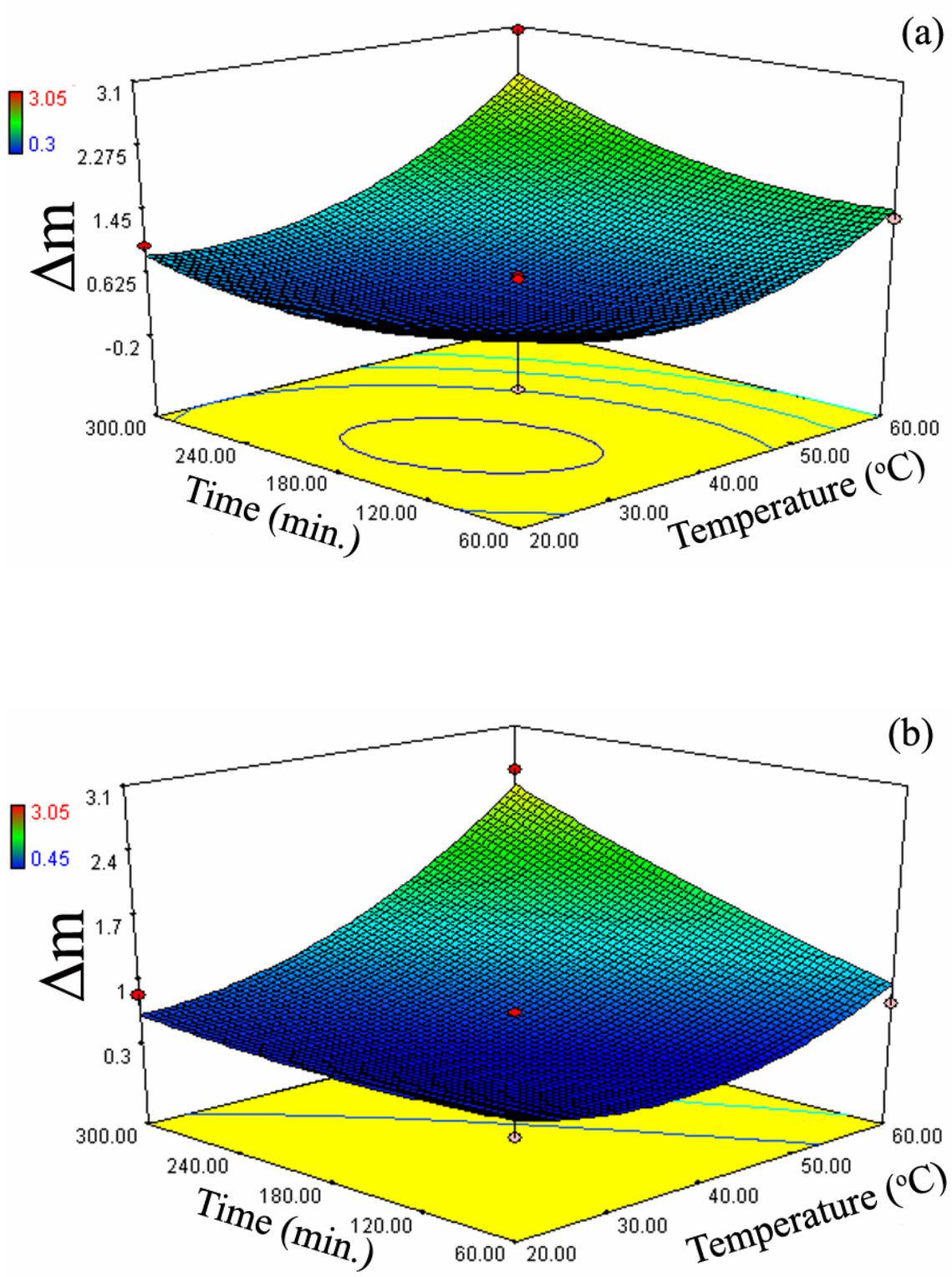

Figure 6.6. The response surface 3D plots of temperature-time of NAT (a) P1 and (b) P2 foam.

The estimated models of AT P1 and P2 foam are given sequentially by the following equations

$$Y=-9.00552+0.710981X_1+0.377461X_2+0.319534X_3+0.002222X_1X_2+0.004348X_1X_3-0.00489X_2X_3-0.06831X_1^2-0.00358X_2^2-0.00687X_3^2$$

and

$$Y=0.41918+0.069847X_1-0.02846X_2-0.09299X_3-0.003333X_1X_2+0.001449X_1X_3+0.003043X_2X_3+0.001852X_1^2+0.000531X_2^2+0.000662X_3^2$$

Normal probability vs. residual graph of AT P1 and P2 foam are shown in Figures 6.7(a) and (b), respectively. Similar to NAT P1 and P2 foam, the noise in the data of AT P2 foam is found relatively lower than those of AT P1 foam. Figures 6.8(a) and (b) further show the design cube of the AT P1 and P2 foam, respectively. Analyses of variance (ANOVA) of AT P1 and P2 foam are further tabulated in Table 6.6. The R^2 values of the quadratic models of AT P1 and P2 foam equal to 0.77 and 0.91, respectively. About 70% of the variability in the data of P2 foam and 90% of the variability in the data of P1 foam response are represented by the models. In addition, based on the ANOVA, the most significant factor for AT P1 ($p<0.1261$) and P2 ($p<0.065$) is the temperature.

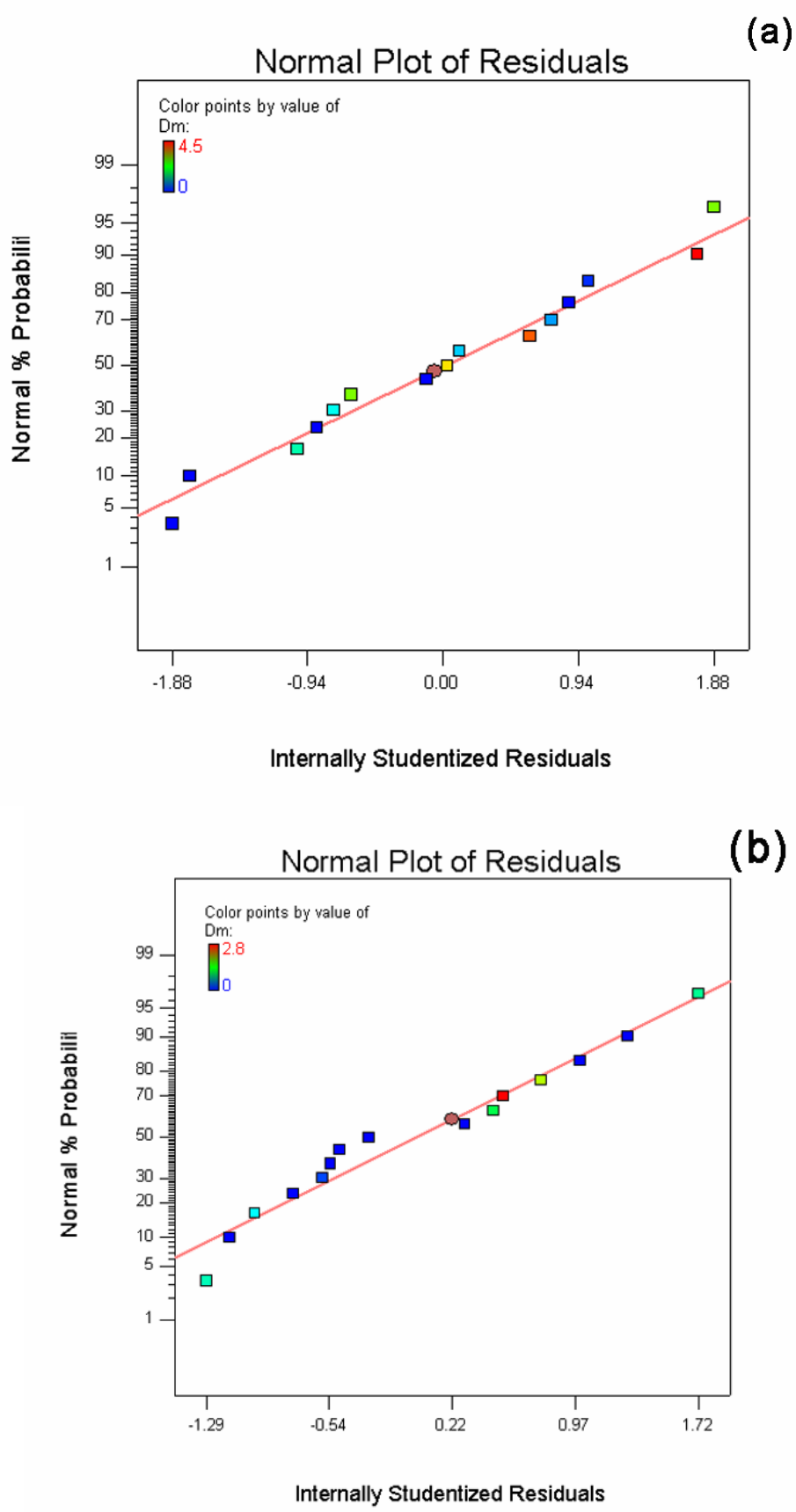

Figure 6.7. Normal plot of probability vs. residual graph of AT (a) P1 and (b) P2 foam.

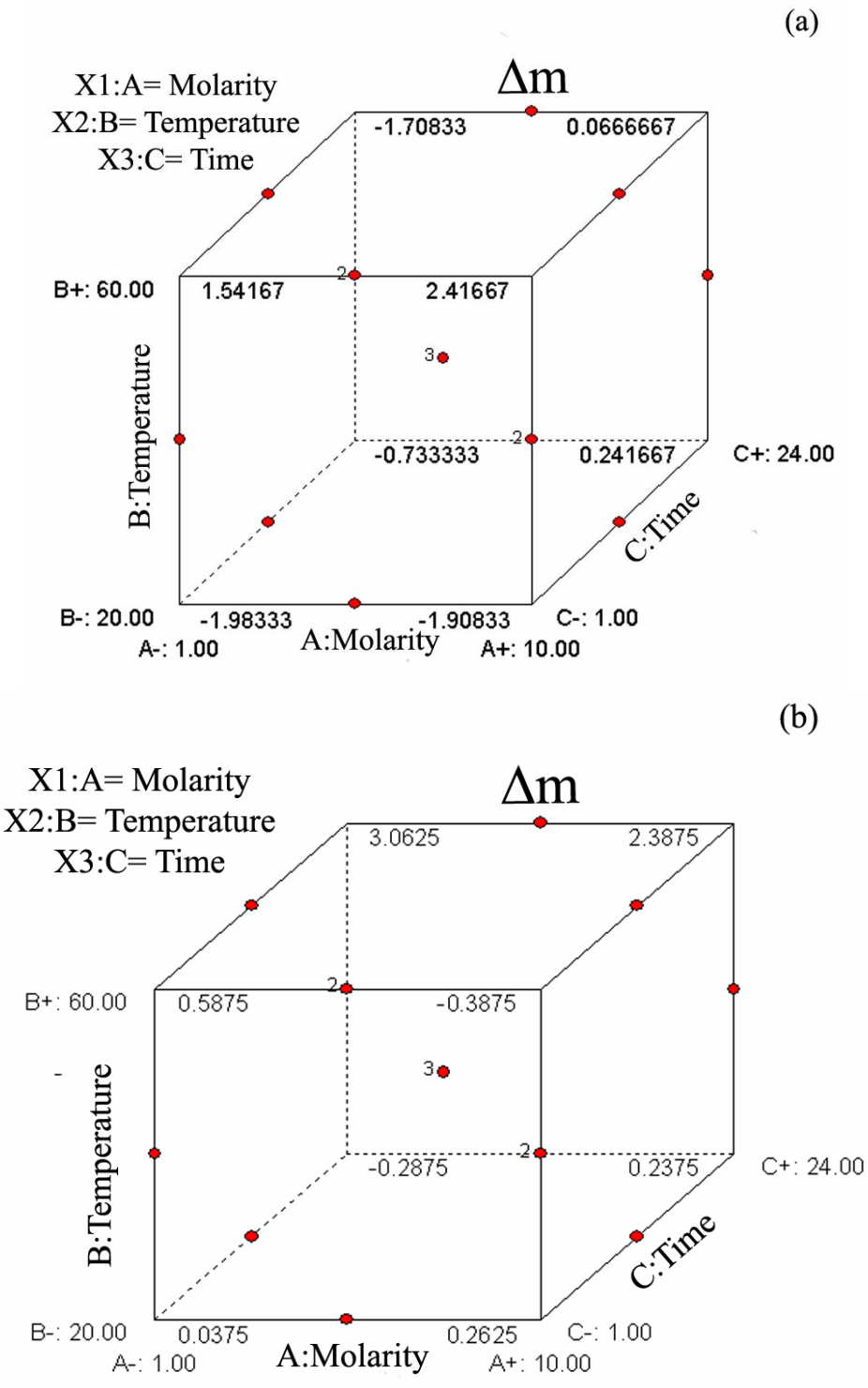

Figure 6.8. Design cube of AT (a) P1 and (b) P2 foam.

Table 6.6. ANOVA table for the responses of AT P1 and P2 foam.

		Effects	Sum of Squares	df	Mean Square	F Value	p > F
P1 Foam	R-squared=0.77 (0.66)*	X_1-Molarity	1.71125	1	1.71125	1.026031	0.3576
		X_2-Temperature	5.61125	1	5.61125	3.364395	0.1261
		X_3-Time	0.605	1	0.605	0.362746	0.5733
		X_1X_2	0.16	1	0.16	0.095933	0.7693
		X_1X_3	0.2025	1	0.2025	0.121415	0.7417
		X_2X_3	5.0625	1	5.0625	3.035375	0.1419
		X_1^2	7.065641	1	7.065641	4.236419	0.0946
		X_2^2	7.585641	1	7.585641	4.548201	0.0861
		X_3^2	3.046410	1	3.046410	1.826567	0.2345
		Residual	8.339167	5	1.667833		
		Lack of Fit	7.4925	3	2.4975	5.899606	0.1484
		Pure Error	0.846667	2	0.423333		
		Cor Total	37.164	14			
P2 Foam	R-squared=0.91 (0.87)*	Effects	Sum of Squares	df	Mean Square	F Value	p > F
		X_1-Molarity	0.10125	1	0.10125	0.557851	0.4887
		X_2-Temperature	3.645	1	3.645	20.08264	0.0065
		X_3-Time	3.00125	1	3.00125	16.53581	0.0097
		X_1X_2	0.36	1	0.36	1.983471	0.2181
		X_1X_3	0.0225	1	0.0225	0.123967	0.7391
		X_2X_3	1.96	1	1.96	10.7989	0.0218
		X_1^2	0.005192	1	0.005192	0.028608	0.8723
		X_2^2	0.166731	1	0.166731	0.918627	0.3819
		X_3^2	0.028269	1	0.028269	0.155753	0.7094
		Residual	0.9075	5	0.1815		
		Lack of Fit	0.3475	3	0.115833	0.41369	0.7630
		Pure Error	0.56	2	0.28		
		Cor Total	10.184	14			

The response surface 3D plots of molarity-temperature, molarity-time and temperature-time of AT P1 and P2 foams are shown sequentially in Figures 6.9(a) and (b), 6.10(a) and (b) and 6.11(a) and (b). As seen in Figures 6.9(a), 6.10(a) and 6.11(a), temperature, molarity and time are effective in CaP deposition; higher molarity levels reduces CaP deposition after a maximum CaP deposition in AT P1 foam, while higher levels of temperature and time increases CaP deposition. In AT P2 foam, time and temperature are very effective in increasing CaP deposition. Higher levels of molarity slightly increase CaP deposition in AT P2 foam.

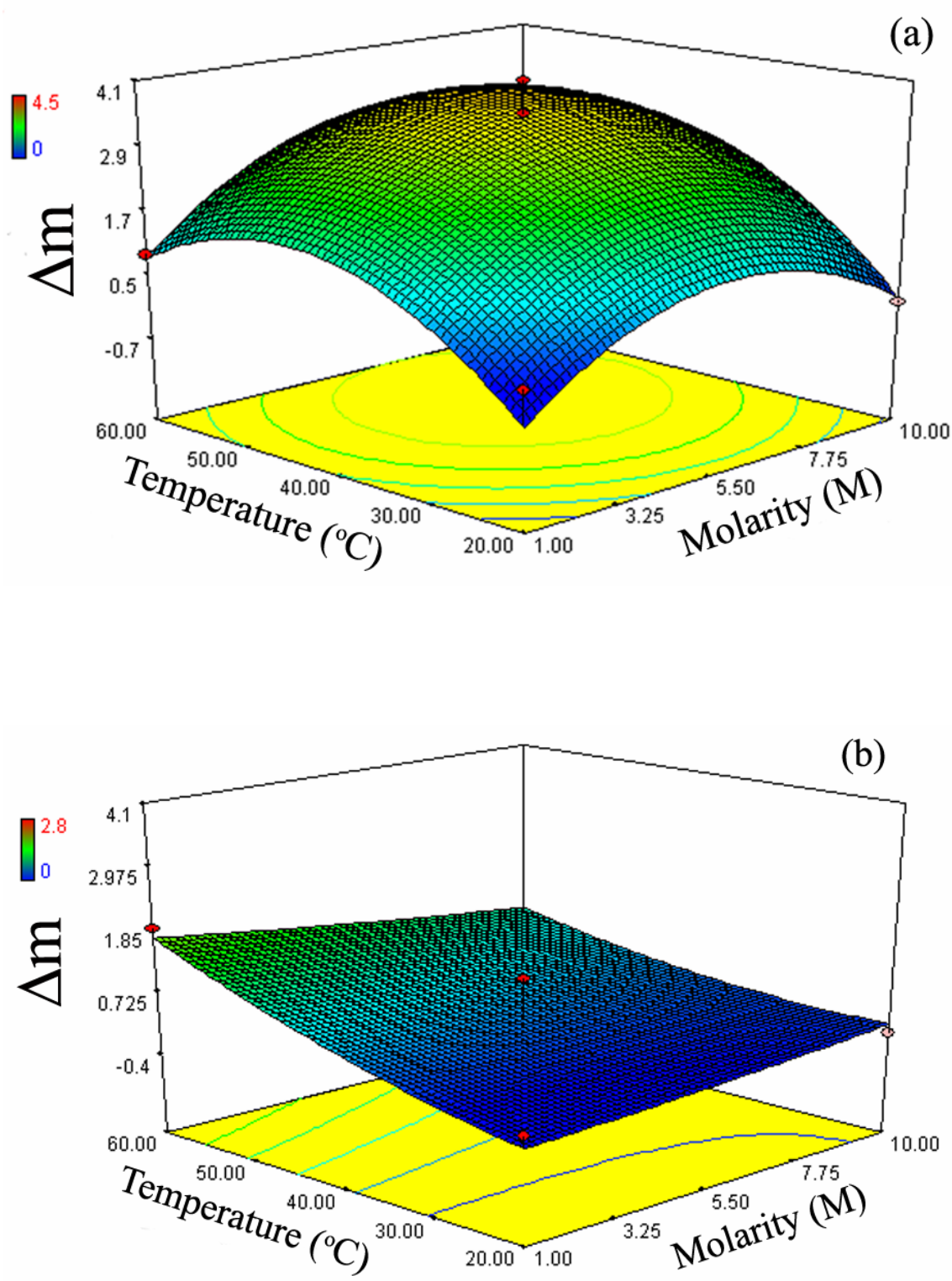

Figure 6.9. The response surface 3D plots of molarity-temperature of AT (a) P1 and (b) P2 foam.

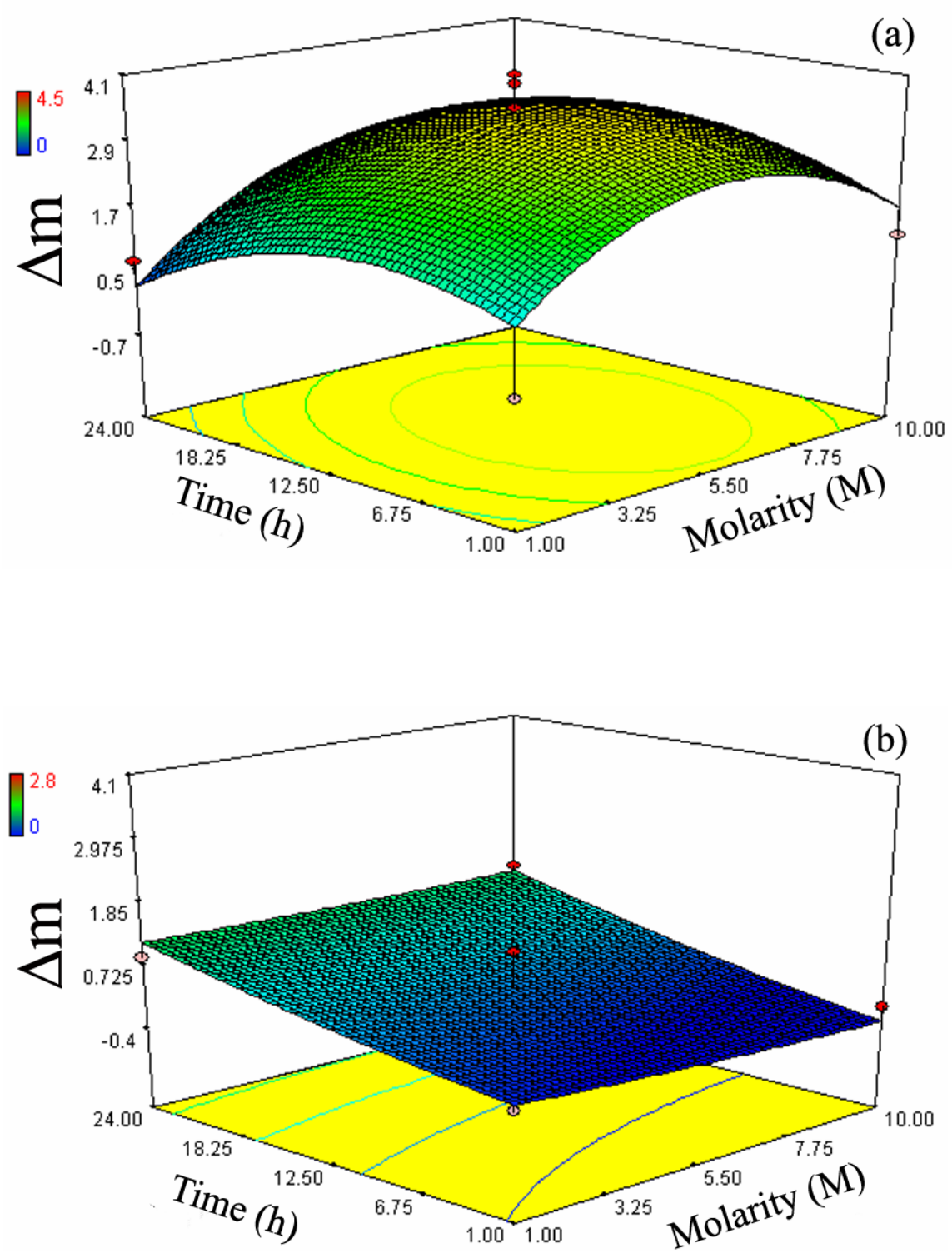

Figure 6.10. The response surface 3D plots of molarity-time of AT (a) P1 and (b) P2 foam.

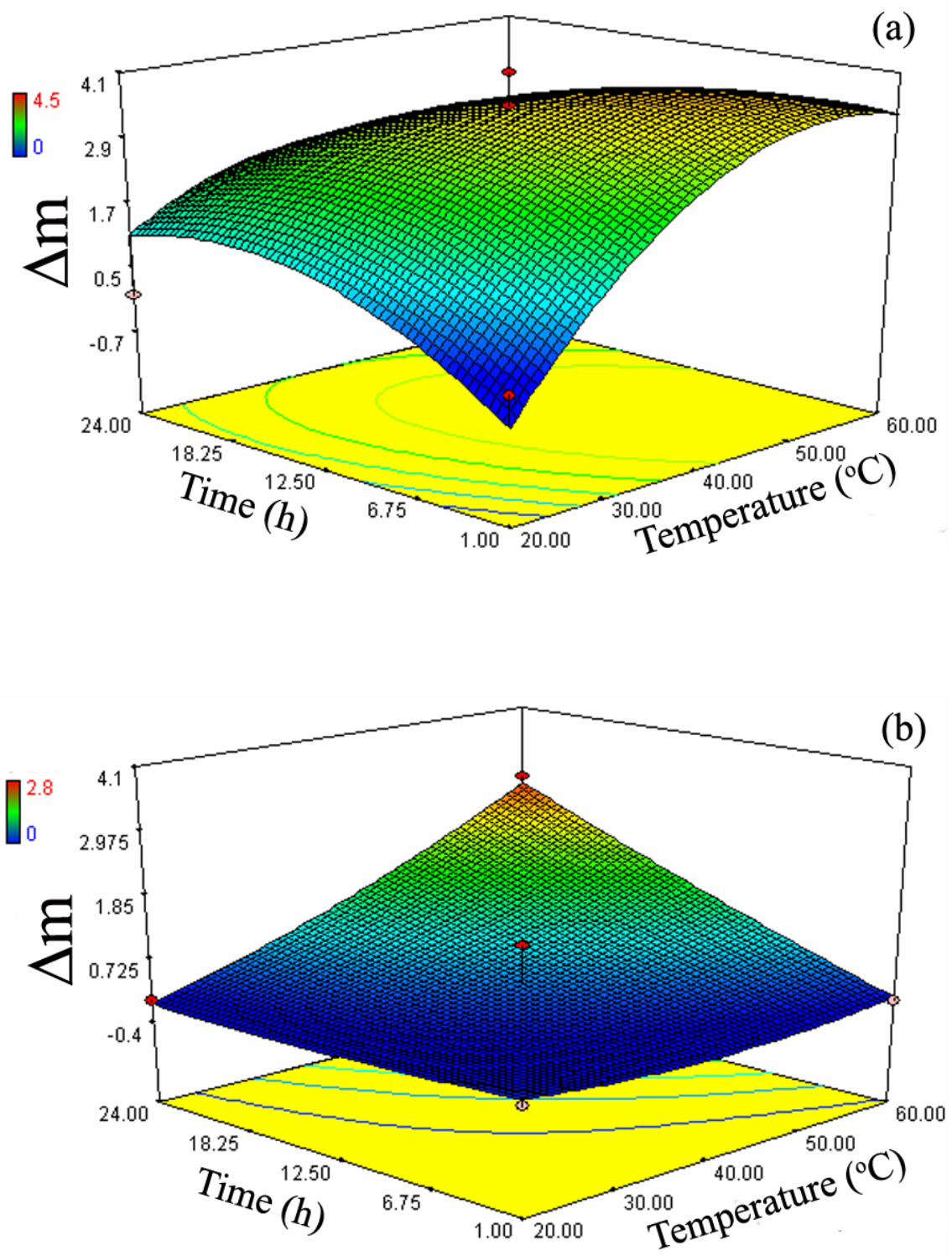

Figure 6.11. The response surface 3D plots of temperature-time of AT (a) P1 and (b) P2 foam.

Nitric acid treatment is commonly used for the passivation of Ti and its alloys. It is interesting to note that although a variety of studies were conducted on the nitric acid passivation of Ti; few of these have been on the biomimetic CaP deposition ability of nitric acid surface treatment. Chen et al. (Chen, et al. 2003) used nitric acid passivation as a pretreatment for alkali treatment to form a bioactive layer on a Ni-Ti alloy. Ca and P adsorption on nitric acid passivated Ti surfaces immersed in Hank's solution showed Ca and P containing layer equivalent to 4.0 ionic monolayers even after 16-day of immersion (Chang and Lee 2002). Lu et al. (Lu, et al. 2008) correlated the bioactivity of Ti with the functional groups formed on the surface after nitric acid treatment. It was also shown that the surface energy of the NAT Ti was higher than that of the polished Ti. In addition, the surface roughness of Ti samples did not change after the nitric acid treatment. The following experimental design conditions were found to induce a uniform coating layer both in NAT P1 and P2 foam specimens: 20% nitric acid treatment at 40°C for 1 h. Uniform CaP coating layer in NAT P1 foam, but not in NAT P2 foam, was observed microscopically for the following conditions: (1) 65% nitric acid treatment at 20°C for 3 h, (2) 20% nitric acid treatment at 20°C for 3 h, and (3) 20% nitric acid treatment at 40°C for 5 h. Uniform CaP coating layer in P2 foam, but not in NAT P1 foam, was observed microscopically for the following conditions: 42.5% nitric acid treatment at 40°C for 3 h. Figures 6.12(a-d) show the SEM micrograph of 14-day SBF immersed NAT P1 and P2 foam with the optimum conditions. The pictures in these figures clearly show that both foam flat surfaces and interior of cell are uniformly coated with CaP layer.

The CaP growth mechanism on alkali and heat treated Ti metal in SBF was previously explained (Kim, et al. 2003, Takadama, et al. 2001a, Takadama, et al. 2001b). The alkali treatment of Ti metal is usually performed in a 10M or 5M NaOH solution at various temperatures. Liang et al. (Liang, et al. 2003) investigated the apatite formation on AT porous Ti. The alkali treatment was carried in a solution of 0.5 to 10M, at 60°C for 24 h. It was shown that AT samples in 0.5 and 1M solution did not induce CaP formation when the samples were soaked in SBF for 28 days. However, the samples treated with 5 and 10M solution formed continues layer of CaP on the surface. In another study, Ti6Al4V specimens were soaked in 3, 5, 10 and 15M NaOH solution at 60 and 80°C for 1, 3 and 7 days (Wei, et al. 2002). The treated samples were heat treated at 500, 600 and 700°C for 1 h. It was shown that 15M NaOH treatment at 60°C for 3 days without any heat treatment resulted in the formation of a dense sodium

titanate layer on the surface. The apatite formation on the surface of all heat treated specimens were observed after soaking in SBF for only 1 day except the specimens heat treated at 700°C. It was reported that the optimum treatment conditions for Ti6Al4V specimens were 5M NaOH solution treatment at 80°C for 3 days and subsequent heat treatment at 600°C for 1 h.

The surfaces of the AT P1 and P2 foam specimens were microscopically analyzed after bioactivity test. The following experimental conditions were observed to induce a uniform coating layer on the surface and interior part of pores of both AT P1 and P2 foam specimens: 1M NaOH solution treatment at 20°C for 12.5 h. These findings contradict with the result of Liang et al. (Liang, et al. 2003), in which no CaP precipitation on Ti was observed in 1M solution at 60 ^{o}C for 1 h. The difference between two results simply arises from the duration of the treatment. The alkali treatment in 5.5M solution at 40°C for 12.5 h also resulted in CaP coating on the surface and interior of pores of P2 foam, while only CaP precipitates were seen microscopically in cells of AT P1 foam. The ANOVA table of AT P2 foam quite agrees with the SEM observations of CaP layer. The treatment temperature and time are more significant than the molarity. Figures 6.13(a-d) show the SEM micrograph of AT 14-day SBF immersed P1 and P2 foam samples at optimum treatment conditions. The observations clearly show that both foam flat surfaces and interior of cell are uniformly coated with CaP layer.

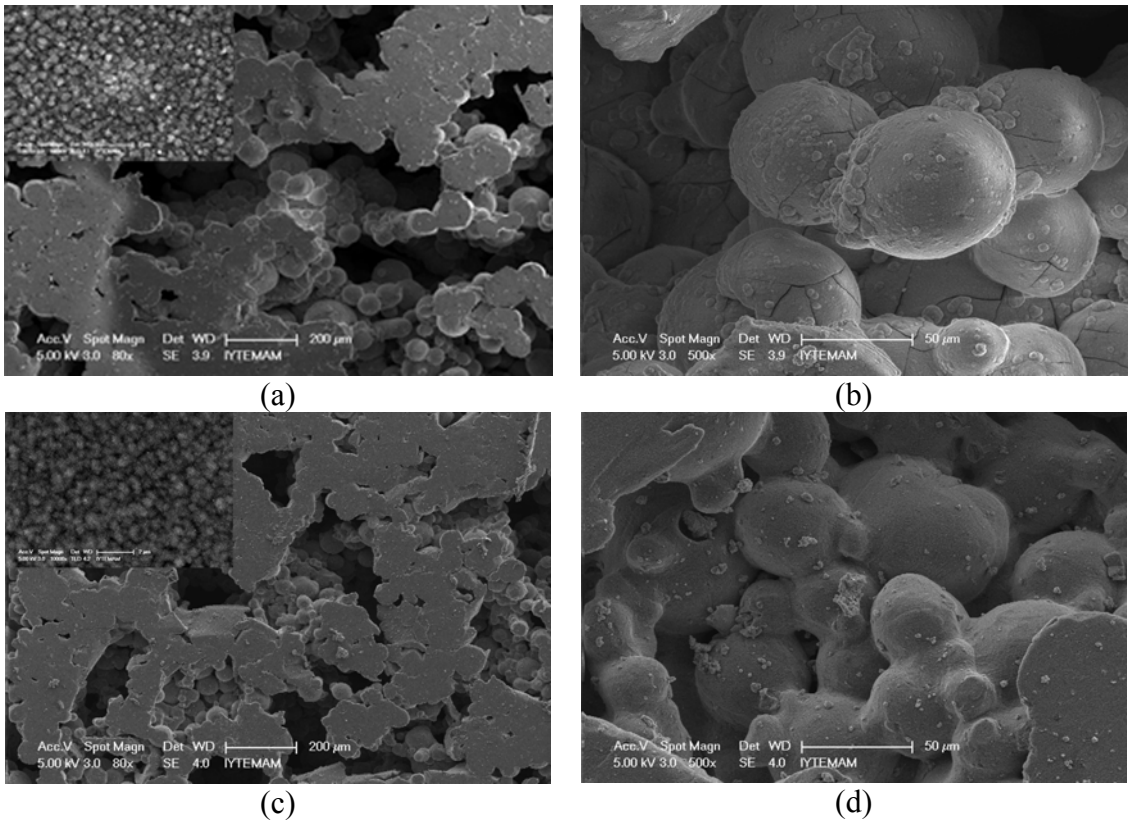

Figure 6.12. SEM micrograph after the response surface design of nitric acid treatment (a) flat surface of P1 foam, (b) interior of the P1 foam, (c) flat surface of P2 foam and (d) interior of the P2 foam.

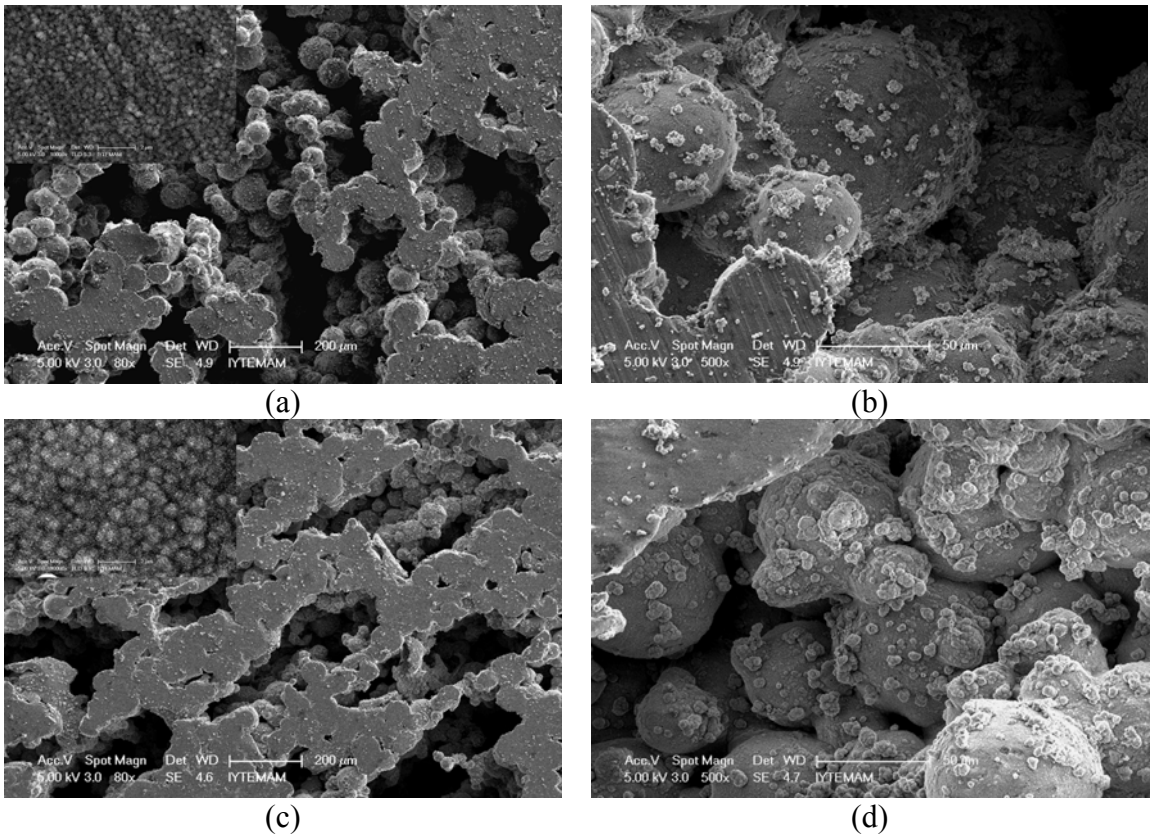

Figure 6.13. SEM micrograph after the response surface design of optimum alkali treatment condition (a) flat surface of P1 foam, (b) interior of the P1 foam, (c) flat surface of P2 foam and (d) interior of the P2 foam.

CHAPTER 7

Staphylococcus epidermidis ADHESION ON OPEN CELL Ti6Al4V FOAMS: THE EFFECT OF SURFACE TREATMENT

7.1. Introduction

It is known that the increased number of the use of prostheses implants rise an important problem of bacterial infection (Darouiche 2004, Sculco 1995). A recent study has shown that surface treatment applied to Ti including sandblasting, micro arc oxidation and SBF CaP coating promoted the bacterial colonization in vitro, which was mainly attributed to the increased surface roughness and the surface area with the applied surface treatment (Wang, et al. 2009a). There are essentially numerous studies and few review papers (An and Friedman 1998, Teughels, et al. 2006, Wang, et al. 2009a) in the literature reporting the increased tendency of the bacterial colonization with increasing surface roughness. The bacterial colonization on Ti6Al4V alloy was previously reported to occur preferentially in vanadium rich regions (Gabriel, et al. 1994), while the surface nitriding and berberine inhibited bacteria adhesion on Ti6Al4V (Sarro, et al. 2006, Wang, et al. 2009b). Despite the studies performed on the bacterial colonization on bulk Ti6Al4V alloy, there has been no investigation on the bacterial colonization on Ti and Ti alloy foams, a group of materials which have been widely investigated for the biomedical applications in the last few years (Chen, et al. 2009b, Cheung, et al. 2007, Dizlek, et al. 2009, Oh, et al. 2003, Ryan, et al. 2006, Takemoto, et al. 2006a, Takemoto, et al. 2007, Takemoto, et al. 2005, Takemoto, et al. 2006b). The aim of this part of the thesis is therefore to investigate the effect of the most widely used nitric acid and alkali surface treatment on *Staphylococcus epidermidis (S. epidermidis)* adhesion on open-cell Ti6Al4V foams, being potentially used in hard tissue applications such as porous spinal inter body fusion cages. *Staphylococcus* group of microorganisms are the most common pathogen in implant related infections (Zimmerli 2006, Zimmerli, et al. 2004). The bacterial colonization is important in biomimetic CaP deposition of the

foams, in which the foam is immersed for a relatively long period of time in SBF solution. In order to assess the effect of surface roughness resulting from the applied surface treatment prior to SBF immersion on the bacteria retention on the foam, the surface roughness of the foam ground flat surfaces was measured in nano metric scale before and after surface treatment.

7.2. Materials and Methods

Open-cell Ti6Al4V foams with ~60% porosity were prepared by means of the space holder method, using the ammonium bicarbonate as the space holing material and two different particle sizes of gas atomized spherical Ti6Al4V alloy powders (Crucible Research). P1 was 45-150 μm in particle size, with an average particle size of 94 μm and P2 30-90 μm in particle size, with an average particle size of 66 μm. The details of the Ti6Al4V foam preparation and the microstructure development after sintering and mechanical properties are given elsewhere (Dizlek, et al. 2009). The foams prepared with the abovementioned method contained nearly 60% porosity with a bimodal pore size distribution: macro pores (300-500 μm) and micro pores (1-30 μm). Micro pores were located in between the sintered Ti6Al4V particles on the cell walls and at the cell edges, while macro pores resulted from the space holder removal.

Figure 7.1(a) shows the picture of a sintered foam plate, which is water jet cut for the extraction of the various geometries of spinal inter body fusion cages. For microbial investigations, small square cross-section plate-like specimens (10x10x3 mm^3) were cut from the sintered Ti6Al4V foam plates using a low speed diamond saw (Figure 7.1(b)). The specimens' square cross-sections were then ground sequentially down to 2400 grit SiC paper. The foam specimen surfaces are therefore composed of ground flat regions and inner cells (pores). The foam specimens were cleaned ultrasonically in acetone, then in ethyl alcohol and finally in deionized water for 15 min for each solution. Before the bacterial adhesion tests, nitric acid treatment was applied to Ti6Al4V foam specimens in a 1:1 volume ratio solution of HNO_3 (65%) and H_2O at 60°C for 5 h. The alkali treatment was applied in a 100 ml 10M NaOH aqueous solution at 60°C for 24 h. Following the surface treatments, the specimens were cleaned ultrasonically in deionized water for 15 min and were dried in air, while AT specimens were dried in an oven at 40°C for 24 h.

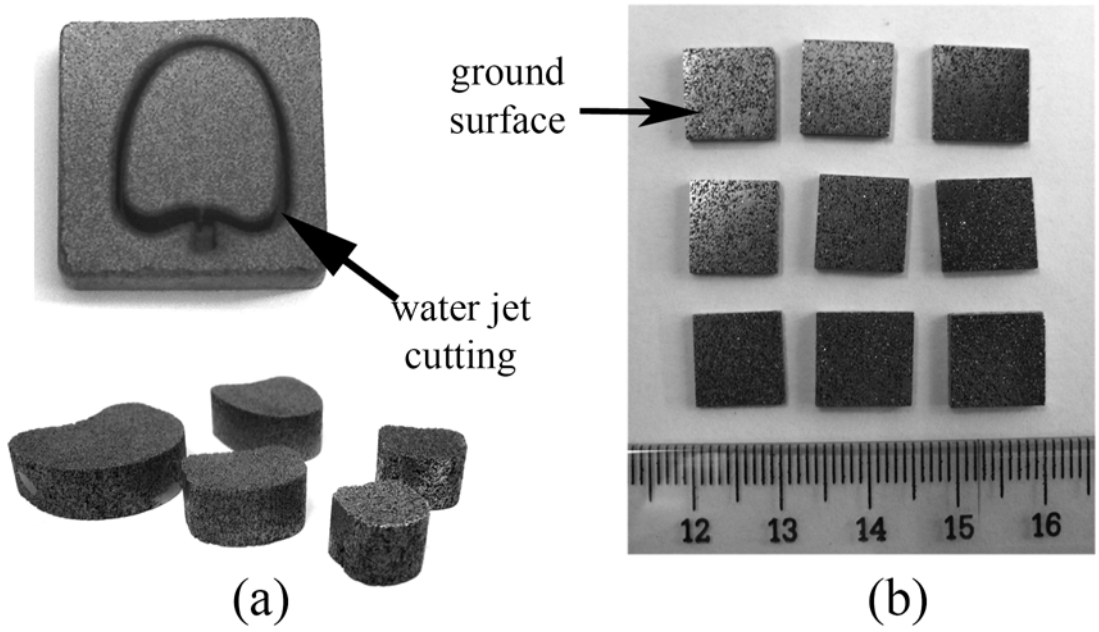

Figure 7.1. (a) Water jet cut foam sample plate and extracted spinal inter body fusion cages and (b) test specimen for microbial investigation.

The surface topography, surface roughness and surface area difference of the foam specimens before and after the surface treatment were determined using a Nanoscope-IV. AFM analyses were performed using taping tips (Vecco Otespa) with the spring constant of 20–100 $N.m^{-1}$. The scanned area was 1.5 x 1.5 μm^2, with vertical and lateral resolutions of 0.001 and 2 nm, respectively. At least three AFM surface scans were conducted on the randomly selected areas of foam specimen ground flat surfaces and were used to calculate average surface roughness values.

S. epidermidis strain YT-169a in McFarland 1.0 (3×10^8 cells ml^{-1}) was inoculated to 10 ml Tryptic Soy Broth+1% sucrose media containing foam specimens. The specimens were then incubated at 37°C for 24 h. During incubation, the foam specimens were vibrated at 60 rpm. Following the incubation, the specimens were washed with sterile phosphate-buffered saline (PBS) three times in order to remove non-adherent bacteria and then transferred into 25 ml PBS. The adherent bacteria were removed from the foam specimens under sonication (15 min) using sterile cell scrapers. The removed bacteria were diluted to 10^{-4} and 10^{-5} with PBS and 100 µL of the diluted bacteria were inoculated to duplicate tryptic soy agar plates. The plates were incubated at $37^{°C}$ for 24 h and the number of *S. epidermidis* colonies was counted and quantified as colony forming units per milliliter, CFU mL^{-1}.

7.3. Results and Discussion

Although, nitric acid treatment results in no new phase formation on the surfaces of the foam particles, alkali treatment forms a thin layer of $Na_2Ti_5O_{11}$ on the particle surfaces. Figures 7.2(a) and (b) show SEM micrographs of P1 and P2 foams cellular structure, respectively. As is seen in the same micrographs, P1 foam specimen accommodates a higher number and a larger size of the micro pores on the cell walls than P2 foam specimen (marked with arrows). The cell walls of P2 foam as clearly seen in these figures is denser than those of P2 foam, mainly resulting from the smaller and biomodal particle size distribution of P2. Furthermore, alkali treatment develops a smaller pore size $Na_2Ti_5O_{11}$ layer in P2 foam than in P1 foam as shown in Figures 7.3(a) and (b). Presumably, the pore size of $Na_2Ti_5O_{11}$ layer on P2 foam is nearly half of that on P1 foam. In the same figures, it is also seen that the porous $Na_2Ti_5O_{11}$ layer accommodates cracks. The thickness of $Na_2Ti_5O_{11}$ layer is about 500 nm for both foam specimens, measured from the SEM pictures of the cross-section of foam particles.

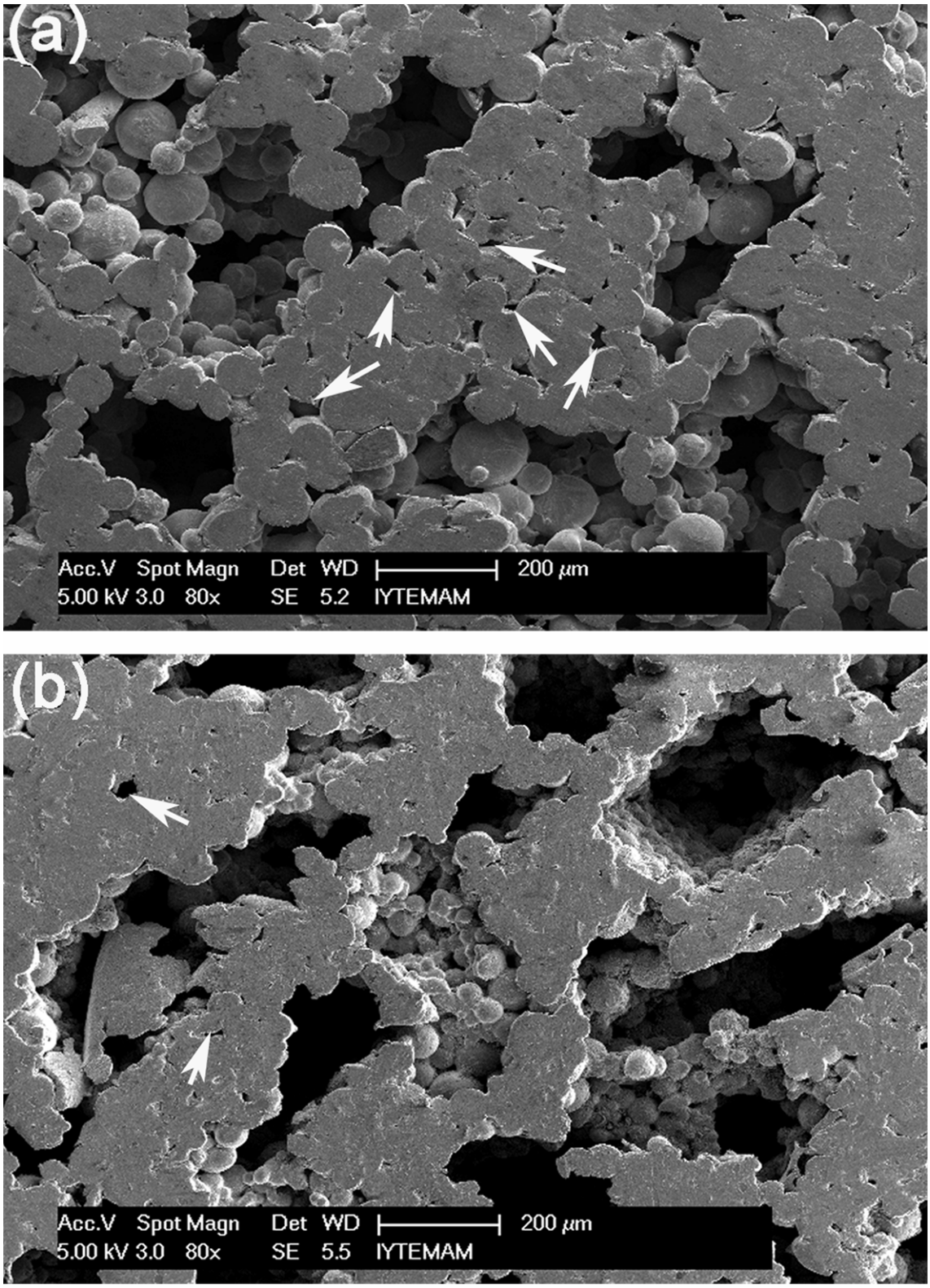

Figure 7.2. SEM micrographs of (a) P1 and (b) P2 Ti6Al4V foam surfaces showing cells, cell walls, and micro pores on the cell walls.

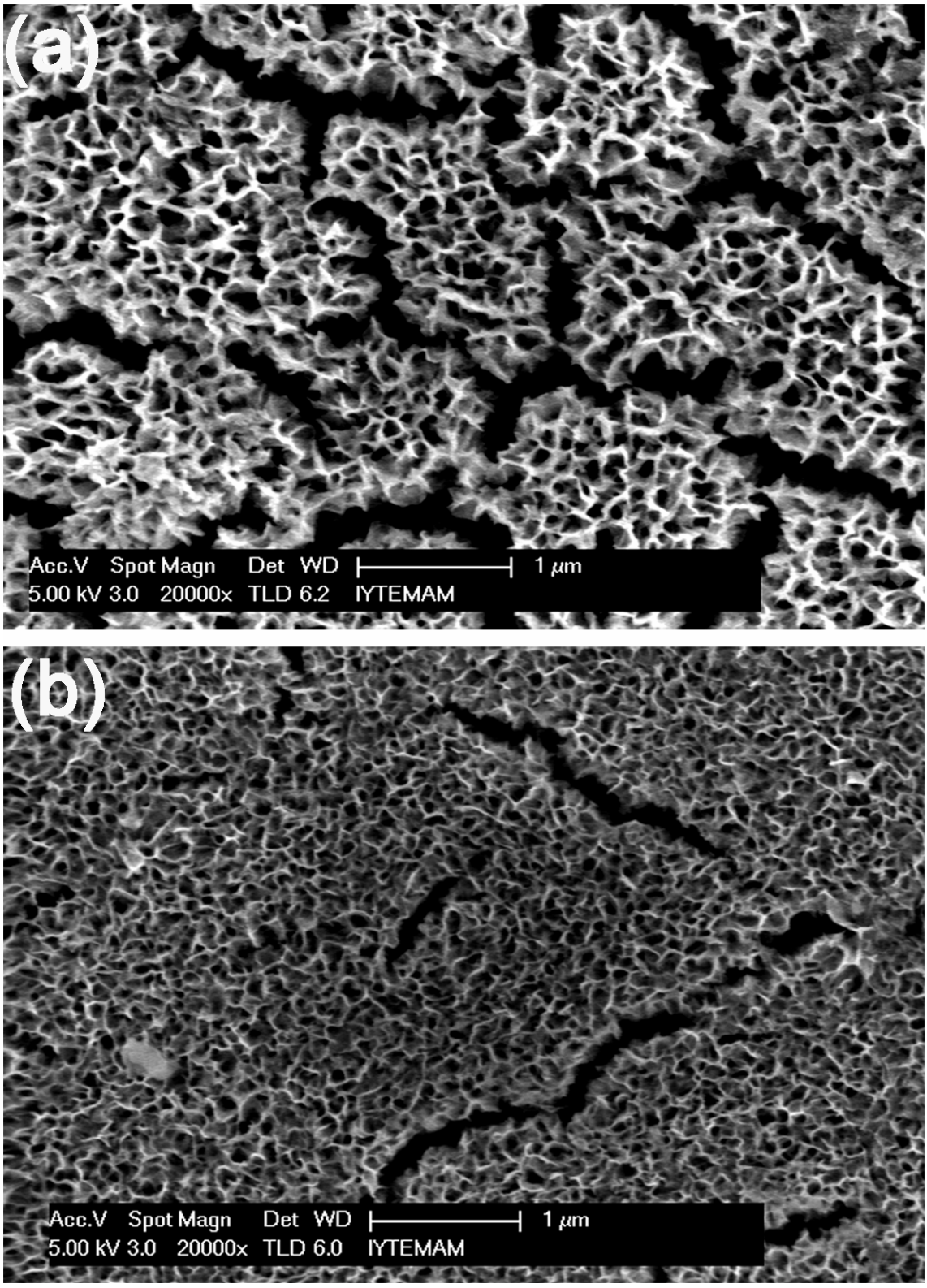

Figure 7.3. SEM micrographs of AT (a) P1 and (b) P2 Ti6Al4V foam flat surfaces showing porous surface layer developed.

Figure 7.4 shows AFM micrograph (1.5x1.5 μm^2) of untreated P2 foam flat surface. The surface is composed of parallel undulations in nano metric scale. The AFM surface topography of P1 foam flat surface is also found similar to that of P2 foam. Figures 7.5(a) and (b) show AFM surface micrographs of NAT P1 and P2 foam flat surfaces, respectively. Nitric acid treatment essentially tends to increase the number of the undulations on the foam flat surfaces. The surface topography of AT P1 and P2 foam flat surfaces are shown in Figures 7.6(a) and (b), respectively. A rougher surface development of AT foam samples surfaces as compared with untreated foam samples surfaces is clearly seen in these micrographs. In addition, AFM micrographs in Figures 7.6(a) and (b) confirm a smaller pore size $Na_2Ti_5O_{11}$ layer development on P2 foam than P1 foam.

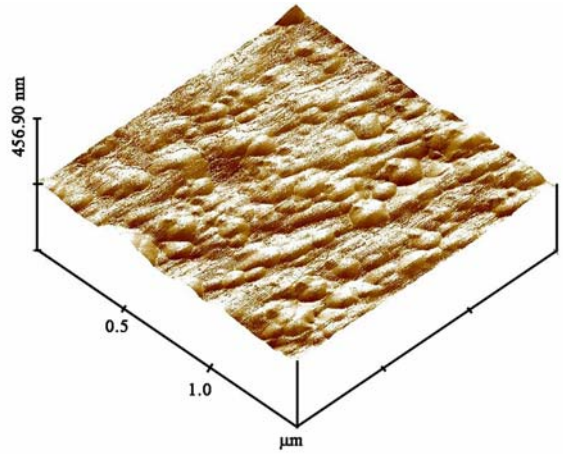

Figure 7.4. 3D AFM micrograph of the surface topography of untreated P1 specimen.

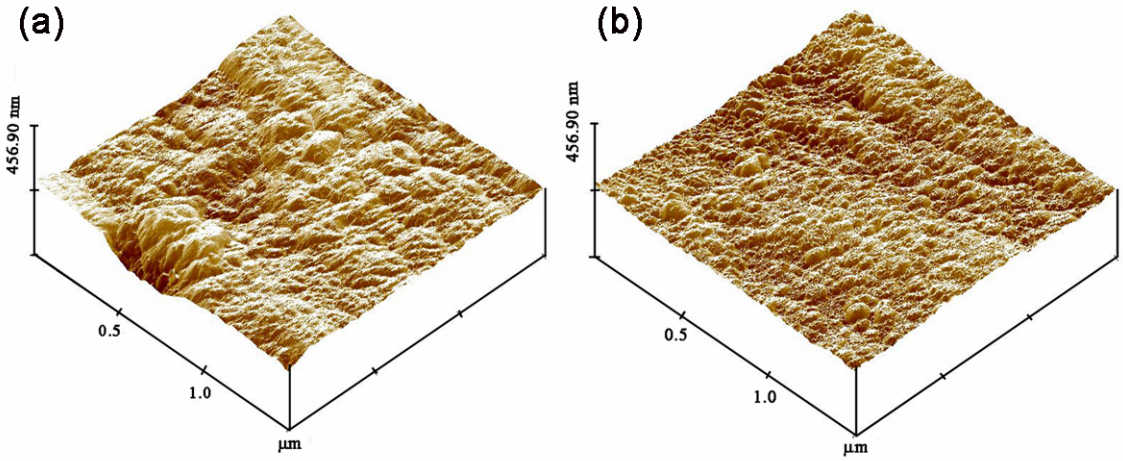

Figure 7.5. 3D AFM micrographs of the surface topography of NAT (a) P1 and (b) P2 foam specimen.

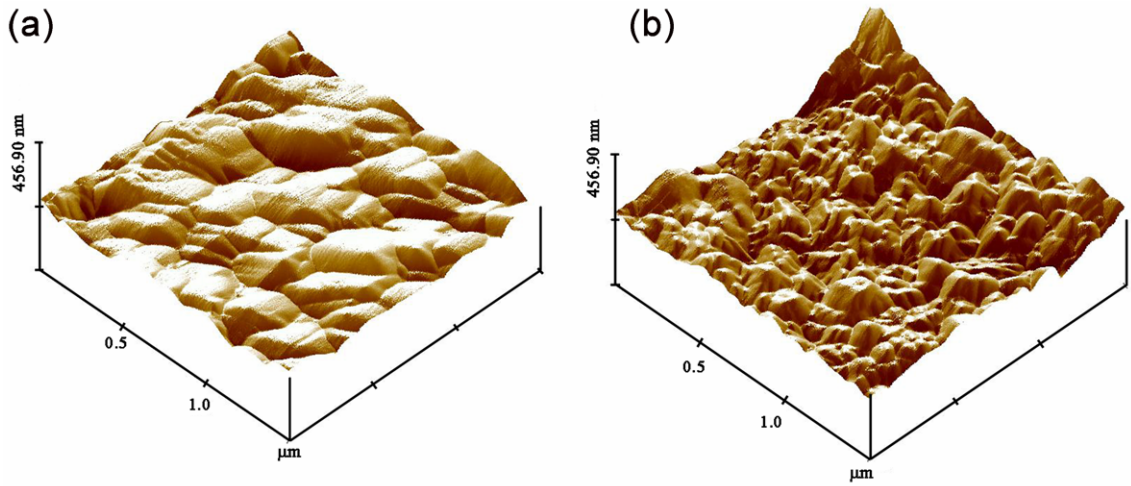

Figure 7.6. 3D AFM micrographs of the surface topography of AT (a) P1 and (b) P2 foam specimen.

The AFM measured R_a and SAD values of P1 and P2 foams are further tabulated in Tables 7.1 and 2, respectively. As tabulated in these tables, the treated P1 foam specimen flat surfaces have higher surface roughness values than those of untreated P1 foam specimen flat surfaces. The surface roughness of the AT P2 foam is noted to be higher than that of AT P1 and untreated P2 foam, while nitric acid treatment decreases the surface roughness of P2 foam below that of untreated P2 foam. It is also noted that SAD values of treated P2 foams are higher than those of treated P1 foams. The surface treatment essentially results in significant increase in the surface area, resulting in finer surface microstructure development, which is more pronounced in smaller particle size P2 foams.

Table 7.1. Surface roughness of P1 foam flat surface before microbial test.

P1	Ra (nm)	SAD (%)
As received	10.715	1.279
AT	15.769	5.477
NA	12.012	3.832

Table 7.2. Surface roughness of P2 foam flat surface before microbial test.

P2	Ra (nm)	SAD (%)
As received	10.517	1.284
AT	15.647	8.127
NA	9.153	7.815

Figure 7.7 shows graphically the number of bacteria attached to the surface of untreated and treated P1 and P2 foam specimens. Bacteria adhesion on P1 foam is higher than that on P2 foam, regardless the type of the surface treatment applied. In P1 foam, the surface treatment increases the number of bacteria adhesion over that of untreated foam specimen: the bacteria adhesion is nearly doubled in NAT P1 foam, while the number of bacteria retention increases four times in AT P1 foam. Although alkali treatment increases the number of bacteria attached to the surface of P2 foam, nitric acid treatment essentially reduces the number of bacteria adhesion below that of untreated P2 foam.

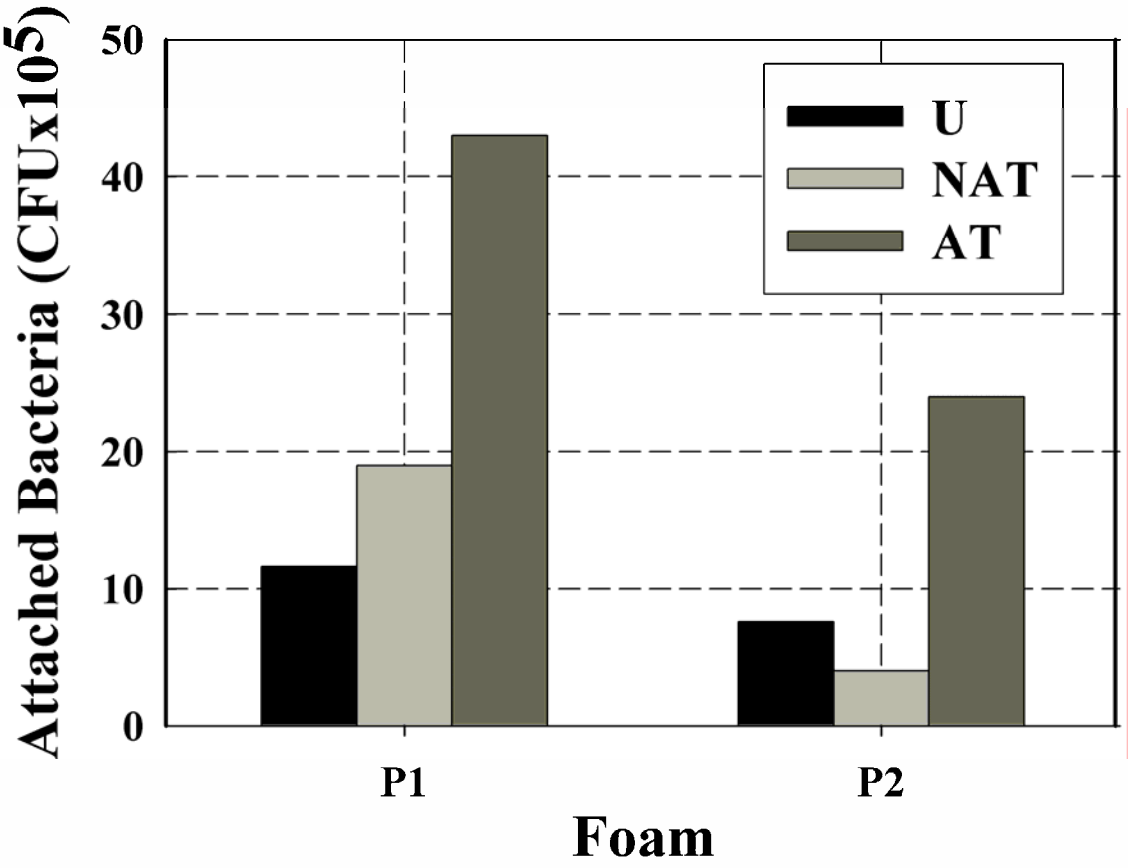

Figure 7.7. Attached bacteria (CFU) *vs.* P1 and P2 foam samples.

Figures 7.8(a) and (b) show sequentially SEM micrographs of the bacteria adhesion on the surface of untreated P1 and P2 foam particles interior of the cells after bacterial adhesion test (prior to bacteria removal). The bacteria adhesion as marked with arrows in Figures 7.8(a) and (b) is relatively high at the particle sintering neck regions. Figures 7.9(a) and (b) show sequentially the SEM micrographs of the bacteria adhesion on AT P1 and P2 foam particles interior of the cells after bacterial adhesion test. In opposite to the measured lower CFU values, a higher number of bacteria adhesion to AT P2 foam particles are seen microscopically as compared with AT P1 foam particles. Figures 7.10(a) and (b) show sequentially SEM micrographs of bacteria retention on NAT P1 and P2 foam particles interior of the cells. Similar to untreated foam particles, preferential bacterial colonization at particle sintering necks is also seen in these foam specimens.

Figures 7.11(a) and (b), Figures 7.12(a) and (b) and Figures 7.13(a) and (b) show sequentially AFM micrograph (1.5x1.5 μm^2) of bacterial adhesion to untreated, AT and NAT P1 and P2 foams surfaces, respectively. As is seen in these micrographs the surfaces of the foams are mostly covered with bacteria and in some parts the underneath surfaces are seen. In some parts as seen in Figure 7.11(b), the sizes of the bacteria are relatively small. This is believed to occur as a result of local death or collapse of the bacteria. The porous $Na_2Ti_5O_{11}$ layer in AT samples is also seen under the bacterial colony in Figure 7.12(a). The sizes of the bacteria colonized in untreated, AT and NAT foam samples surfaces are also seen to be similar.

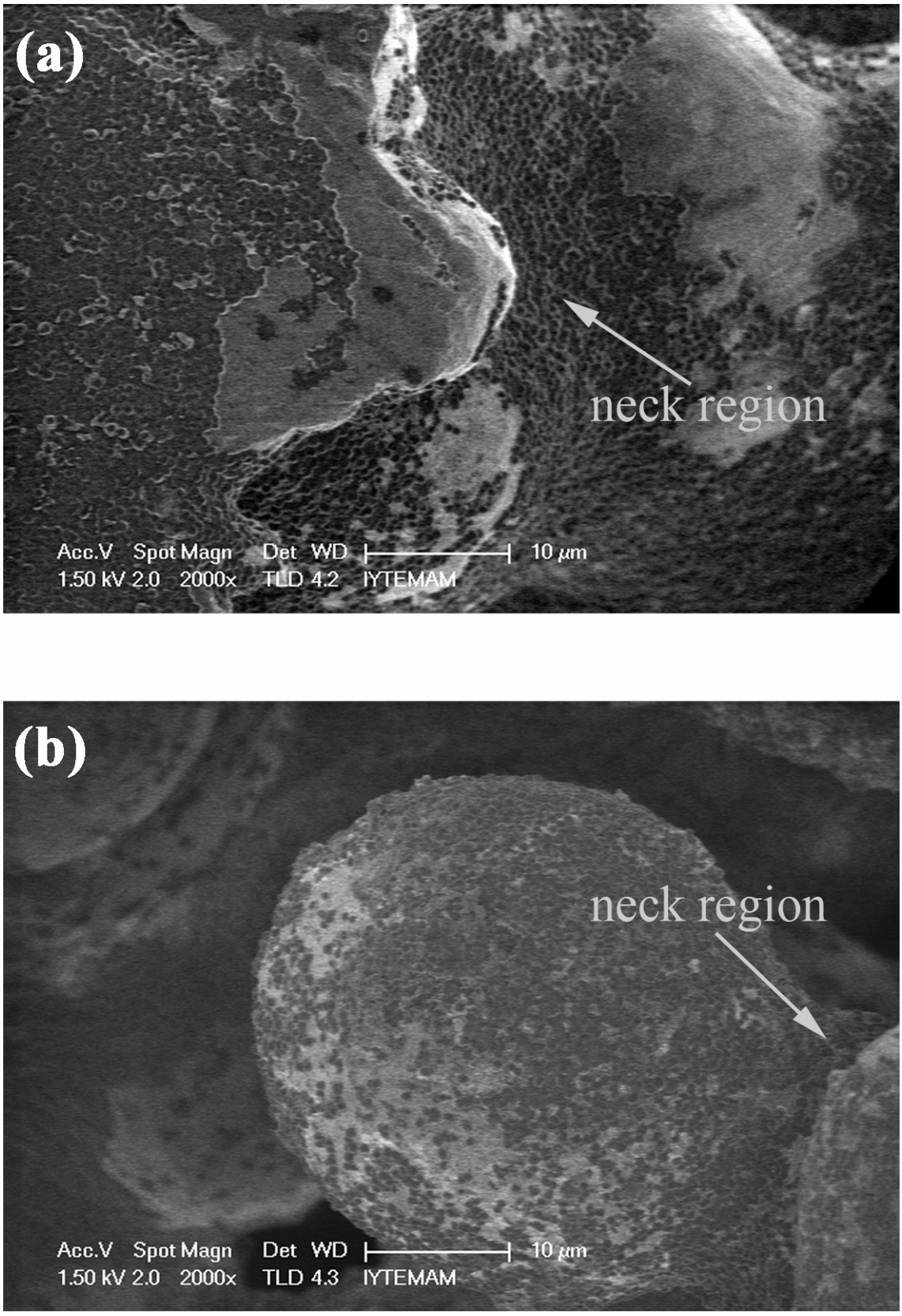

Figure 7.8. SEM micrographs of *Staphylococcus epidermidis* bacteria attached to untreated Ti6Al4V particles in (a) P1 and (b) P2 foam.

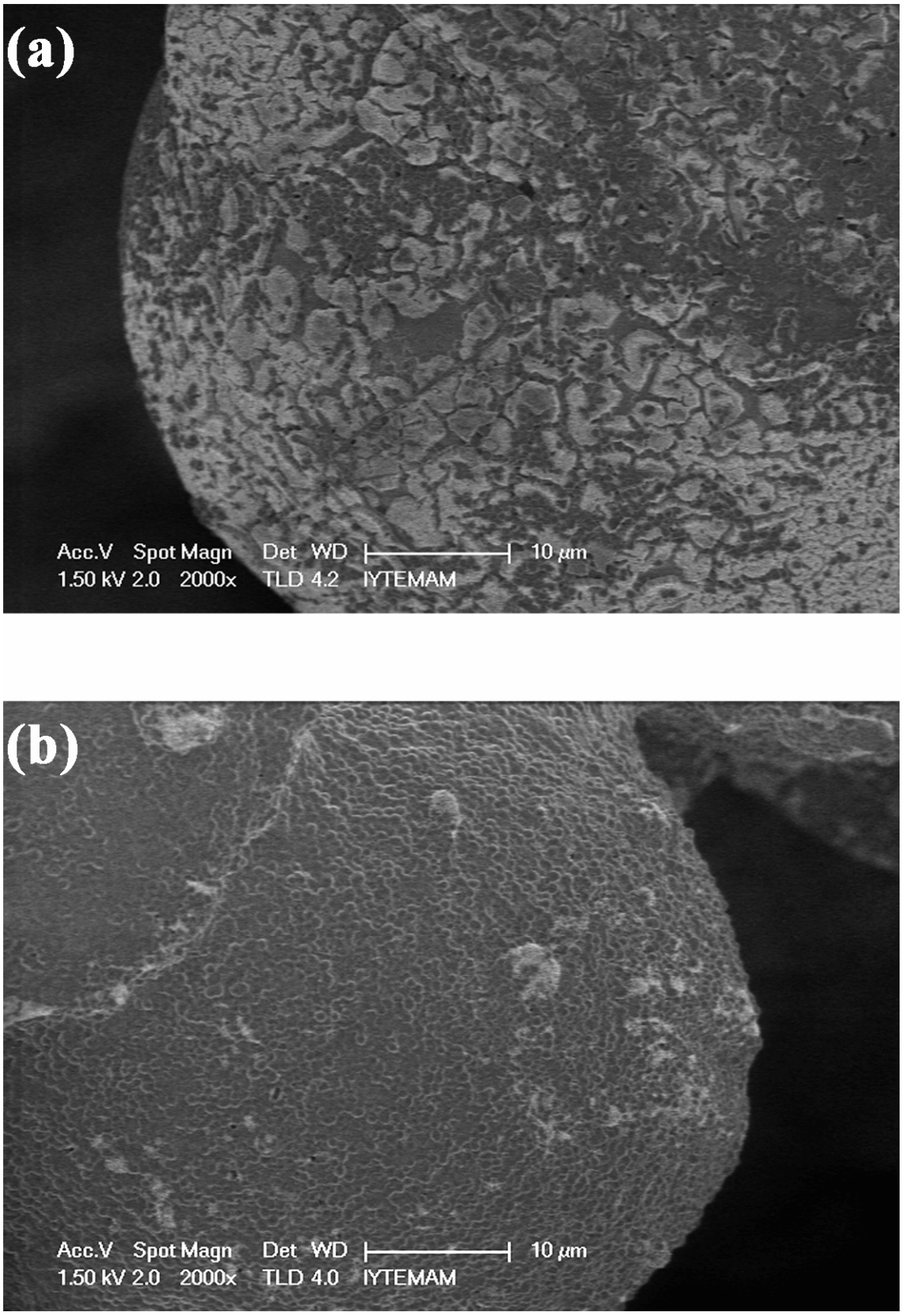

Figure 7.9. SEM micrographs of *Staphylococcus epidermidis* bacteria attached to AT Ti6Al4V particles in (a) P1 and (b) P2 foam.

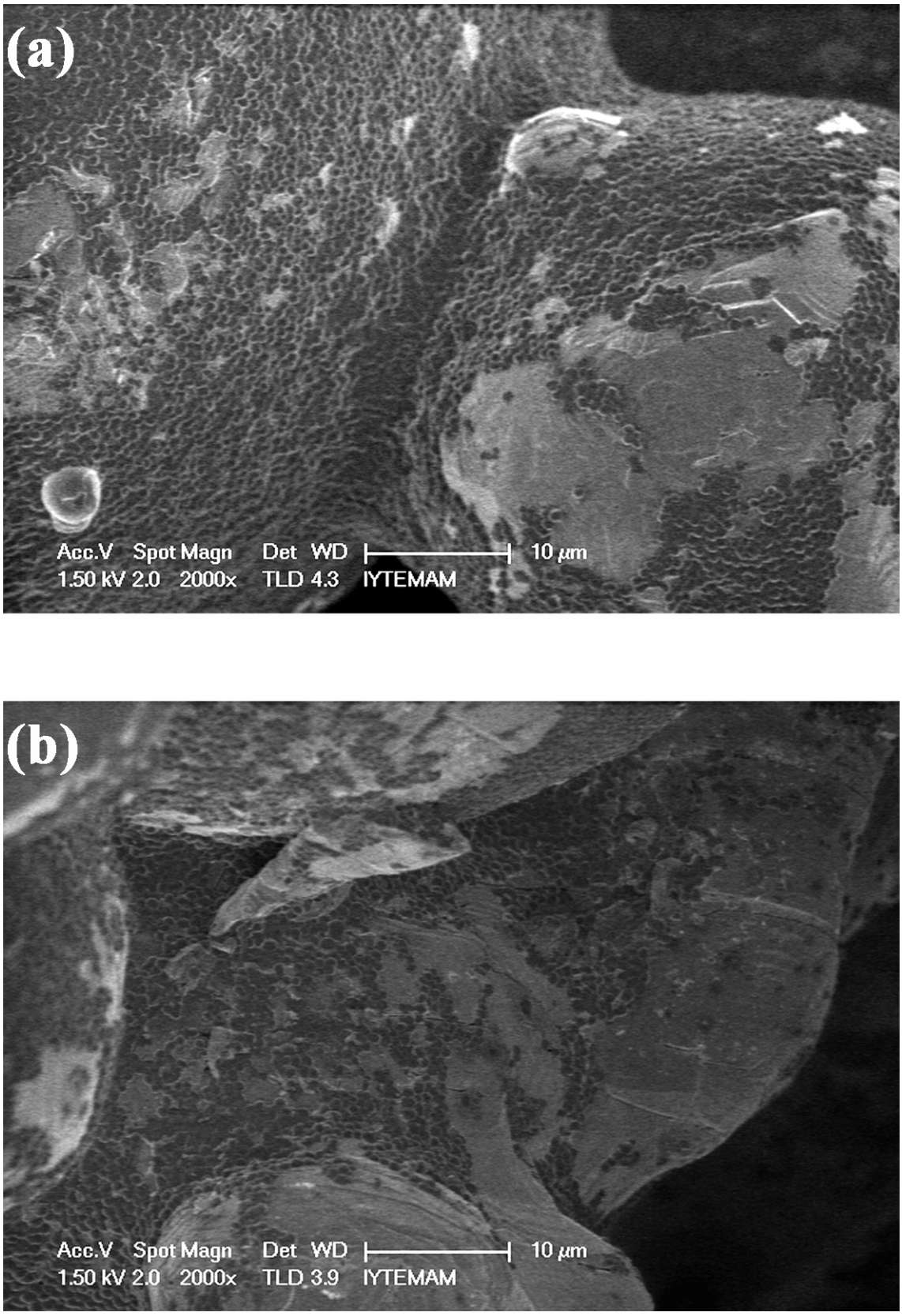

Figure 7.10. SEM micrographs of *Staphylococcus epidermidis* bacteria attached to NAT Ti6Al4V particles in (a) P1 and (b) P2 foam.

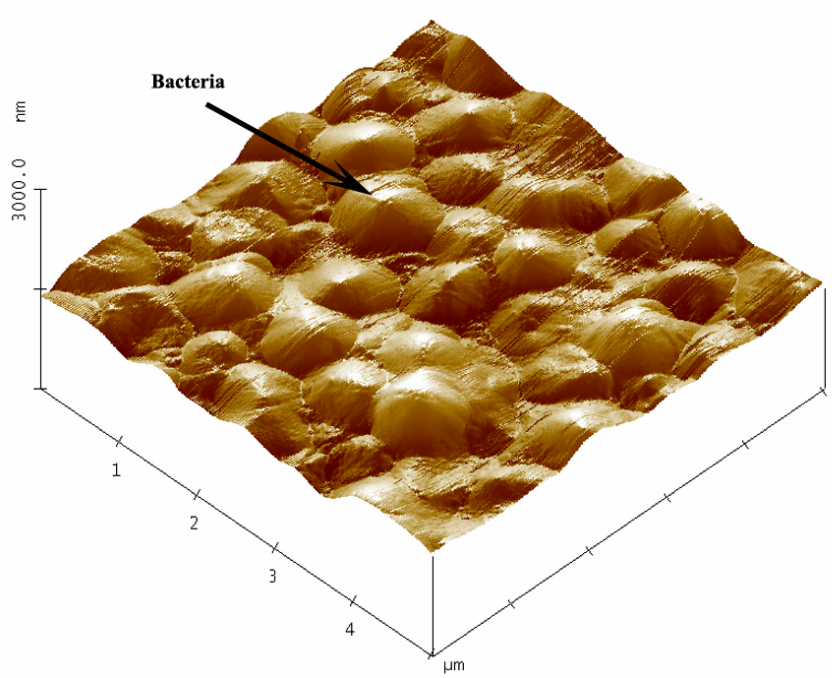

(a)

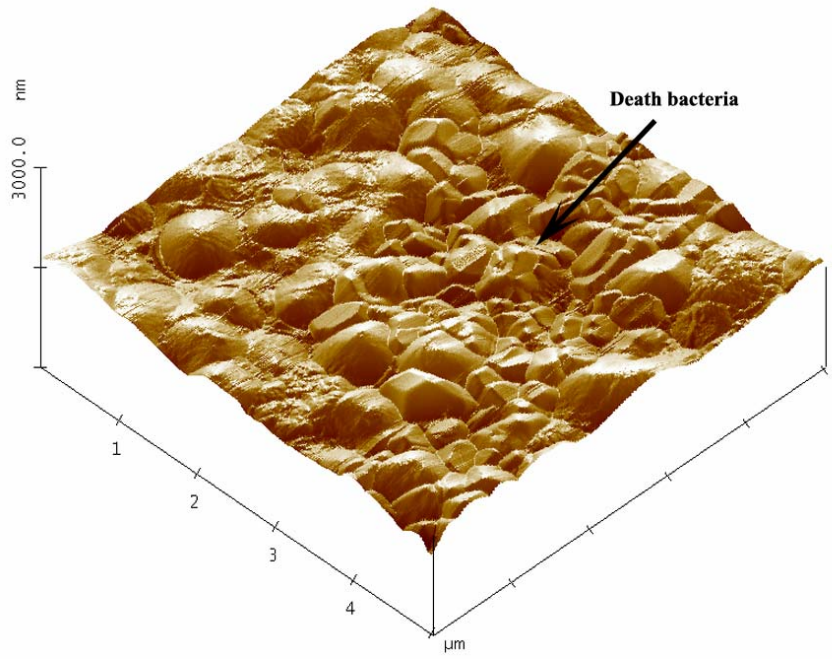

(b)

Figure 7.11. AFM micrograph of the surface topography of bacterial adhesion on untreated (a) P1 and (b) P2 foam.

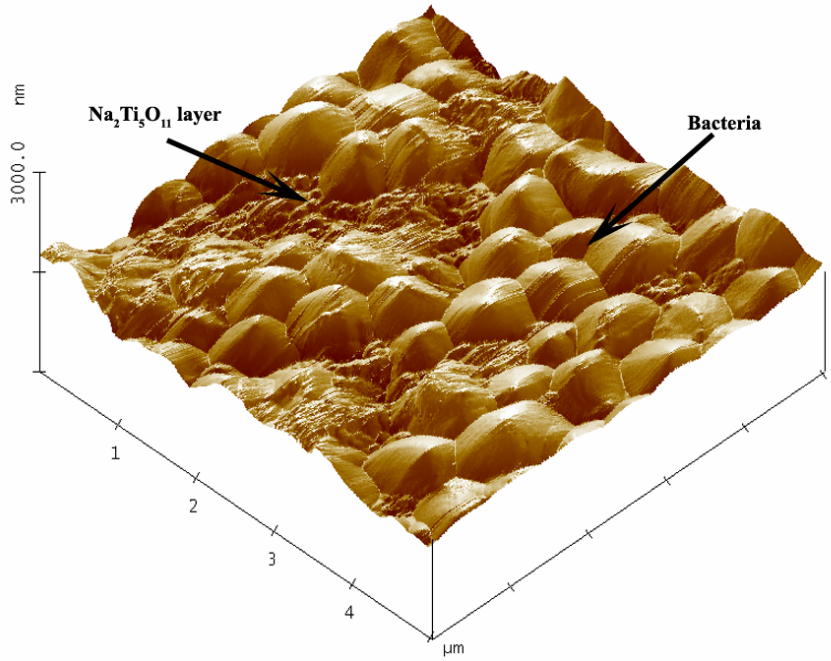

(a)

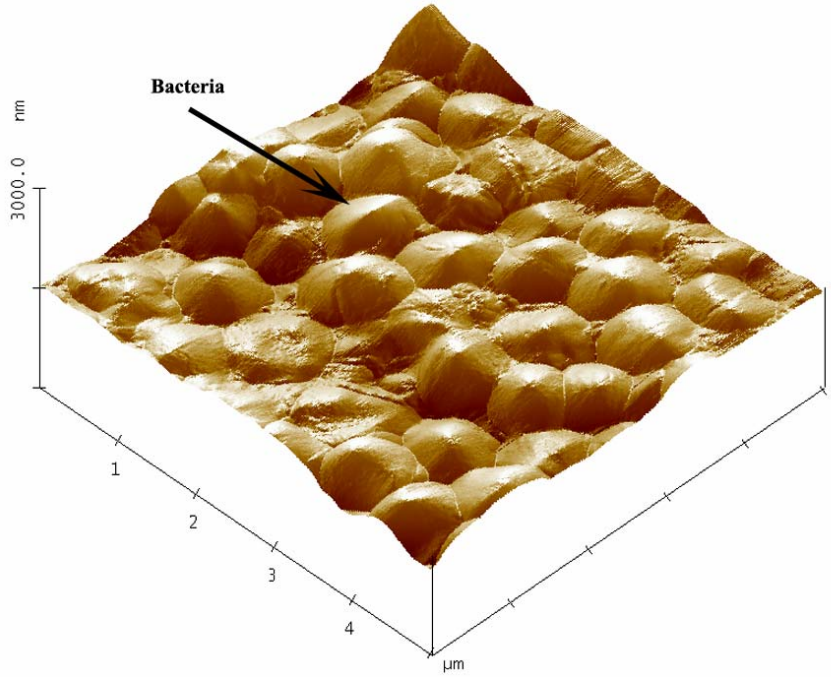

(b)

Figure 7.12. AFM micrograph of the surface topography of bacterial adhesion on AT (a) P1 and (b) P2 foam.

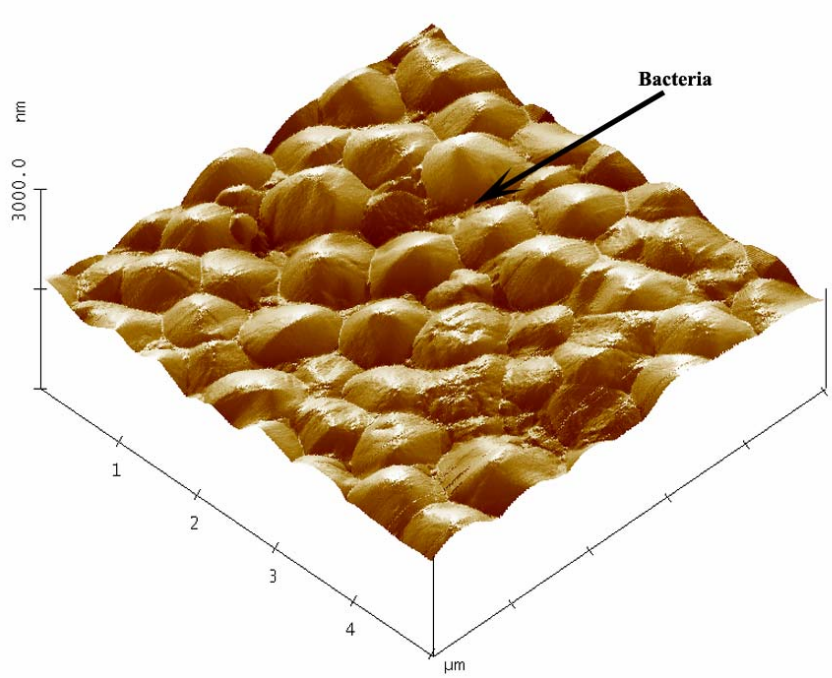

(a)

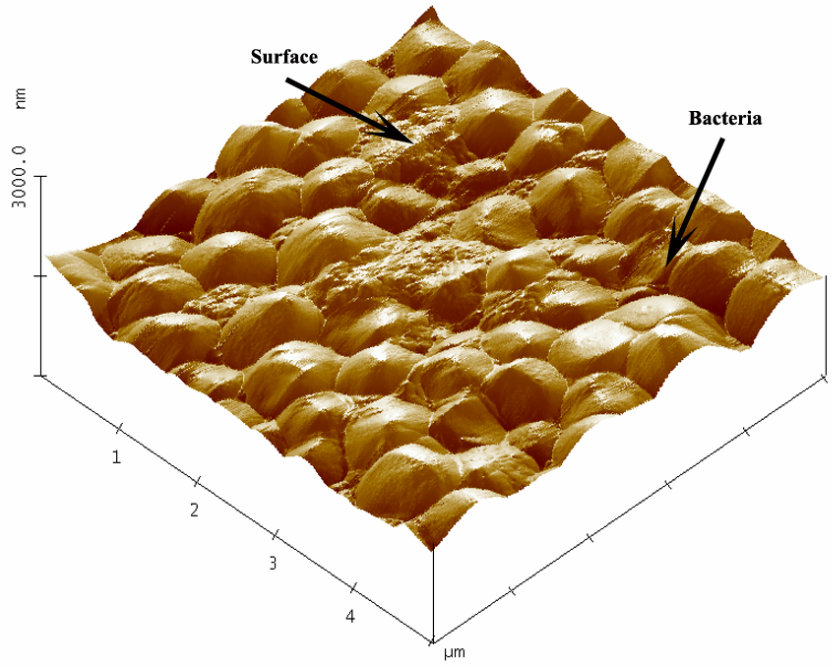

(b)

Figure 7.13. AFM micrograph of the surface topography of bacterial adhesion on NAT (a) P1 and (b) P2 foam.

Alkali treatment is known to form a porous and rough thin surface layer of sodium titanate on Ti metal (Kim, et al. 1996, Kokubo 2008, Lee, et al. 2002, Wei, et al. 2002). The morphology of this layer changed with the conditions of surface treatment conditions and the applied heat treatment (Wei, et al. 2002). Although, nitric acid treatment was shown not to affect the surface roughness of Ti significantly, it increased the surface energy (Lu, et al. 2008). The similar AFM surface roughness values of NAT and untreated foam specimens found in this study are noted to agree with the results of Lu et.al (Lu, et al. 2007) and Sittig et. al. (Sittig, et al. 1999).

In order to analyze the effect of nano surface roughness on the bacterial colonization, CFU values of the investigated foam specimens are drawn as function of surface roughness and shown in Figure 7.14. As seen in Figure 7.14, CFU values in both P1 and P2 foams increase with increasing measured nano surface roughness values. However, the CFU values of P1 foam specimens are higher than those of P2 foam. The measured specific particle surface area of P2 foam (0.112 $m^2.g^{-1}$) is nearly twice that of P1 foam (0.0694 $m^2.g^{-1}$). SAD values of P2 foams are also higher than those of P1 foams. P2 foams would therefore be expected to provide a larger surface area for the bacterial adhesion at the similar surface roughness values and hence higher bacteria retention on the surface. As already stated earlier, the micro pores between the particles, which are considered as the channels for the fluid flow to the inner cells, are relatively small in P2 foam due to the smaller particle size used to make cellular structure. This may result in a relatively low rate of fluid flow; hence, bacterial transport to inner cells. The thickness of the foam specimens was kept small (3 mm), each foam specimen containing nearly 4-5 cells which were not directly exposed to the microbial fluid. The increased number of bacteria retention in AT foam specimens is attributed to the increase in the surface roughness by the formation of a porous Na-Ti layer. The present results also confirm that surface roughness is the dominant factor for the bacteria retention on the foam particle surfaces.

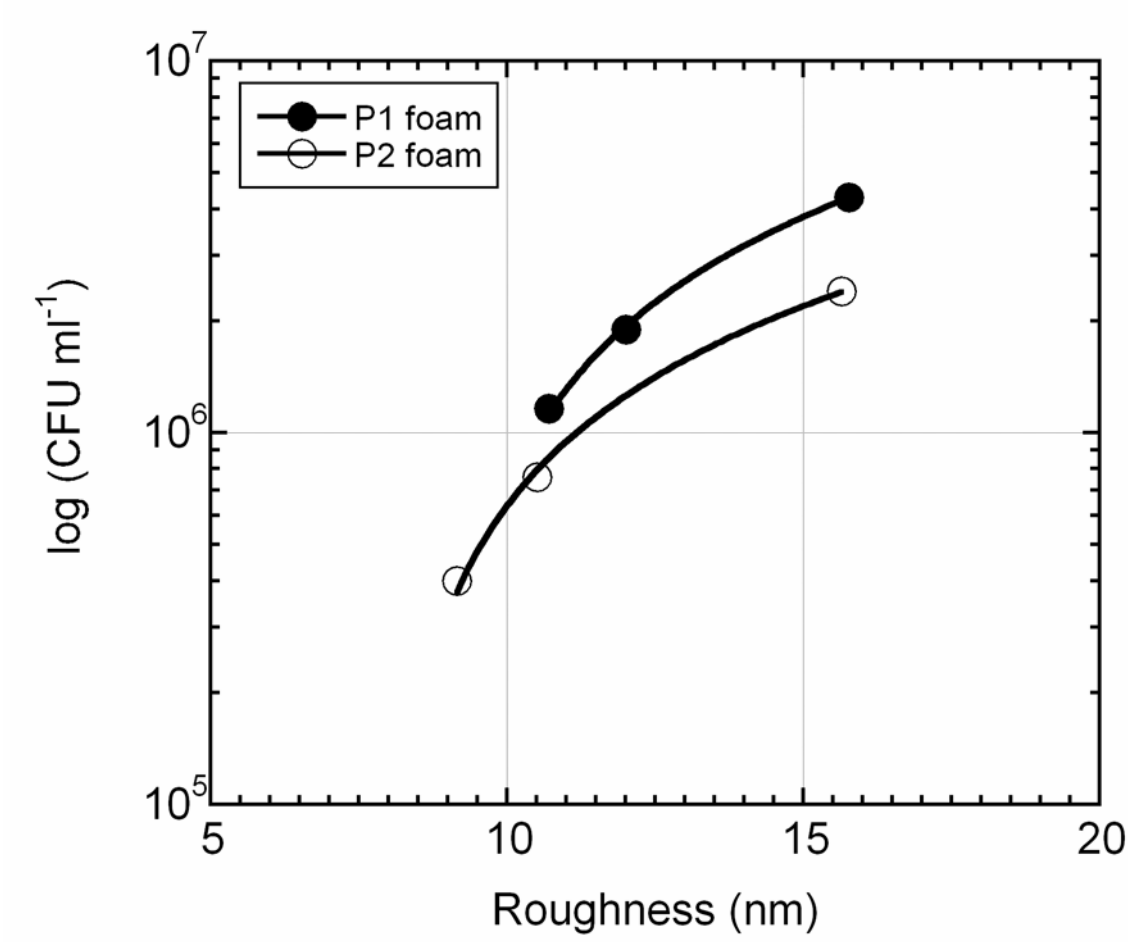

Figure 7.14. CFU *vs.* surface roughness of untreated and treated foam specimens.

It should be noted that the surface roughness of the particles interior of the cells cannot be measured directly using AFM. Therefore, the resultant surface roughness of the particles after surface treatment was determined indirectly by measuring the surface roughness of foam specimen ground flat surfaces. The SEM micrographs of the flat surfaces of untreated and treated P1 and P2 foam samples are shown in Figures 7.15(a-f). The surface morphologies of the untreated P1 and P2 foams are nearly the same, ground with 2400 grit. The major grinding lines at a distance of ~5 μm are clearly seen in Figure 7.15(b). In between the major grinding lines, the minor grinding lines are also detected on the flat surfaces of P2 foam specimen in Figure 7.15(b). These minor grinding lines are agreed with the AFM surface topography of P2 foam shown in Figure 7.4. The pronounced grinding line in P2 foam specimen flat surfaces may be attributed to the small particle size which may introduce a higher degree of grinding lines. Nitric acid treatment tends to remove the grinding lines from the flat surfaces of P1 and P2 foam as seen in Figures 7.15(c) and (d), but it introduces small undulations on the

surface, which is also detected in AFM surface topography images in Figures 7.5(a) and (b). The heights of the undulations are seen to be bigger in P2 foam specimens. The surface morphology of AT foam specimens is however, dictated by the nitric acid treatmenture of Na-Ti layer as depicted in Figures 7.15(e) and (f). The cracks spaced at a distance of 3-5 μm are also seen on this layer. The particles interior of the cells of untreated P1 and P2 foams contain thermal etch facets on the surface (Figures 7.16(a) and (b)). The heights of the thermal etch facets were further measured using SEM micrographs of the particles. Thermal etch facets heights were found to vary with the locations on the particle surfaces; therefore, at least 15 measurements were taken from randomly selected particles and the results were averaged. The thermal etch facets heights are found nearly the same for both untreated P1 (211 nm) and P2 (213 nm) foam particles (Figures 7.16(a) and (b)). Nitric acid treatment has almost no effect on the thermal etch facets heights (217 nm) of P1 foam particle surfaces (Figure 7.16(c)), while it reduces the average height to 130 nm in P2 foam particles (Figure 7.16(d)). The development of nano surface roughness following the nitric acid treatment are clearly seen on the thermal etch facets (Figures 7.16(c) and (d)). The sodium titanate layer resulting from alkali treatment completely covers the thermal etch facets on the particle surfaces as shown in Figures 7.16(e) and (f). The roughness measurements taken from the foam specimen flat surfaces are considered pretty much reflecting the surface roughness of the particles interior of the cells. An effort to correlate the surface roughness resulting from thermal etch facets with the bacterial colonization essentially shows a decreasing number of bacterial retention with increasing thermal etch facets heights.

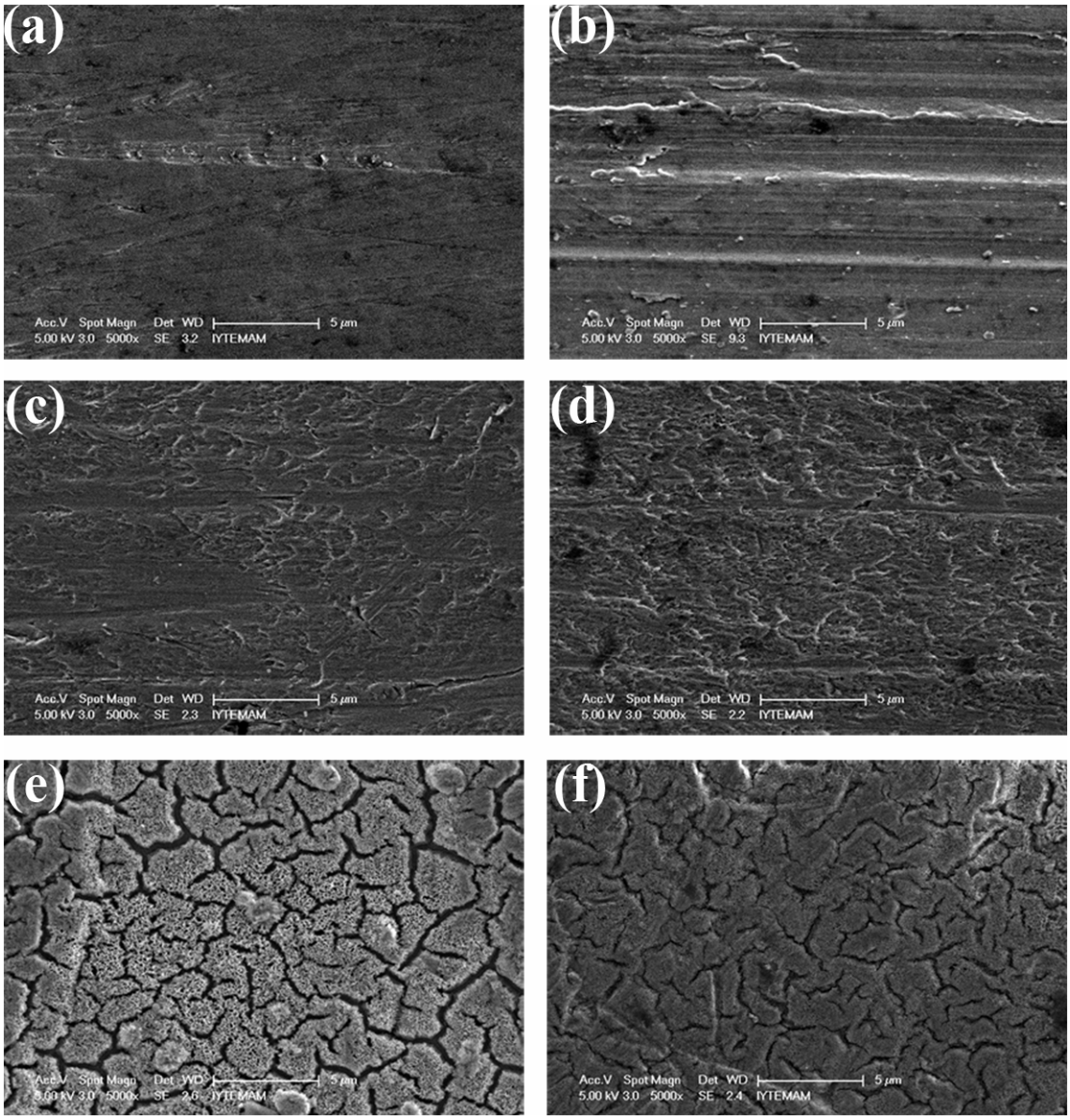

Figure 7.15. SEM micrographs of the foam flat surfaces (a) untreated P1 foam, (b) untreated P2 foam, (c) NAT P1 foam, (d) NAT P2 foam, (e) AT P1 foam and (f) AT P2 foam.

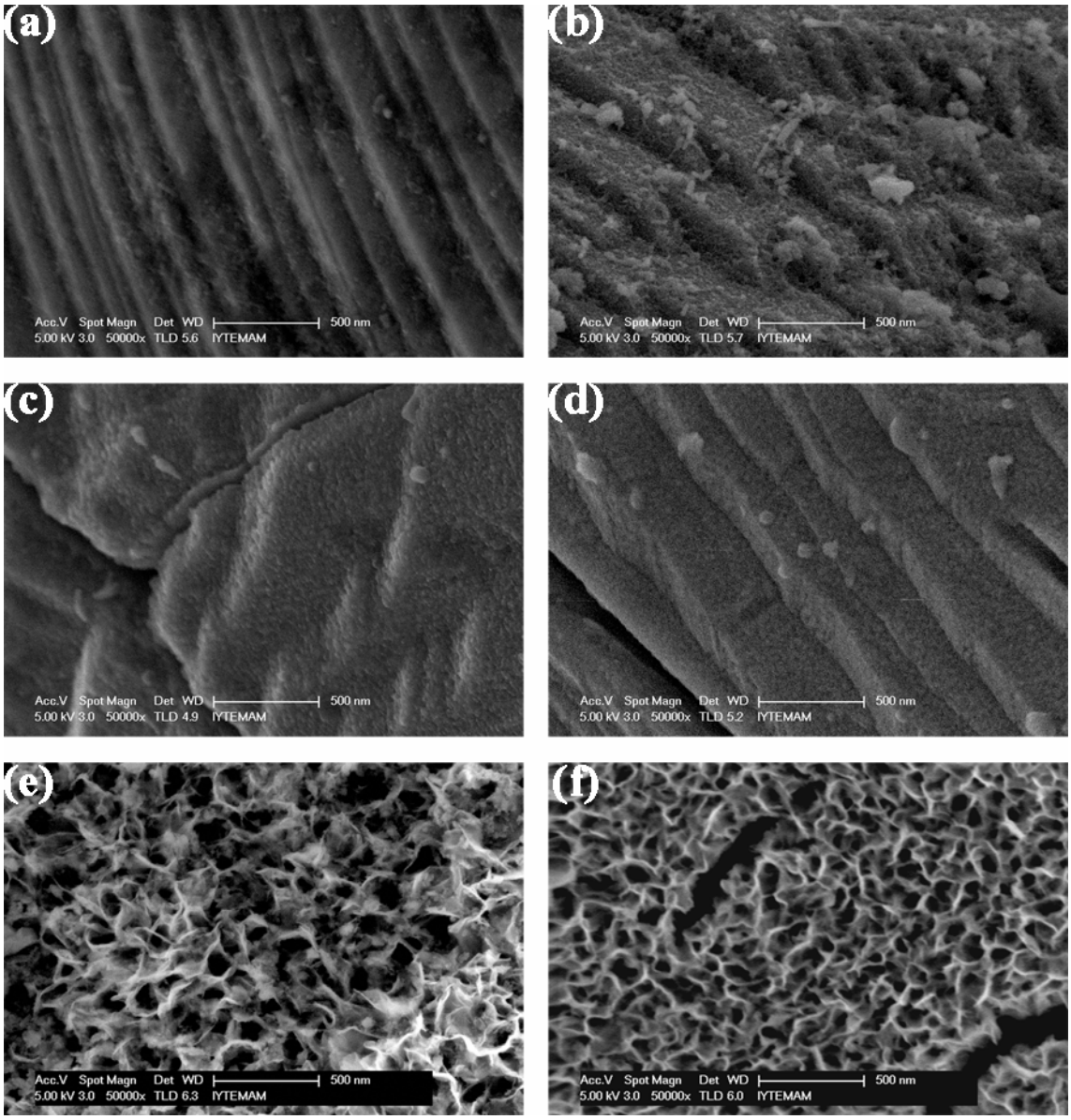

Figure 7.16. SEM micrographs of the particle surfaces interior of cells (a) untreated P1 foam, (b) untreated P2 foam, (c) NAT P1 foam, (d) NAT P2 foam, (e) AT P1 foam and (f) AT P2 foam.

CHAPTER 8

CONCLUSIONS

8.1. Summary and Conclusions

In the present study, the effects of commonly used surface treatments including alkali and nitric acid treatment and acid etching on the CaP deposition of an open cell Ti6Al4V foam was investigated in a SBF solution up to 14-day. Untreated foam specimens were also tested for comparison. The foams were prepared by space holder method using commercially available gas atomized spherical powders. P1 was 45-150 μm in particle size, with an average particle size of 94 μm and P2 30-90 μm in particle size, with an average particle size of 66 μm. P1 particles showed a mono modal particle size distribution, while P2 particles a bimodal particle size distribution. Angular shape ammonium bicarbonate powder with a particle size range of 315-500 μm was used as space holder with an addition of 60 vol%. The Ti6Al4V foams compacted were sintered at 1300 ^{o}C in a tube furnace under argon atmosphere. The microstructure of the as-received powders was composed of needle-like α phase, referred acicular α. Sintering at 1300°C transformed needle-like α into Widmanstätten structure, composed of β lathes (bcc and rich in V) and α platelets (hcp and rich in Al).

Small square cross-section plate-like specimens (10x10x3 mm^3) were cut from the sintered Ti6Al4V foam plates using a low speed diamond saw. The specimens' square cross-sections were then ground sequentially down to 2400 grit SiC paper. The foam specimen surfaces were therefore composed of ground flat regions and inner cells (pores). The surface roughness of the foam specimens flat surfaces were measured in nano metric scale before and after SBF immersion using AFM. In acid etching, the foam specimens were immersed into an 1:1:1 volume ratio solution of H_2SO_4 (98%), HCl (36%) and H_2O at 60°C for 1 h. Nitric acid treatment was performed in a 1:1 volume ratio solution of HNO_3 (65%) and H_2O at 60°C for 5 h. In alkali treatment, the specimens were kept in 100 ml 10M NaOH aqueous solution at 60°C for 24 h. The optimum conditions of nitric acid and alkali surface treatment for the biomimetic CaP

coating of the studied open cell Ti6Al4V foams were investigated using the surface response methodology.

A uniform CaP layer formation was found on the flat surface and interior part of the pores of untreated P1 and P2 foam samples after 14-day of SBF immersion. However, the pores were filled with CaP precipitates after 14-day of SBF immersion. Alkali treatment increased the surface roughness as compared with untreated foam specimen in nano metric scale, forming $Na_2Ti_5O_{11}$ surface layer. The sodium titanate layer thickness was measured from the SEM images and found to be nearly 500 nm. The uniform CaP layer formation was found on the flat surface and interior parts of pores of alkali treated P1 foam after 14-day of SBF immersion, while it was formed on alkali treated P2 foam after 7-day of SBF immersion. Although nitric acid treatment was found to not affect the surface roughness, it tended to remove the grinding lines and increased surface area difference greatly by introducing nano scale undulations on the surface. The uniform CaP layer was formed on the nitric acid treated P1 and P2 foam samples after 14 and 5 days SBF immersion, respectively. Although, acid etching preferentially dissolved β phase, nitric acid treatment showed relatively low and equal dissolution rates of α and β-phase of the Widmanstätten structure of the studied Ti6Al4V foams. The GIXRD, SEM and FTIR analysis showed that the formed CaP layer was in the form of carbonated hydroxyapatite (CHA). In addition, the FTIR analysis showed that CHA was B-type.

The increased surface area difference was found to be more pronounced in smaller particle size foam samples. The surface roughness of the foam specimens further increased with CaP deposition in SBF. A significant increase in the surface roughness of AT foam specimens as compared with untreated and NAT specimens following the SBF immersion further proved the smaller crystal size CaP deposition. This result was also confirmed by the AFM micrographs taken from the foam specimen surfaces after SBF immersion. The microscopic evaluation of the CaP deposition on the cell wall surfaces of foam (interior of cells) clearly showed that alkali treatment and nitric acid treatment induced a continuous uniform CaP layer deposition.

CaP layer thicknesses were measured based on SEM images and found to be 1.2 and 1.5 μm for untreated P1 and P2 foam sample, respectively. It was found to be 3 and 3.2 μm for the alkali treated P1 and P2 foam samples, respectively. However, the nitric acid treatment induced a relatively thin CaP layer measured as 0.65 and 0.9 μm for P1 and P2 foam samples, respectively. This shows that nitric acid treatment induced a

relatively thinner CaP coating layer on the foam particles, leading to more open-cellular structure.

Bacterial tests on nitric acid and alkali treated foams were also performed. The foam specimens were incubated at 37°C for 24 h and the number of *S. epidermidis* colonies was counted and quantified as colony forming units per milliliter, CFU mL^{-1}. In accord with surface roughness measurements, a higher number of bacterial retention was detected in alkali treated foam specimens. The porous $Na_2Ti_5O_{11}$ surface layer formed in alkali treated foam specimens promoted the bacterial retention on the foam particles. The increased number of bacterial adhesion on the smaller particle size foam specimens was attributed to the higher degree of bacterial transport to the inner cells of the foam specimens through relatively large sizes of micro pores in between the sintered Ti6A4V particles. Since, nitric acid treatment was found to not significantly affect the surface roughness of the foam particles, its effect on the bacterial adhesion was found not significant. A correlation between the nano metric scale surface roughness and the associated bacterial colonization was also shown.

Based on response surface methodology, the following experimental design conditions were found to induce a uniform coating in alkali treated P1 and P2 foam specimens: 1M NaOH at 20°C for 12.5 h. For nitric treated P1 and P2 foams the optimum condition were found as 20% nitric acid solution at 40°C for 1 h.

8.2. Future Works

This study clearly indicated that the chemical surface treatment has beneficial effects on the bioactivity of open cell Ti6Al4V foams used as hard tissue replacements. However, the experiments were performed only in vitro. In vivo experiments are also required in order to understand the behavior of the CaP coated foam specimens. The mechanical behavior, particularly the bonding strength of CaP coating to particles, after the surface treatments should be also studied using nano indentation in future.

REFERENCES

An, Y. H. and Friedman, R. J., 1998, Concise review of mechanisms of bacterial adhesion to biomaterial surfaces. *Journal of Biomedical Materials Research*. 43(3): p. 338-348.

Auer, S. and Frenkel, D., 2001, Prediction of absolute crystal-nucleation rate in hard-sphere colloids. *Nature*. 409(6823): p. 1020-1023.

Barrere, F., Snel, M. M. E., van Blitterswijk, C. A., de Groot, K. and Layrolle, P., 2004, Nano-scale study of the nucleation and growth of calcium phosphate coating on titanium implants. *Biomaterials*. 25(14): p. 2901-2910.

Bayraktar, D. and Tas, A. C., 1999, Chemical preparation of carbonated calcium hydroxyapatite powders at 37 degrees C in urea-containing synthetic body fluids. *Journal of the European Ceramic Society*. 19(13-14): p. 2573-2579.

Biehl, V. and Breme, J., 2001, Metallic biomaterials. *Materialwissenschaft Und Werkstofftechnik*. 32(2): p. 137-141.

Bobyn, J.D. and Miller, J.E. ,1994,Features of biologically fixed devices,American Academy of Orthopaedic Surgeons

Boehm, H. P., 1971, Acidic and basic properties of hydroxylated metal-oxide surfaces. *Discussions of the Faraday Society*. (52): p. 264-&.

Bram, M., Stiller, C., Buchkremer, H. P., Stover, D. and Baur, H., 2000, High-porosity titanium, stainless steel, and superalloy parts. *Advanced Engineering Materials*. 2(4): p. 196-199.

Callen, B. W., Lowenberg, B. F., Lugowski, S., Sodhi, R. N. S. and Davies, J. E., 1995, Nitric-acid passivation of Ti6Al4V reduces thickness of surface oxide layer and increases trace-element release. *Journal of Biomedical Materials Research*. 29(3): p. 279-290.

Chang, E. and Lee, T. M., 2002, Effect of surface chemistries and characteristics of Ti6Al4V on the Ca and P adsorption and ion dissolution in Hank's ethylene diamine tetra-acetic acid solution. *Biomaterials*. 23(14): p. 2917-2925.

Chang, Y. S., Oka, M., Kobayashi, M., Gu, H. O., Li, Z. L., Nakamura, T. and Ikada, Y., 1996, Significance of interstitial bone ingrowth under load-bearing conditions: A comparison between solid and porous implant materials. *Biomaterials*. 17(11): p. 1141-1148.

Chen, M. F., Yang, X. J., Liu, Y., Zhu, S. L., Cui, Z. D. and Man, H. C., 2003, Study on the formation of an apatite layer on NiTi shape memory alloy using a chemical treatment method. *Surface & Coatings Technology*. 173(2-3): p. 229-234.

Chen, X. B., Li, Y. C., Hodgson, P. D. and Wen, C., 2009a, The importance of particle size in porous titanium and nonporous counterparts for surface energy and its impact on apatite formation. *Acta Biomaterialia*. 5(6): p. 2290-2302.

Chen, Y. J., Feng, B., Zhu, Y. P., Weng, J., Wang, J. X. and Lu, X., 2009b, Fabrication of porous titanium implants with biomechanical compatibility. *Materials Letters*. 63(30): p. 2659-2661.

Cheung, S., Gauthier, M., Lefebvre, L. P., Dunbar, M. and Filiaggi, M., 2007, Fibroblastic interactions with high-porosity Ti-6Al-4V metal foam. *Journal of Biomedical Materials Research Part B-Applied Biomaterials*. 82B(2): p. 440-449.

Darouiche, R. O., 2004, Current concepts - Treatment of infections associated with surgical implants. *New England Journal of Medicine*. 350(14): p. 1422-1429.

Deligianni, D. D., Katsala, N. D., Koutsoukos, P. G. and Missirlis, Y. F., 2001, Effect of surface roughness of hydroxyapatite on human bone marrow cell adhesion, proliferation, differentiation and detachment strength. *Biomaterials*. 22(1): p. 87-96.

Dizlek, M. E., Guden, M., Turkan, U. and Tasdemirci, A., 2009, Processing and compression testing of Ti6Al4V foams for biomedical applications. *Journal of Materials Science*. 44(6): p. 1512-1519.

Dorozhkin, S. V., 2007, Calcium orthophosphates. *Journal of Materials Science*. 42(4): p. 1061-1095.

Dorozhkin, S. V. and Epple, M., 2002, Biological and medical significance of calcium phosphates. *Angewandte Chemie-International Edition*. 41(17): p. 3130-3146.

Ducheyne, P., Beight, J., Cuckler, J., Evans, B. and Radin, S., 1990, Effect of calcium-phosphate coating characteritics on early postoperative bone tissue ingrowth. *Biomaterials*. 11(8): p. 531-540.

Erdem, B., Hunsicker, R. A., Simmons, G. W., Sudol, E. D., Dimonie, V. L. and El-Aasser, M. S., 2001, XPS and FTIR surface characterization of TiO2 particles used in polymer encapsulation. *Langmuir*. 17(9): p. 2664-2669.

Faure, J., Balamurugan, A., Benhayoune, H., Torres, P., Balossier, G. and Ferreira, J. M. F., 2009, Morphological and chemical characterisation of biomimetic bone like apatite formation on alkali treated Ti6Al4V titanium alloy. *Materials Science & Engineering C-Biomimetic and Supramolecular Systems*. 29(4): p. 1252-1257.

Feng, B., Chen, J. Y., Qi, S. K., He, L., Zhao, J. Z. and Zhang, X. D., 2002, Characterization of surface oxide films on titanium and bioactivity. *Journal of Materials Science-Materials in Medicine*. 13(5): p. 457-464.

Fujibayashi, S., Nakamura, T., Nishiguchi, S., Tamura, J., Uchida, M., Kim, H. M. and Kokubo, T., 2001, Bioactive titanium: Effect of sodium removal on the bone-bonding ability of bioactive titanium prepared by alkali and heat treatment. *Journal of Biomedical Materials Research*. 56(4): p. 562-570.

Gabriel, B. L., Gold, J., Gristina, A. G., Kasemo, B., Lausmaa, J., Harrer, C. and Myrvik, Q. N., 1994, Site-specific adhesion of staphylococcus-epidermidis (RP12) in Ti-Al-V metal systems. *Biomaterials*. 15(8): p. 628-634.

Gasser, U., Weeks, E. R., Schofield, A., Pusey, P. N. and Weitz, D. A., 2001, Real-space imaging of nucleation and growth in colloidal crystallization. *Science*. 292(5515): p. 258-262.

Gil, F. J., Padros, A., Manero, J. M., Aparicio, C., Nilsson, M. and Planell, J. A., 2002, Growth of bioactive surfaces on titanium and its alloys for orthopaedic and dental implants. *Materials Science & Engineering C-Biomimetic and Supramolecular Systems*. 22(1): p. 53-60.

Guden, M., Celik, E., Akar, E. and Cetiner, S., 2005, Compression testing of a sintered Ti6Al4V powder compact for biomedical applications. *Materials Characterization*. 54(4-5): p. 399-408.

Guden, M., Celik, E., Cetiner, S. and Aydin, A.,2004,Metals foams for biomedical applications: Processing and mechanical properties, ed. N. Hasirci and V. Hasirci,257-266,

Guden, M., Celik, E., Hizal, A., Altindis, M. and Cetiner, S., 2008, Effects of compaction pressure and particle shape on the porosity and compression mechanical properties of sintered Ti6Al4V powder compacts for hard tissue implantation. *Journal of Biomedical Materials Research Part B-Applied Biomaterials*. 85B(2): p. 547-555.

Hacking, S. A., Bobyn, J. D., Toh, K. K., Tanzer, M. and Krygier, J. J., 2000, Fibrous tissue ingrowth and attachment to porous tantalum. *Journal of Biomedical Materials Research*. 52(4): p. 631-638.

Hahn, H. and Palich, W., 1970, Preliminary evaluation of porous metal surfaced titanium for orthopedic implants. *J Biomed Mater Res* 4(4): p. 571-577.

Hallab, N., Link, H. D. and McAfee, P. C., 2003, Biomaterial optimization in total disc arthroplasty. *Spine*. 28(20): p. S139-S152.

Healy, K. E. and Ducheyne, P., 1992, Hydration and preferential molecular adsorption on titanium in vitro. *Biomaterials*. 13(8): p. 553-561.

Hulbert, S.F., F.A., Young, R.S., Mathews, J.J., Klawitter and Stelling, Talbert C.D.and F.H., 1970, Potential of ceramic materials as permanently implantable skeletal prostheses. *J Biomed Mater Res*. 4(3): p. 433-456.

Jalota, S., Bhaduri, S. B. and Tas, A. C., 2006, Effect of carbonate content and buffer type on calcium phosphate formation in SBF solutions. *Journal of Materials Science-Materials in Medicine*. 17(8): p. 697-707.

Jalota, S., Bhaduri, S. B. and Tas, A. C., 2007a, Osteoblast proliferation on neat and apatite-like calcium phosphate-coated titanium foam scaffolds. *Materials Science & Engineering C-Biomimetic and Supramolecular Systems*. 27(3): p. 432-440.

Jalota, S., Bhaduri, S., Bhaduri, S. B. and Tas, A. C., 2007b, A protocol to develop crack-free biomimetic coatings on Ti6Al4V substrates. *Journal of Materials Research*. 22(6): p. 1593-1600.

Johnsson, M. S. A. and Nancollas, G. H., 1992, The role of brushite and octacalcium phosphate in apatite formation. *Critical Reviews in Oral Biology & Medicine*. 3(1-2): p. 61-82.

Jonasova, L., Muller, F. A., Helebrant, A., Strnad, J. and Greil, P., 2004, Biomimetic apatite formation on chemically treated titanium. *Biomaterials*. 25(7-8): p. 1187-1194.

Karageorgiou, V. and Kaplan, D., 2005, Porosity of 3D biornaterial scaffolds and osteogenesis. *Biomaterials*. 26(27): p. 5474-5491.

Katti, K. S., 2004, Biomaterials in total joint replacement. *Colloids and Surfaces B-Biointerfaces*. 39(3): p. 133-142.

Kienapfel, H., Sprey, C., Wilke, A. and Griss, P., 1999, Implant fixation by bone ingrowth. *Journal of Arthroplasty*. 14(3): p. 355-368.

Kilpadi, D. V., Raikar, G. N., Liu, J., Lemons, J. E., Vohra, Y. and Gregory, J. C., 1998, Effect of surface treatment on unalloyed titanium implants: Spectroscopic analyses. *Journal of Biomedical Materials Research*. 40(4): p. 646-659.

Kim, H. M., Himeno, T., Kawashita, M., Lee, J. H., Kokubo, T. and Nakamura, T., 2003, Surface potential change in bioactive titanium metal during the process of apatite formation in simulated body fluid. *Journal of Biomedical Materials Research Part A*. 67A(4): p. 1305-1309.

Kim, H. M., Miyaji, F., Kokubo, T. and Nakamura, T., 1996, Preparation of bioactive Ti and its alloys via simple chemical surface treatment. *Journal of Biomedical Materials Research*. 32(3): p. 409-417.

Kim, H. M., Miyaji, F., Kokubo, T. and Nakamura, T., 1997, Effect of heat treatment on apatite-forming ability of Ti metal induced by alkali treatment. *Journal of Materials Science-Materials in Medicine*. 8(6): p. 341-347.

Kim, H. M., Takadama, H., Miyaji, F., Kokubo, T., Nishiguchi, S. and Nakamura, T., 2000, Formation of bioactive functionally graded structure on Ti-6Al-4V alloy by chemical surface treatment. *Journal of Materials Science-Materials in Medicine*. 11(9): p. 555-559.

Kokubo, T., 1998, Apatite formation on surfaces of ceramics, metals and polymers in body environment. *Acta Materialia*. 46(7): p. 2519-2527.

Kokubo, T., 2008, Development of bioactive materials based on surface chemistry. *Journal of the European Ceramic Society*. 29(7): p. 1267-1274

Kokubo, T., Kim, H. M., Kawashita, M. and Nakamura, T., 2004, Bioactive metals: preparation and properties. *Journal of Materials Science-Materials in Medicine*. 15(2): p. 99-107.

Kokubo, T., Miyaji, F., Kim, H. M. and Nakamura, T., 1996, Spontaneous formation of bonelike apatite layer on chemically treated titanium metals. *Journal of the American Ceramic Society*. 79(4): p. 1127-1129.

Kokubo, T. and Takadama, H., 2006, How useful is SBF in predicting in vivo bone bioactivity? *Biomaterials*. 27(15): p. 2907-2915.

Kumta, P. N., Sfeir, C., Lee, D. H., Olton, D. and Choi, D., 2005, Nanostructured calcium phosphates for biomedical applications: novel synthesis and characterization. *Acta Biomaterialia*. 1(1): p. 65-83.

Lee, B. H., Kim, Y. D., Shin, J. H. and Lee, K. H., 2002, Surface modification by alkali and heat treatments in titanium alloys. *Journal of Biomedical Materials Research*. 61(3): p. 466-473.

Lee, T. M., Chang, E. and Yang, C. Y., 1998, Surface characteristics of Ti6Al4V alloy: effect of materials, passivation and autoclaving. *Journal of Materials Science-Materials in Medicine*. 9(8): p. 439-448.

Li, J. P., Li, S. H., Van Blitterswijk, C. A. and de Groot, K., 2005, A novel porous Ti6Al4V: Characterization and cell attachment. *Journal of Biomedical Materials Research Part A*. 73A(2): p. 223-233.

Liang, F. H., Zhou, L. and Wang, K. G., 2003, Apatite formation on porous titanium by alkali and heat-treatment. *Surface & Coatings Technology*. 165(2): p. 133-139.

Liu, X. Y., Chu, P. K. and Ding, C. X., 2004, Surface modification of titanium, titanium alloys, and related materials for biomedical applications. *Materials Science & Engineering R-Reports*. 47(3-4): p. 49-121.

Long, M. and Rack, H. J., 1998, Titanium alloys in total joint replacement - a materials science perspective. *Biomaterials*. 19(18): p. 1621-1639.

Lu, X. and Leng, Y., 2005, Theoretical analysis of calcium phosphate precipitation in simulated body fluid. *Biomaterials*. 26(10): p. 1097-1108.

Lu, X., Wang, Y. B., Yang, X. D., Zhang, Q. Y., Zhao, Z. F., Weng, L. T. and Leng, Y., 2008, Spectroscopic analysis of titanium surface functional groups under various surface modification and their behaviors in vitro and in vivo. *Journal of Biomedical Materials Research Part A*. 84A(2): p. 523-534.

Lu, X., Zhao, Z. F. and Leng, Y., 2007, Biomimetic calcium phosphate coatings on nitric-acid-treated titanium surfaces. *Materials Science & Engineering C-Biomimetic and Supramolecular Systems*. 27(4): p. 700-708.

Markov, L.V.,1995,Crystal growth for Beginners: Fundamentals of Nucleation, Crystal Growth, and Epitaxy,Worl Scientific

Mathew, M., Brown, W. E., Schroeder, L. W. and Dickens, B., 1988, Crystal-structure of octacalcium bis(hydrogenphosphate) tetrakis(phosphate)pentahydrate, CA8(HPO4)2(PO4)4.5H2O. *Journal of Crystallographic and Spectroscopic Research*. 18(3): p. 235-250.

Mullin, J.W.,2001,Crystallization,Butterworth-Heinemann

Nanci, A., Wuest, J. D., Peru, L., Brunet, P., Sharma, V., Zalzal, S. and McKee, M. D., 1998, Chemical modification of titanium surfaces for covalent attachment of biological molecules. *Journal of Biomedical Materials Research*. 40(2): p. 324-335.

Narayanan, R., Seshadri, S. K., Kwon, T. Y. and Kim, K. H., 2008, Calcium phosphate-based coatings on titanium and its alloys. *Journal of Biomedical Materials Research Part B-Applied Biomaterials*. 85B(1): p. 279-299.

Nguyen, H. Q., Deporter, D. A., Pilliar, R. M., Valiquette, N. and Yakubovich, R., 2004, The effect of sol-gel-formed calcium phosphate coatings on bone ingrowth and osteoconductivity of porous-surfaced Ti alloy implants. *Biomaterials*. 25(5): p. 865-876.

Oh, I. H., Nomura, N. and Hanada, S., 2002, Microstructures and mechanical properties of porous titanium compacts prepared by powder sintering. *Materials Transactions*. 43(3): p. 443-446.

Oh, I. H., Nomura, N., Masahashi, N. and Hanada, S., 2003, Mechanical properties of porous titanium compacts prepared by powder sintering. *Scripta Materialia*. 49(12): p. 1197-1202.

Peters, C. Leyens and M.,2003,Titanium and Titanium Alloys: Fundamentals and Applications,WILEY-VCH

Pilliar, R. M., 1983, Powder metal-made orthopedic implants with porous surface for fixation by tissue ingrowth. *Clinical Orthopaedics and Related Research*,(176): p. 42-51.

Pilliar, R. M., 1987, Porous-Surfaced Metallic Implants for Orthopedic Applications. *Journal of Biomedical Materials Research-Applied Biomaterials*. 21(A1): p. 1-33.

Rho, J. Y., Kuhn-Spearing, L. and Zioupos, P., 1998, Mechanical properties and the hierarchical structure of bone. *Medical Engineering & Physics*. 20(2): p. 92-102.

Ryan, G., Pandit, A. and Apatsidis, D. P., 2006, Fabrication methods of porous metals for use in orthopaedic applications. *Biomaterials*. 27(13): p. 2651-2670.

Sarro, M. I., Moreno, D. A., Ranninger, C., King, E. and Ruiz, J., 2006, Influence of gas nitriding of Ti6Al4V alloy at high temperature on the adhesion of Staphylococcus aureus. *Surface & Coatings Technology*. 201(6): p. 2807-2812.

Sayer, M., Stratilatov, A. D., Reid, J., Calderin, L., Stott, M. J., Yin, X., MacKenzie, M., Smith, T. J. N., Hendry, J. A. and Langstaff, S. D., 2003, Structure and composition of silicon-stabilized tricalcium phosphate. *Biomaterials*. 24(3): p. 369-382.

Sculco, T. P., 1995, The economic-impact of infected joint arthroplasty. *Orthopedics*. 18(9): p. 871-873.

Sittig, C., Textor, M., Spencer, N. D., Wieland, M. and Vallotton, P. H., 1999, Surface characterization of implant materials cp Ti, Ti-6Al-7Nb and Ti-6Al-4V with

different pretreatments. *Journal of Materials Science-Materials in Medicine*. 10(1): p. 35-46.

Slosarczyk, A. and Piekarczyk, J., 1999, Ceramic materials on the basis of hydroxyapatite and tricalcium phosphate. *Ceramics International*. 25(6): p. 561-565.

Song, Y., Xu, D. S., Yang, R., Li, D., Wu, W. T. and Guo, Z. X., 1999, Theoretical study of the effects of alloying elements on the strength and modulus of beta-type bio-titanium alloys. *Materials Science and Engineering a-Structural Materials Properties Microstructure and Processing*. 260(1-2): p. 269-274.

Taborelli, M., Jobin, M., Francois, P., Vaudaux, P., Tonetti, M., SzmuklerMoncler, S., Simpson, J. P. and Descouts, P., 1997, Influence of surface treatments developed for oral implants on the physical and biological properties of titanium .1. Surface characterization. *Clinical Oral Implants Research*. 8(3): p. 208-216.

Tache, A., Gan, L., Deporter, D. and Pillar, R. M., 2004, Effect of surface chemistry on the rate of osseointegration of sintered porous-surfaced Ti-6Al-4V implants. *International Journal of Oral & Maxillofacial Implants*. 19(1): p. 19-29.

Takadama, H., Kim, H. M., Kokubo, T. and Nakamura, T., 2001a, TEM-EDX study of mechanism of bonelike apatite formation on bioactive titanium metal in simulated body fluid. *Journal of Biomedical Materials Research*. 57(3): p. 441-448.

Takadama, H., Kim, H. M., Kokubo, T. and Nakamura, T., 2001b, An X-ray photoelectron spectroscopy study of the process of apatite formation on bioactive titanium metal. *Journal of Biomedical Materials Research*. 55(2): p. 185-193.

Takemoto, M., Fujibayashi, S., Matsushita, T., Suzuki, J., Kokubo, T. and Nakamura, T.,2006a,Enhanced osteoinductivity of porous titanium implant by sodium removal, ed. T. Nakamura, K. Yamashita and M. Neo,1315-1318,

Takemoto, M., Fujibayashi, S., Neo, M., So, K., Akiyama, N., Matsushita, T., Kokubo, T. and Nakamura, T., 2007, A porous bioactive titanium implant for spinal interbody fusion: an experimental study using a canine model. *Journal of Neurosurgery-Spine*. 7(4): p. 435-443.

Takemoto, M., Fujibayashi, S., Neo, M., Suzuki, J., Kokubo, T. and Nakamura, T., 2005, Mechanical properties and osteoconductivity of porous bioactive titanium. *Biomaterials*. 26(30): p. 6014-6023.

Takemoto, M., Fujibayashi, S., Neo, M., Suzuki, J., Matsushita, T., Kokubo, T. and Nakamura, T., 2006b, Osteoinductive porous titanium implants: Effect of sodium removal by dilute HCl treatment. *Biomaterials*. 27(13): p. 2682-2691.

Takeuchi, M., Abe, Y., Yoshida, Y., Nakayama, Y., Okazaki, M. and Akagawa, Y., 2003, Acid pretreatment of titanium implants. *Biomaterials*. 24(10): p. 1821-1827.

Tasdemirci, A., Hizal, A., Altindis, M., Hall, I. W. and Guden, M., 2008, The effect of strain rate on the compressive deformation behavior of a sintered Ti6Al4V powder compact. *Materials Science and Engineering a-Structural Materials Properties Microstructure and Processing*. 474(1-2): p. 335-341.

Teughels, W., Van Assche, N., Sliepen, I. and Quirynen, M., 2006, Effect of material characteristics and/or surface topography on biofilm development. *Clinical Oral Implants Research*. 17: p. 68-81.

Tsukeoka, T., Suzuki, M., Ohtsuki, C., Tsuneizumi, Y., Miyagi, J., Sugino, A., Inoue, T., Michihiro, R. and Moriya, H., 2005, Enhanced fixation of implants by bone ingrowth to titanium fiber mesh: Effect of incorporation of hydroxyapatite powder. *Journal of Biomedical Materials Research Part B-Applied Biomaterials*. 75B(1): p. 168-176.

Vanzillotta, P. S., Sader, M. S., Bastos, I. N. and Soares, G. D., 2006, Improvement of in vitro titanium bioactivity by three different surface treatments. *Dental Materials*. 22(3): p. 275-282.

Vehof, J. W. M., Spauwen, P. H. M. and Jansen, J. A., 2000, Bone formation in calcium-phosphate-coated titanium mesh. *Biomaterials*. 21(19): p. 2003-2009.

Wang, C. C., Chsu, Y., Hsieh, M. C., Yang, S. P., Su, F. C. and Lee, T. M., 2008, Effects of nano-surface properties on initial osteoblast adhesion and Ca/P adsorption ability for titanium alloys. *Nanotechnology*. 19(33).

Wang, X. J., Wang, G. W., Liang, J., Cheng, J. T., Ma, W. and Zhao, Y. M., 2009a, Staphylococcus aureus adhesion to different implant surface coatings: An in vitro study. *Surface & Coatings Technology*. 203(22): p. 3454-3458.

Wang, X. Q., Qiu, S. J., Yao, X., Tang, T. T., Dai, K. R. and Zhu, Z. A., 2009b, Berberine Inhibits Staphylococcus Epidermidis Adhesion and Biofilm Formation on the Surface of Titanium Alloy. *Journal of Orthopaedic Research*. 27(11): p. 1487-1492.

Webmineral-Brushite,http://webmineral.com/data/Brushite.shtml, (accessed 15 March 2010)

Webmineral-hydroxyapatite,http://webmineral.com/data/Apatite-(CaOH).shtml, (accessed 15 March 2010)

Webmineral-Monetite,http://webmineral.com/data/Monetite.shtml, (accessed 15 March 2010)

Wei, M., Kim, H. M., Kokubo, T. and Evans, J. H., 2002, Optimising the bioactivity of alkaline-treated titanium alloy. *Materials Science & Engineering C-Biomimetic and Supramolecular Systems*. 20(1-2): p. 125-134.

Welsh, R. P., Pilliar, R. M. and Macnab, I., 1971, Surgical implants-role of surface porosity in fixation to bone and acrylic. *Journal of Bone and Joint Surgery-American Volume*. A 53(5): p. 963-&.

Wen, C. E., Mabuchi, M., Yamada, Y., Shimojima, K., Chino, Y. and Asahina, T., 2001, Processing of biocompatible porous Ti and Mg. *Scripta Materialia*. 45(10): p. 1147-1153.

Wen, C. E., Yamada, Y., Shimojima, K., Chino, Y., Asahina, T. and Mabuchi, M., 2002a, Processing and mechanical properties of autogenous titanium implant materials. *Journal of Materials Science-Materials in Medicine*. 13(4): p. 397-401.

Wen, C. E., Yamada, Y., Shimojima, K., Chino, Y., Hosokawa, H. and Mabuchi, M., 2002b, Novel titanium foam for bone tissue engineering. *Journal of Materials Research*. 17(10): p. 2633-2639.

Wen, H. B., de Wijn, J. R., Cui, F. Z. and de Groot, K., 1998a, Preparation of calcium phosphate coatings on titanium implant materials by simple chemistry. *Journal of Biomedical Materials Research*. 41(2): p. 227-236.

Wen, H. B., van den Brink, J., de Wijn, J. R., Cui, F. Z. and de Groot, K., 1998b, Crystal growth of calcium phosphate on chemically treated titanium. *Journal of Crystal Growth*. 186(4): p. 616-623.

Wen, H. B., Wolke, J. G. C., deWijn, J. R., Liu, Q., Cui, F. Z. and deGroot, K., 1997, Fast precipitation of calcium phosphate layers on titanium induced by simple chemical treatments. *Biomaterials*. 18(22): p. 1471-1478.

Xie, J. H. and Luan, B. L., 2008, Nanometer-scale surface modification of Ti6Al4V alloy for orthopedic applications. *Journal of Biomedical Materials Research Part A*. 84A(1): p. 63-72.

Yan, W. Q., Nakamura, T., Kawanabe, K., Nishigochi, S., Oka, M. and Kokubo, T., 1997a, Apatite layer-coated titanium for use as bone bonding implants. *Biomaterials*. 18(17): p. 1185-1190.

Yan, W. Q., Nakamura, T., Kobayashi, M., Kim, H. M., Miyaji, F. and Kokubo, T., 1997b, Bonding of chemically treated titanium implants to bone. *Journal of Biomedical Materials Research*. 37(2): p. 267-275.

Yau, S. T. and Vekilov, P. G., 2000, Quasi-planar nucleus structure in apoferritin crystallization. *Nature*. 406(6795): p. 494-497.

Zhang, Q. Y., Leng, Y. and Xin, R. L., 2005, A comparative study of electrochemical deposition and biomimetic deposition of calcium phosphate on porous titanium. *Biomaterials*. 26(16): p. 2857-2865.

Zhu, X. L., Son, D. W., Ong, J. L. and Kim, K., 2003, Characterization of hydrothermally treated anodic oxides containing Ca and P on titanium. *Journal of Materials Science-Materials in Medicine*. 14(7): p. 629-634.

Zimmerli, W., 2006, Prosthetic-joint-associated infections. *Best Practice & Research in Clinical Rheumatology*. 20(6): p. 1045-1063.

Zimmerli, W., Trampuz, A. and Ochsner, P. E., 2004, Current concepts: Prosthetic-joint infections. *New England Journal of Medicine*. 351(16): p. 1645-1654.

VITA

Uğur TÜRKAN

EDUCATION

- ✓ *B.Sc: (2000)* Department of Physics, Ege University, Turkey.
- ✓ *M.Sc:(2004)* Materials Science and Engineering Programme, Izmir Institute of Technology, Turkey (in English).
- ✓ *PhD: (2010)* Department of Mechanical Engineering, Izmir Institute of Technology.

EMPLOYMENT HISTORY

- ✓ Research Assistant in Mechanical Engineering 12/2006-present
  İzmir Institute of Technology
- ✓ Research Assistant in Material Science & Engineering Dept. 12/2001-12/2006
  İzmir Institute of Technology

SELECTED PUBLICATIONS

- ✓ O. Ozturk, U. Turkan, A. Eroglu, "Metal ion release from nitrogen ion implanted CoCrMo orthopedic implant material" Surface and Coatings Technology, Volume 200, Issues 20-21
- ✓ M. E. Dizlek, U. Turkan, M. Guden, A. Tasdemirci, "Processing and compression testing of Ti6Al4V foams for biomedical applications" Journal of Material Science (2009) Volume 44, pages:1512-1519
- ✓ U. Turkan, M. Guden, "Effects of surface treatment on the CaP deposition in open cell Ti6Al4V foams" (Ceramics International doi:10.1016/j.ceramint.2010.03.030)
- ✓ U. Turkan, M. Guden, "The effect of nitric acid surface treatment on CaP deposition of Ti6Al4V open cell foams in SBF solution" Surface amd Coating Tech.(accepted for publication)